THE IMPACT BEHAVIOUR OF LOW VELOCITY CHARGED MICROSPHERES ON PLANAR TARGET SURFACES

Stephen Cook, B.Sc., M.Sc.

A Thesis submitted for the Degree of Doctor of Philosophy.

The University of Aston in Birmingham

April 1982

The University of Aston in Birmingham

The impact behavour of low velocity charged microspheres on planar target surfaces

A thesis submitted for the degree of Doctor of Philosophy by Stephen Cook (1982)

SUMMARY

Details are given of an experimental and theoretical investigation into the low-velocity ($< 50\ ms^{-1}$) impact behaviour of charged microspheres on planar target surfaces under zero field conditions. The experimental technique is based on a vertically mounted dust-source gun which fires positively charged ($\leqslant 5 \times 10^{-14}C$) microspheres onto a microzone ($\sim 200\ \mu m^2$). Experiments have been performed on a range of microsphere/target combinations, (i.e. Fe/Cu, Ti, Al, W, Mo, stainless steel, Si, glass, p.v.c., mica, ebonite, tufnal, red-fibre and cellulose), and a variety of metal target surface conditions (ambient oxide and highly oxidised): the physical state of the micro-impact zones are monitored using a laser-based ellipsometer.

The investigation concentrated on comparing the incidence of "bouncing" events on the various target materials and established the important general distinction between metals and insulators that they respectively promote <1% and>99% of "bouncing" events per incident sample. Highly oxidised metal surfaces show an increased incidence of "bouncing" events that depends inversely on the impact microsphere charge. The mean mechanical behaviour of the "bouncing" events as measured by the coefficient of restitution, exhibits general trends similar to macroscopic experiments, but with a large scatter in the data which is thought to arise from variations in the dynamic hardness and microtopography of the target surface. The electrical behaviour, as measured by the charge modification ratios, indicates that there is negligible charge exchange in a metal/insulator impact event.

The "sticking" behaviour on metallic and semi-conducting surfaces is interpreted in terms of thermal heating and results in micro-welding or larger adhesive forces during the impact process, produced by electron-phonon scattering in the oxide contact junction where transient electron tunnelling is taking place.

The technological implications of these findings have been exploited in the development of a micron-sized, non-destructive, dynamic hardness measuring device incorporating a computer controlled data acquisition and processing system.

Microparticle, bouncing impact / microhardness / charge exchange

ACKNOWLEDGEMENTS

I would like to thank my supervisor, Dr. R.V. Latham for his advice and many hours of helpful discussion throughout the course of this project.

I would also like to thank the following -
The Physics Workshop staff, especially Mr. F. Lane, for their help in the construction of many components.
Mr. A. Marriott-Reynolds for his help and organization.
Professor S.E. Hunt for the use of the departmental facilities.
The S.E.R.C. for their financial support

My wife, for her unending patience during the course of study.

LIST OF CONTENTS

CHAPTER 5

CHAPTER 6

LIST OF FIGURES

CHAPTER 1

1.0 Introduction

This study is predominantly concerned with the impact behaviour of low velocity, positively charged, microspheres on planar target electrodes, the main aim of this work being to look in more detail at the mechanisms involved in the impact process. In many respects the investigation is the microscopic analogy of a typical macroscopic impact experiment involving say a ball bearing bouncing on a planar anvil. There are, however, several important differences between the microscopic and macroscopic systems which lead to differing impact responses. Firstly, in the microscopic system, the impact takes place over a small area (i.e. approaching single crystal dimensions), so that the local variations in the surface mechanical properties of a typical extended area target electrode lead to a large scatter in the impact behaviour. Conversely, collisions in a macroscopic system will be between polycrystalline surfaces, thus "smoothing out " such variations. Secondly, the critical velocities above which inelastic processes occur are, respectively, $\sim 250\ ms^{-1}$ and $\sim 0.1\ ms^{-1}$ for the microscopic and macroscopic systems. Thus in many macroscopic impact events the collision will involve some form of plastic flow. Thirdly, the variations in surface microtopography of the target surface play a crucial role in a microscopic impact where "multi-impacts" and oblique angle reflections can arise and then give rise, again, to a large scatter in the impact behaviour.

The impacting microspheres used in this study are produced from a modified, low velocity, version of the dust source gun (1) originally developed by Shelton et al (2) and subsequently used by Friichtenicht (3) for use in hypervelocity micrometeorite simulation

experiments. The particles delivered by this type of "gun" possess a positive charge which not only allows them to be detected electrically but has the advantage of providing a means of characterising the particle in terms of its mass and velocity. However, the particle charge has the disadvantage that it complicates the impact process. Thus, whereas in a macroscopic experiment only the mechanical behaviour of the surfaces has to be considered, in the microscopic case the electrical interactions associated with the particle charge also have to be taken into account, i.e. representing a further "difference" between the macro and micro impacting systems.

In introducing the present investigation it should be pointed out that it has evolved directly from the earlier work of Brah (4) and Mohindra (5), in this laboratory, who were studying the impact behaviour of charged microspheres under high field conditions. The principle aim of their work was to simulate the conditions prevailing in a high voltage vacuum gap and hence study under controlled conditions a multiple bouncing mechanism whereby a microparticle can initiate the electrical breakdown of such a gap (6). In this context they were particularly interested in the fundamental physical mechanisms by which the charge on say a positively charged particle can be reversed during a bouncing impact on a negatively charged electrode. Since one of the central themes of the work described in this thesis is to gain a better understanding of the general phenomena of charge exchange during a bouncing impact, it is appropriate at this point to briefly review the main findings of this earlier work and indicate its relevance to the practical situation of a H.V. gap. It is also important to note that many of the techniques used in these earlier studies have been applied in the present study.

The concept of microparticle initiated breakdown was first

proposed by Cranberg (7) and later modified by Slivkov (8). In this model a microparticle is assumed to be torn from an electrode surface by the applied field and, because of its charge, accelerated across the gap to impact on the opposite electrode as a high velocity projectile. Thus, if the impact K.E. is sufficient to cause localised fusion and vaporisation of the electrode material it is possible for such an event to trigger the breakdown of the gap. However, to account for the observation of microparticle initiated breakdown at low gap voltages where the incident K.E. is initially too low to generate a microplasma, Latham (6), as mentioned above, has proposed a further modification to this earlier single transit, impact initiated, breakdown model whereby the kinetic energy of a microparticle can be enhanced to a critical value following a multi-transit bouncing sequence between the electrodes of a high voltage gap; the essential requirement of this model is that there is a reversal of the particle charge and momentum at each impact, (see Figure 1.1). The results

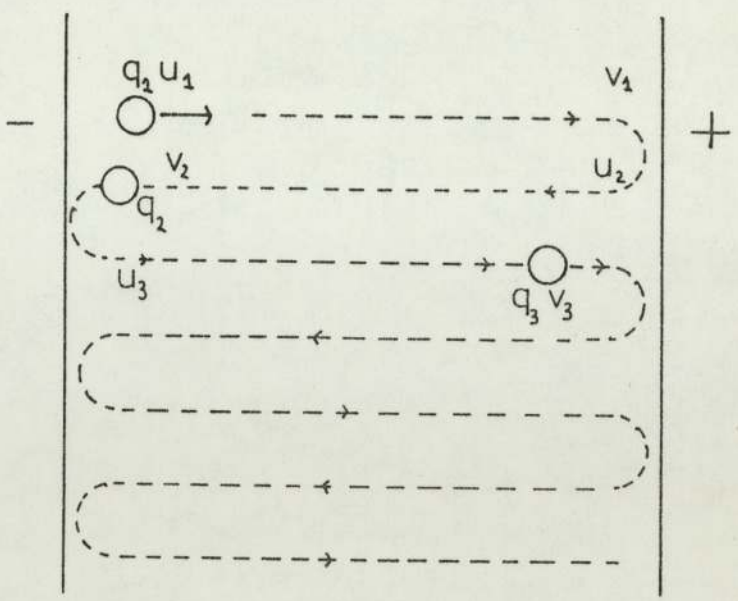

Figure 1.1: Particle "bouncing" in an inter-electrode gap

of the simulation experiments, outlined above, indicated that the charge reversal process and hence the momentum enhancement were dependant upon the target material. In order to obtain more detailed information about the important physical parameters that control this mechanism, these earlier workers undertook an extended investigation involving a variety of particle/target regimes. For these measurements, the response of a surface was characterised, firstly, by measuring the incident and reflected particle velocity for each particle bouncing event, and hence determining the local coefficient of restitution, while, secondly, the measurement of the particle charge before and after impact leads to information on the charge exchange process. It was found that although the microscopic mechanical properties of the target surface play a significant role in the bouncing mechanism, the controlling factor was the electrical properties of the colliding surfaces,in particular the level and type of oxidation, since these determine the charge reversal mechanism during the bouncing impact. In fact, a later study (9) showed that the efficiency of the charge reversal mechanism was greatly enhanced as the target oxide film was removed. Conversely, a thick surface oxide tended to inhibit the process. Summarising therefore, these initial simulation experiments have shown that both the elastic character of the impact event and the efficiency of the charge exchange mechanism are strongly dependant on (i) the combination of target and particle materials, (ii) the target surface conditions (oxide coverage) and (iii) the magnitude of the gap field. It is however important to emphasize that the data obtained from these simulation experiments showed a large amount of scatter, due, it was thought, to large local variations in the microscopic conditions across the extended area electrode.

The starting point of this study was to look more closely at the large variations in the microscopic properties across the target surface which give rise to the scatter in the recorded data, and hopefully obtain more detailed information on the impact process. This has involved reducing the impact zone for the "test" microparticles and the spot size of the analytical ellipsometric facility so that it is possible to more accurately correlate the local properties of the surface with the observed particle impact behaviour. Experimentally, this has required developing a vertical microparticle facility and a laser based ellipsometer. To reduce the variables involved in the complex impact process, measurements are made under zero field conditions. The major part of the present investigation has been devoted to the study of the differing impact responses obtained from ambient oxide metal, high oxidised metal, semi-conducting and insulating surfaces since these represent extremes in electrical and mechanical properties. Further experimental modifications include (i) a sophisticated target manipulator, (ii) target assembly modules, (iii) an extended series of particle collimators and (iv) improved signal detection amplifiers.

Since it is necessary to take a large sample of events to obtain a meaningful average impact response, the measurement and calculation of the mechanical and electrical processes occurring during the impact event is performed using a computer controlled data acquisition system. This allows on-line determination of the coefficient of restitution, together with the charge modification ratios, to be made using analogue-to-digital techniques. A particularly attractive practical application of this data handling system is that from the data associated with an insulating surface a micron-sized, non-destructive, dynamic hardness testing tool can be envisaged, (see Chapter 6).

To complement these experimental studies, a theoretical survey of the mechanical and electrical properties of the process is presented. This includes all the existing impact theories, suitably modified for the zero field regime of this study, together with a detailed analysis of the physical mechanisms that can operate before and during the impact event and hence influence the "bouncing" behaviour of a particle; these include the influence of the image force, Van der Waal forces, and adhesive forces. Furthermore, a corresponding theory of mechanical energy loss due to surface elastic processes, elastic waves, surface topography, etc., will be applied to the impact behaviour of metal and insulating surfaces. As another point in this survey, particular attention will be given to the thermal effects resulting from the electron tunnelling mechanism in the oxide junction (electron-phonon scattering) since this is thought to account for the widely differing particle "bouncing" behaviour between the various metal targets studied. These ideas will be further highlighted in the discussion chapter (5) where the microscopic mechanical properties together with the electrical properties of the surface oxide will be discussed as a means of accounting for the differing responses observed during the impact of microspheres on a target electrode.

CHAPTER 2

2.0 Theoretical considerations

The theoretical expressions derived in the following sections, for zero field conditions, will be used more fully in Chapter 5 where the interpretation of the mechanical and electrical data arising from the impact of charged microspheres on planar target electrodes, together with the associated ellipsometric readings will be considered in detail. Primarily we are concerned with the fundamental process arising during a low velocity impact, i.e., at velocities less than the critical velocity for plastic impact (see later) however for completeness the zero field data arising from hypervelocity experiments will be included. Specifically we can divide the impact event into mechanical and electrical processes which, respectively, govern the momentum and charge exchange behaviour.

2.1 Mechanical considerations

The impact between two surfaces is extremely complex and can involve elastic and plastic processes, together with elastic waves and shock waves at the solid-solid interface. The extent to which of these processes can dominate depends, firstly on the K.E. of the impacting surfaces (i.e., the impact velocity and masses of the associated bodies), and secondly on such physical properties as Young's Modulus, density, restitution coefficient, melting point, specific heat capacity and thermal conductivity.

In this present study we are predominantly concerned with the low velocity impact regime, i.e., below 100 ms^{-1}, where, as suggested by Bjork (10) no cratering or impact ionization is likely to occur. This limiting condition, for this regime, has been confirmed theoretically by Cook (11) who has obtained an expression for the critical velocity (V_c),

beyond which semi-elastic or plastic behaviour begins, using the hydrodynamic theory of fluid jets, such that :

$$V_c = 2.7 \left(\frac{\rho}{P}\right)^{\frac{1}{2}} \quad \ldots 2.1$$

where P and ρ are the yield strength and density of the material respectively.

On substituting values relevant to the present study it is found that $V_c \sim 360\ ms^{-1}$. Since this value is well in excess of the velocities used in the present microparticle studies it is expected that no plastic flow will occur.

2.1.1 Elastic impact

It is apparent that, in practise, the topographical character of the surface of the target electrode will have a significant effect on the dynamic process involved in a collision between a sphere and a plane. Thus, if the sphere dimensions are comparable with the size of the undulations and asperities on the target, as is the case with the present microscopic experiments, the impact event may be determined by the real area of contact. However, for convenience of the theoretical analysis, consider the situation of a perfectly smooth sphere in contact with a planar surface, under a light load such that the total process is elastic.

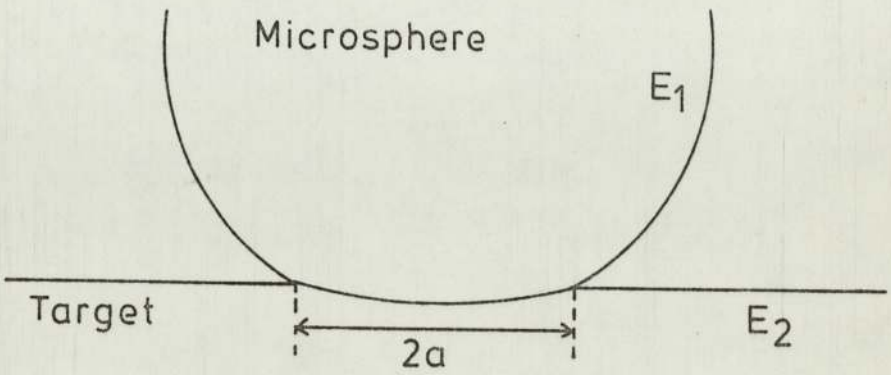

Figure 2.1: Microsphere / Planar target impact model

Referring to Figure 2.1, the contact radius (a) derived by Hertz (12) is given by

$$a = 1.1 \left(\frac{W}{2} Rp \left(\frac{1}{E_1} + \frac{1}{E_2}\right)\right)^{1/3} \quad \ldots 2.2$$

where it is assumed that Poissons ratio is 0.3, W is the applied load, Rp the radius of the sphere and E_1 and E_2 Youngs Modulus for the sphere and the plane respectively. The contact area (πa^2) of the resulting indentation is proportional to $W^{2/3}$ and the mean contact pressure P_m , given by $W/\pi a^2$ is proportional to $W^{1/3}$. Using a similar approach Hutchings (13) has applied the Hertz theory of elastic impact to obtain an expression for the mean contact pressure (P_m) during an elastic impact, viz :

$$P_m^5 = \frac{1280}{243\pi^4} \rho \, u^2 \left(\frac{1}{f(E)}\right)^4 \quad \ldots 2.3$$

where ρ is the density of the target material, u the impact velocity of the sphere and f(E) is a function of the sphere/target mechanical constants having the form

$$f(E) = \frac{1 - \sigma_1^2}{E_1} + \frac{1 - \sigma_2^2}{E_2} \quad \ldots 2.4$$

where σ and E are Poissons Ratio and Youngs Modulus respectively. It should be noted that an important consequence of equation 2.3 is that the mean contact pressure is independant of the size of the impacting particle. For the case where the contact plane is mechanically softer than the impacting microsphere , Andrews (14) has shown that the Hertz theory can be used to obtain an expression for the contact time, viz:

$$t_c = 5.886 \left[\frac{5M}{16K}\right]^{2/5} \frac{1}{u^{1/5}} \quad \ldots 2.5$$

where M is the mass of the sphere and $K = \pi E_{1/3} \sqrt{Rp}$ in which all the parameters have been previously defined. Substituting for K in equation 2.5, gives the contact time as

$$t_c = 5.886 \left[\frac{15M}{16 \pi E_1 Rp^{\frac{1}{2}}} \right]^{2/5} \frac{1}{u^{1/5}} \qquad \ldots 2.6$$

Simplifying further, using the expression for the mass of the microsphere (i.e. $M = 4/3 \; Rp^3 \rho$) leads to

$$t_c = 5.886 \left[\frac{15}{12} \cdot \rho \cdot \frac{Rp^{5/2}}{E_1} \right]^{2/5} \frac{1}{u^{1/5}} \qquad \ldots 2.7$$

Alternatively Hutchings assumes that the time (t_e) taken for the contact pressure to reach its maximum is half the contact time.

i.e.

$$t_e = t_{c/2} = 1.47 \left(\frac{5\pi}{4}\right)^{2/5} \rho^{2/5} \frac{Rp}{u^{1/5}} (f(E))^{2/5} \qquad \ldots 2.8$$

where all the above parameters have been previously defined. It can be seen that the contact time is proportional to the radius of the particle. For the impact of a 2 μm radius carbonyl iron microsphere with a stainless steel target, the variation of the contact time with the impact velocity is shown in Figure 2.2

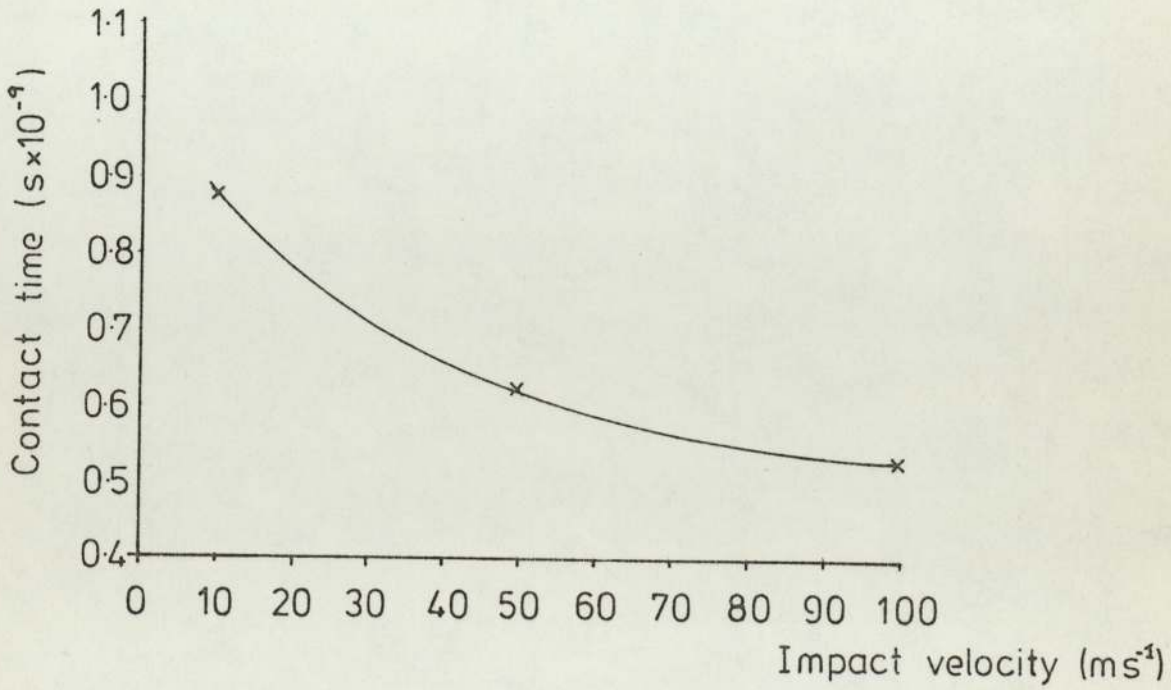

Figure 2.2: The variation of the contact time with particle velocity

An estimation of the mean chordal radius during an elastic impact may be derived using the equation of Tabor (15) for the average strain (A_{st}) for a plastic indentation :

$$A_{st} \simeq 0.2\ a/R_p \qquad \ldots 2.9$$

where a is the chordal radius of the indentation. Hutchings assumes that this estimate of strain is also valid for an elastic impact indentation, giving the mean strain rate during an elastic impact as

$$\dot{A}_{st} = A_{st}/t_e \qquad \ldots 2.10$$

2.1.2 Plastic Impact

If the load is increased between the sphere and the plane (see Figure 2.1) a situation soon arises which leads to the onset of plasticity. Since the load is not uniform across the contact area Timoshenko (16) deduced that the condition for plasticity is first reached at a point below the contact surfaces, while the results of Davies (17) indicate that the maximum value of shear stress occurs at a position $\sim 0.5a$ below the centre of the circle of contact (see Figure 2.3). If the yield stress of

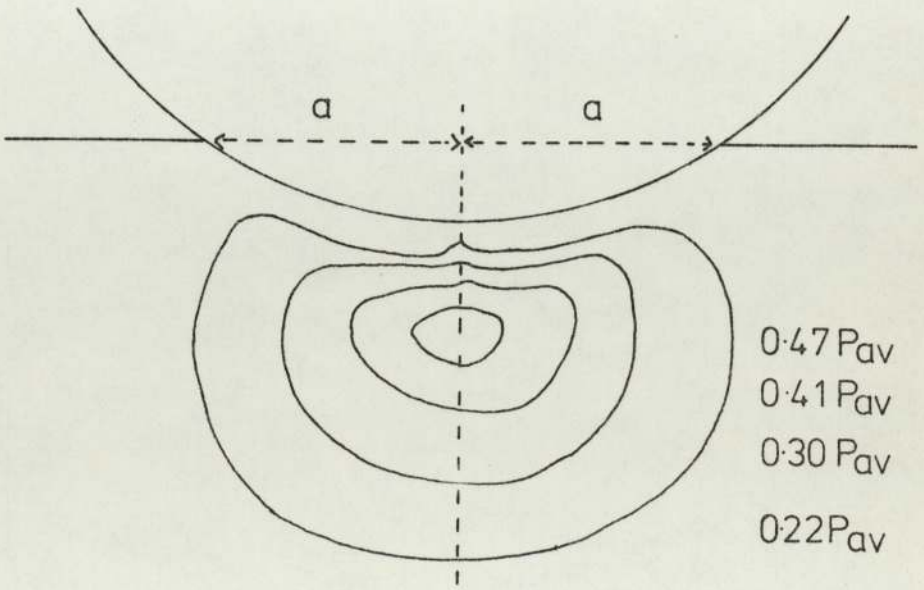

Figure 2.3: Stress distribution under contact area; P_{av} = average pressure [17]

the material is Y, plastic deformation starts when

$$P_m \sim 1.1Y \qquad \ldots 2.11$$

Full plasticity occurs when $P_m \sim 2.7Y$, which means that all regions within the contact area are now undergoing plastic flow. Ishlinsky (18) has suggested that $P_m = 2.6 \rightarrow 2.9Y$ for the case of a flat punch in contact with a planar surface. Subsequently Tabor (19) has refined the value, letting $P_m = cY$, where c is a constant whose value is close to 3 (depending on the shape and size of the surface irregularities), and has shown that for work-hardened materials, the yield pressure is independent of the load and size of the indentation. The maximum pressure developed before plastic flow begins can be obtained by replacing 'u' in equation 2.3 by the critical velocity (V_c) for an elastic impact.

Tabor (15) has shown that the loading time t_p for a purely plastic collision process is given by :

$$t_p = M/2 \quad R\rho \quad (2\rho/3P)^{\frac{1}{2}} \qquad \ldots 2.12$$

where P is the mean pressure during the formation of the indentation. The mean strain rate for a perfectly plastic process is determined by dividing equation 2.9 by t_p. Alternatively Hutchings (13) has derived the radius of the indentation (a_p) produced during the plastic process by equating the initial kinetic energy of the sphere with the work done in forming the indentation, i.e.

$$a_p = 2^{3/2} R\rho \, u^{\frac{1}{2}} \quad (2\rho/3P)^{1/4} \qquad \ldots 2.13$$

Hence from equation 2.10

$$\dot{A}_{st} = \frac{2^{3/2}}{5\pi} \quad \frac{u^{\frac{1}{2}}}{R} \quad \left(\frac{3P}{2\rho}\right)^{1/4} \qquad \ldots 2.14$$

Figure 2.4 shows the variation of the strain rate with the impact velocity

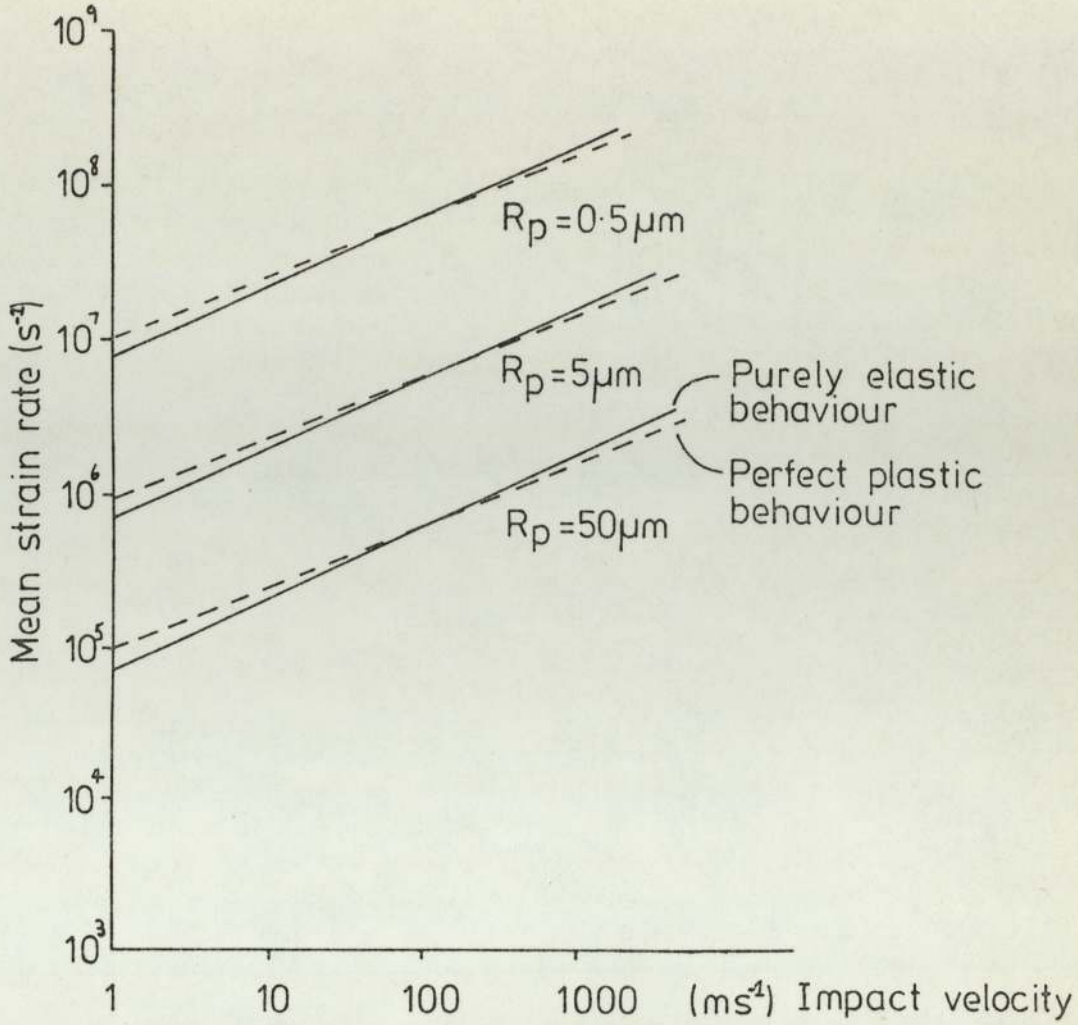

Figure 2·4: The variation of the mean strain rate with impact velocity[13]

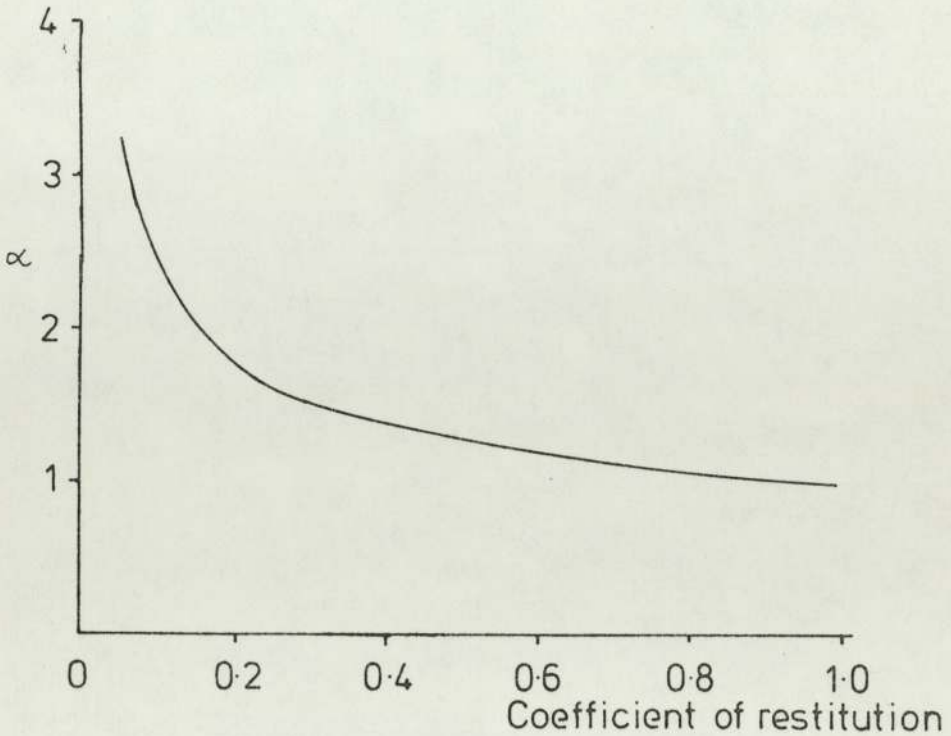

Figure 2.5: The variation of α with the coefficient of restitution[27]

for both elastic and plastic deformation, for the case of a carbonyl iron microsphere impacting on a stainless steel target. In the plastic case, P = 2G.Pa as indicated by the static hardness measurements. From Figure 2.4 it is observed that high strain rates exist for the conditions of the present study and hence could significantly influence the impact event.

2.1.3 Coefficient of restitution

For a perfectly elastic collision between a sphere and a plane the theory of the conservation of energy states that the impact velocity (u) is equal to the return velocity (v), with no energy being lost during the collision. However, in practice, a small amount of energy can be lost in generating elastic waves, K.E. heating of the collision interface, and overcoming the adhesive force, etc. Thus a term called the coefficient of restitution (e) is introduced to account for the energy loss

$$\text{i.e.} \quad e = \frac{v}{u} = \frac{\text{return velocity}}{\text{impact velocity}} \qquad \ldots 2.15$$

For a purely elastic collision e = 1, and so v = u, while for a purely plastic collision e = 0 ("sticking"process) and all the incident kinetic energy is lost in producing an indentation. In general, for a constant impact velocity the harder the impacting materials the greater the value of e.

2.1.4 Elastic waves

During the impact of a hard microsphere on a target which deforms plastically, most of the initial kinetic energy is lost as work in the plastic deformation. However, some is restored, by the elastic forces, to kinetic energy of the returning particle (20). Furthermore a small amount of the impact kinetic energy is used in the

generation of elastic waves. In this connection Lamb (21) has investigated the effect of short duration impulses applied to a point on a plane face of an elastic solid. The main shock, resulting from the impulse, travels along the surface as a solitary surface wave with its total energy remaining unaltered, i.e., unattenuated. Using Lamb's findings, Raman (22) proceeded to develop a theory to enable the coefficient of restitution to be obtained using shock wave effects. At a later date, an estimate of the energy absorbed by elastic waves during the normal impact of a sphere on a plane was carried out by Hunter (23) who, making use of the relations of Miller et al (24,25) and assuming a sudden impulse on a free surface calculated the energy in an elastic wave. For the case of a hard sphere in contact with a steel target, the fraction of the initial kinetic energy dissipated as elastic waves (λ) in the target is :

$$\lambda \sim 1.04 \quad (v/C_0)^{3/5} \qquad \ldots 2.16$$

and for hard spheres on glass

$$\lambda \sim 1.27 \quad (v/C_0)^{3.5} \qquad \ldots 2.17$$

where v is the impact velocity and C_0 the velocity of longitudinal elastic waves along a thin rod of the target material. However, the above expressions are only valid for perfectly elastic impacts, whereas the results of many authors (14,26,4) and for the insulating materials in this study indicate that the 'e' values are less than 1, making the above equations invalid. Hutchings (27) has however determined the amount of energy dissipated in an elastic wave in a semi-infinite target where a certain amount of plastic deformation of the target occurs, and obtained the following expression for λ :

$$\lambda = \alpha\beta\left(\frac{1+\sigma}{1+e}\right)\left(\frac{1-\sigma^2}{1-2\sigma}\right)^{\frac{1}{2}}\frac{4\pi\sqrt{6}}{C^3}\frac{\rho_s}{\rho_t}\left(\frac{P}{\rho_s}\right)^{3/2} \qquad \ldots 2.18$$

where α and β are dimensionless quantities (defined below), σ is Poissons ratio for the target, e the coefficient of restitution, P the constant plastic indentation pressure, ρ_s and ρ_t the densities of the sphere and target respectively and $C_0 = (E/\rho_t)^{\frac{1}{2}}$ with E being Youngs Modulus of the target. It has been shown by Hutchins that α is given by :

$$\alpha = \frac{8}{E_0^2\,\omega_0}\int_0^\infty w^2\left|F(\omega)\right|^2\,dw \qquad \ldots 2.19$$

where $E_0 = 4\pi Rp^2\rho_s u\,(3P/2\rho_s)^{\frac{1}{2}}/3$ with Rp being the radius of the sphere, $F(\omega)$ the Fourier component of $F(t)$ and $\omega_0 = 2\omega_p/(1+e)$ where $\omega_p = (3P/2\rho_s)^{\frac{1}{2}}/r$. Figure 2.5 shows the variation of α with e as plotted by Hutchins. The other dimensionless quantity β is given by equation 17 of Hunter (23), and is fairly insensitive to changes in σ taking values of 0.537 when $\sigma = 0.25$ and 0.415 when $\sigma = 0.333$. Subsequently Hutchins has shown that the expression $\beta(1+\sigma)\left(\frac{1-\sigma^2}{1-2\sigma}\right)^{\frac{1}{2}}$ takes a value of 0.919 for $\sigma = 0.25$ and 0.904 for $\sigma = 0.333$.

For the impact between a carbonyl iron microsphere and a stainless steel target, the process is elastic, so that using equation 2.16, and substituting the relevant parameters, yields a value of $\lambda \sim 2.4 \times 10^{-2}$, i.e., 2.4% of the initial kinetic energy is dissipated as elastic waves within the target. However, for the impact between a microsphere and an insulating target (P.V.C.) which according to Bitter (28) is in a full state of plasticity during collisions, the Hutchings derivation can be used giving, for the P.V.C. surface (see Chapter 4), a value of $\lambda \sim 0.4\%$. Both of these results are in agreement with the theoretical values of Chaudhri et al (29).

In conclusion it can be seen that the fraction of energy dissipated as elastic waves is small. Miller et al (25) have determined the amount of energy contained by the three components constituting the elastic wave for a value of $\sigma = 0.25$. It was found that 6.8% of the energy is carried by compressional waves, 25.8% by shear waves and 67.4% by surface (Rayleigh) waves.

2.1.5 Hypervelocity impact - mechanical effects

It has already been established that the critical velocity (V_c) above which plastic impact behaviour begins is ~0·2-0·4 km.s^{-1}. Therefore it is to be expected that in a high velocity impact (at velocities $\gtrsim$ 500 ms^{-1}) that severe deformation of the target will take place. This has subsequently been confirmed by Dietzel et al (30), in their micrometeroid studies, involving the impact of iron particles on various target electrodes. It was observed that for impact velocities < 0.5 kms^{-1} the particles underwent semi-elastic reflections from all the target materials studied, while at 0.8 kms^{-1} impact cratering began. For velocities between 1 and 1.5 kms^{-1} the particle remained almost intact but completely embedded in the impact crater, while at still higher velocities up to 10 kms^{-1} the impacting particle was deformed to an approximately coherent layer inside the crater together with the occurrence of impact ionization. From an X-ray analysis used to discover the products of the crater, Dietzel et al were able to form the following relation :

$$I_{rel}\,(K) = m\, f\,(u) \qquad \ldots 2.20$$

where I_{rel} (K) is related to the projective material in the crater, m is the particle mass and f(u) is a function connecting the velocity of the particle with the impacting target materials. Using an expression obtained by Rudolph (31) for the diameter (D) of the impact crater, i.e.

$$D = c\ m^{1/3}\ u^{2/3} \quad \text{for} \quad u \geqslant 1\ \text{kms}^{-1} \qquad \ldots 2.21$$

where c is a material constant and u the impact velocity of the particle, Dietzel et al were able to determine the mass (m) and velocity (u) of the impacting particle.

$$\text{i.e.} \quad f(u)\ u^2 = c'\ I_{rel}\ (K)/D^3 \qquad \ldots 2.22$$

where c′ is another constant. Similar impact behaviour has also been observed by Smith et al (32), Auer et al (33) and Hansen (34). However the fundamental physical processes which arise in the impact event, i.e., shock impact phenomena and the partition of the impact energy, will be discussed, more conveniently, in Chapter 5.

2.2 Electrical Interaction

It is apparent that even under the zero field conditions of this study that the role played by the charge on the microsphere, the surface oxides of the microsphere/target combination and the type of the impacting materials can all influence the electrical processes arising in the impact event. At relatively large approach distances, $\sim 1000\text{Å}$, the attractive forces arising from the image charge and Van der Waal interactions act upon the microsphere, while at even smaller sphere/plane separations, $\sim 250\text{Å}$, metal-vacuum-metal tunnelling and field emission processes, involving electron transfer from the target to the microsphere, may give rise to microsphere charge reduction. Once contact arises the amount of charge exchanged via the tunnelling process depends on the conductivity of the surface oxide films, bias voltage (arising from the microsphere potential) across the tunnelling oxide junction and the work function of the microsphere / target combinations. Therefore it is important to determine the extent to which these parameters affect the impact event.

2.2.1 Metal-vacuum-metal tunnelling

Consider the diagram of a metal-vacuum interface, Figure 2.6. At 0°K all the allowed electronic states are filled in the metal up to an upper level called the Fermi level, E_F, while electrons within the vacuum possess a certain minimum energy, E_{vac}. In general, for all known metals, the Fermi level lies below the vacuum level, therefore energy must be given to electrons in the metal if they are to surmount the metal-vacuum barrier. The minimum energy for this to occur is called the work function and is denoted by $\emptyset$. As the temperature of the metal is increased, there is a finite probability of electrons being thermionically excited to a higher energy level. In the free electron model of Sommerfield, where all the available energy is kinetic (Potential energy is zero and no interaction occurs between electrons) the relationship between energy (E) and momentum (P) is thus :

$$E = \frac{1}{2m} (P_x^2 + P_y^2 + P_z^2) \qquad \ldots 2.23$$

where m is the mass of the electron and x, y, z refer to a 3 dimensional co-ordinate system. For an electron to escape it must possess this amount of energy and be moving in the correct direction. If x is the direction perpendicular to the face of the potential barrier

$$\frac{P_x^2}{2m} > E_F + \emptyset \qquad \ldots 2.24$$

However, modifications to the model allow for the effect of (i) an electrostatic field and (ii) an applied field to be introduced. If the image charge is included, the potential barrier changes from that in Figure 2.7(a) to that indicated in Figure 2.7(b) while the effect of an applied field alone is indicated in Figure 2.7(c). If both effects are included the barrier shape changes to that shown in Figure 2.7(d). At higher temperatures it is possible for an electron to escape from

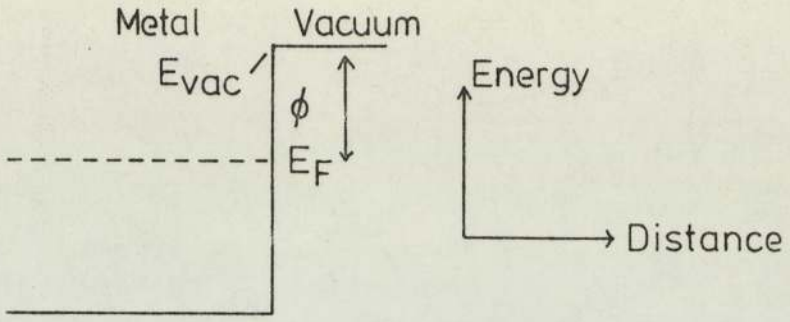

Figure 2.6 : The metal/vacuum interface

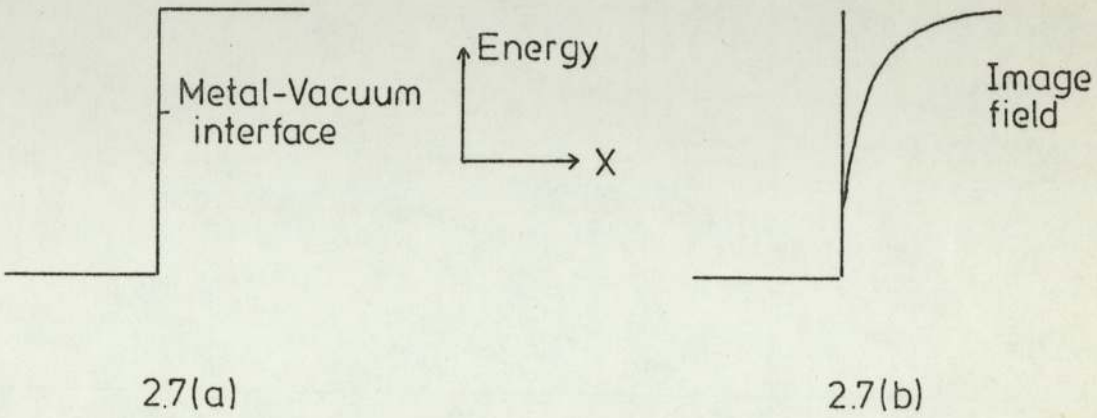

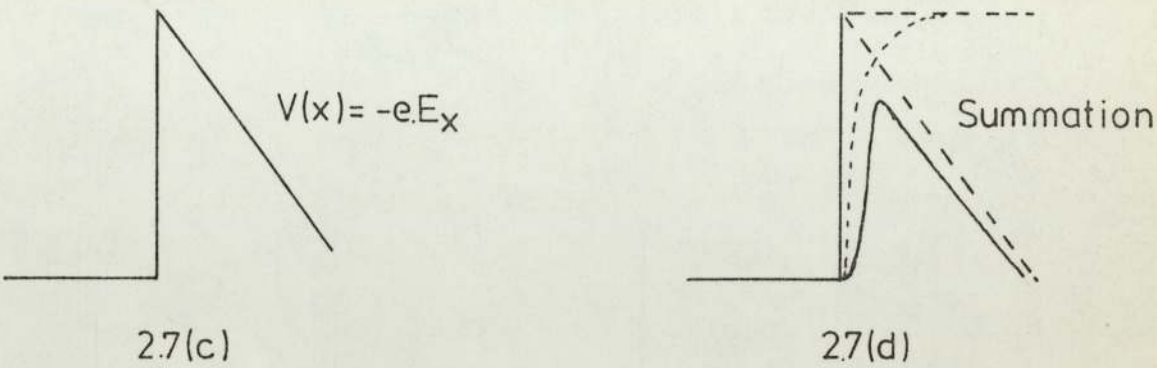

Figure 2.7 : (a) Ideal potential barrier, (b) Potential barrier changed by image charge, (c) Potential barrier changed by the applied field, (d) Potential barrier including the effects of image charge and applied field

the metal, i.e., it becomes thermionically emitted. The emitted current density is given by the Richardson equation, however, if the effect of the image force and the applied field is considered the thermionic emission current density, J is given by the Richardson-Schottky equation :

$$\text{i.e. } J = A_0 (1 - r) T^2 \exp \left[-\left\{ \phi - e\sqrt{(eE/4\pi\varepsilon_0)} \right\} / kT \right] \quad \ldots 2.25$$

where $A_0 = 4\pi e m K^2/h^3$. In the above expression e and m are the charge and mass of the electron respectively, h is Planck's constant, K is Boltzmann's constant, r is the reflection coefficient, T is the absolute temperature , ε_0 is the dielectric constant of free space and E the applied field. There has been much experimental evidence to confirm that Schottky (field assisted thermionic emission) phenomena is valid at low fields $\lesssim 10^5$ Vm^{-1} (35) however at higher fields the relationship between the observed current and the emitted current density failed.

According to classical physics, the probability of finding an electron, which has a smaller energy than the potential barrier, beyond the potential barrier is zero - only reflection should occur. However, due to the wave nature of the electron, quantum mechanics predicts otherwise. The Schrodinger equation indicates that there is a finite probability of finding an electron beyond the potential barrier provided the barrier is sufficiently thin $\lesssim 50$ Å (less than the mean free path of an electron). For the condition of a large applied field the potential barrier, shown in Figure 2.7(d) falls abruptly as indicated in Figure 2.8, where the energy of an electron at a distance $\triangle S$ is the same as that of an electron at the Fermi level.

In the case of two similar metals, of work function ϕ,

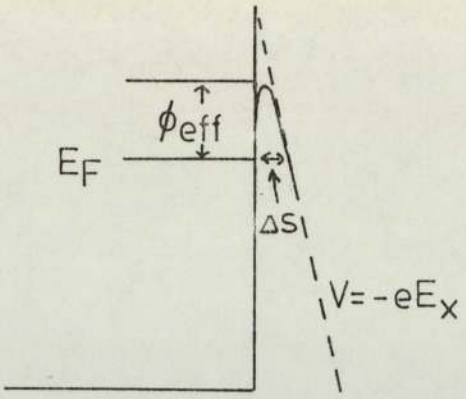

Figure 2.8 : Field Emission tunnelling

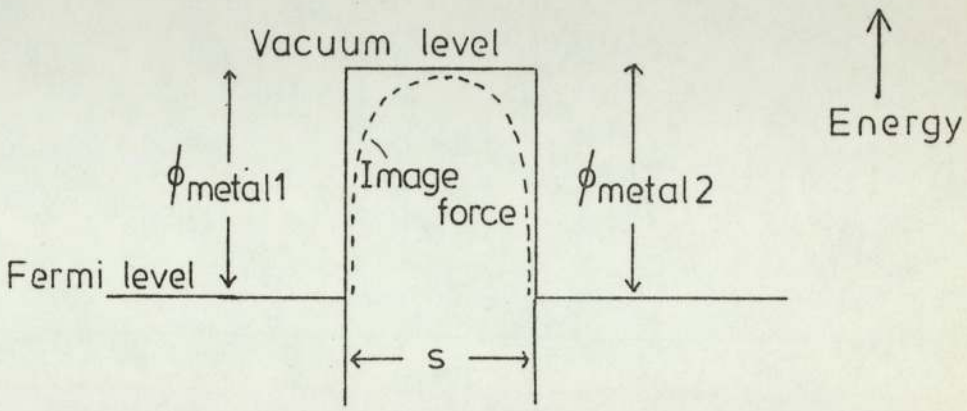

Figure 2.9: Potential barrier shape for similar metal electrodes separated by a distance 's'.

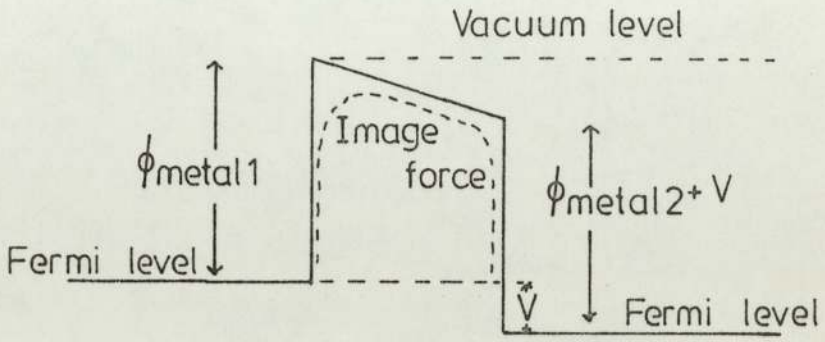

Figure 2.10:Potential barrier shape on the application of a voltage 'V'

tunnelling occurs such that the tunnel current densities are the same in either direction giving a net effect of zero current, see Figure 2.9. While in Figure 2.10 where the barrier heights are different, either due to the work functions originally being different or more probably due to the application of a voltage then the tunnelling currents are not equal, with the largest current being that flowing from the negative metal to the positive one.

For the case of two electrodes separated by a small vacuum gap, two different processes may arise under the application of a high voltage For small gaps $< 250\text{Å}$ and for low bias conditions metal-vacuum-metal tunnelling occurs which has the property that it is essentially Ohmic in character, while at relatively large interelectrode gaps and for large gap voltages Fowler-Nordheim (36) tunnelling arises. Both of these regions have been experimentally verified by Young et al (37).

The Fowler-Nordheim tunnelling describing field emission is based on four assumptions.

(i) The temperature of the metal is at 0°K

(ii) Inside the metal the free electron model is obeyed

(iii) The surface of the metal is smooth and plane

(iv) The potential barrier close to the surface in the vacuum region consists of an image force potential (arising from the attraction towards the surface of an electron outside, due to its induced charge in the metal) and an applied field potential.

An extension of the tunnelling theory has been carried out by Simmons (38,39) who has derived expressions for the tunnelling current density, in a metal-insulator-metal (M.I.M.) junction (for various bias voltages and electrode configurations), which can be applied to the microsphere/target charge exchange process.

2.2.2 The tunnelling process through the M.I.M. system

For the case of a metal electrode in contact with an insulator, the energy diagram of Figure 2.11 is applicable. Here electrons at the Fermi level of the metal see a barrier whose height is $E_g/2$, i.e. below the vacuum level. The height of the potential barrier and the shape of the bottom of the conduction band within the insulator is described by the conditions, (i) the Fermi levels of the electrode and insulator are coincident across the interface and (ii) the energy difference between the insulator vacuum level and the Fermi level at distances far away from the interface will be equal to the work function of the insulator.

In the absence of surface states the height of the interfacial barrier Ψ_o will be :

$$\Psi_o = \phi_{metal} - \chi \qquad \ldots 2.26$$

where χ is the insulator electron electron affinity and ϕ_{metal} the work function of the metal.

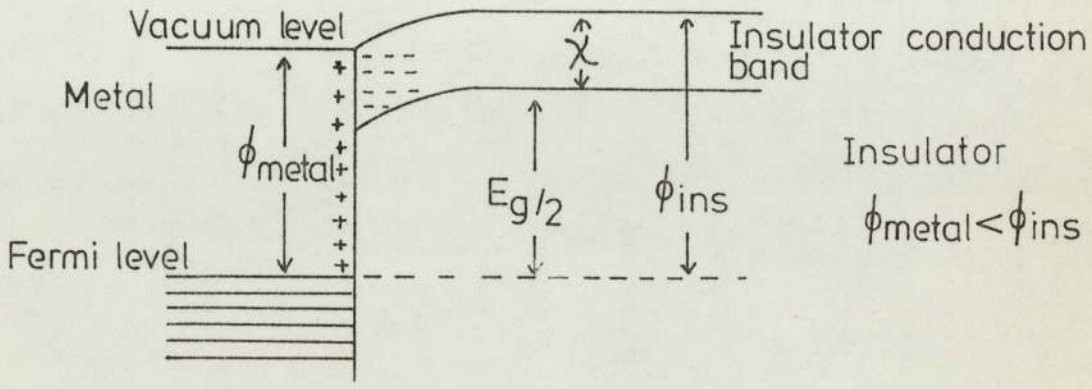

Figure 2.11: Metal / Insulator energy diagram

The type of contact that exists between the insulator and metal electrode is one of the factors which determines the conduction process; three possibilities exist, (a) Ohmic contact, (b) Neutral contact and (c) Blocking contact, each of which will be considered in some detail.

(a) The Ohmic contact involves an insulator whose work function ϕ_{ins} is larger than that of the metal electrode, ϕ_{metal}. Figure 2.12 illustrates the situation before and after contact. Once in contact electrons flow from the metal to the insulator conduction band until the Fermi levels become alligned. A space-charge effect (giving rise to a space charge field) causes band bending and extends a distance L_s into the insulator. This type of contact is 'bulk limited' since electrons are limited to the rate they can pass through the bulk of the insulator.

(b) The neutral contact is illustrated in Figure 2.13 and is seen to involve metals and insulators which have the same work function. The Fermi levels allign up naturally without any movement of charge. No band bending occurs and the conduction band is 'flat' on the metal surface. For small bias voltages the conduction process is ohmic with saturation occurring at high voltages.

(c) A Blocking Contact is illustrated in Figure 2.14 and occurs when the metal has a higher work function than the insulator. Electrons flow from the valence band of the insulator to the empty states above the Fermi level of the metal until equilibrium is established. A space charge region then exists at the interface stopping the flow of charge carriers and causing the insulator conduction band to bend until the Fermi level lies a distance ϕ_{ins} below the vacuum level.

If these assumptions are applied to a metal-insulator-metal (M.I.M.) contact where there are similar electrode materials for the various

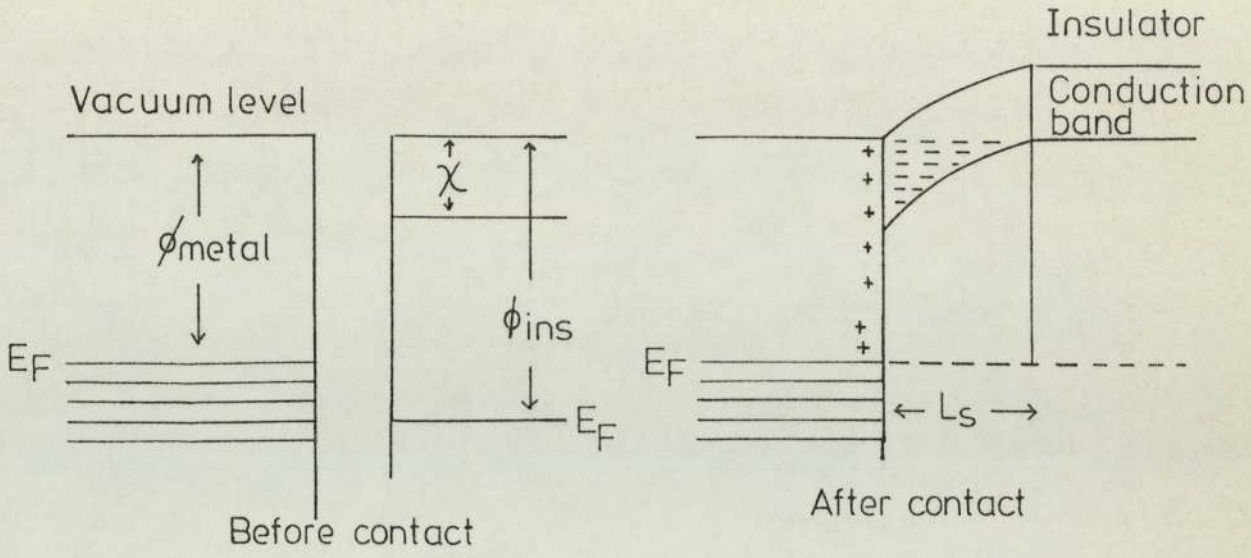

Figure 2.12: Metal/Insulator ohmic contact

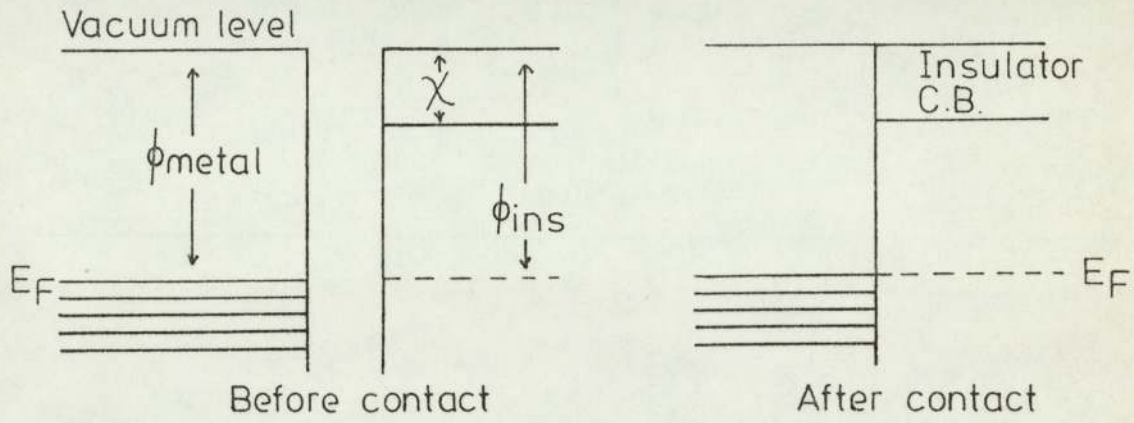

Figure 2.13: Metal/Insulator neutral contact

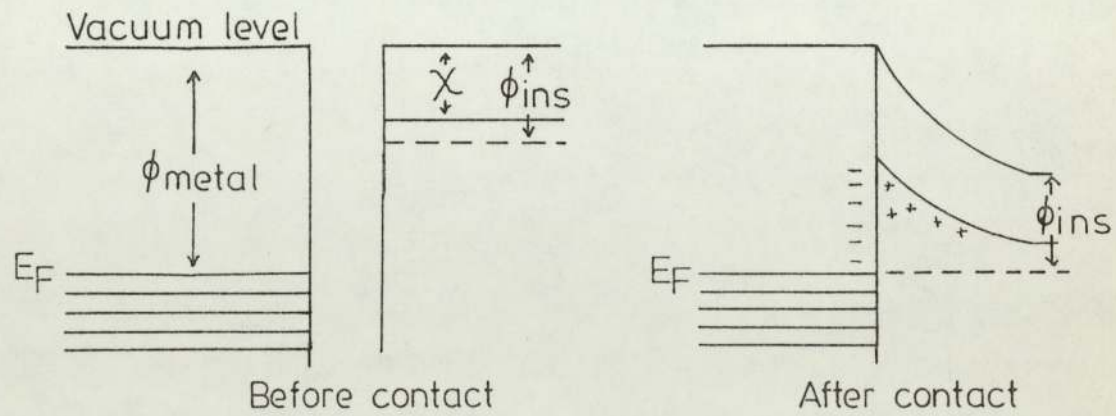

Figure 2.14: Metal/Insulator blocking contact

possible regimes, the band bending will be as shown in Figure 2.15. Figures (i) and (iii) refer, respectively, to the situation of a very thin insulator which is incapable of "shielding" the interior from conditions at the interface and thus bending occurs throughout. In constrast figures(ii) and (iv) represent, respectively, the effect for ohmic and blocking contacts for a thick insulator where band bending is only apparent at the interface, with the inner regions being effectively "shielded" and reflecting the intrinsic qualities of the insulator. Figures (v) and (vi) indicate the effect of neutral contacts, where (v) represents similar metals interfaced to an insulator and (vi) dissimilar metals (different work functions). In the first case, the Fermi levels allign so that there is no transference of charge and hence no band bending is evident; however, in the second case, the interfacial potential barriers differ in energy by an amount

$$(\phi_{\text{metal 2}} - \chi) - (\phi_{\text{metal 1}} - \chi) = \phi_{\text{metal2}} - \phi_{\text{metal 1}} \quad \ldots 2.27$$

with the intrinsic field inside the insulator being given by

$$(\phi_{\text{metal 2}} - \phi_{\text{metal 1}}) / es = E_{\text{int}} \quad \ldots 2.28$$

where s is the thickness of the insulator. In this case electrons are transferred from metal 1, having the lower work function, to metal 2, where the amount of charge transferred to give the equilibrium situation of Figure 2.15 (vi) is

$$Q = C (\phi_{\text{metal2}} - \phi_{\text{metal 1}}) / e$$

or

$$Q = A \varepsilon_0 \varepsilon_r (\phi_{\text{metal2}} - \phi_{\text{metal 1}}) / es \quad \ldots 2.29$$

where A is the electrode area, ε_0 the dielectric constant of free spare and ε_r the dielectric constant of the medium.

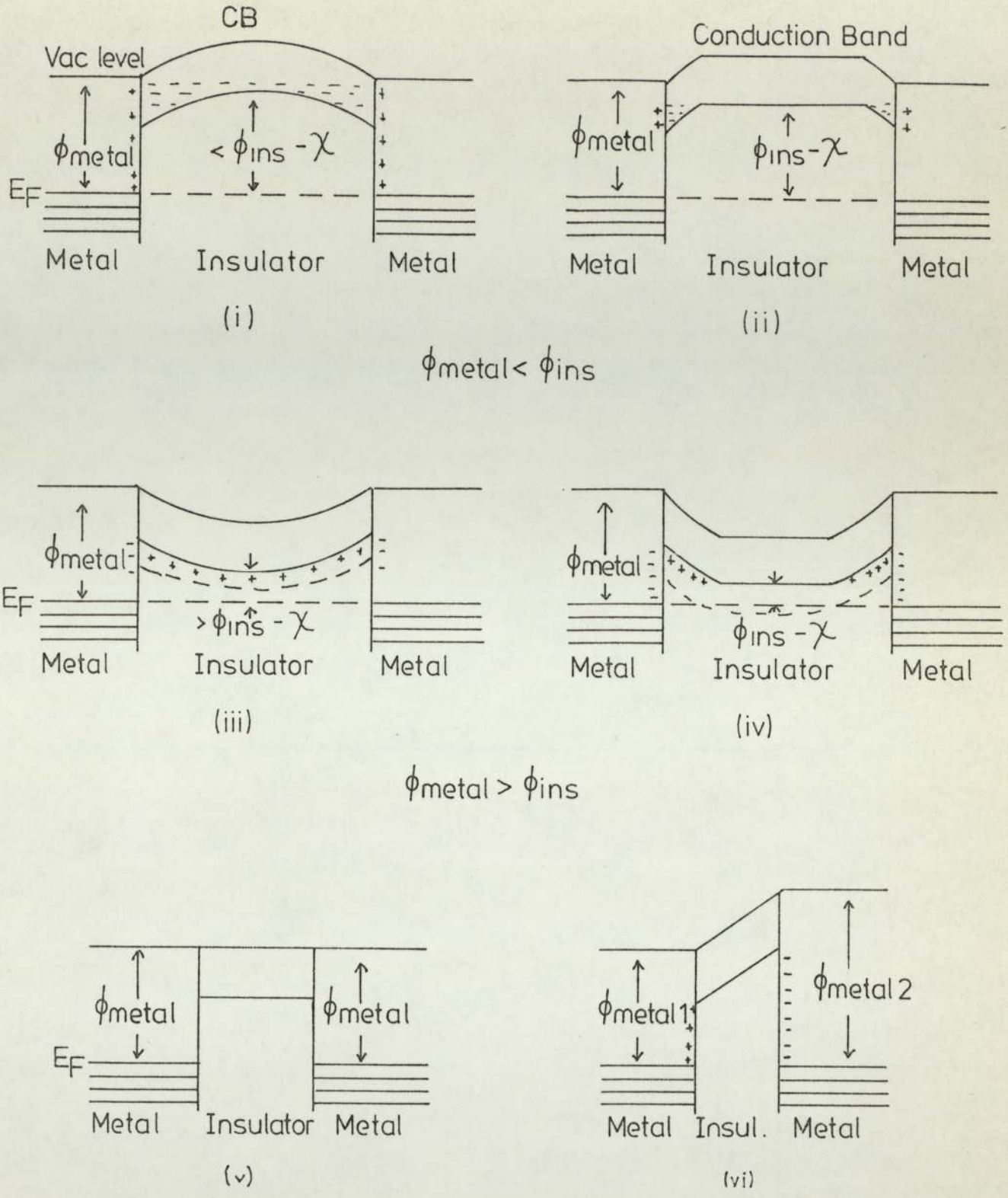

Figure 2.15: Energy diagrams for the M-I-M configuration

The process of charge flow and tunnelling has been the study of many investigations (40,41), however, Simmons (38,39) has derived the tunnel current densities for similar and dissimilar metal electrodes sandwiching an insulator. For metal electrodes possessing equal work functions Simmons has shown that the tunnel current density can be given by :

$$J = Jo \left\{ \bar{\varphi} \exp(-A\bar{\varphi}^{\frac{1}{2}}) - (\bar{\varphi} + eV) \exp\left[-A (\bar{\varphi} + eV)^{\frac{1}{2}} \right] \right\} \quad \ldots 2.30$$

where $Jo = e/2\pi h (\beta \Delta s)^2$ and $A = (4\pi\beta\Delta s/h) (2m)^{\frac{1}{2}}$ in which m and e are the mass and electronic charge of the electron, Δs the width of the barrier at the Fermi level of the negative electrode, $\bar{\varphi}$ the mean barrier height above the Fermi level of the negative electrode, β the correction factor depending on the barrier shape, ~ 1, h, Plancks constant and V the applied voltage across the film.

Equation 2.30 has the advantage that it can be applied to any shape of potential barrier provided the mean height of the barrier is known.

For low bias voltages an alternative expression can be obtained, from equation 2.30, for the current density J.

$$\text{i.e. } J = J_L \bar{\varphi}^{\frac{1}{2}} V \exp(-A \bar{\varphi}^{-\frac{1}{2}}) \quad \ldots 2.31$$

where $J_L = [2m^{\frac{1}{2}}/\Delta S] (e/h)^2$

where it is evident that J varies linearly with V thus giving an ohmic junction at low voltages. Applying equation 2.30 to the low voltage ($V \sim 0$), intermediate voltage ($V < \varphi_0/e$) and high voltage ($V > \varphi_0/e$) conditions leads, respectively, to band diagrams as shown in Figure 2.16, i, ii and iii. Although all the above expressions are derived for an ideal barrier, the introduction of the image theory tends to cause a 'rounding' of the potential barriers at the interface

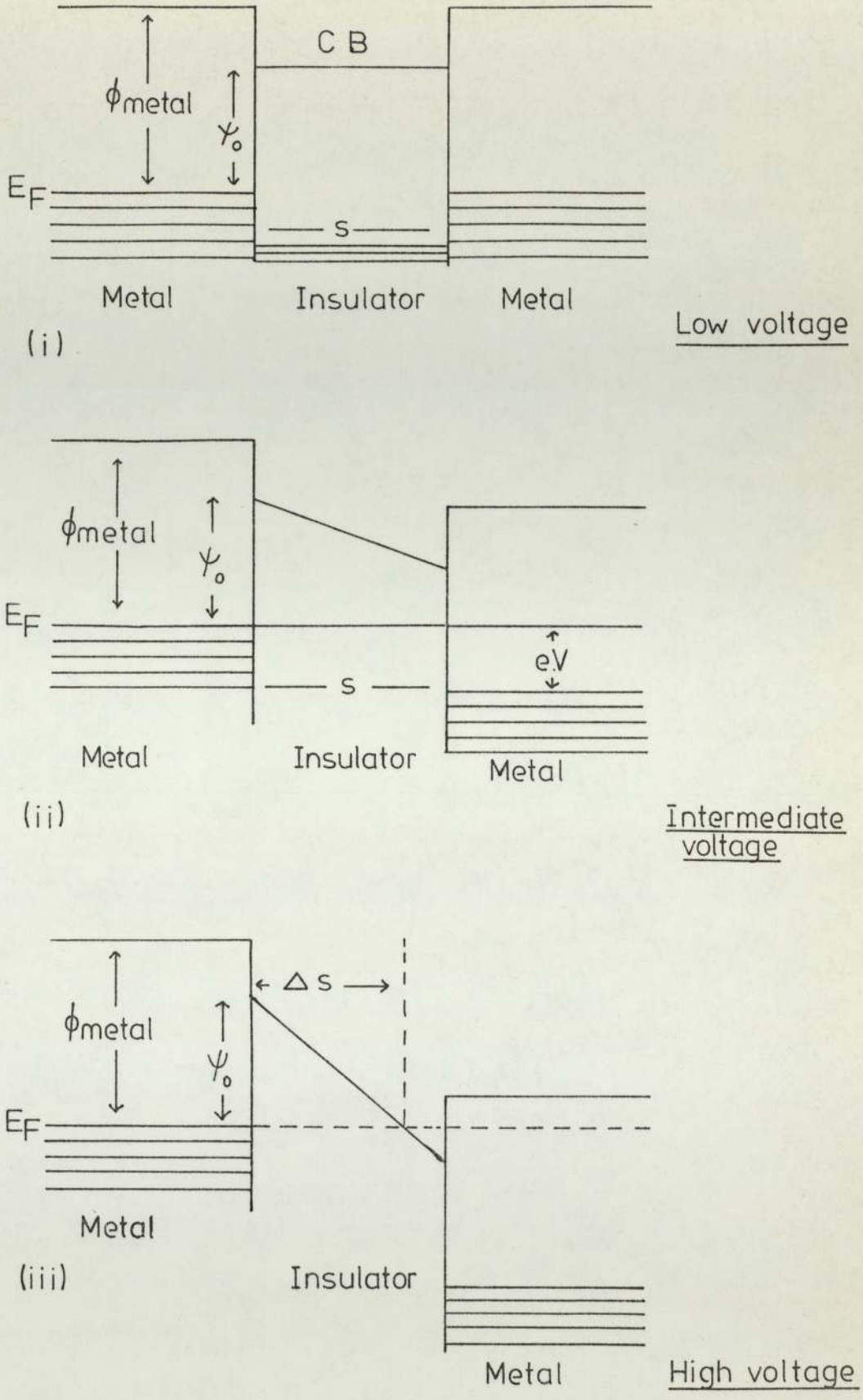

Figure 2.16: Idealized band diagrams for similar electrodes

A case of greater interest to the present work, is that which occurs for dissimilar work function electrodes which is the usual condition when, for example, a carbonyl iron microsphere impacts onto a target electrode. Figure 2.17 indicates the energy diagram for this situation. By convention, the 'forward' characteristic is defined as the situation where the electrode of lower work function is "positively biased" while the 'reversed' characteristic refers to the case of the lower work function electrode being "negatively biased". Using the general equation (2.30) given above, and adopting the low, intermediate and high voltage regimes as in the similar electrode case, the tunnel current density has been derived. In the low voltage case, the tunnel current density is the same as that for similar electrodes. However, for intermediate voltages $0 < V \lesssim \Psi/e$, it is necessary to consider the current flow in either direction. If the mean barrier height is given by $\bar{\Psi} = (\Psi_1 + \Psi_2 - eV)/2$ and $\Delta s = s$, it follows that :

$$J_1 = (e/4\pi k^2)\{(\Psi_1 + \Psi_2 - eV)\exp[E(4\pi s\, m^{\frac{1}{2}}/h)(\Psi_1 + \Psi_2 - eV)^{\frac{1}{2}}] - (\Psi_1 + \Psi_2 + eV)\exp[-(4\pi s m^{\frac{1}{2}}/h)(\Psi_1 + \Psi_2 + eV)^{\frac{1}{2}}]\} \quad \ldots 2.32$$

in which J_1 is the current density flowing in the reverse direction, i.e., from electrode 1 to electrode 2. In the forward direction, the current density J_2 can be derived from the conditions :

$$\bar{\Psi} = (\Psi_1 + \Psi_2 - eV)/2 \quad \text{and} \quad \Delta s = s$$

It is readily observed that these conditions are the same as for J_1, i.e. $J_1 = J_2$. Thus for the intermediate voltage range ($0 < V < \Psi/e$) the tunnelling current density is independent of the bias polarity. Figures 2.18 (i) and (ii) show the effect of reverse and forward bias voltages across the barrier at this intermediate voltage.

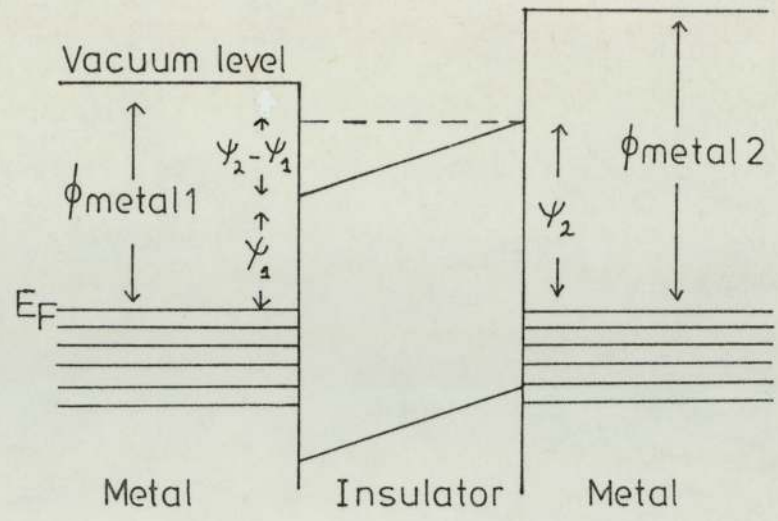

Figure 2.17: Band diagram for dissimilar electrodes

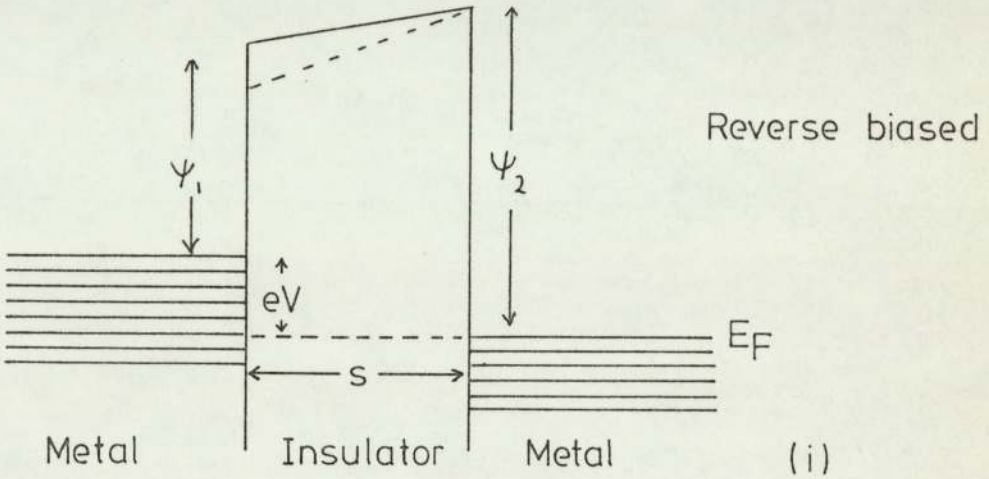

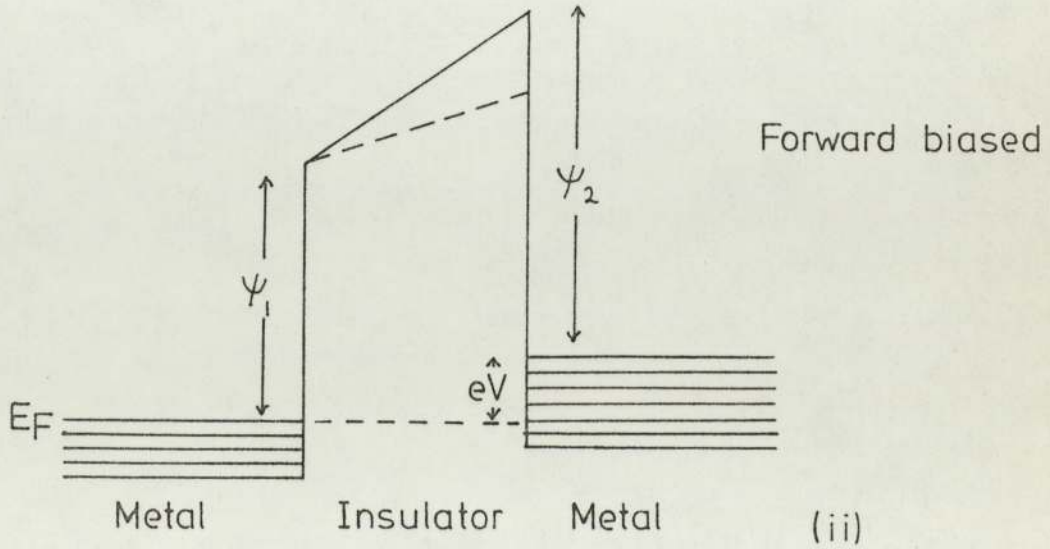

Figure 2.18: Band diagrams for dissimilar electrodes under intermediate voltage conditions

At high voltages, $V > \bar{\Psi}/e$, the current flowing in the reverse direction for conditions, where

$$\bar{\Psi} = \Psi_{1/2}$$

and $\Delta s = s \cdot \Psi_1/(eV-\Delta\Psi)$

is given by

$$J_1 = \frac{1.1e \cdot (eV - \Delta\Psi)^2}{4\pi h \Psi_1 s^2}\left\{ \exp\left[\left(\frac{-23\pi m^{\frac{1}{2}}}{6h}\right)\left(\frac{s\Psi_1^{3/2}}{eV - \Delta\Psi}\right)\right] - \left(1 + \frac{2eV}{\Psi_1}\right) \exp\left[\left(\frac{-23\pi m^{\frac{1}{2}}}{6h}\right)\left(\frac{s\Psi_1^{3/2}\cdot[1 + (2eV/\Psi_1)]^{\frac{1}{2}}}{eV - \Delta\Psi}\right)\right]\right\} \quad \ldots 2.33$$

where $\Delta\Psi = \phi_2 - \phi_1$

while in the forward direction

$$\bar{\Psi} = \Psi_{2/2}$$

and $\Delta s = s\Psi_2/(eV + \Delta\Psi)$

leading to

$$J_2 = \frac{1.1e(eV + \Delta\Psi)^2}{4\pi h \Psi_2 s^2}\left\{\exp\left[-\left(\frac{23\pi m^{\frac{1}{2}}}{6h}\right)\left(\frac{s\Psi_2^{3/2}}{eV + \Delta\Psi}\right)\right] - \left(1 + \frac{2eV}{\Psi_2}\right)\exp\left[-\left(\frac{23\pi m^{\frac{1}{2}}}{6h}\right)\left(\frac{s\Psi_2^{3/2}[1 + (2eV/\Psi_2)]^{\frac{1}{2}}}{eV + \Delta\Psi}\right)\right]\right\} \quad \ldots 2.34$$

which clearly indicates that $J_1 \neq J_2$. Furthermore the J-V characteristic is assymetrical in this range and that rectification reverses at some particular voltage. Figures 2.19(i) and (ii) indicate the reverse and forward bias characteristics at high bias voltage.

To illustrate the above, Simmons has determined the tunnel resistivity σ (defined as V/J) as a function of V for s = 20, 30 and 40Å, ϕ_1 = 1V and $\Delta\Psi$ = 1V. Figure 2.20 illustrates that σ is smaller in the forward direction. As the bias voltage is increased the

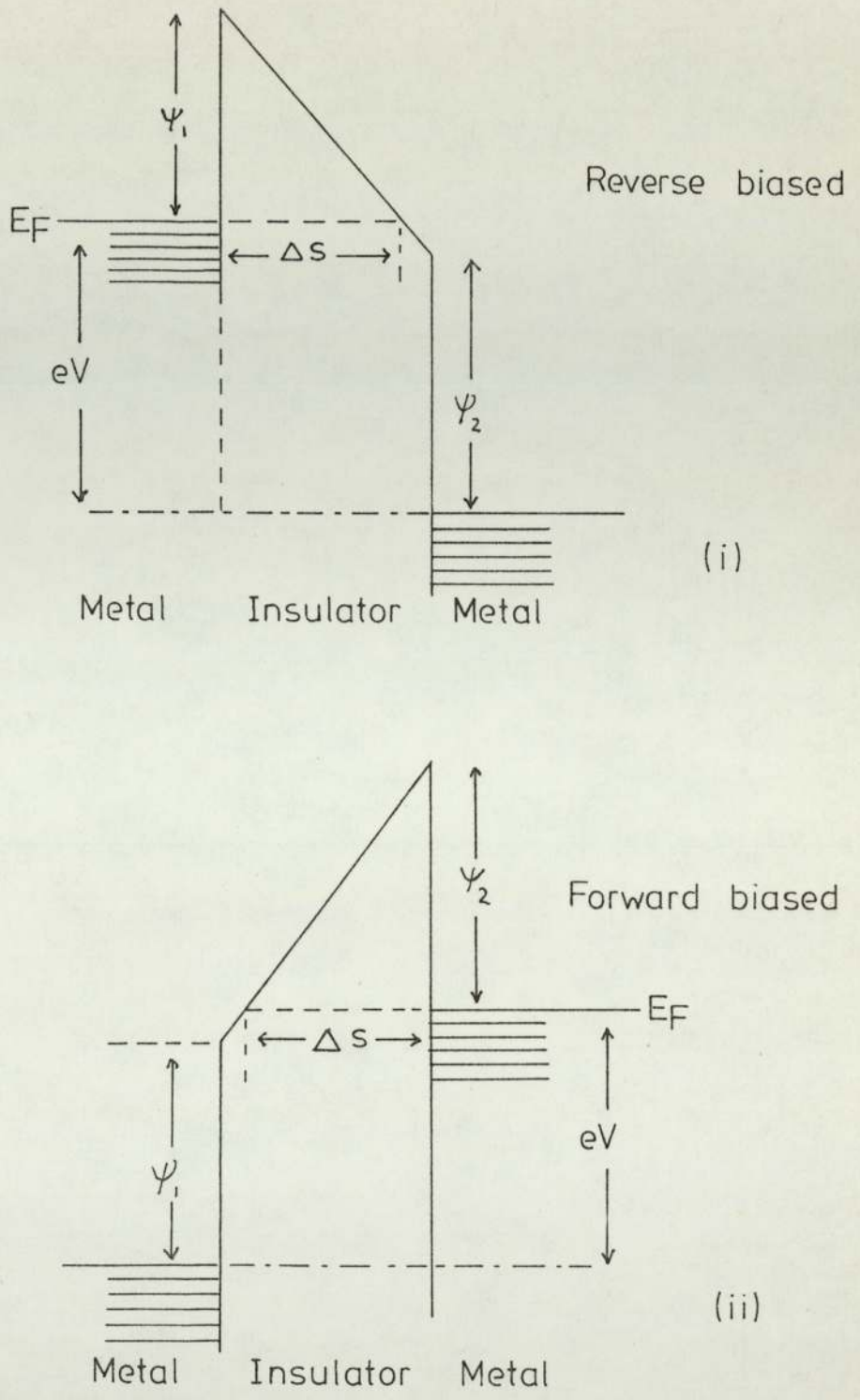

Figure 2.19 : Band diagrams for dissimilar electrodes under high voltage conditions

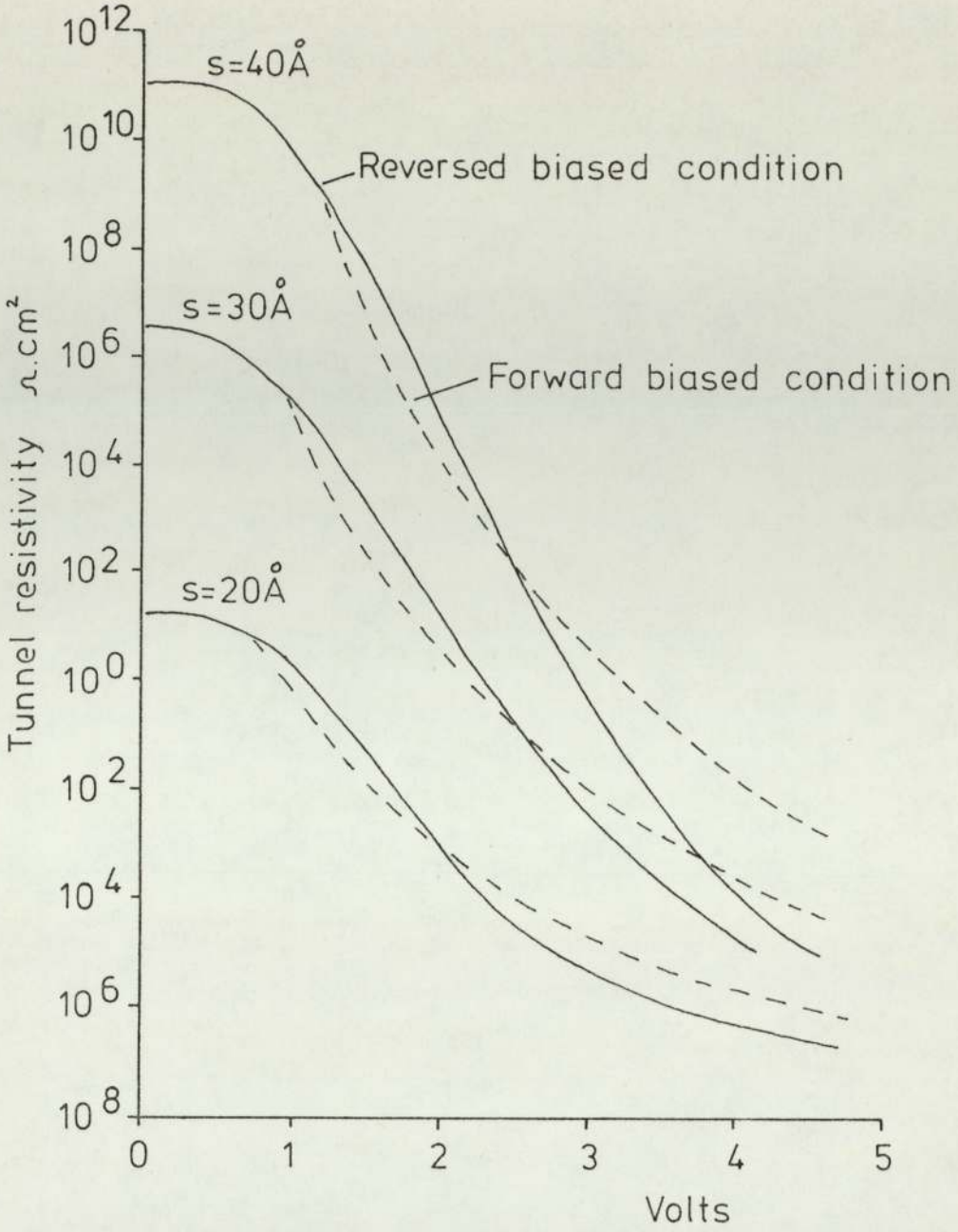

Figure 2.20: Theoretical σ-V characteristics for an ideal barrier[39]

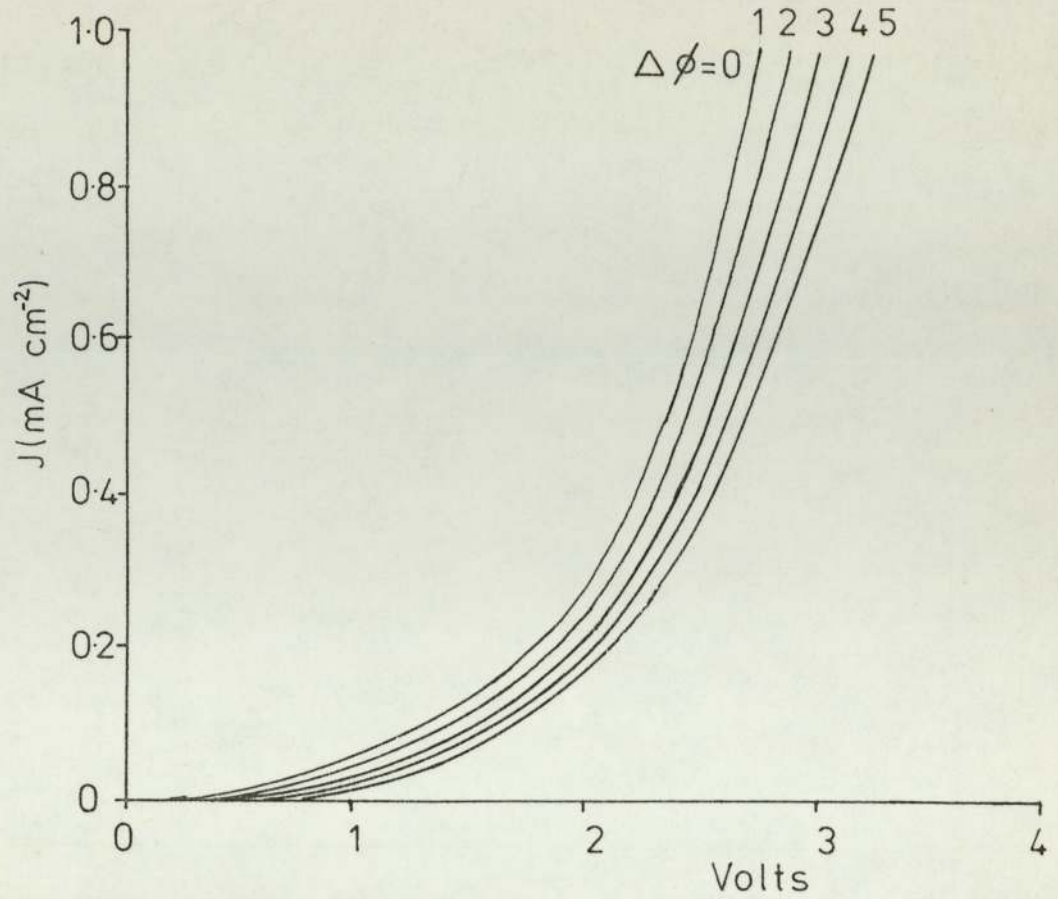

Figure 2.21: Forward characteristics for assymetric junctions[43]

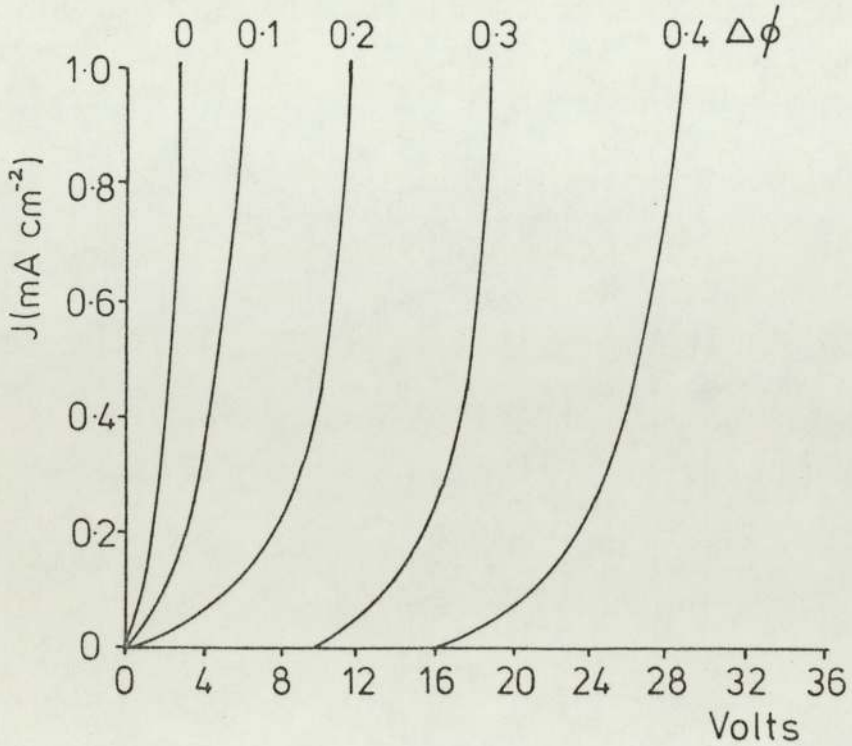

Figure 2.22 : Reverse characteristics for assymetric junctions[43]

forward and reverse characteristics cross-over (42) with a corresponding decrease in the tunnel resistivity. The almost linear plot at low bias voltages indicates the ohmic region already mentioned.

Figure 2.21 illustrates the 'forward' J-V charactersitics for five assymetric junctions with the work function difference $\Delta\Psi$ (varying from 0.1 to 0.4 eV in steps of 0.1 eV), Ψ_1 = 0.5 eV, S = 200Å and ξ = 5. The symmetrical junction is also represented as the condition $\Delta\Psi$ = 0 . The characteristics are represented by a convergent set of curves and displacement between any two, along the voltage axis, is equal to the difference in work function of the two electrode materials. The corresponding reverse characteristics are shown in Figure 2.22. The forward and reverse characteristics are quite assymetrical and exhibit good rectifying properties (43).

Finally, the variation of the tunnel current density as a function of temperature, for an assymetric junction, is shown in Figure 2.23 for Ψ_1 = 2eV , Ψ_2 = 1.5eV, s = 50Å and at temperatures of 300 and 250K. For bias voltages in the range $0 < V < \Psi/e$. there is a reversal of the polarity for the forward direction as the temperature of the junction decreases (43) . It should be noted that it is only the J-V characteristic resulting from the electrode of lower work function being positively biased which shows a temperature dependance.

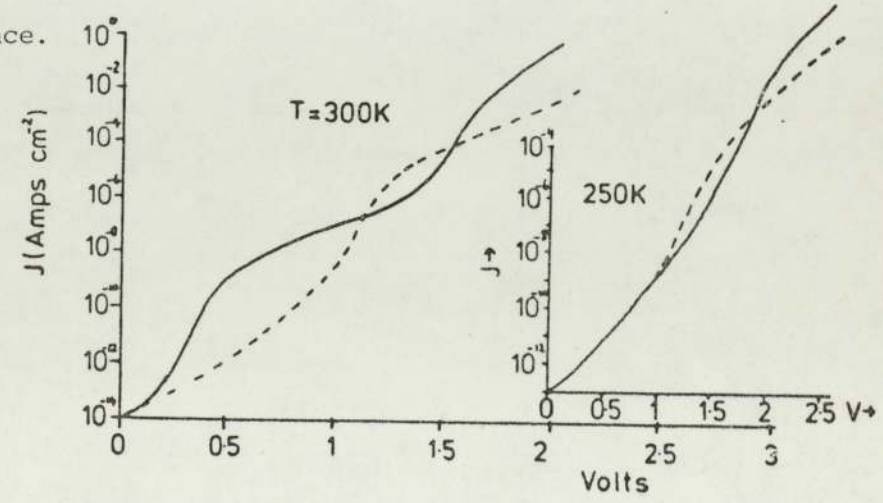

Figure 2.23: The variation of tunnel current density with temperature (43)

2.3 Electric field across the M.I.M. configuration

It has already been mentioned that the field across the M,I.M. configuration can play a significant role in the tunnelling and charge exchange that occurs between similar and dissimilar electrode materials, hence it is important to have some knowledge of the macroscopic gap field existing between the charged microsphere and the earthed target; a question that has been considered by many investigators (44, 45, 46). However, much of the original work in this area has been to consider the trigger discharge process which can arise as a charged particle approaches a high voltage electrode.

In such a process, field enhancement occurs between the electrode and charged conducting particle which may be sufficient to cause a field emission current to be drawn from the electrode surface to the particle. This may in turn cause thermal instability of the electron bombarded area with the generation of sufficient metal vapour between the particle and the electrode to produce a discharge. The mechanism was first discussed by Olendzkaya (47) who found that when steel spheres were placed between the electrodes the probability of breakdown increased. A polarity effect was also evident, so that breakdown was most likely to occur when the spheres were travelling towards the cathode. A similar trigger discharge form of process has been noted by Udris (48), when using a 2mm diameter steel sphere, such that breakdown was able to occur when the sphere approached within 0.1 mm of the cathode surface.

Chakrabarti and Chatterton (49) have investigated the onset of a trigger discharge when gold and tungsten wires were bombarded by various diameter iron microspheres. Particles with velocities

in the range 50 → 200 ms^{-1} and diameters >4μm produced melting on impact with a tungsten target although it was confined to the contact area while in the case of 10 - 25 μm diameter particles extensive melting occurred due to the trigger discharge process, and in some cases complete breakdown of the main gap followed. It should also be mentioned that melting is not due to the kinetic energy exchange process involved during the impact (see Chapter 1) due to the low velocities involved.

Martynov (50) and Chatterton et al (51) have developed field theories to explain the trigger discharge process associated with the breakdown event but the actual cause of breakdown differs in both models. Briefly, the Martynov model proposes that after a trigger discharge a plasma is produced which extends into the gap forming a positive ion sheath which eventually triggers the main gap. Subsequently Martynov has derived an expression for the field intensity (E) between a conducting sphere (radius ⩾ 10μm) and a plane at large approach distances, and obtained the following relationship :

$$E(g/_{Rp}) = E_p f_1(g/_{Rp}) + E_0 f_1(g/_{Rp}) \quad \ldots 2.35$$

where E_p and E_0 are, respectively, the field intensity at the surface of the free sphere and the external field, while f_1 and f_2 are functions describing the effect of the conducting plane on E_p and E_0. Rp and g are the sphere radius and sphere/plane gap respectively. Under the zero field conditions of the present study where $E_0 = 0$, equation 2.35 reduces to

$$E(g/_{Rp}) = E_p f_1(g/_{Rp}) \quad \ldots 2.36$$

The determination of E_p, arising from the actual physical charge on the

sphere, involves the solution of Laplaces equation (52) and the method of images outlined in Section 2.4. At close distances of approach, where $g \sim Rp$, the function f_1 increases rapidly while for $g/Rp \lesssim 0.3$, which is relevant to the experimental situation arising in the present simulated impact studies, the function f_1 is given by :

$$f_1 \sim 1.29 \quad (Rp/g)^{0.8} \qquad \ldots 2.37$$

Substituting equation 2.37 into 2.36 leads to

$$E_g = 1.29 \ (Rp/g)^{0.8} \ . \ E_p \qquad 2.38$$

where $E_p = Q_p / 4\pi\varepsilon_0 (Rp)^2$ in which Q_p is the charge on the sphere and ε_0 the dielectric constant of free space. Thus finally,

$$E_g = 1.29 \ (Rp/g)^{0.8} \ . \ \frac{Q_p}{4\pi\varepsilon_0 (Rp)^2} \qquad \ldots 2.39$$

In this derivation, however, Martynov failed to take into account any variations in the charge due to field emission between the sphere and the plane. Furthermore the curvature of the sphere was neglected, while in the condition where $g \sim 0.3Rp$ a uniform field was thought to exist between the sphere and the plane.

The model of Chatterton et al (51) requires a high field to exist between a microprotrusion on the cathode and the approaching particle. Charge flow occurs before impact causing particle melting and gas desorption. It is further proposed that a rebounding particle drags some of the molten material with it, which on cooling gives rise to a protrusion. Breakdown of the main gap can only occur when the protrusion becomes unstable after the particle has moved two or three particle radii from the electrode allowing the main field to exert its influence. On this basis. Chatterton et al have computed

an estimate of the minimum radius of a microsphere required to undergo a trigger discharge process when opposite a cathode irregularity. Consider the arrangement shown in Figure 2.24. As the microsphere approaches the surface, the cathode protrusion 'sees'

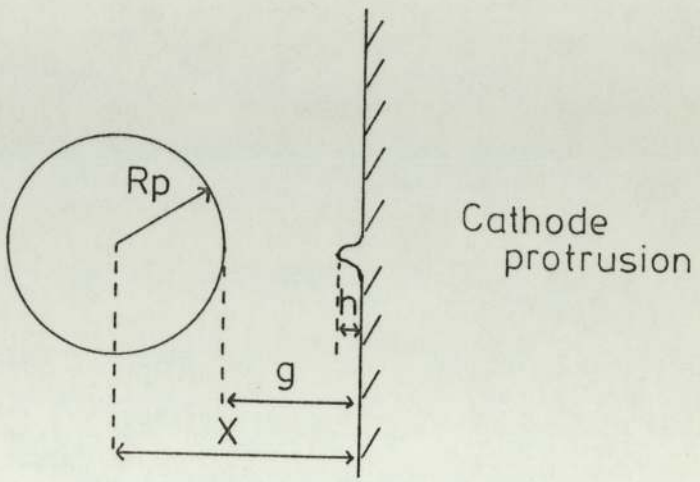

Figure 2.24: Microsphere opposite a cathode protrusion

the positively charged microsphere as the anode. The electric field at the protrusion tip can thus be considered to be made up of the two components.

(i) a contribution due to the charge on the microsphere

and (ii) a contribution due to the distortion of the uniform field by the presence of the charged microsphere.

Condition (i) can be obtained from image force calculations and is given by

$$E_p = Q_p / 4\pi\varepsilon_o R_p^2 \qquad \ldots 2.40$$

where E_p is the electric field due to the changed microsphere, Q_p the charge on the microsphere, ε_o the dielectric constant of free space

and Rp the radius of the microsphere. For the case of a microsphere moving in zero field the contribution due to (ii) can be ignored. Hence provided g << X the field of the microprotrusion tip (E_T) is given by

$$E_T \sim \beta \left[1/g \left(Q_p / 4\pi \varepsilon_0 . Rp\right)\right] \quad \ldots 2.41$$

where β is the field enhancement factor of the protrusion. The variation of β as the microsphere approaches the protrusion can be derived from the following formula of Miller (53)

$$\beta = \beta_\infty \left[(g - h)/g\right] \quad \ldots 2.42$$

where h is the height of the protrusion. This apporach is again limited since no account was taken of charge transfer or the charge distribution at the surface of the plane.

In a more complete analysis Beukema (45) has proposed a modified trigger discharge process, based on the work of Olendzkaya where, provided the conditions are correct, field emitted electrons bombard a small area of the positively charge microsphere, as it approaches the cathode, causing its temperature to rise with subsequent welding on impact.

To calculate the local surface temperature rise of the microsphere, under zero field conditions, it is useful to define the potential energy of the microsphere to be

$$W = 1/2 \cdot Q_p . V = Q_p^{\,2} / 2C \quad \ldots 2.43$$

where Q_p is the charge on the microsphere and V its potential

According to Beukema the potential of a charged sphere V, with respect

to a plane is (54)

$$V = Q_p \; 4\pi\varepsilon_0 R_p \sum_{n=0}^{\infty} \frac{2\left\{[(g + Rp)/Rp]^2 - 1\right\}^{\frac{1}{2}}}{\left[\left((g + Rp)/_{Rp} + \left\{[(g + Rp)/_{Rp}]^2 - 1\right\}^{1/2}\right)\right]^{2n+1}}$$

... 2.44

where Rp is the radius of the microsphere and g the distance between the microsphere and target. Beukema has shown that the above summations can be approximated by 1 giving

$$V = Q_p 4\pi\varepsilon_0 R_p \qquad \ldots 2.45$$

For field emission to occur between the microsphere and target, the critical field strength E_c is $\sim 5 \times 10^9$ V m^{-1}. This condition will be satisfied for a microsphere/plane separation equal to g_c, then

$$E_c = \frac{V_p(g_c)}{g_c} \qquad \ldots 2.46$$

where $V_c(g_c) = Q_p/4\pi\varepsilon_0 R_p$ ... 2.47

The maximum time (t_m) that the microsphere is bombarded by field emitted electrons is

$$t_m = g_c/u \qquad \ldots 2.48$$

where u is the velocity of the approaching microparticle.

To simplify the argument the current I flowing during the time which electrons are bombarding the microsphere is assumed to be constant and is given by I_o. Now if g decreases, then I increases, thus reducing the charge on the microsphere, Q_p. As Q_p decreases, the electric field between the microsphere and the surface decreases together with I.

For a constant gap field

$$\frac{d\ (V_c / g)}{dg} = 0 \qquad \ldots 2.49$$

so that from equation 2.49

$$\left(g \cdot \frac{d(V_c)}{dg} - V_c \cdot \frac{d(g)}{dg}\right) / g^2 = 0 \qquad \ldots 2.50$$

Rearranging gives

$$g \frac{d(V_c)}{dg} = V_c \qquad \ldots 2.51$$

Substituting equation 2.47 into equation 2.51 leads to

$$g \cdot \frac{d}{dg} \left(\frac{Q_p}{4\pi \varepsilon_0 Rp} \right) - Q_p / 4\pi \varepsilon_0 Rp = 0$$

or $$g \cdot \frac{dQ_p}{dg} - Q_p = 0 \qquad \ldots 2.52$$

Solving equation 2.52 gives

$$\frac{dQ_p}{dg} = Q_p / g$$

$$\text{or } \log_e Q_p = \log_e g + \log_e A$$

$$\text{thus } Q_p = Ag \qquad \ldots 2.53$$

At the critical conditions of $g = g_c$ then $Q_p = Q_p\ (g_c)$

$$\text{thus } E_c = \frac{V_c (g_c)}{g_c} = \frac{Q_p\ (g_c)}{4\pi\ \varepsilon_0\ Rp\ g_c} \qquad \ldots 2.54$$

The current I_o can then be found by differentiating

$$\text{i.e. } I_o = \frac{dQ_p}{dt} = \left(\frac{dQ_p}{dg} \right) \left(\frac{dg}{dt} \right) = u \cdot \frac{dQ_p}{dg}$$

$$= 4\pi\ \varepsilon_o\ Rp \cdot u \cdot E_c \qquad \ldots 2.55$$

The temperature rise of the microsphere can be calculated from the formula developed by Charbonnier et al (55) for intermediate pulse lengths

$$\text{i.e.} \quad \Delta T = 2IV\, t^{\frac{1}{2}} / \pi R_a^2 \quad (\pi K \rho c)^{\frac{1}{2}} \qquad \ldots 2.56$$

where V is the potential of the charged sphere with respect to the target, I is an approximately constant emission current that flows for an 'approach' time t, R_a is the radius of the electron impact region, whilst K, ρ and c and the thermal conductivity, density and specific heat of the sphere respectively.

Since the area bombarded by field emitted electrons is a small section of the total area of the microsphere, Beukema has suggested that the emission from the target can be neglected with respect to the current, in the central region, once the field between the plane and the sphere has fallen by 10%.

With this assumption the bombarded surface is now given by

$$\pi R_a^2 = 0.2\, \pi\, Rp.g \qquad \ldots 2.57$$

Therefore the mean bombarded area during field emission is

$$R_a^2 \sim 0.1\, \pi\, Rp.g_c \qquad \ldots 2.58$$

Using the above expressions the temperature rise ΔT can be determined and this will be evaluated, for the experimental conditions of this study, in Chapter 5.

As a final point it should be noted that as the microsphere approaches the plane the microsphere/plane capacitance increases, thus causing a lowering of the microsphere/plane potential (for a constant microsphere charge Q_p). However, this effect will be

evaluated in Section 2.4

2.3.1 The charge exchange process

In order to determine the amount of charge transferred during the contact tunnelling process, it is first necessary to look at the effect played by the contaminating surface (oxide) on both the microsphere and the target. Consider the case illustrated in Figure 2.25 of a microsphere in contact with a planar target surface, having respectively oxide film thicknesses of S_S and S_T and dielectric constants of ε_S and ε_T; the contact area being 'a'

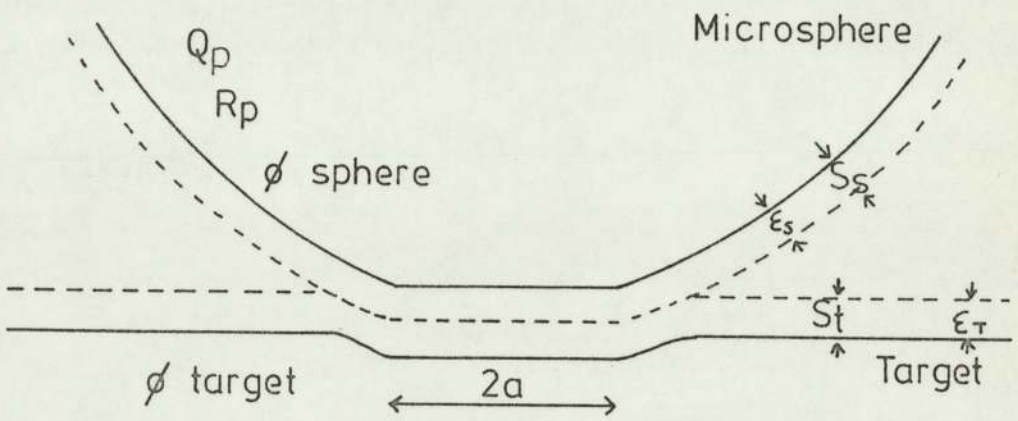

Figure 2.25: Microsphere/Plane contact separation

The gap field Eg, between the sphere and target, is made up of two components E_1 and E_2, where E_1 is the contribution due to the enhancement of the macroscopic field E_0 by the conducting sphere and E_2 arises from the actual physical charge on the sphere. In a zero field situation E_1 is zero, while E_2 can be evaluated by the electrical image theory (52).

$$\text{i.e.} \quad E_g \equiv E_2 = \frac{Q_p}{\bar{\varepsilon}\, C_0(g)\, g} \qquad \ldots 2\,59$$

In the above expression Q_p is the charge on the sphere, $C_0(g)$ the sphere-plane capacitance in vacuum and g the gap separation between the sphere and the plane whilst $\bar{\varepsilon}$ is the effective dielectric constant whose value is given by

$$\bar{\varepsilon} = \frac{\varepsilon_S \varepsilon_T}{\varepsilon_S + \varepsilon_T} \qquad \ldots 2.60$$

The total potential on the sphere $V_p(g)$ is given by

$$V_p(g) = E_g \cdot g = \frac{Q_p}{C_0(g)} \qquad \ldots 2.61$$

However, Latham and Brah (9) have derived an expression for the charge transferred via a tunnelling process, based upon the theoretical analysis of Simmons (38, 39). According to this treatment, for low bias conditions, the tunnel resistivity σ (Ωm^2) is defined by

$$\sigma = V_p(g)/J_T \qquad \ldots 2.62$$

where Vp(g) is the bias voltage across the film and J_T the tunnel current density. In practice the tunnel resistivity is highly dependent on the film thickness 's', the effective dielectric constant of such a film $\bar{\varepsilon}$ and the bias voltage $V_p(g)$.

To apply this theory, the following assumptions were made :

(i) The contact area is given by the mean value $\pi a^2/2$ and is effectively constant during the impact.

(ii) The linear dependance of the tunnel resistivity is given by

$$\lg \sigma = \lg \sigma_0 - KV_p(g) \qquad \ldots 2.63$$

where σ_0 is a constant which is dependent on the film thickness, band gap and dielectric properties of the film and K is a constant.

(iii) The exponential decay of $V_p(g)$ with time

Latham et al (9) have derived an expression for the total charge transferred between the microsphere and target, Qr, such that

$$Qr = [\pi a^2 t_c \exp (K V_{op})] / 2\sigma_0 K \quad \ldots 2.64$$

where V_{op} is the sphere potential at the instant of contact.

The above equation (2.64) yields a value of $Qr \sim 10^{-16}$C which is in agreement with the typical charge exchange value of $\sim 10^{-15}$C observed experimentally by Latham and Brah (9) in their high field studies.

Mohindra (5) has modified the above treatment to take into account the difference in the work function ($\triangle\phi$) of the particle and target materials, which gives rise to an additional field component E_3 given by $\triangle\phi / e g$. The modified expression for Qr is thus :

$$Qr = \frac{\pi a^2 t_c}{2\sigma_0 K} \exp K\left\{ Q_{p/\xi} C_0(g) \pm \frac{\triangle\phi}{e} \right\} \quad \ldots 2.65$$

where $\left\{ Q_{p/\varepsilon_0} C_0(g) \pm \frac{\triangle\phi}{e} \right\} = V_{op}$

For 'forward biased' conditions E_3 is positive while for 'reversed biased' condition E_3 is negative.

In addition, the linear dependance of σ on V_p has been shown by Mohindra to be an unrealistic approximation and which has subsequently been revised to produce a better agreement between the theoretical and experimental results for Qr, under high field

conditions. As a further limitation, the above expressions have been derived for an ideal sphere-plane geometry whereas in practice the microtopography of a surface is found to be non-ideal, i.e. possessing many protrusions (dust particles) and scratch grooves. Hence the values of E_g and C_0 are likely to be altered and together with the variations in oxide film thickness and work function variations, will produce wide differences in the impact and charge exchange behaviour.

2.3.2 Electron scattering within the tunnelling junction

It has been pointed out by Beukema (45) that a significant temperature rise of the impacting microsphere may be caused by a modified trigger discharge process. However, it is important to consider the possible heating effects caused by the tunnelling (38,39) electrons through the surface dielectric (insulator) during the impact process in which charge exchange is taking place. Thus it is possible that impact ionization occurs during the tunnelling process giving rise to an "electronic modified thermal switching" process as observed by many authors (56, 57, 58, 59, 60). To initiate such an event, fields of the order of 10^6 V m^{-1} and above are required across the dielectric. In thick insulators, the breakdown process may involve a stepwise progression across the insulator due to successive impact ionization events while in thin dielectrics no such complication exists. Events are initiated locally in a solid by an electronic process which may lead to local instability and current runaway. At the instability spot, the electrostatic energy discharges, leading to irreversible changes by melting and evaporation. Experimentally breakdown and switching by the above process, have been observed by Klein et al (60), Morgan et al (58,59) and Kawamura et al (56) for times $\lesssim 10^{-8}$ s.

Klein (61) assumes that the process takes the following form for a thick dielectric: An electron is injected into the conduction band of the insulator and causes impact ionization by either interband transitions or by impurity ionization. As a result a finite avalanche of free electrons is produced behind which are the immobile positive ions. Figure 2.26 shows the positions of the positive charges

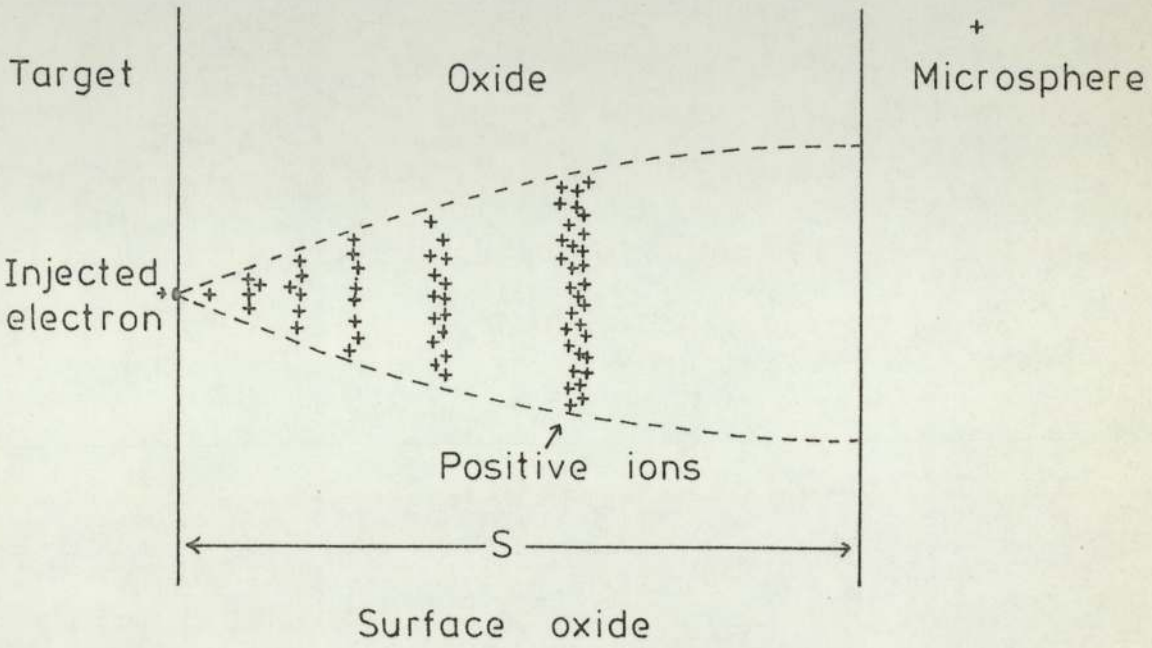

Figure 2.26: Position of positive charges after impact ionisation within the target oxide

after the electrons have been swept out at the anode. Each positive space -charge indicates a region where impact ionization has taken place. Neglecting fluctuations in the collision distance, each positively charged region occurs at a distance separated by the mean free path for ionization by electrons. Due to the positive charges increasing the opposing field, the gap between each positive space charge increases towards the anode. The last charge layer is at a distance a_v from the cathode, where a_v is the mean avalanche length. The effective

field acting on the electrons in the film is so low beyond a_v that no more impact ionization occurs. It is assumed that at breakdown field free electrons are readily available (62,63) and that the heat produced by the electrons in the avalanche is assumed to start destruction at the anode . (60). O'Dwyer (64,65) has pointed out that large avalanches cannot occur in the breakdown of the dielectric since the immobile positive space-charge left behind produces a sufficiently high field to oppose the applied field across the dielectric. However, Klein suggests that most of the energy for destruction does not occur in the avalanche but is stored in the specimen. In addition the avalanche process triggers the destructive breakdown by producing a temperature increase of a few hundred degrees centigrade in the breakdown channel. The electrical conductivity of the channel thus increases making the breakdown channel thermally unstable.

Let n be the number of ionizing collisons made by the injected electron in its course through the insulator, V_i the ionizing potential and E the applied field. Then the avalanche length a_v is given by :

$$a_v = \frac{KnV_i}{E} \qquad \ldots 2.66$$

where K is a factor > 1 which takes into account the average increase of the mean free path during ionization towards the anode, and E/V_i is the ionization coefficient for high fields (66). If the electrons undergo a sideways diffusion as they proceed towards the anode the cross section of the avalanche cone A_v is given by

$$A_v = 4\pi l_p a_{v/3} \qquad (63) \qquad \ldots 2.67$$

where A_v is the cross section of the last ionizing collision and

l_p the mean free path for phonon collisions.

If ionization ceases after the n^{th} collision due to the presence of the positive charges, it can be shown that the positive charge is related to the applied field by

$$\eta E = \frac{eN}{\varepsilon_0 \varepsilon_r A_v} \quad \ldots 2.68$$

where η is a coefficient whose value is between 0 and 1 and represents the influence of the opposing field of the positive charges, ε_0 the permittivity of free space (vacuum), ε_r the dielectric constant of the insulator and N the size of the largest avalanche that can develop. Substituting 2.66 and 2.67 in 2.68 yields for N

$$N = \frac{4\pi\varepsilon_0}{3e} \cdot \eta \cdot K n \varepsilon_r l_p V \quad \ldots 2.69$$

Assuming η lies between 0.7 amd 0.9, and a stepwise avalanche development across the insulator, Klein has calculated the value of K to lie between 1.4 and 2.

The local temperature rise T caused by the passing avalanche, assuming no loss of heat away from the avalanche channel by conduction, has been shown to be

$$T \sim \frac{Nes\,E}{cs\,A_v} \quad \ldots 2.70$$

where c is the specific heat per unit volume of the insulator and s the oxide thickness.

Substituting for A_v leads to the expression

$$T = \frac{\eta \varepsilon_0 \varepsilon_r E^2}{c} \quad \ldots 2.71$$

It is readily seen that the size of the largest avalanche, N, is independant of the applied field while a_v and A_v are inversely proportional to the applied field. When $a_v > s$ full avalanches do not occur so that temperature rises within the insulator are limited.

Experimentally Klein et al (60) have determined the following parameters for a thick silicon oxide dielectric under pulse conditions; the breakdown time t_B is $\lesssim 10^{-9}$s and the cross sectional area of the breakdown channel A_v is~4 x $10^{-14}m^2$. Moreover, the calculated temperature rise ΔT is $\gtrsim 337°c$ while the total energy and charge required to cause this event are $\lesssim 1.4 \times 10^{-11}$J and $\lesssim 6.7 \times 10^{-14}$C respectively. Other short breakdown times, under pulse conditions, have been observed by Kawamura et al (56) who determined the statistical time lag to be $< 6 \times 10^{-8}$s for a mica surface. Furthermore Morgan et al (59) have measured the total switching time for a 50 nm Al_2O_3 film and have found this time to be < 45 ns. It should also be pointed out that these switching times are extremely voltage dependant, thus for a high overvoltage, the switching times can be reduced (56, 67. 68, 69).

2.4 Attractive forces between a sphere and a plane

When a charged microsphere comes into close proximity with a planar target electrode, it experiences several attractive forces. These are principally, the electrical image force, arising from the induced charge on the plane, and Van der Waals force. Moreover, the induced surface charge distribution on the target depends on the proximity of the charged sphere. On coming into contact with the target adhesive forces arise. Thus for a particle to "bounce" from a target surface, it must have sufficient energy

to overcome all of these forces. This section deals with the relative importance of the above forces in the microsphere impact regime of the present study.

2.4.1 The Image force

In the method of images a volume or spatial distribution of charge is replaced by a series of point charges such that the conducting surfaces can be represented by equipotentials at the same potential. In the case of a sphere-plane geometry, suitable point charges are used to replace the sphere and the plane such that the surfaces are equipotentials.

With reference to Figure 2.27, let Q be the total charge

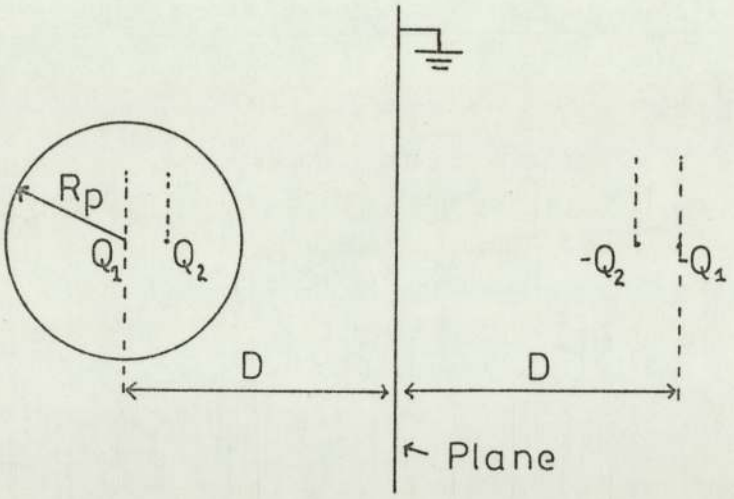

Figure 2.27 : Charged sphere opposite an earthed plane

on the sphere and Q_1 the charge at its centre which makes the sphere an equipotential (52). To make the plane an equipotential a charge of $-Q_1$, must be placed as shown. This upsets the spherical equipotential, so that a charge Q_2 (the image of $-Q_1$) must be placed inside the sphere

to bring its surface back to an equipotential, however this upsets the plane. This process has to be continued until convergence occurs. Thus, if $Rp/_{2D} = p$, the charges Q_1, Q_2, Q_3, Q_4, e.t.c. are given in terms of Q_1 as :-

$$Q_1 = Q_1$$

$$Q_2 = pQ_1$$

$$Q_3 = \frac{p^2}{1-p^2} \cdot Q_1$$

$$Q_4 = \frac{p^3}{(1-p^2)(1-p^2/1-p^2)} \cdot Q_1 \qquad \text{and so on}$$

Table 2.1 shows the position and magnitude of the charges for this system.

Left of plane		Right of plane	
Charge	Distance from centre of sphere	Charge	Distance from centre of sphere
Q_1	0	$-Q_1$	2D
$Q_2 = \frac{Rp}{2D} Q_1$	$\frac{Rp^2}{2D}$	$-Q_2$	$2D - \left(\frac{Rp^2}{2D}\right)$
$Q_3 = \frac{\left(\frac{Rp}{2D}\right)^2 Q_1}{1-\left(\frac{Rp}{2D}\right)^2}$	$\frac{\frac{Rp^2}{2D}}{1-\left(\frac{Rp}{2D}\right)^2}$		

Table 2.1: Point charges and their relative distances from the centre of the sphere

The total charge Q on the sphere is then given by

$$Q = Q_1 \left(1 + p + p^2/1-p^2 + \ldots\right) \qquad 2.72$$

and its potential by

$$V = Q_1/4\pi\varepsilon_0 Rp \qquad \ldots, 2.73$$

since only Q_1 contributes to the potential of the sphere (Gauss's law)

From the above expression it follows that the capacitance of the sphere/plane system will be given by

$$C = Q/V = \frac{Q_1 \ (1 + p^2 + \ldots)}{Q_{1/4\pi \varepsilon_0 Rp}}$$

$$= 4\pi\varepsilon_0 Rp \ (1 + p^2 + \ldots\ldots) \qquad 2.74$$

which increases as the sphere/plane separation decreases.

To facilitate easy manipulation of the above series, the following substitutions have been used (70) :

$$C = 4\pi\varepsilon \, Rp \, . \, \sinh\alpha \sum_{n=1}^{\infty} \operatorname{csch} n\alpha \qquad \ldots 2.75$$

where $D/Rp = \cosh\alpha$

Accordingly the corresponding expression for the image force becomes

$$F_I = V^2/2 \ \frac{\partial C}{\partial D} = -2\pi\varepsilon_0 Rp^2 \ V^2 \left\{ \frac{1}{2D^2} + \frac{8 \ RpD}{(4D^2 - Rp^2 D)^2} \right\}$$

$$= 2\pi\varepsilon_0 V^2 \sum_{n=1}^{\infty} [\operatorname{csch} n\alpha \, (\coth\alpha - n \coth n\alpha)] \ \ldots 2.76$$

For the case of a 2μm radius iron microsphere, equations 2.75 and 2.76 have been evaluated for sphere /plane separations of 500Å, 400Å 300Å, 200Å, 100Å, 50Å and are shown in Figures 2.28 and 2.29. For clarity Figures 2.30 and 2.31 show the evaluation for the hyperbolic summation formulae used in these computations. Thus the potential of the sphere at these given separations can be calculated. As an example of this approach, the variation of the sphere/plane potential can be evaluated with regard to the trigger discharge process outlined by Beukema (45), discussed in Section 2.3. The values of F_I and V

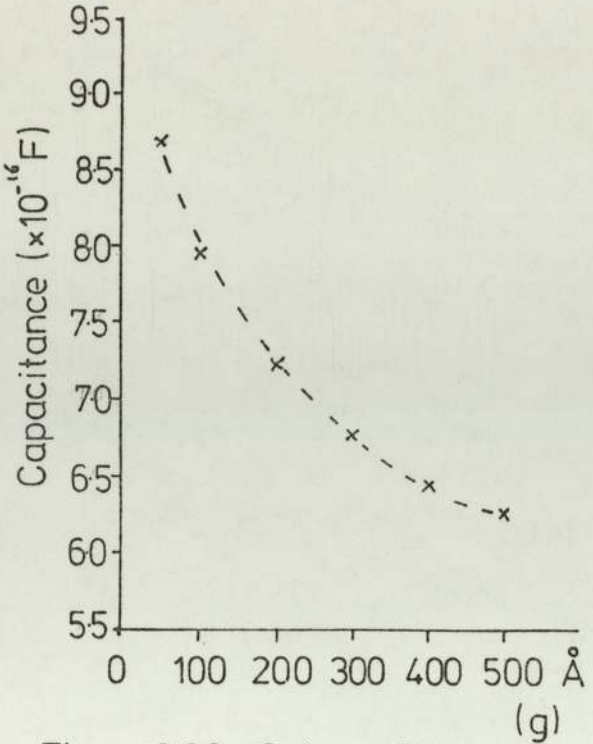

Figure 2.28 : Sphere/Plane capacitance as a function of gap separation

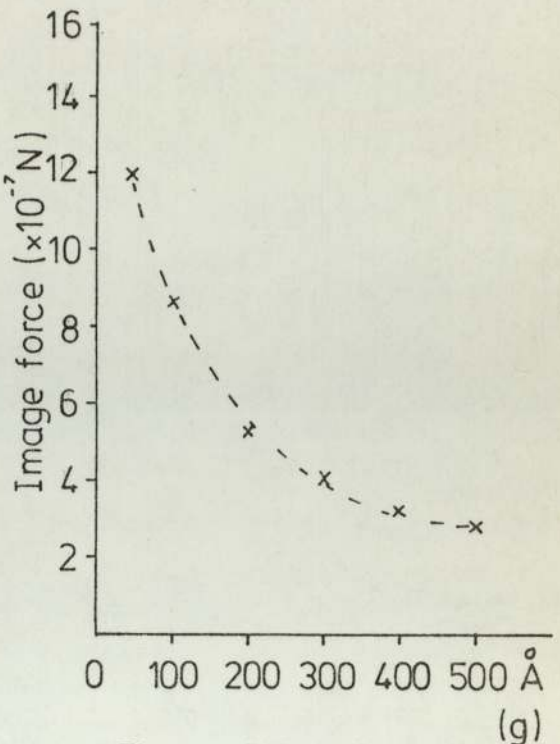

Figure 2.29: Image force as a function of sphere/plane gap separation

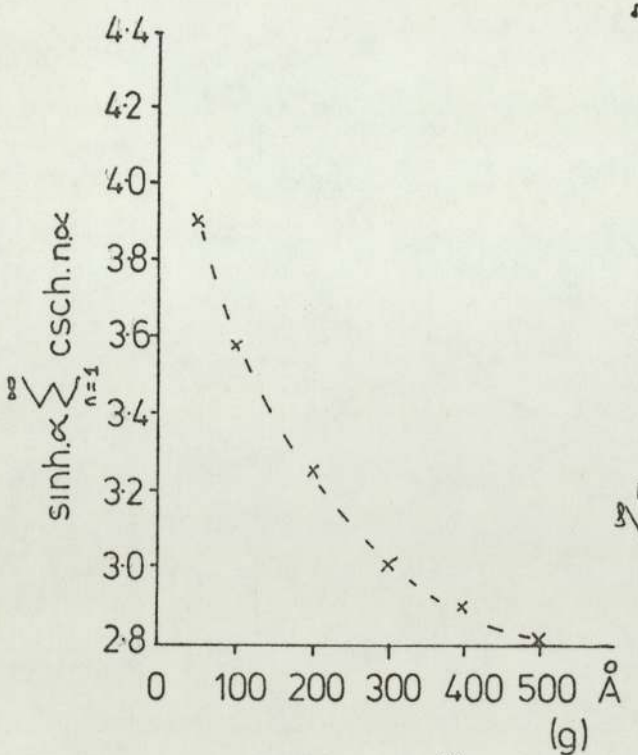

Figure 2.30 : $\sinh\alpha\sum_{n=1}^{\infty}\operatorname{csch} n\alpha$ as a function of sphere/plane gap separation

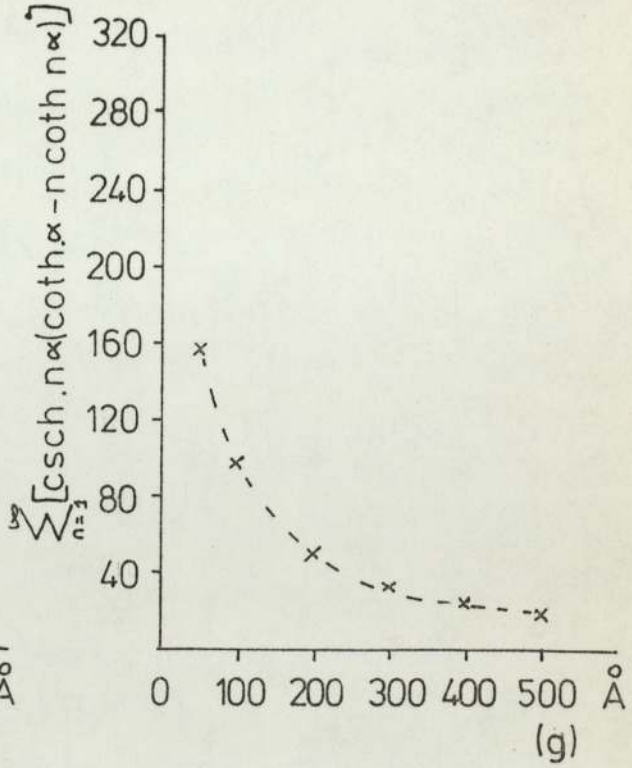

Figure 2.31: $\sum_{n=1}^{\infty}[\operatorname{csch} n\alpha(\coth\alpha - \coth n\alpha)]$ as a function of sphere/plane gap separation

determined via the above functions will be discussed in more detail in Chapter 5.

As a final point it should be noted that an alternative derivation for F_I can be obtained via a method outlined by Davis (71) however the case outlined above besides being more accurate, allows (i) the capacitance of the sphere/plane gap and (ii) the potential of the sphere with respect to the plane to be determined.

2.4.2 Van der Waals Force

To explain why some gases did not obey the PV-RT gas law, Van der Waal postulated the existance of attractive forces between molecules and rearranged the ideal gas equation to include a pressure term to account for the intermolecular force. Subsequently, London (72) explained these intermolecular forces using the Quantum theory and hence derived an expression showing that the force between two atoms, in free space, varied as the inverse seventh power of their separation. However, the simplicity of London's theory had many drawbacks and was later refined by Lifshitz et al (73)

The main features of these forces are :

(i) They are long range forces, effective from large distances $> 500\mathring{A}$, down to interatomic dimensions.

(ii) The forces may be repulsive as well as attractive and in general they do not follow a simple power law.

(iii) The Van der Waal (V.D.W.) force between two atoms or molecules is usually accompanied by a torque.

It can be shown that for large bodies, i.e. a sphere and a half space that at small distance $< 100\mathring{A}$ the V.D.W. force F_D is proportional to $1/D^2$, where D is the separation, while at large

distances $F_D \propto 1/D^4$. In both cases the non-retarded forces is used, (see later).

2.4.2(a) Short range effects

For two particles containing m atoms per cm^3 the energy of the interaction between them is, according to Hamaker (74),

$$E = -\int_{V_1} dv_1 \int_{V_2} dv_2 \frac{mP}{r^6} \quad \ldots 2.77$$

where dv_1, dv_2, V_1 and V_2 designate respectively volume elements and the total volumes of the two particles, r is the distance between them and P is the London V.D.W. constant. The total energy of interaction between the spheres, radius r_1 and r_2 is then

$$E = -\pi^2 m^2 P \frac{1}{6} \left(\frac{2 r_1 r_2}{c^2-(r_1+r_2)^2} + \frac{2 r_1 r_2}{c^2-(r_1-r_2)^2} + \ln \frac{c^2-(r_1+r_2)^2}{c^2-(r_1-r_2)^2} \right) \quad \ldots 2.78$$

where g is the separation of the spheres and $c = r_1 + r_2 + g$

Introducing the new variables

$$a = \frac{g}{2r_1} = \frac{g}{D_1} \quad \text{and} \quad b = \frac{D_2}{D_1} = \frac{r_2}{r_1}$$

where D_1 and D_2 refer to the diameters of the two spheres

$$E = -A \frac{1}{12} \left(\frac{b}{a^2 + ba + a} + \frac{b}{a^2 + ab + a + b} + 2 \ln \frac{a^2 + ab + a}{a^2 + ab + a + b} \right) \quad \ldots 2.79$$

In this expression $A = (\pi^2 m^2 P)$ and is known as the Hamaker constant. For the case of a sphere and a plane, illustrated in Figure 2.32, $b \rightarrow \infty$ so that

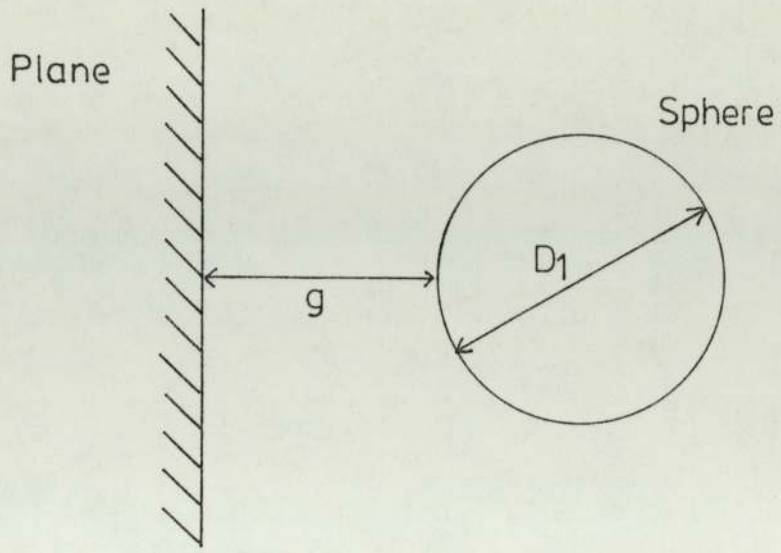

Figure 2.32 : Sphere/Plane molecular interaction model

Force (N)	Separation 'g' Å
$6{\cdot}67\times10^{-12}$	500
$1{\cdot}04\times10^{-11}$	400
$1{\cdot}85\times10^{-11}$	300
$4{\cdot}17\times10^{-11}$	200
$1{\cdot}67\times10^{-10}$	100
$6{\cdot}67\times10^{-10}$	50
$1{\cdot}85\times10^{-9}$	30

Table 2.2: Short range V D W force as a function of sphere/plane separation

$$E = -A\frac{1}{12}\left(\frac{1}{a} + \frac{1}{a+1} + 2\ln\frac{a}{a+1}\right) \quad \ldots 2.80$$

For small values of a (which is applicable for a 2 μm radius carbonyl iron microsphere at a separation of $\lesssim 500\mathring{A}$ from a planar target surface), equation 2.80 reduces to

$$E = \frac{-A}{12}\left(\frac{1}{a}\right) \quad \ldots 2.81$$

where, differentiating of this equation with respect to g leads to the expression for the attractive force between the sphere and the plane (F_∞)

Thus since $\frac{\partial}{\partial g} = \frac{\partial a}{\partial g} \cdot \frac{\partial}{\partial a} = \frac{1}{D} \cdot \frac{\partial}{\partial a}$

it follows that $F_\infty = \frac{\partial E}{\partial g} = -\frac{A}{12D_1} \cdot \frac{\partial}{\partial a}\left(\frac{1}{a}\right)$

or finally $F = \frac{A}{24D_1} \quad \frac{1}{a^2} \quad \ldots 2.82$

In the particular application of this theory to the present study where a 2μm radius carbonyl iron microsphere is at separations of 50, 100, 200, 300, 400 and $500\mathring{A}$ from the plane, the value of F_∞ can be found at each separation in terms of the Hamaker constant A. From the values of A given by Dahneke (75), it is possible to determine a magnitude value for F_∞ i.e. using $A \sim 10^{-19}$J, the values shown in Table 2.2 can be obtained.

2.4.2(b) Long Range effects

At separations greater than $\sim 200\mathring{A}$, the V,D.W. force law between two atoms gradually changes from an inverse seventh to an inverse eighth power law. This is called the retardation effect and likewise the forces at these large separations are called retarded V.D.W. forces. Thus when two atoms are more than $\sim 500\mathring{A}$ apart the V.D.W. interaction should be almost completely retarded. It may also arise that retarded and non-retarded forces have different signs, i.e., the force may be attractive at large separations but repulsive at small separations. In this case particles may approach and come to rest at a finite distance away from each other solely as a result of the V.D.W. attractions. One of the first theories for retarded V.D.W. forces was developed by Casimir (76) who found for the interaction force per unit area (F) between two half-spaces that

$$F = \frac{\pi^2}{240} \cdot \frac{\hbar c}{g^4} \qquad \ldots 2.83$$

where $\hbar = h/2\pi$ with h being Plancks constant, c the velocity of light in vacuo and g the separation of the two half-spaces. It should be added that this expression is only valid for ideally conducting half-spaces at zero temperature . However real metals are not perfect conductors and to overcome this problem Lifshitz (77) has subsequently modified the above theory. In an alternative approach Hargreaves (78) has produced a simplified method for correcting the result of Casimir for non-ideal conductors in which electromagnetic waves were considered to penetrate a very short distance into a real metal. For wavelengths below 10 μm, the penetration depth (d) is given, in the first approximation by :

$$d = \left(\frac{mc^2}{4\pi Ne^2} \right)^{\frac{1}{2}} = c/\omega_p \qquad \ldots 2.84$$

where e and m are the charge and mass of the electron respectively, N is the number of free electrons per unit volume and ω_p is the plasma frequency. Hargreaves suggested altering the calculation for the retarded force (equation 2.83) by adding one or two times the penetration depth to the real separation g

$$\text{i.e.} \qquad F = F_0 \left(\frac{g}{g + nd} \right)^4 \sim F_0 \left(1 - \frac{4nd}{g} \right) \qquad \ldots 2.85$$

In the above, F_0 is the force value as given by Casimir and n is a number between 1 and 2. Summarising therefore, whereas the Hamaker relation of section 2.4.2(a) is valid for small separations ($< 500\mathring{A}$) the Casimir and Hargreaves expressions for F are only applicable at large distances ($\gtrsim 1000\mathring{A}$).

Van Blokland and Overbeek (79) have applied the above expressions to the special case of the force between a sphere and a flat plate. Their argument is based on an assumption of Derjaguin (80) which states that the force between a flat plate and a sphere is given by

$$F(g) = 2\pi Rp.\, U(g) \qquad \ldots 2.86$$

where Rp is the radius of the sphere and U(g) is the interaction energy per unit area between two flat plates at a separation g. Applying this transformation to the equations of Casimir and Hargreaves, Van Blokland et al obtained :

$$F_{Cas}(g) = \frac{\pi^3 . Rp\hbar c}{360\, g^3} \qquad \ldots 2.87$$

and

$$F_{Harg}(g) = \frac{\pi^3 Rp\hbar c}{360\, (g + nd)^3} \sim \frac{\pi^3 Rp\hbar c}{360\, g^3} \left(1 - \frac{3nd}{g} \right) \qquad \ldots 2.88$$

For the case of a 2μm radius sphere opposite a plane at separations

F(Cas), N	Separation Å
$5{\cdot}428\times10^{-12}$	1000
$2{\cdot}01\times10^{-13}$	3000
$4{\cdot}34\times10^{-14}$	5000
$1{\cdot}58\times10^{-14}$	7000
$7{\cdot}45\times10^{-15}$	9000

Table 2.3: Long range VDW force as a function of sphere/plane separation

of 1000Å, 3000Å, 5000Å, 7000Å and 9000Å equation 2.87 has been evaluated giving values of F as shown in Table 2.3. According to Hargreaves results these values are consistently high but for this study, the order of magnitude values, shown inTable 2.3 will be used since the variation in F is extremely small.

2.4.3 Adhesive forces

The force of adhesion between one body to another has been of considerable interest for many years. In 1805 Young (81) observed liquid droplets clinging to a solid surface and suggested some form of attractive force must exist to account for this. Later Dupré (82) outlined an equation defining the work of adhesion $\triangle\gamma$ (per unit area of contact), required to remove one body from another, in terms of the energies of the solid/vacuum interfaces γ_1 and γ_2 and the solid-solid interface γ_{12}, viz

$$\triangle \gamma = \gamma_1 + \gamma_2 - \gamma_{12} \qquad \ldots 2.89$$

Values of $\triangle\gamma$ have been obtained for rubber and gelatine (83), while Gane et al (84) in their measurements on non-ductile solids, found that the effect of surface roughness was to make the adhesive forces much smaller than would have been expected for a given value of $\triangle\gamma$

Measurements of the total mechanical force, required to separate two bodies, have been made but with little consistency. However, for the particular case of a non-deformable sphere of radius Rp on a flat substrate, Bradley (85) has found that the "sticking" force is given by:-

$$F_0 = 2\pi Rp.\gamma \qquad \ldots 2.90$$

where F_0 is the adhesive force between the sphere and the substrate at the point of contact and γ the specific energy of adhesion. This expression has subsequently been used in two different approaches to determine the adhesive force between a sphere and a plane. In the first, Derjaguin et al (86) assume that the molecular attractive forces do not change the shape of the sphere even after accounting for non-contact (V,D.W. forces) and contact forces, while on impact the Hertz theory is used to predict the shape of the contacting bodies. In an alterantive approach, due to Johnson et al (83), the interaction forces between the elastic sphere and the plane (both repulsion and attraction) are considered as purely contact forces. Moreover, the "sticking" force does not depend on the elastic constants of the sphere but is defined by a relationship analogous to equation 2.90, in which a coefficient of 1.5 is used instead of 2.

The approach of Derjaguin et al, mentioned previously, allows expressions for the molecular attractive force, F_s, and the elastic

repulsive force, F_e, to be determined, where the expression for F_s is given by :

$$F_s = F_o \left[1 - 2b (\alpha)^{\frac{1}{2}} \ldots\right] \qquad \ldots 2.91$$

with $F_o = A.Rp/6t^2$ as given by Bradley (85) and Hamaker (74) in which A is the Hamaker constant, Rp the radius of the sphere, t is the separation where the attractive and repulsive forces between the sphere and plane just compensate each other, resulting in zero net attraction of the molecules, b is a positive constant and α is the imaginary separation the unflattened sphere and plane would obtain had they retained their original shape. The corresponding expression for the elastic repulsive force F_e is given by

$$F_e = \frac{4(Rp)^{\frac{1}{2}} E}{3(1-\sigma^2)} \cdot \alpha^{3/2} = K\alpha^{3/2} \qquad \ldots 2.92$$

where E and σ are Youngs Modulus and Poissons ratio for the sphere respectively.

It is readily observed that the value of F_e is proportional to $\alpha^{3/2}$. The corresponding expression for F_s developed by Derjaguin et al for the conditions of $\alpha < t$ and $\alpha > t$ are :

$$\frac{F_s(\alpha)}{F_o} = 1 - \frac{3(2)^{\frac{1}{2}}}{4}\left(\frac{\alpha}{t}\right)^{\frac{1}{2}} + \frac{1}{4}\frac{\alpha}{t} \ldots \quad \alpha < t \qquad \ldots 2.93$$

and

$$\frac{F_s(\alpha)}{F_o} = \frac{1}{2} + \frac{\pi^2}{9(3)^{1/2}(6\pi)^{1/3}}\left(\frac{t}{\alpha}\right) + \ldots \alpha > t \qquad \ldots 2.94$$

Equation 2.94 reduces to $F_s(\alpha) = F_o/2$ when $\alpha >> t$.

The area of contact in the collision between a sphere and a flat plate is given by 's' where $s = \pi a^2$ (a is the contact radius), while an alternative formula has been derived (86) leading to $s = \pi \alpha Rp$.

Combining these two results leads to :

$$\alpha = a^2/_{Rp} \qquad \ldots 2.95$$

For a 2 μm radius carbonyl iron microsphere impacting on a stainless steel surface with an impact velocity of 10 ms^{-1}, the contact radius is $\sim 2 \times 10^{-7}$ m (see Section 5.2.5). Assuming $t \sim 3 \times 10^{-10}$ m (86) it follows that $\alpha/t >> 1$ so that it is possible to evaluate the "sticking" force using $F_s(\alpha) = F_0/2$. For the present study $F_s(\alpha) = 1.85 \times 10^{-7}$ N

To obtain the equilibrium value of α, it is possible to use the condition which corresponds to $F_s(\alpha) = F_{0/2} = F_e$, thus

$$\frac{ARp}{12t^2} = \frac{4 (Rp)^{\frac{1}{2}} E \alpha^{3/2}}{3 (1 - \sigma^2)} \qquad \ldots 2.96$$

leading to :

$$\alpha = \frac{2^{1/3} Rp^{1/3} A^{2/3} (1 - \sigma^2)^{2/3}}{8 t^{4/3} . E^{2/3}} \qquad \ldots 2.97$$

In the case of a particle resting on the rigid substrate the force required to remove the particle from the surface (F_r) is obtained by letting $\alpha = 0$. This leads to :

$$F_r = F_0 \qquad \ldots 2.98$$

where F_0 has been previously defined. Numerically for the practical impact regime just referred to $F_r \sim 3.7 \times 10^{-7}$ N

In contrast, evaluating the elastic repulsive force given by eqution 2.92 leads to a value of 1.155×10^{-3} N, which indicates that in a collision between a microsphere and the target the elastic repulsive force would dominate the process.

In subsequent work Muller, Yushchenko and Derjaguin (87) have used a numerical computational technique to evaluate :

(i) the distribution of pressures within the contact zone

(ii) the profile of the particle during contact

and (iii) the contact and non-contact components of the force of interaction of the particle with the substrate at different particle/plane separations.

In particular the force required to separate the particle from the plane was found to depend on a single parameter μ , given by

$$\mu = \frac{8}{3\pi^2} \left\{ \frac{A^2 \, Rp \, (1 - \sigma^2)^2}{2 \xi^7 . E^2} \right\}^{1/3} \qquad \ldots 2.99$$

where all the above parameters have been previously defined. The conclusion of Muller et al was that if $\mu < 1$, then the formulae outlined above could be used to determine the molecular attractive forces, however if $\mu > 1$ the derivation of Johnson et al (83) should be considered. Substituting the appropriate values for this study - a 2 μm radius carbonyl iron microsphere in contact with a stainless steel surface, yields a value for μ of 0.252 thus validitating the values of F_s and F_r determined above. Experimentally Pollock et al (88) have obtained a value of 55 μN for the adhesive force between a platinum tip and a tungsten surface in which there was evidence of single asperity contact. However, when both surfaces possessed a surface contaminating layer the adhesive force was found to be 1.5×10^{-7} N which is of the order calculated above. Gane et al (84) have similarly shown that exposure of an iron surface to oxygen reduced the adhesion considerably.

2.5 The variation in surface charge density

Recently, there has been considerable interest in the nature of the forces responsible for adhesion at interfaces, (89, 90, 91, 92). Electrostatic attraction (image forces) can arise from either the charge transfer between bodies of different work functions, to give a space charge layer at the interface, or one of the bodies may carry a charge on its surface, (i.e. a charged microsphere). Krupp (89) has shown that, in general, dispersion forces (V.D.W. forces) predominate over electrostatic forces. However, for the metal/insulator case, high densities of charge may give rise to an attractive electrostatic force whose magnitude is many times greater than the dispersion forces. In fact, this has been observed by Higginbotham et al (93) for a gold-mica interface. Thus it is of great interest to be able to calculate the surface charge density distribution which gives rise to an attractive force. Berry et al (94) and Berry (95) have derived expressions for the surface charge density on an approaching uncharged spherical conductor when a uniform charge density is placed on an insulating planar surface. However, in the particular case of a charged microsphere approaching an uncharged planar target electrode the surface charge density on the plane is unknown. An estimate can, nevertheless, be determined by involving the method of images outlined in Section 2.4.1, and used by Lorraine and Corson (52). Referring to Figure 2.33 at point A, where co-ordinates are r and $\emptyset$, the potential is given by :

$$V = \frac{1}{4\pi\varepsilon_0}\left(\frac{q}{r} - \frac{q}{r'}\right) \qquad \ldots 2.100$$

where $r' = \sqrt{r^2 + 4g^2 - 4rg\cos\theta}$, ε_0 is the dielectric constant of free space and g is the distance the point is away from the plane.

The components of the electric field intensity at A are thus the components of ∇V

$$\text{i.e.} \quad 4\pi\varepsilon_0 E_r = -4\pi\varepsilon_0 \frac{\partial V}{\partial r} = \frac{q}{r^2} \frac{-q\,(r-2g\cos\phi)}{(r')^3} \qquad \ldots 2.101$$

and

$$4\pi\varepsilon_0 E_\phi = -4\pi\varepsilon_0 \frac{\partial V}{\partial \phi} = \frac{-2q\,g\sin\phi}{(r')^3} \qquad \ldots 2.102$$

To calculate the induced charge density σ' on the surface of the plane due to the presence of the charge, the normal component of the electric field (E_n) is required, such that

$$E_n = \frac{\sigma'}{\varepsilon_0} \qquad \ldots 2.103$$

For the case of a positively charged particle, it is clear that, the surface charge density is negative. Referring to Figure 2.33, the value of E_n to the right of the conducting plane is given by Lorraine and Corson to be

$$E_n = E_r \cos\phi - E_\phi \sin\phi = \frac{2qg}{4\pi\varepsilon_0 r^3} = -\frac{\sigma'}{\varepsilon_0} \qquad \ldots 2.104$$

For a point on the plane $r = \sqrt{g^2 + l^2}$, where l is the distance along the plane, it is possible to write for the surface charge density :

$$\sigma' = \frac{-q\,g}{2\pi(g^2 + l^2)^{\frac{1}{2}}} \qquad \ldots 2.105$$

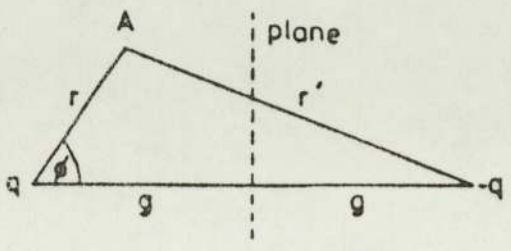

Figure 2.33: Point charge (q) opposite a plane; (-q) is the image charge

To calculate the surface charge density on an earthed plane due to the presence of a charged microsphere involves determining each point charge on the axis within the spherical shell and its exact location from the earthed plane. For a sphere/plane separation of 500Å , each point charge $q_1 \rightarrow q_n$, at its known distance from the plane $g_1 \rightarrow g_n$, is used, for a range of values of 'l' (0 → 10 μm), to compute the value $\sigma_1 \rightarrow \sigma_n$ which represents the charge density on the plane arising from each point charge inside the spherical shell. Finally the total surface charge density on the plane is found by adding all the $\sigma_1 \ldots \sigma_n$ values at each value of l . Figure 2.34 shows the normalised surface charge distributions at the sphere/plane separations of 500Å and 100Å, for a 2 μm radius microsphere. It is readily observed that the normalised distribution is sharper at 100Å than at 500Å .

In the presence of a thin dielectric medium on the surface of the target electrode, it is possible to compute the surface charge density on the metal surface supporting the dielectric (oxide). The surface charge density σ' as given by equation 2.105, can be modified to include the dielectric constant, ε_r, of the medium as derived by Lorraine and Corson.

If a dielectric constant of 4 is used, the value of σ' (dielectric) is given by :

$$\sigma'(\text{dielectric}) = \frac{-(\varepsilon_r - 1) q g}{2\pi(\varepsilon_r + 1)(g^2 + l^2)^{3/2}}$$

$$= \frac{3}{5}\sigma' \qquad \ldots 2.106$$

The above calculation is simplified by using the values of σ' determined by equation 2.105 and multiplying by a constant factor. On this basis the surface charge density, in the presence of a

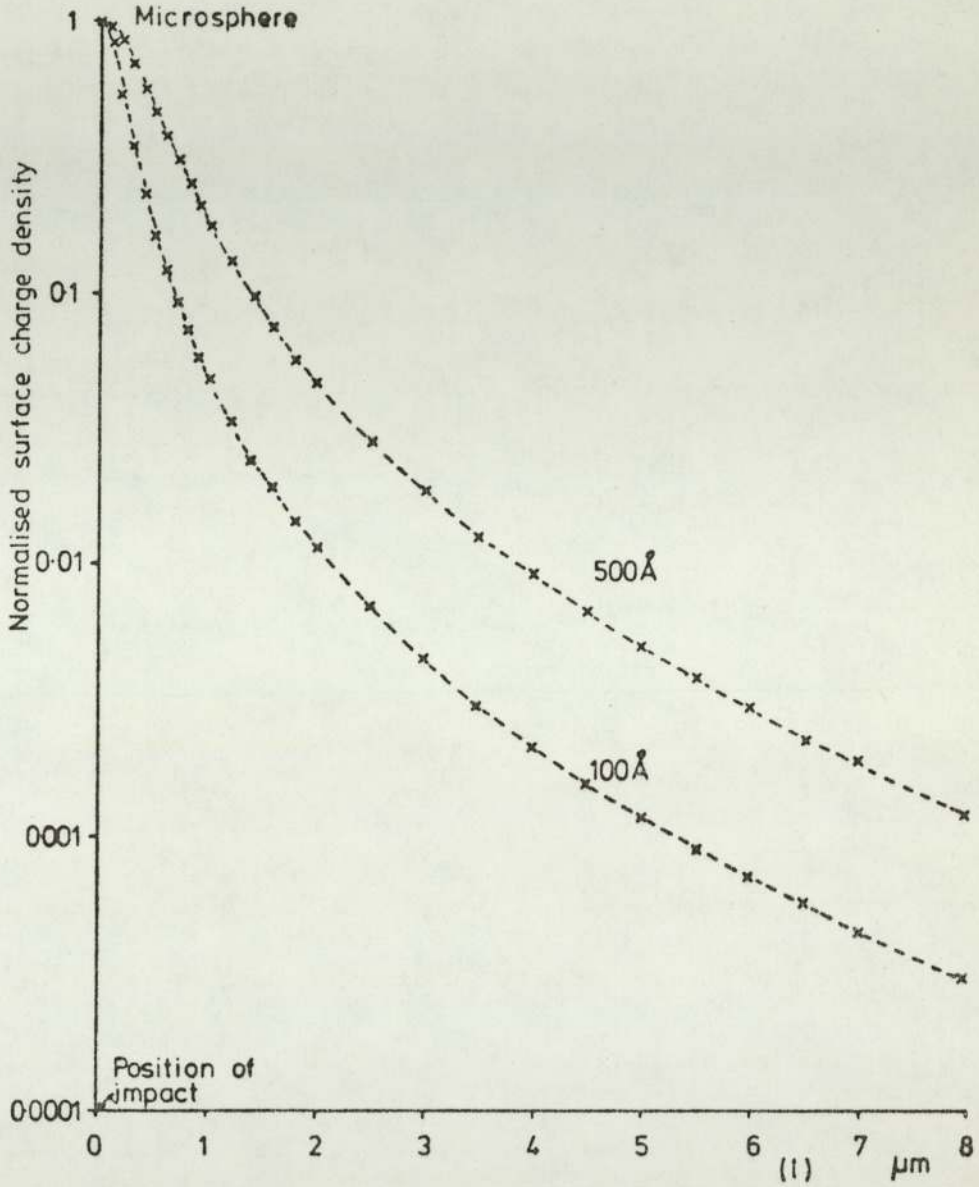

Figure 2.34 : The variation of surface charge density with distance along the target surface (l)

dielectric, on a conducting planar surface has the same form as for a planar metal surface without dielectric, but lower or higher for a given particle charge.

2.6 Hypervelocity impact-electrical phenomena

Much of the earlier high velocity work has been to study the effect of microsphere impact in space (96, 97, 98) with regard to the flux of space debris entering the atmosphere. There has, however, been much interest to simulate this behaviour within the laboratory and notably the work of Friichtenicht (96) has brought to light the effect of charge emission at high velocity impact by microspheres. In a later study, Auer and Sitte (33) examined the effect of firing high velocity carbonyl iron microparticles (with velocities ranging from 1.5 to 15 kms^{-1} and masses of the order of 3×10^{-16} to 3×10^{-13} kg) onto tungsten targets. Characterisation of the particles, before impact, was performed using a cylindrical drift tube detector the basis of which is described in Section 3.2. Measurement of the total charge released on impact was performed using an extraction grid (97% transparency) placed in front of the target. It was found that the total emission of positive and negative charges was proportional to the following :

$$m^{\alpha} v^{\beta} \qquad \ldots 2.107$$

where α and β are parameters which depend on the velocity of the microparticle and the material constants, while m and v are the mass and velocity of the impacting microparticle respectively. A mass spectrum of the positive charge produced from the impact of a particle on a slatted tungsten electrode indicated no W^{+} ions but ions of Na, K, Fe, Rb and Cs which is in agreement with Friichtenicht (96).

However, it should be pointed out that the ions of the alkali metals were formed at a higher rate than Fe ions.

Dietzel et al (30) in their micrometeoroid studies have studied the total charge occurring, due to impact ionization, for impact velocities up to 40 kms^{-1} using a grid assembly in front of the target. It was found that the charge (Q) was given by the relation :

$$Q = \text{const.}\ f(\theta, u)\ m^{\alpha} u^{\beta} \qquad \ldots 2.108$$

where θ is the angle of incidence, u the impact velocity, m the mass of the projectile and α, β are constants. However no impact ionization was observed below 1 kms^{-1}. Smith and Adams (32) have extended these measurements further to investigate the plasma generated by the impact of hypervelocity microspheres on a slatted target electrode. Using a similar extraction procedure to Dietzel et al it was observed that, for the case of carbonyl iron particles impacting at velocities 0.05 to 10 kms^{-1} onto a molybdenum target, equal numbers of positive ions and electrons were produced which obeyed a power law similar to that of Auer et al (33),

$$\text{i.e.,}\quad Q \propto m^{\alpha}\ u^{\beta} \qquad \ldots 2.109$$

In this expression $\beta = 3.2 \pm 0.1$ for impact velocities (u) in the range $0.05 < u < 10\ kms^{-1}$ while α takes the values 0.85 for $u > 1\ kms^{-1}$ and 1.33 for $u < 1\ kms^{-1}$. However from the mass spectrometer results, similar to that of Hansen (34) and Auer et al, the plasma generated on impact was found to be mainly due to the impacting projectile. Furthermore the amount of charge released depended on the impact angle with a four fold increase being evident using

a slatted target at 45° to the incident particle beam. As a final point the charge extraction at impact was found to reach a peak several seconds after impact and decay exponentially with time.

3.0 EXPERIMENTAL SYSTEMS

3.1 Introduction

The simulated microsphere impact studies, previously carried out within this laboratory, (1,9,26,97,98,99,100) and elsewhere, (101,102), have shown that both the mechanical and electrical impact responses depend upon (a) the type of impacting materials, (b) the oxide or contaminating layer on the target and (c) the magnitude of the gap field. However, the microscopic impact behaviour obtained from these experiments has been characterised by a very large scatter in the data arising from the impact events occurring over a large area. This was attributed to the use of a horizontal microparticle facility, in which the impacting microspheres were subjected to gravitional effects causing them to depart from their original trajectory, and the need to define both the mechanical and electrical impact behaviour on a sub-micron scale. To obtain more precise information on the impact process, a vertical microparticle facility has been developed which removes the effect of gravity on the microsphere trajectory and thereby gives an improved spatial resolution. By reducing the impact zone for the "test" microspheres, and using a laser ellipsometric facility, it has been possible to more accurately correlate the local properties of the surface with the observed particle impact behaviour. The impact regime is further simplified by making measurements under zero field conditions.

The new facility has been used to investigate (i) the impact of carbonyl iron microspheres on ambient oxidised metal, highly oxidised metal, semiconducting and insulating targets, (ii) the variation of the oxide conditions from one impact site to another, (iii) contact time measurements, (iv) the role played by an oxide in the charge exchange (tunnelling) mechanism, (v) microsphere impact in a high field, and (vi) the effect of different microsphere dust-source materials.

3.2 Subsidiary microparticle system

In order to determine whether the dust source gun described by Brah and Latham (1) could be used in the vertical mode, a preliminary experiment was performed using the apparatus shown in Figure 3.1. The vacuum system consists of a double stage rotary pump (Edwards 2SC50B), backing an Edwards E02 oil diffusion pump (using DOW CORNING 705 diffusion pump fluid) giving an ultimate system pressure of $\sim 10^{-9}$ m bar, after baking and using a liquid nitrogen cold trap. The microparticle facility for this pilot system consists of three elements :

(i) The microparticle gun which can be mounted vertically upward or downward, being interchangeable with the target assembly ceramic feedthrough.

(ii) The 'in-flight' detector (see later) which consists of a stainless steel drift tube (25 mm diameter, 25 mm long), without end facing grids, mounted onto a glass-to-metal feedthrough. Its output is connected to a voltage amplifier (gain 100) which feeds one channel of a Hewlett Packard storage oscilloscope (Type 180A). The trace can subsequently be photographed on a polaroid plate for presentation purposes. Details of the type of voltage amplifier and its characteristics will be given in Section 3.3.5.

(iii) The target assembly shown schematically in Figure 3.2, consists of a machined "button" which is mechanically polished with progressively finer emery paper and then with diamond paste down to $\frac{1}{4}$ μ. Finally, before it is mounted in the experimental chamber it is subjected to ultrasonic cleaning in iso-propyl alcohol and removed through the alcohol vapour. Immediately in front of the target is located a second cylindrical drift tube detector (10 mm long and 10 mm diameter), with end facing grids having a 90% particle transparency. To monitor the impact process the combined target and

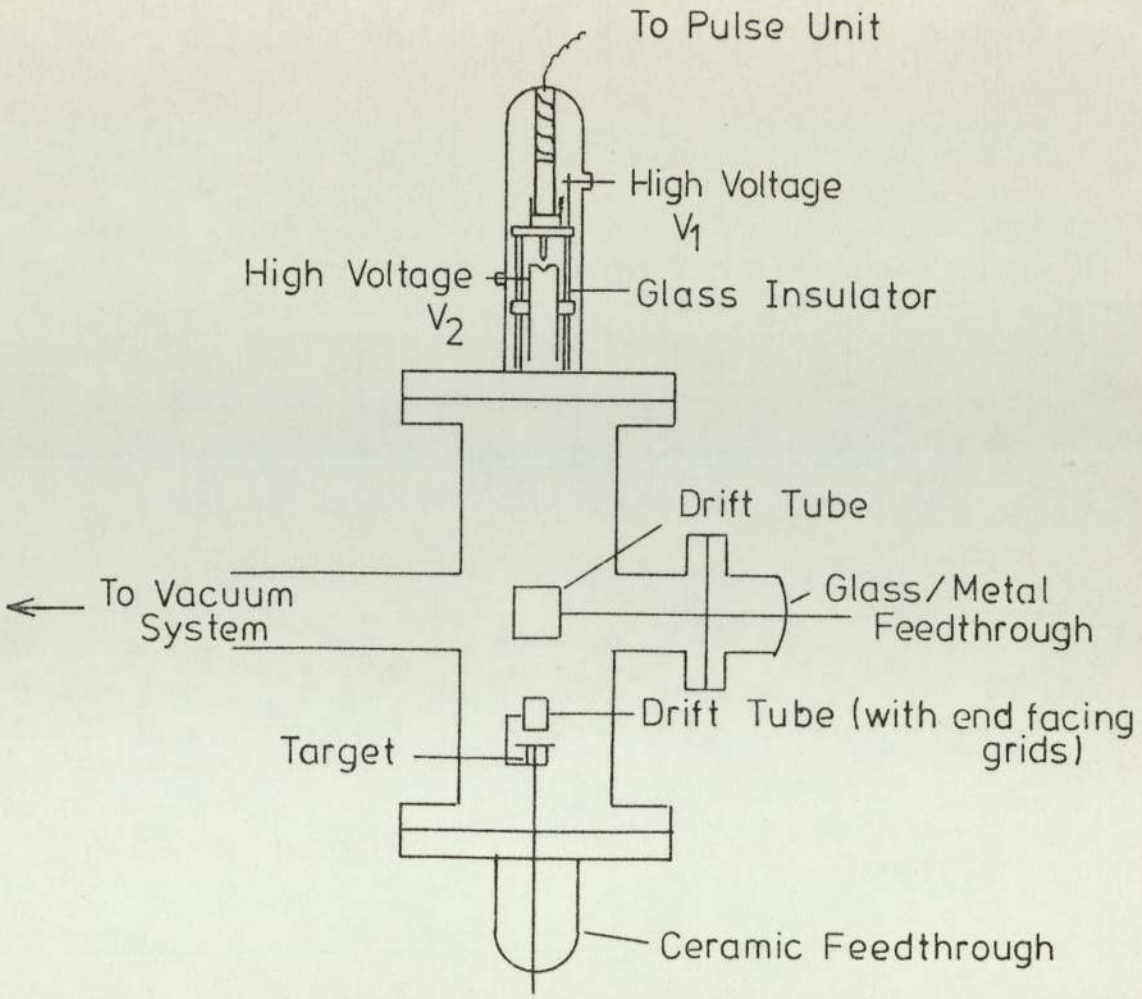

Figure 3.1: The Subsidiary Microparticle System

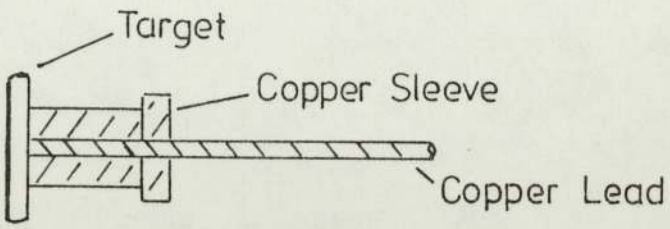

Figure 3.2: The Target Assembly

drift tube assembly are connected via a similar voltage amplifier (gain 100) to the second channel of the storage oscilloscope.

When a charged microsphere (0.1→5 μm diameter) passes through the large drift tube it induces upon it an equal and opposite charge which is displayed as a trapezoidal pulse on the first channel of the oscilloscope, see Figure 3.3 The microsphere then passes through the target drift tube and finally impacts onto the target surface. A similar form of detection is used in this latter drift tube assembly as discussed above for the large drift tube, however, the effect of the end-facing grids causes the observed trace to be much sharper, cf. the large drift tube trace. Schematic waveforms showing the path of the microsphere through the system in which a "sticking" or "bouncing" event occurs are shown in Figure 3.3. Referring to this figure the "sticking" event is characterised by all the particle charge being "dumped" upon the target, which decays with a time constant dependant upon the input capacitance and resistance of the voltage amplifier (see later). In practice, on applying the necessary gun voltages (4), the microparticle gun was found to perform equally well in either mode, (upwards or downwards) with typical experimental traces being shown in Figure 3.4. An interesting point to note is that for the titanium target used in this pilot study it was typical for $\sim$ 10% of the particles to undergo some form of bouncing event; this arises from surface contaminations within the system. Having determined the feasibility of using the dust-source gun in either vertical mode the more sophisticated microparticle facility previously used by Brah (4) and Mohindra (5) was redesigned to allow microspheres to be fired vertically downwards onto a modified target system.

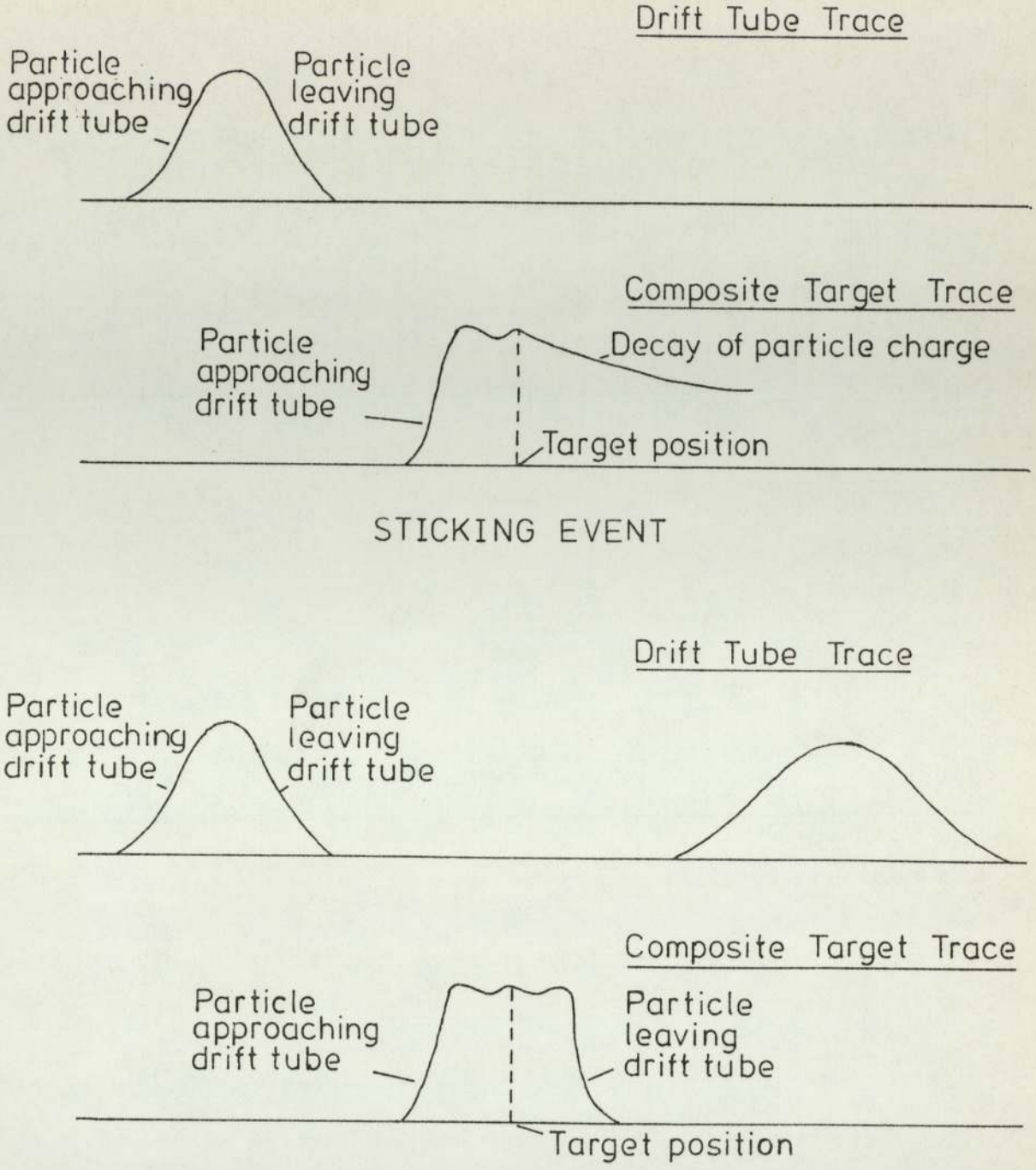

Figure 3.3: Schematic Sticking and Bouncing waveforms for the subsidiary microparticle system

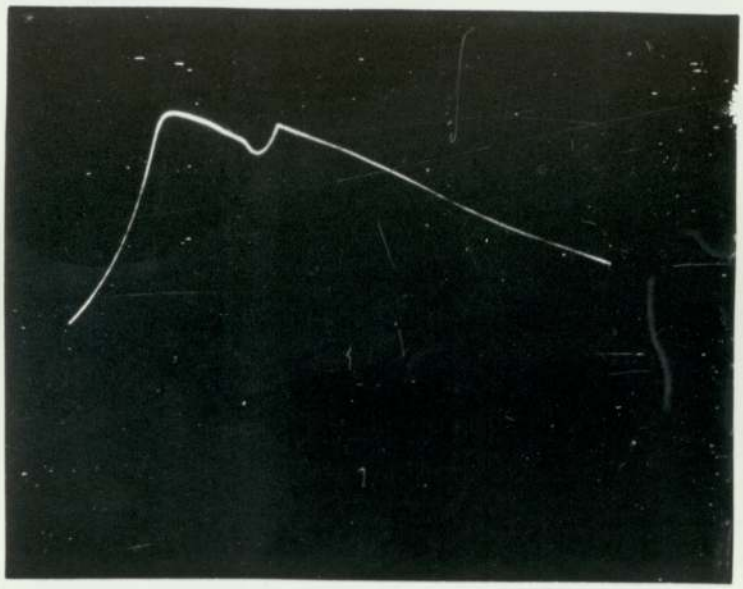

Composite target trace

Sen 0·02V/Div

Time Base 2ms/Div

"Sticking" Event

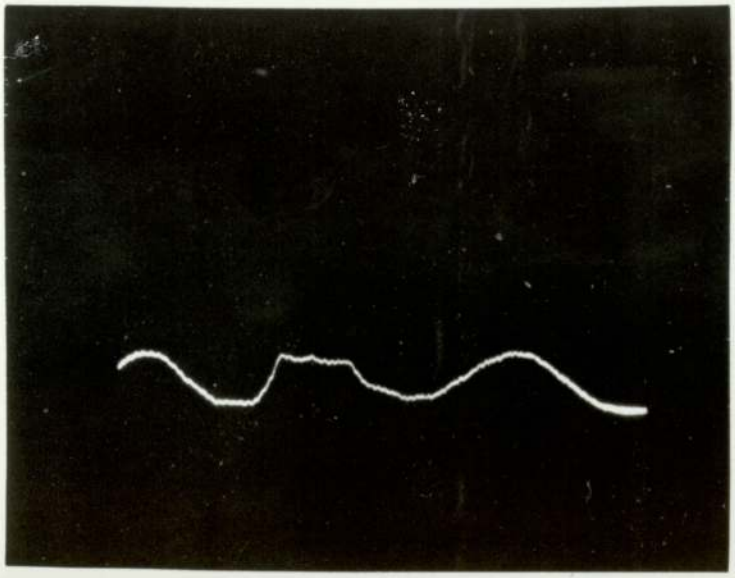

Combined drift tube and composite target trace

Sen 0·02 V/Div

Time Base 1ms/Div

"Bouncing" Event

Figure 3.4: Oscilloscope waveforms for the subsidiary microparticle system

3.3 Vertical microparticle facility

Figures 3.5 and 3.6 show the new vertical microparticle facility used in this study. The U.H.V. experimental chamber, which is mounted onto a standard Vacuum Generators pumping system (DP UHV - 2/4), consists of two sections, (i) the microparticle facility incorporating the dust source gun together with the electrostatic focussing/decellerating elements, collimating apertures, drift tube detector and associated amplifier, A1 and (ii) the target assembly consisting of a single target mounted in a new manipulator capable of accurately positioning the target under the collimating apertures . As will be described later in Section 3.3.6, rotation of the target manipulator through 90° allows an external laser ellipsometric facility to be used via the two optical ports at the side of the chamber. The target amplifier A2 is used to record the impact event.

3.3.1 Vacuum System

In order to study how the surface properties of a given target material influences the impact processes, it is essential that the "test" surface is maintained contamination free for the duration of the experiment. At pressures of 10^{-6} mbar, clean surface conditions remain for only a few seconds, whereas at 10^{-9} mbar, this time can be extended to a few hours. Therefore, U.H.V. conditions (i.e. pressures of $\lesssim 10^{-9}$ mbar) are an essential prerequisite for any experiments in which atomic cleanliness is imperative. Thus Figure 3.7 is a schematic representation of the complete U.H.V., bakeable, stainless steel vacuum system used for these studies. The experimental chamber (A) is mounted directly on the service well (B) and is pumped by a liquid nitrogen trapped oil diffusion pump (D.P.).

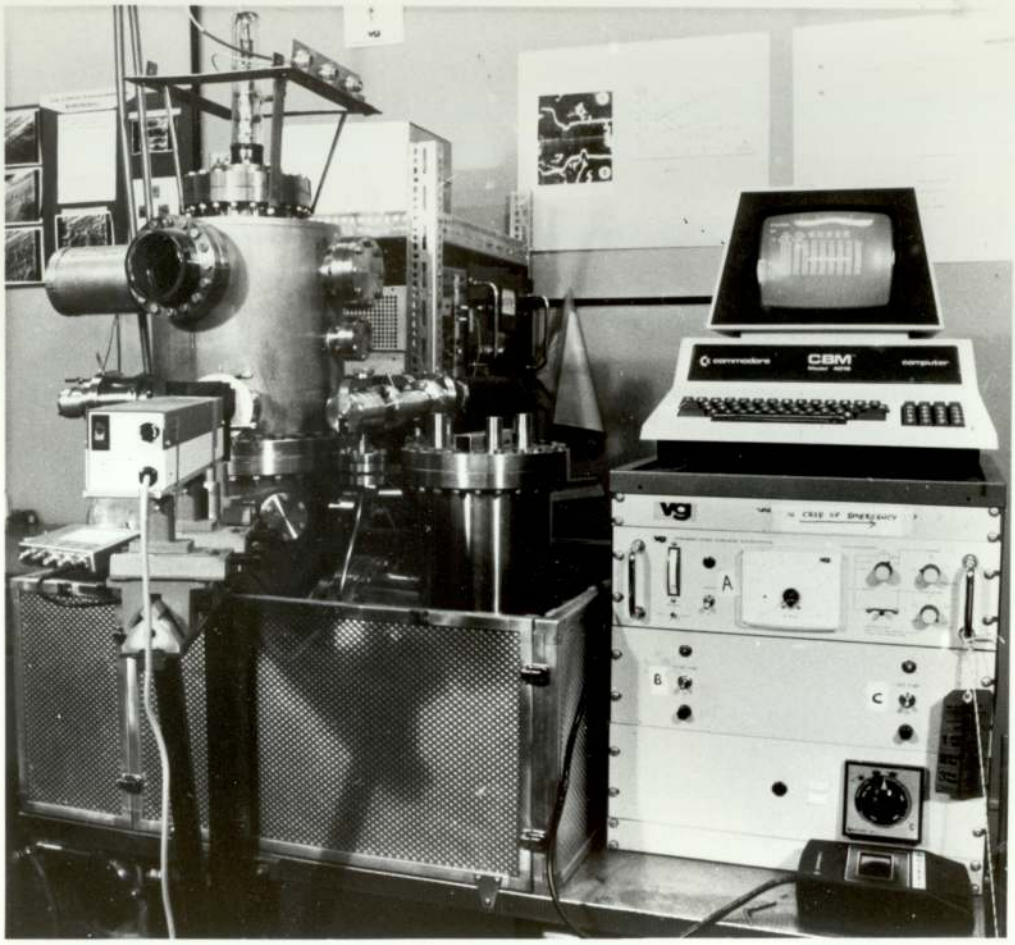

Figure 3.5: The experimental system

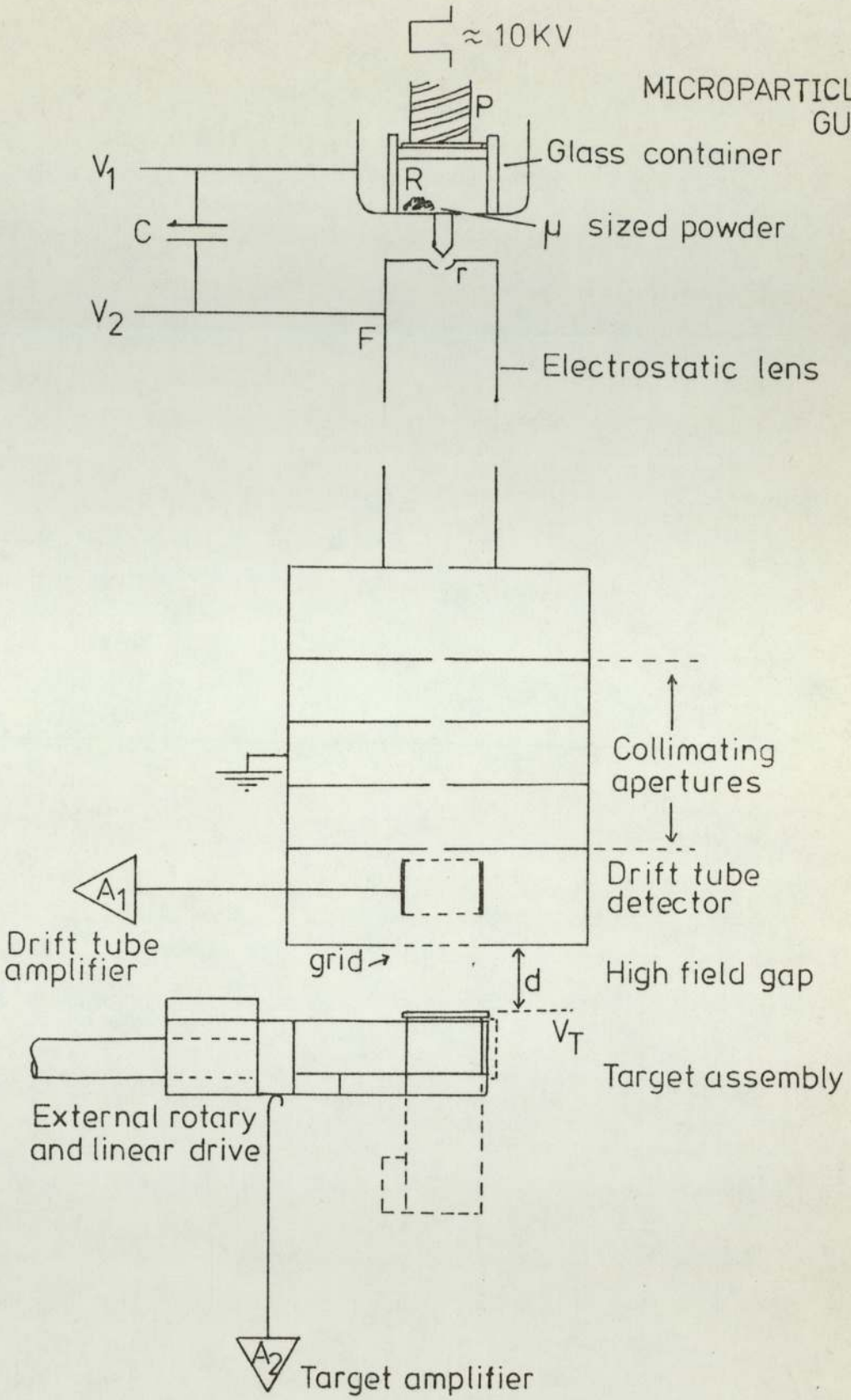

Figure 3.6: Experimental regime of the vertical impact microparticle facility

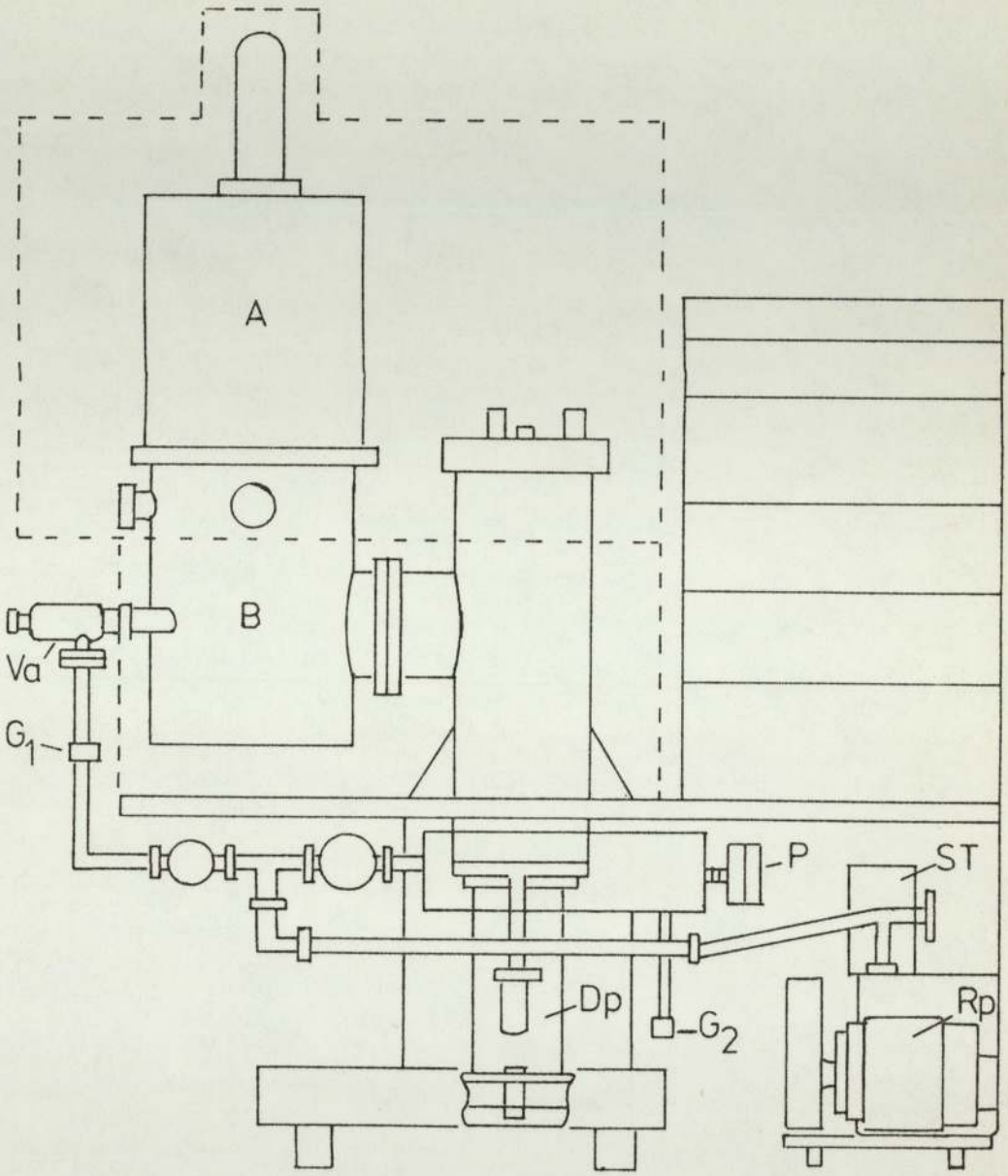

Figure 3.7 : The vacuum system

To achieve the desired U.H.V. performance the pump uses a special polyphenyl ether fluid possessing an extremely low vapour pressure: it is also of interest to note that this type of oil gives rise to conducting polymers when bombarded with electrons (103). Both the nitrogen trap (V.G. C.C.T 100) and the four stage oil diffusion pump (Edwards 106) have high pumping speeds of 480 Ls^{-1} and 1350 Ls^{-1} respectively. A two stage rotary pump (R.P.), with a pumping speed of 350 Ls^{-1}, 'backs' the oil diffusion pump via a sorption trap (S.T.). This trap prevents any hydrocarbon contamination, from the rotary pump, back-streaming to the diffusion pump. Safety mechanisms designed to protect the system against emergency consist of (i) a pressure protection swith (P) which cuts off the diffusion pump heater supply current if the 'backing' pressure rises above $\sim 5 \times 10^{-2}$ mbar; (i.e. preventing hydrocarbons from the diffusion pump contaminating the system) and (ii) a thermal cut-out which monitors the temperature of the diffusion pump cooling system. To facilitate a rapid turn around in changing the targets and reloading of the dust-source gun, a viton sealed isolation valve (bakeable to 250°C when open) can be operated across the service well, thereby allowing the nitrogen trap/diffusion pump to remain under vacuum. The experimental chamber can then be roughed out via the isolation valve (Va). The backing pressure is monitored by two pirani gauge heads attached at points G_1 and G_2 while a nude ionization gauge head measures the experimental chamber pressure. Without baking the ultimate system pressure, is $\sim 10^{-8}$ mbar while after baking $< 10^{-9}$ mbar can be routinely attained.

3.3.2 The Microparticle gun

The operating principles of the basic gun design have been described in detail in the original papers (2,9); there have, however, been subsequent modifications and this account deals with those developed by Brah and Latham (1). Referring to Figure 3.6, the microparticle powder, usually carbonyl iron microspheres with diameters in the range 0.5—10 μm, is placed in the reservoir (R) formed by the I shaped glass cup and the back face of a machined stainless steel charging electrode;the reservoir being mechanically located by a stainless steel plunger electrode (P) that also serves to provide an electrical coupling for firing the gun (see later). An escape hole connects the reservoir to the high field charging region which contains a bunch of splayed carbon fibres that act as the positive electrodes, and a radiused aperture (r) of 1 mm diameter that is positioned under the charging fibres. The size of the escape hole is critical and is governed by two limits,(i) if the escape hole is too large, an excessive amount of powder is wasted during the 'agitation' pulse thus reducing the life of the powder 'charge' and (ii) if the escape hole is too small powder collects around it eventually causing a blockage. More details of the above two processes can be found in section 3.3.3.

The 'firing' principle of the dust-source gun can be understood by considering the electrical arrangement of Figure 3.6 which shows the electrode (F) and the charging electrode are permanently maintained at potentials V_1 and V_2 via an isolating high voltage capacitor (C). In the 'rest' state the plunger (P) and the charging electrode (F) are at the same potential, thus leaving the micron-sized powder in a field free region. To 'fire'

the gun, a negative going pulse, $\sim$ 10 KV and 10 — 100 ms long, is applied to the reservoir via the plunger. The particles become charged by contact with the back face of the charging electrode and hence repel each other. In fact this phenomena is sufficiently violent to give rise to an explosive action with a small percentage of the particles leaving the reservoir via the escape hole and appearing in the charging region. The action of the electric fields in this region cause several of the particles to come in contact with the charging fibres thus acquiring a positive charge. Due to the approximate radial accelerating field acting between the fibres and the radiused aperture, the charged particles are accelerated towards the experimental zone. The effective potential through which the particles are accelerated is given by $V_1 - V_2$ and is denoted by V_G (the gun voltage).

The charge q acquired by a particle in a glancing collision with a fibre is determined by the quantum mechanical tunnelling process of contact electrification (104). Thus, although the size of the particle and the enhanced field at the tip of the charging electrode are the dominant parameters in determining the magnitude of q, the charging process may also be significantly influenced by the contact time and the nature of the surfaces. For the ideal case of a particle in contact with a fibre tip which is in the form of a hemispherically capped cylinder of radius r, it can be shown (2) that the equilibrium charge q acquired is :

$$q = 2\pi^3 \frac{Rp^2}{r + Rp} \cdot E_r r^2 \qquad \ldots 3.1$$

where E_r is the enhanced electric field and Rp is the radius of

the particle, Hence when Rp >> r, and assuming $E_T \propto V_G$,

$$q \propto V_G r^2 \qquad \ldots 3.2$$

Therefore, it follows that the larger the particle, the bigger the acquired charge. As a final point, to use a splayed bunch of carbon fibres as the charging electrodes has the dual advantages of, first increasing the field enhancement factor by an order of 10 (105) with respect to a single conically shaped metal electrode, and secondly, a charging system which possesses no electrically insulating oxide layers which are normally present on metallic electrodes. As a consequence, it is possible, with this arrangement to obtain an adequate single particle charging efficiency with $V_1 - V_2 = 3$ K V, giving a corresponding particle velocity of $\sim 10\ ms^{-1}$.

3.3.3 Paralysis of the microparticle gun

One undesirable function of the microparticle gun, that has frequently been observed, is that the powder becomes paralysed in the reservoir. This effect has been noted previously, by Mohindra (5) and was subsequently found to be caused by the removal of the vacuum deposited conductive coating on the rear face of the glass cup (see Figure 3.6) which gave rise to a non-uniform field across the reservoir, when the high voltage pulse was applied. However, several other mechanisms have been found to cause a similar paralysis effect :

(i) The type of powder plays a significant role in the agitation behaviour in the reservoir. Two types of carbonyl iron powder have been used predominantly throughout this study, namely types E and H (of which more details can be found in Section 4.2), where the particle size distribution for the 'E type' powder is centred around 3 μm diameter while that for the 'H type' is around 2 μm diameter. It has been observed that it is very rare for paralysis to occur with the 'E type' powder while the opposite takes place for the 'H type'. In fact, the adhesive properties of the 'H type' powder appears to be a major factor since even before agitation pulses are applied, the microparticles can be seen adhering to the inner surface of the reservoir. Therefore 'E type' powder has been used predominantly in the microparticle impact studies.

(ii) With the micrpoarticle gun in the vertical mode, the escape hole from the resevoir is normally covered by powder which increases the probability of the hole becoming blocked. To overcome this problem an alternative design for the

exit hole system has been used, see figure 3.8, in which most of the powder remains at the sides of the reservoir.

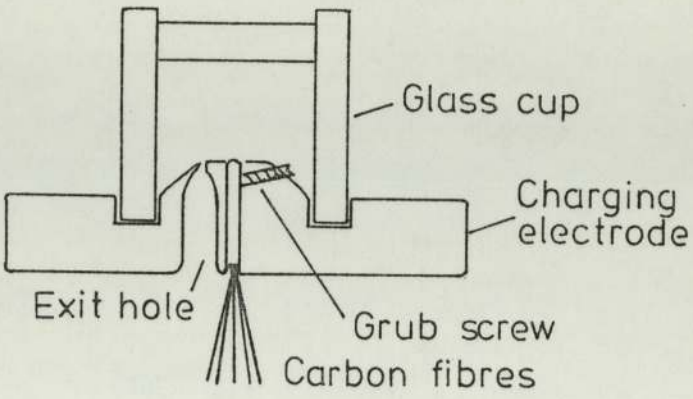

Figure 3.8 Charging electrode assembly

Finally, if the gap between the charging fibres and radiused aperture is small, any "aggregates" appearing in the high field charging region may 'short out' the fibres to the radiused aperture thus paralysing the gun. However, if the gap is too large, the radial accelerating field is small leading to a reduction in the particle flux. Thus it should be arranged that the charging fibres are alligned 'flush' with the stainless steel electrode supporting the radiused aperture.

3.3.4 Electrostatic decellerating element

To produce a low velocity paraxial distribution of particles a decellerating electrostatic lens is employed. The exact design and construction of the lens can be found in reference 106, where it is discussed fully. For the present studies, a decellerating voltage V_2 ($\sim$2.5 KV) has been used throughout since it was found to produce the correct conditions for reducing the

particle velocity and for focussing them in front of the first collimating aperture (see Figure 3.6) One of the most notable features of an electrostatic lens is that its focussing properties are independent of the q/m ratio of the particles, although it is however, still dependant on their approach velocity. As a consequence severe chromatic aberation occurs, with the slower velocity particles being focussed further from the collimating aperture. Hence by adjusting the lens voltage some degree of velocity selection can be obtained.

3.3.5 Microparticle detection

In this new facility, positively charge microspheres emerge from the dust-source gun and its associated electrostatic focussing/decellerating lens to pass successively through a series of four collimating apertures and an in-flight detector, before impacting on the target surface, see Figure 3.6. The impact zone is now governed principally by the size of the final collimating aperture which for the present measurements was chosen to have a diameter of 1 mm. Characteristation of the microsphere before impact is performed by a drift-tube detector of which the operating principles have already been discussed in Section 3.2. After detection, the signal is amplified and appears as a trapezoidal voltage transient (if a voltage amplifier is used) on a storage oscilloscope. A typical schematic trace of a drift-tube waveform is shown in Figure 3.9, where the amplitude of the pulse is proportional to the microsphere charge and the length inversely proportional to the microsphere velocity. Using the equation of the conservation of energy, it is then possible to determine the mass of the microsphere (m) and so

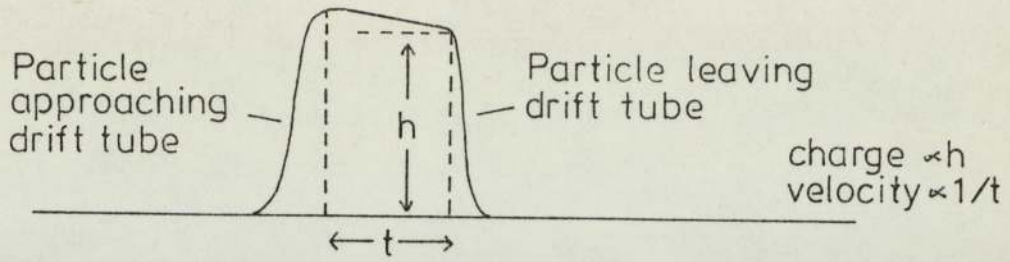

Figure 3.9: Schematic drift tube waveform

characterise it completely, i.e.,

$$\tfrac{1}{2} mv^2 = qV_G \qquad \ldots 3.3$$

where q and v are respectively the charge and velocity of the microsphere determined from the trapezoidal pulse, and V_G is the gun voltage. A similar form of detection is used to record the impact of the microsphere onto the target electrode. Thus as the microsphere emerges from the earthed grid (see Figure 3.6) it induces a negative charge on the target which is sensed and amplified. Figure 3.10 shows a typical waveform obtained, for a "sticking" event, when a single voltage amplifier is connected to both the drift tube and the target.

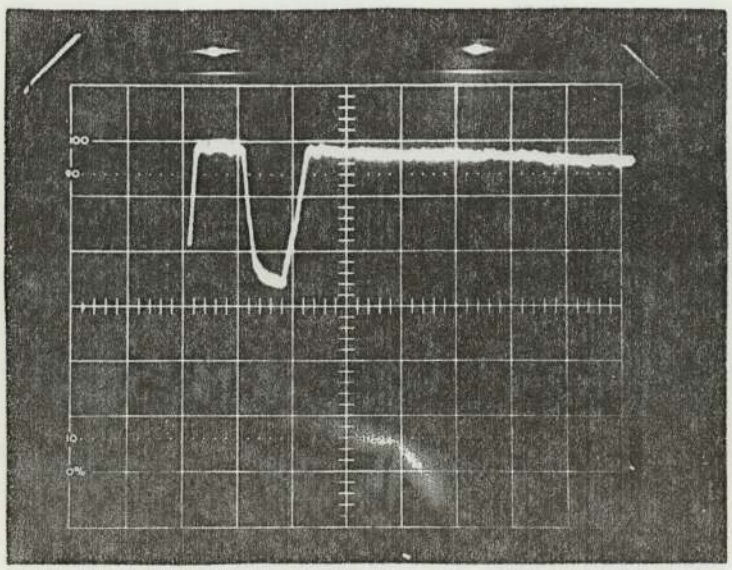

Combined drift tube and target waveforms

Sen 0·02 V/Div

Time Base 1ms/Div

Figure 3.10 Oscilloscope trace showing a particle "sticking" event

To enable detailed information to be obtained from the drift tube and target system, it is important to be able to measure the transient events accurately. This requires an amplifier which, ideally, possesses the following characteristics

(1) A low noise level in comparison with the input signal

(2) A high input impedance - to avoid differentiation of the input signal: from this it follows that the input time constant of the amplifier should be large compared with the transit time of the microparticle through the drift tube.

(3) A low input capacitance giving maximum sensitivity to the input signal.

(4) A high "slew" rate to allow the amplifier to follow rapid changes in the input signal.

(5) A wide bandwidth - typically $\geq$ 100 MHz, in order to give no distortion of the rise and fall of the drift tube and target traces.

(6) The output impedance must match the input impedance of the oscilloscope to ensure efficient coupling.

However, it is not always possible to obtain an amplifier which possesses a high slew rate, an extended frequency response and a high input impedance, therefore the voltage amplifier shown in Figure 3.11 has been designed to fulfil the above criteria. In this circuit, the operational amplifier has been adapted to have, not only a high input impedance, typical of an F.E.T. amplifier, but also a high slew rate. It can be readily observed that the non-inverting configuration is used, and with a voltage gain of 100 a charge detectability of $\leq 8 \times 10^{-16}$ coulombs can be realised.

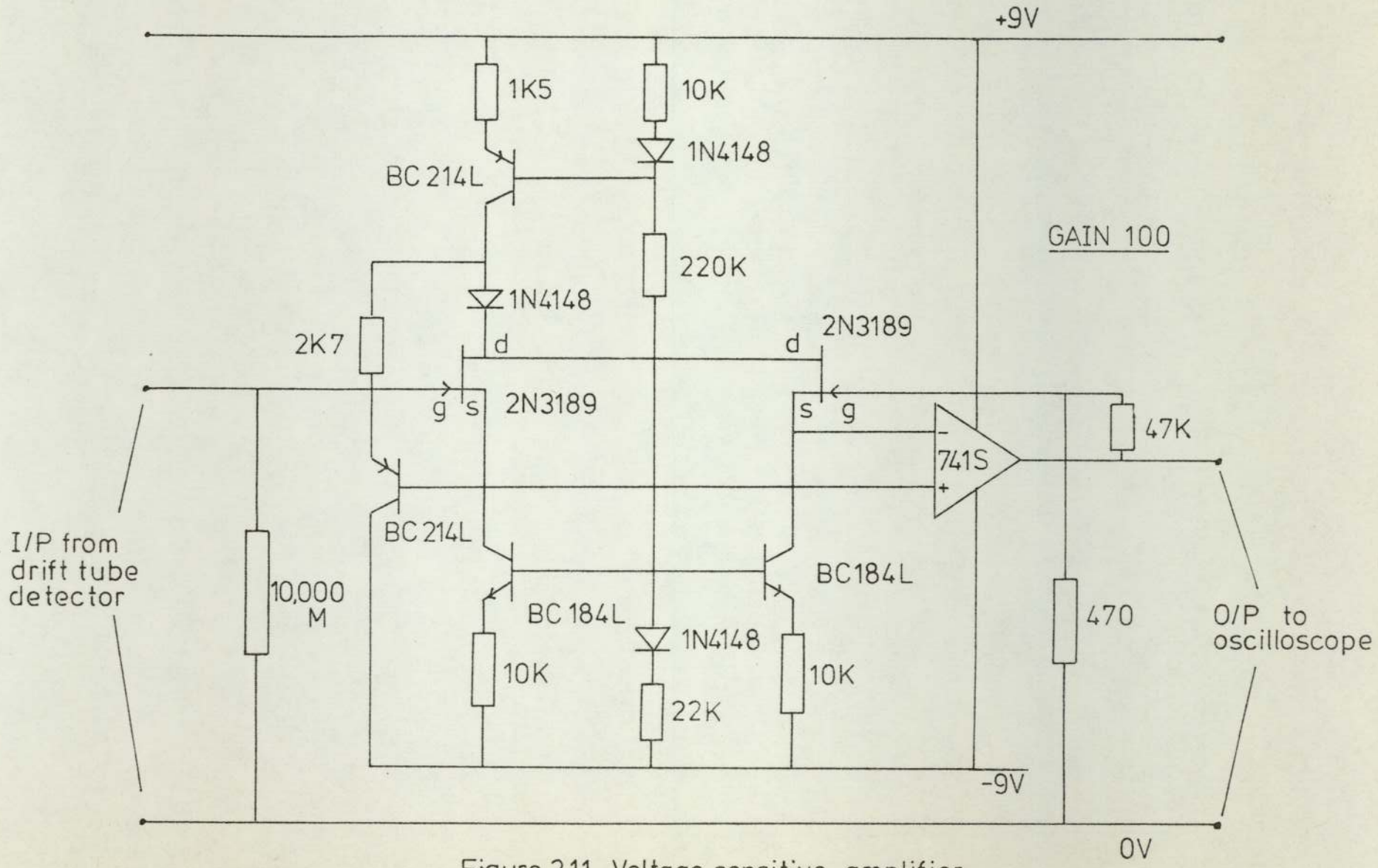

Figure 3.11 Voltage sensitive amplifier

Figure 3.12 indicates the second type of amplifier used for the charge measurements. This is a charge-sensitive amplifier (type EC 501), built by Daresbury Laboratories, having a charge efficiency of $\leq 2 \times 10^{-15}$ C. Its design allows the input capacitance of the drift tube or target system to be neglected in comparison with its effective feedback capacitance. The major advantage of a charge-sensitive amplifier over the voltage-sensitive type is that the stray input capacitance (arising from leads, etc.,) can be ignored whereas for a voltage-sensitive amplifier its presence leads to a reduction in the output voltage. A particular advantage of the charge-sensitive amplifier used in this study is that the charge can be detected in the presence of a high field, thus allowing the charge "dumped" during the impact event to be ascertained in the charge reversal/repulsion measurements, see Section 4.8. Thus referring to Figure 3.13, which shows the general form of a charge sensitive amplifier, C_f is the feedback capacitor which takes the place of the feedback resistor used in an inverting voltage amplifier, and C_{in} represents the input capacitance of the amplifier plus the additional capacitance of the cables. If the input current to the amplifier is I, of which the major part flows through C_f, V_{in} is small. Therefore it may be written that :

$$I = C_f \frac{d}{dt} (V_{in} - V_{out}) \qquad \ldots 3.4$$

However, since $V_{in} << V_{out}$ equation 3.4 may be approximated by

$$I \approx - C_f \frac{d}{dt} (V_{out}) \qquad \ldots 3.5$$

so that

$$V_{out} = \frac{-1}{C_f} \int I.dt \qquad \ldots 3.6$$

If the current flows for a very short time, equation 3.6 may be further modified by using the relation :

$$V_{out} = -q/C_f \qquad \ldots 3.7$$

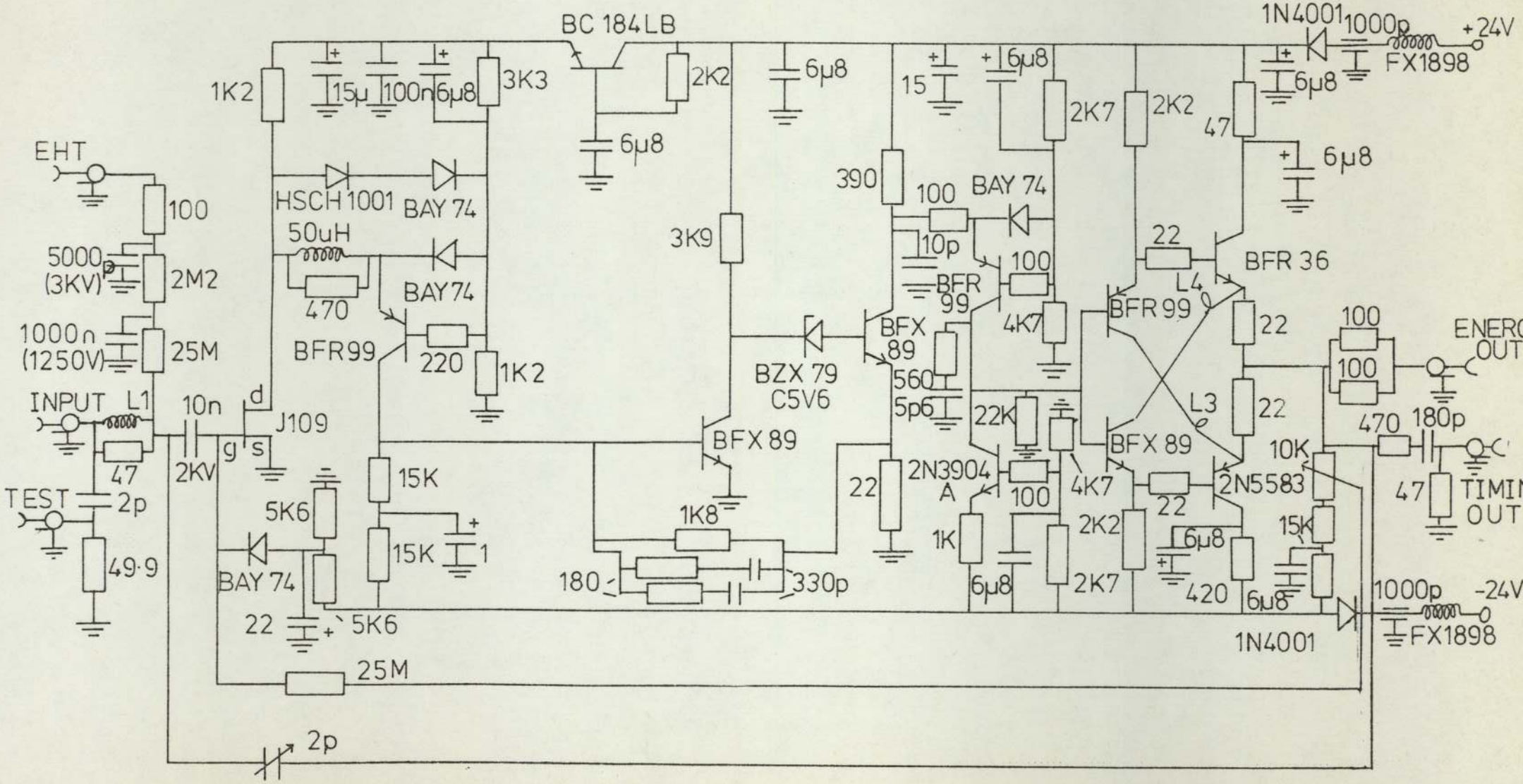

Figure 3.12: Charge sensitive amplifier

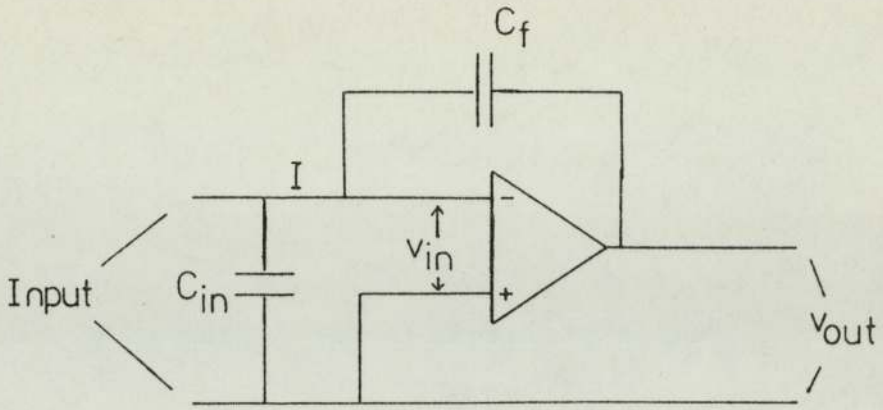

Figure 3.13: General form of a charge sensitive amplifier

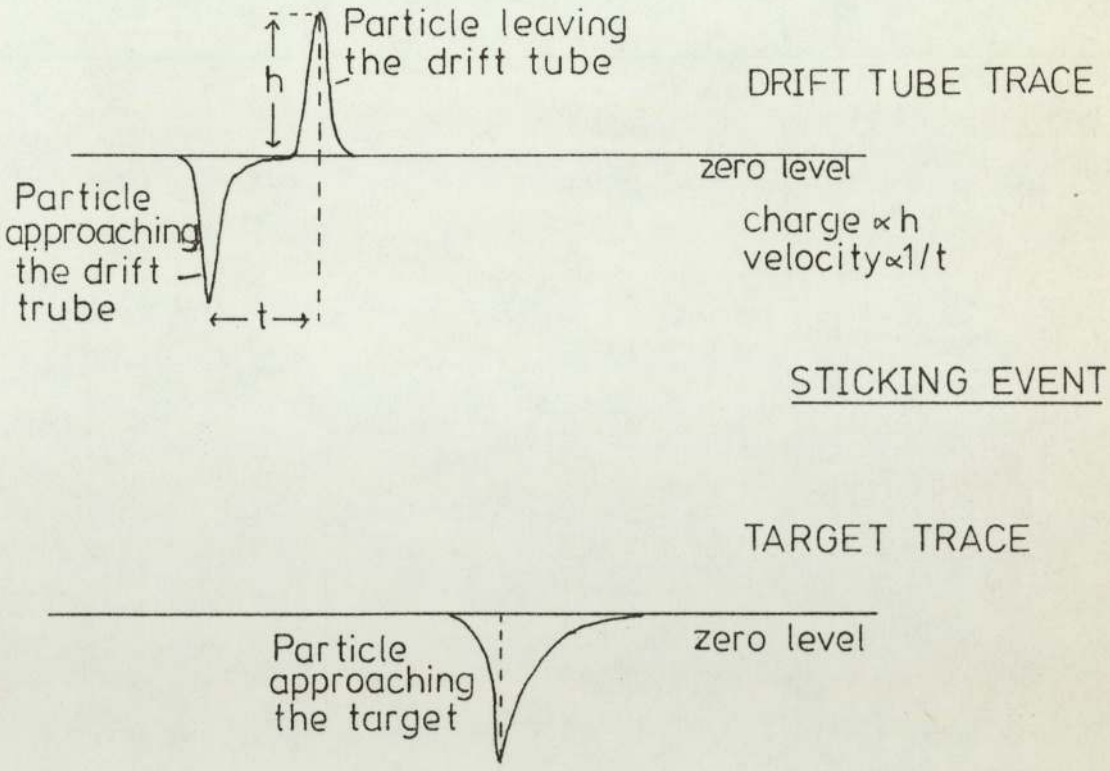

Figure 3.14: Schematic drift tube and target waveforms for a charge sensitive amplifier

where the output voltage is seen to depend only on the feedback capacitor C_f and the change q on the microsphere. The charge sensitive amplifier can be assumed to perform correctly provided the following condition , $A \cdot C_f >> C_{in}$, is satisfied, where A is the closed loop gain of the amplifier; thus for A = 100 and C_{in} = 10 pF, a suitable value of C_f would be 1 pF. Typical schematic traces for both the drift tube and target waveforms using a charge-sensitive amplifier are shown in Figure 3.14, where it can be seen that differentiation and inversion of the signal occurs in both waveforms.

3.3.6 Target assembly

Figure 3.15 shows the metal target modules used in this study. All the metal targets were machined from the solid material except for titanium 117 and 318 which were constructed using titanium sheet mounted onto an aluminium shoulder. Each

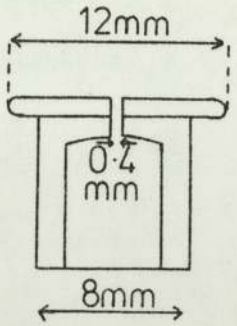

Figure 3.15: Metal target module

target has a 0.4 mm hole in its centre which is used in the alignment process (see Section 3.3.7) and the target surface preparation is similar to commercial polishing techniques of which mention has

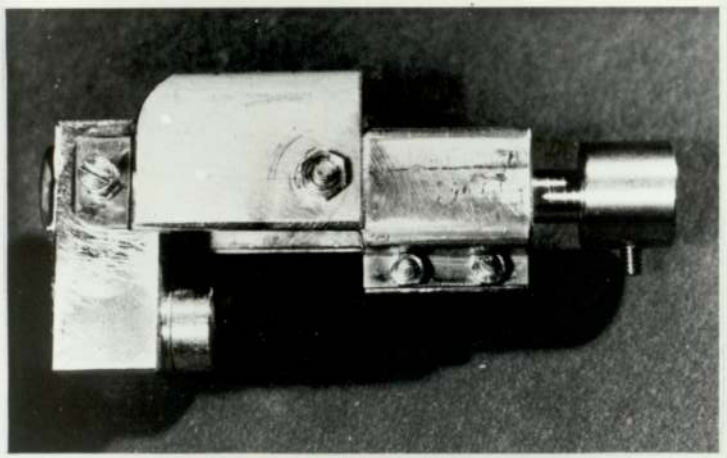

Open view
(a)

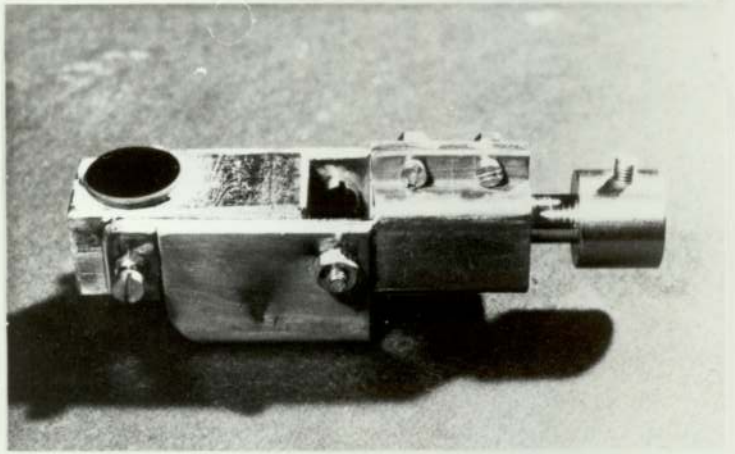

Closed view
(b)

Figure 3.16: The mark 1 target assembly

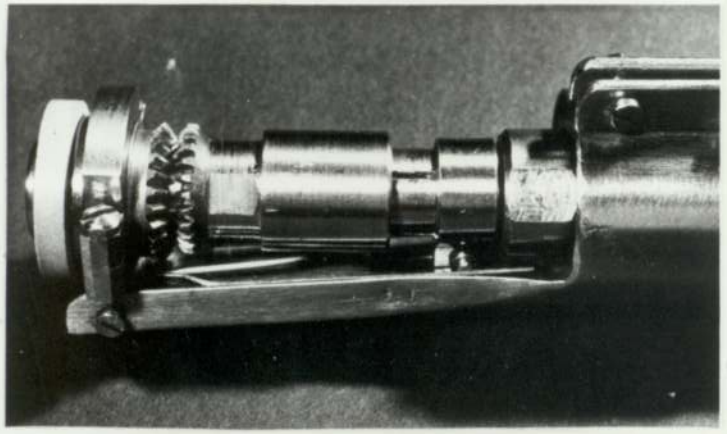

Open view
(a)

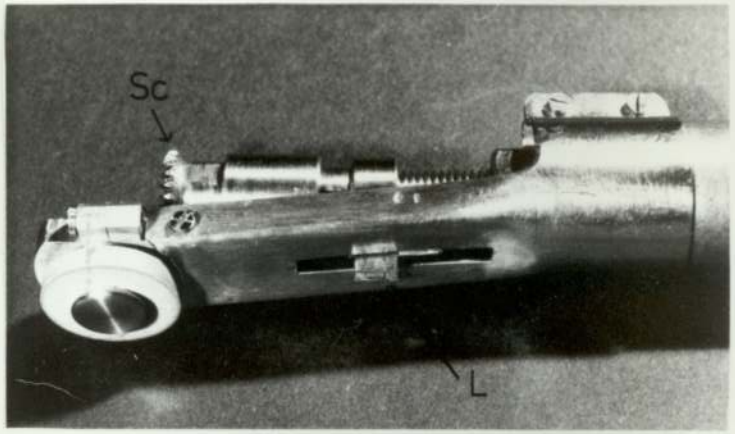

Closed view
(b)

Figure 3.17: The mark 2 target assembly

already been made in Section 3.2. To allow the complementary ellipsometric facility, for the characterisation of the mean condition of the impact zone, to be performed two alternative target assemblies have been developed for use with the vertical microparticle system. Figure 3.16(a) and 3.16(b) are the open and closed views of the mark 1 unit, while Figures 3.17(a) and 3.17(b) are the corresponding views of the mark 2 unit. The mark 1 unit, which has been used predominantly throughout this study, allows the target to be bombarded by microspheres when in the horizontal plane (see Figure 3.6), but on rotation by 180°, the cradle supporting the target pivots under the action of gravity thus bringing the target into a vertical position, as shown by the dotted lines in Figure 3.6, where the ellipsometric facility can be used. A final rotation of 180° causes the cradle to return under gravity to its original position bringing the target back into its horizontal plane. The unit is secured to the shaft of a new manipulator, described in Section 3.3.7, around a ceramtec insulator to provide isolation from the chamber.

The mark 2 unit shown in Figures 3.17(a) and 3.17(b) consists of a target holder mounted into a 'ceramtec' disc around which is fixed a gear wheel. In the horizontal mode, the target can be bombarded by microspheres, while rotation of the external manipulator drive (see Section 3.3.7) in the anti-clockwise direction causes the target assembly to revolve around its central axis. However, after $2 \rightarrow 3$ revolutions the spring driving cog (S_c) is withdrawn allowing the target assembly to fall due to the retraction of level (L). In this way, the target holder is pulled into a vertical position to allow the laser ellipsometric facility to be used. Rotation of the external manipulator drive in the clockwise direction reverses the above process, with the gear wheels meshing automatically. Continued

clockwise rotation then rotates the target holder in the horizontal plane allowing alternative impact sites to be used on the same target. It should finally be noted that for U.H.V. requirements, all the metal sections on both target assemblies are made from stainless steel.

The insulating surfaces, used in the later experiments were in disc form, the diameter of which corresponded to the surface diameter of a metal target (12 mm). Table 3.1 lists the thickness and type

SPECIMEN SAMPLE	THICKNESS. μm
Mica (1)	100
Mica (2)	50
Mica (3)	3
Ebonite (1)	400
Ebonite (2)	800
Cellulose	400
Glass	200
Red-fibre	320
P.V.C	400
Tufnal	280
Paxolin	220

Table 3.1: Insulator specimen data

of insulator used. Each insulator is mounted on the top of a metal target (usually nickel) with silver conductive paint, thus ensuring a good electrical contact between the insulator and target. A considerable amount of care was taken in the cleaning process of the insulators, since damage could easily result when using chemical solutions. A similar mounting technique was used for the semi-conducting (silicon) slices.

3.3.7 Manipulation System

To allow the target electrode to be positioned with great accuracy, underneath the collimated microparticle probe, it was necessary to develop a sophisticated target manipulator. Referring to the schematic diagram of Figure 3.18 this was based around a Vacuum Generators rotary motion feedthrough, type R.D.6., which was connected via a copper gasket to a 50 convolution stainless steel bellows assembly having internal and external diameters of 1.39" and 1.89" respectively and terminated at either end with standard FC38T flanges. The bellows assembly is bolted directly to the experimental chamber via studs fixed within the bellow flange, see Figure 3.18. Located around the outside of this flange is a stainless steel collar (C) secured by a locking bolt (b) to a stainless steel tube, (t). The two pivots (p) which support the bellows flange at the rotary drive face enter a stainless steel collar (d) which can rotate on the outer supporting tube (t), thus enabling the manipulator to move in or out of the experimental chamber. From a knowledge of the number of threads to the inch (24 in this case), the target manipulator can be set at a known distance from the alignment position (see later). Fine adjustment can be obtained using external 45° markings on the collar (d). Once alignment is complete a sprung aluminium cap allows the rotary drive to be locked in position. Although a linear 'shift' can be obtained in the 'x' direction, see Figure 3.18, only a sweep motion occurs in the 'y' direction due to the action of the pivots. This latter motion is obtained using two thumbscrews (th) operating on a tiller (a), as shown in Figure 3.18. Figure 3.19 shows the manipulator with the mark I target assembly attached.

To align the target under the microparticle collimator

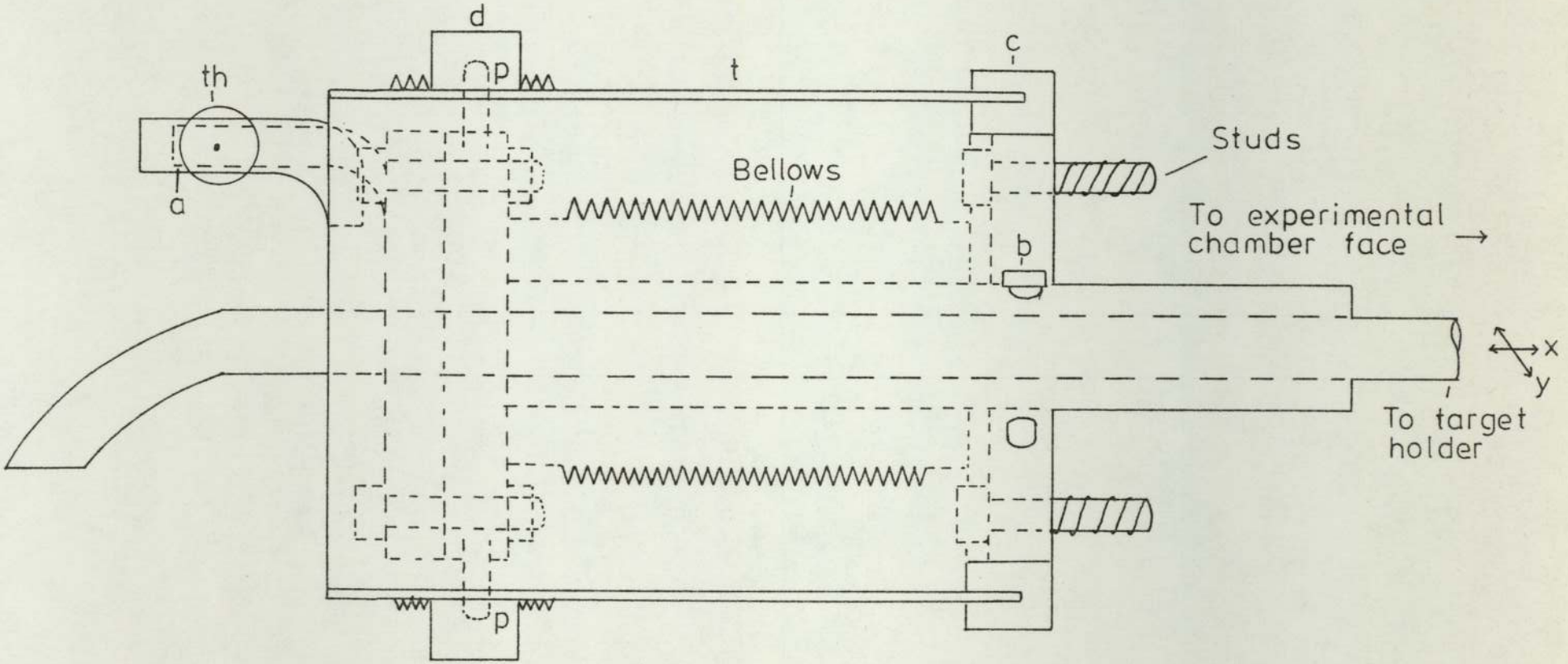

Figure 3.18: Schematic view of the target manipulator

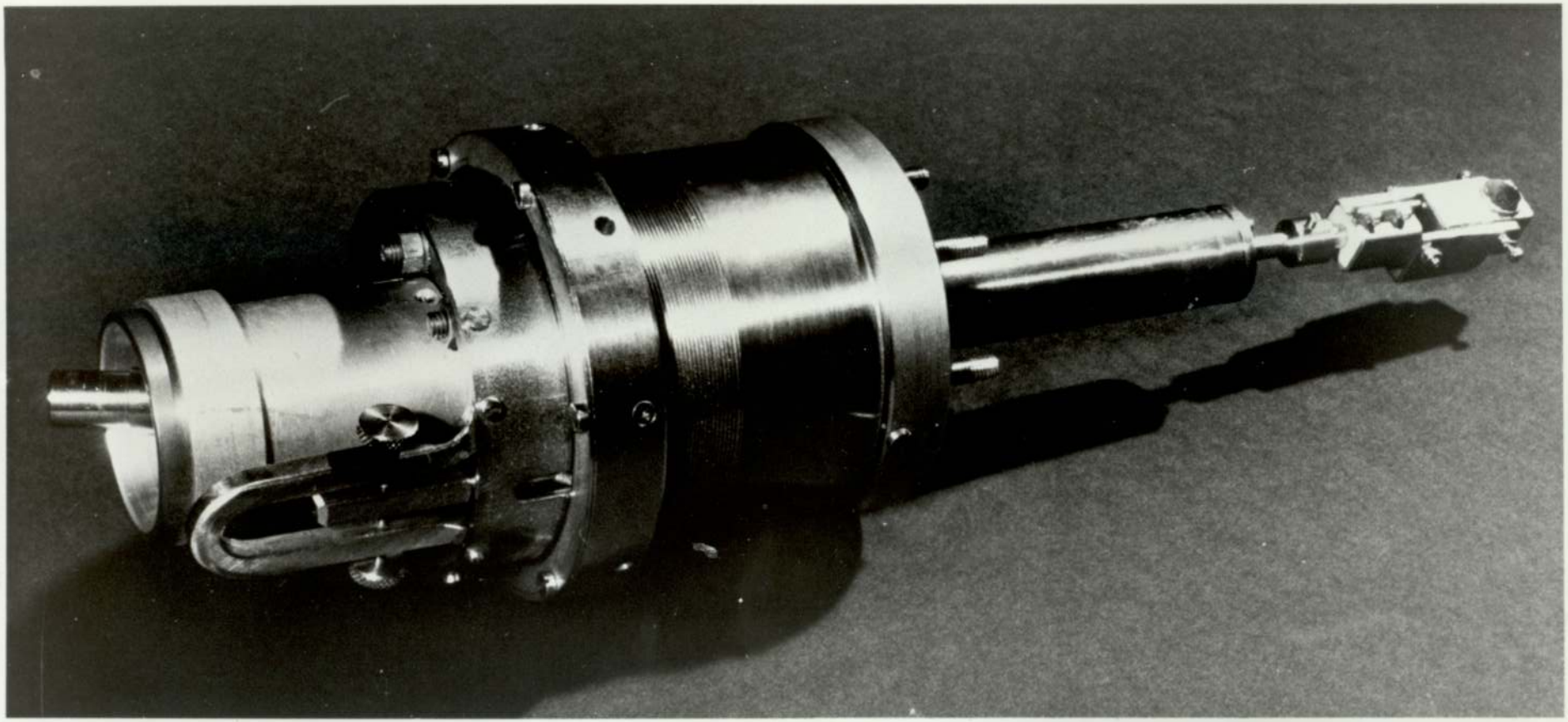

Figure 3.19: The target manipulator

assembly requires the removal of the microparticle gun and its replacement by a high intensity light source that projects an image, of the final collimating aperture, onto the target surface. Using the external manipulator controls, the target can be positioned until the light beam passes through the 0.4 mm hole in the target and is reflected from a glass mirror (supported on a stainless steel frame) under the target. Figure 3.20 indicates the arrangement when light passes through the target, is incident upon the mirror, and is finally reflected through one of the ellipsometer entry ports, (see later). In practice the external manipulator is adjusted until maximum intensity of the reflected light is observed. After alignment, the target is moved a known distance away from the central position ready for the impact experiments. Thus, the central hole can be used as a fixed reference allowing the "test" microspheres to be found with relative ease, in an S.E.M., once bombardment is complete.

3.4.1 Argon-Ion gun

The erosion of a surface exposed to ion-bombardment has been known for a long time (107). Farnsworth et al (108), have subsequently developed a technique to produce atomically clean surfaces possessing only a small proportion of surface defects and a similar approach has been adopted in this study. Figure 3.21 shows the auxilliary gas handling system which is initially evacuated to $\sim 10^{-2}$ mbar using a sorption pump (V.G. M.S.200). Argon gas is then allowed into the system up to the leak value (V.G. M.D.6) which, during etching, is opened to maintain a chamber pressure of between 5×10^{-5} and 10^{-6} mbar.

The saddle-field ion source, with its associated external circuitry, is sectionalised in Figure 3.22. It consists of a spherical

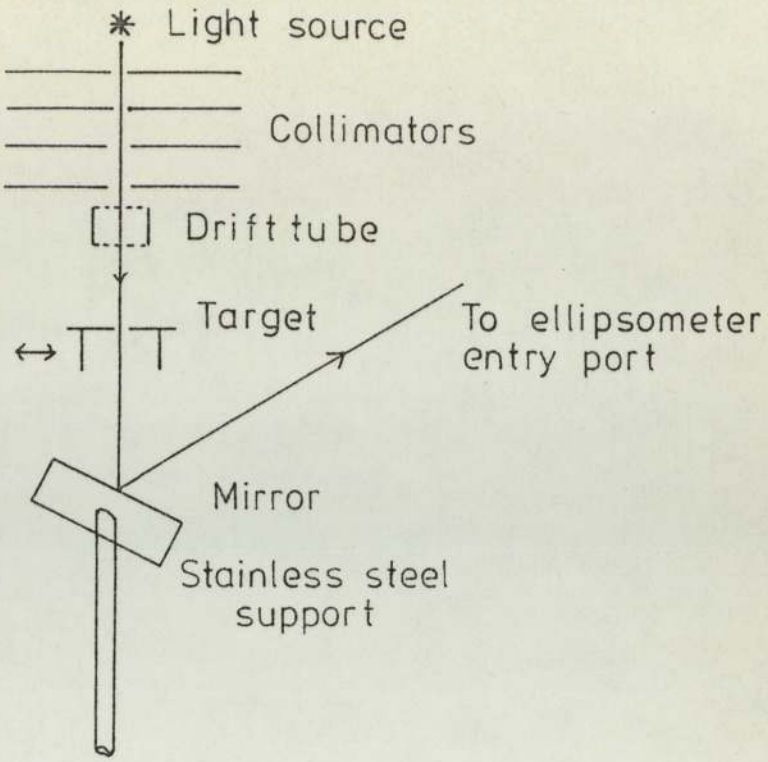

Figure 3.20: Target allignment system

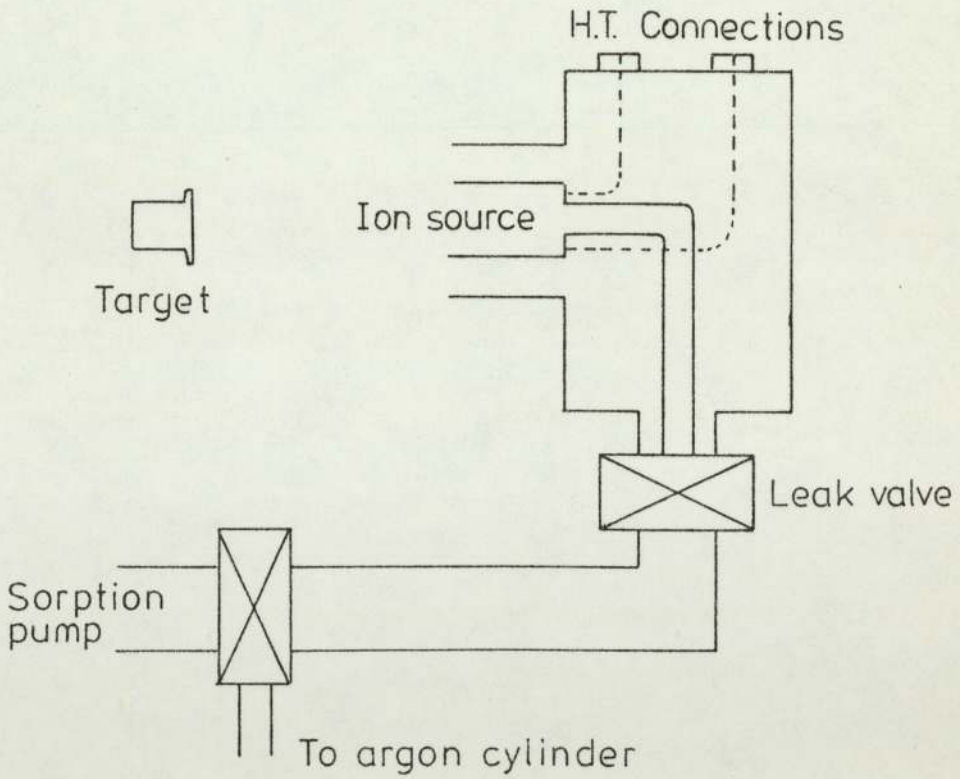

Figure 3.21: Experimental arrangement of the ion source

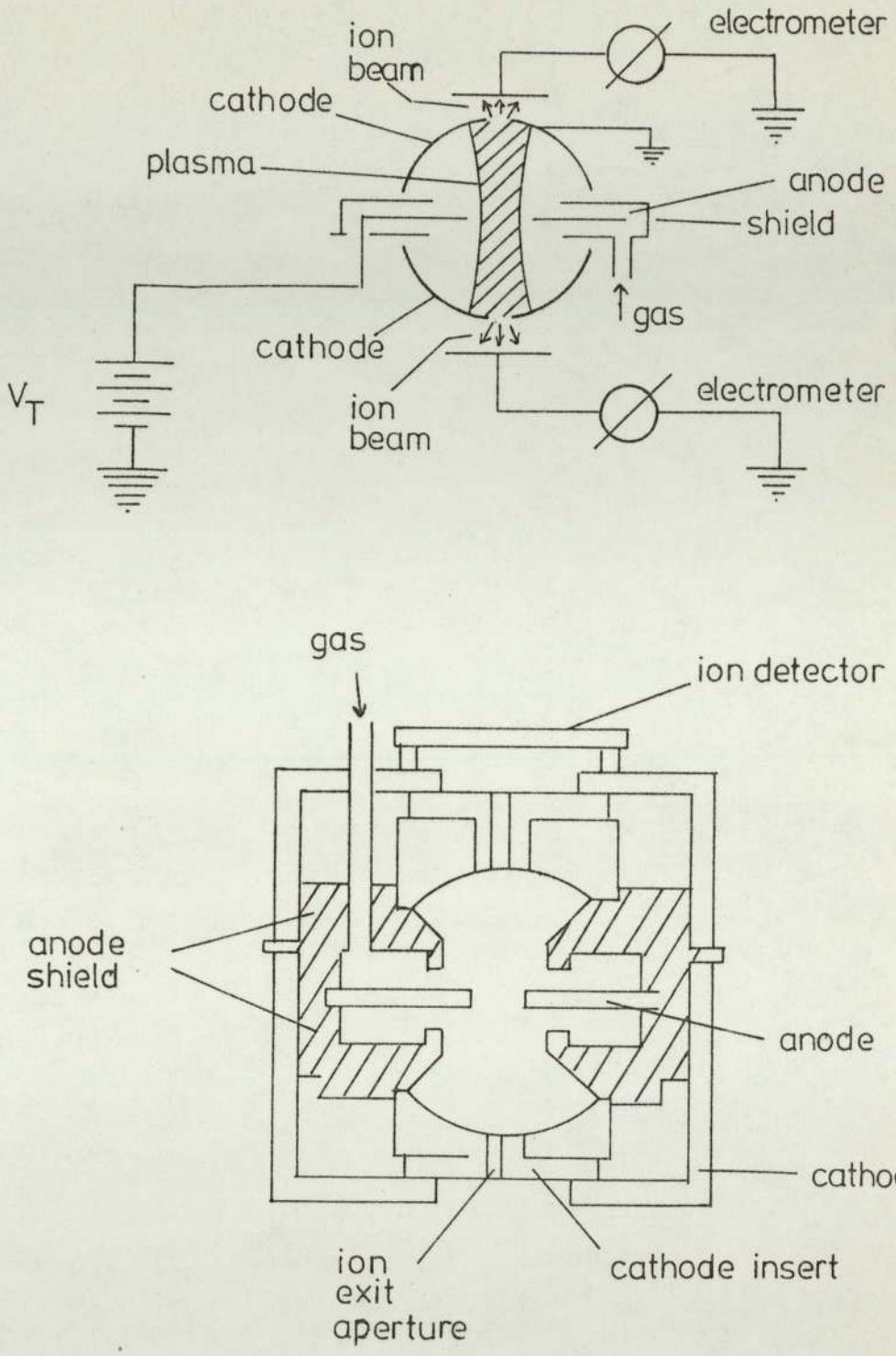

Figure 3.22 : Spherical Ion source

ionization chamber supporting an axially symmetrical electrostatic saddle-field produced by two ceramtec-insulated hemispherical aluminium cathodes around a central stainless steel annular anode. As an approximation to the annular anode a plate anode can be used with the central aperture shielded either side by plates at cathode potential.

Two ion beams (consisting of a high percentage of neutrals (109)),directed in opposite directions, emerge from the ion source. One beam is used to etch the surface whilst the other has its current continuously monitored by the ion-collector mounted on the source. For the present experimental studies it was found that the optimum operating conditions involved an argon pressure of 5×10^{-5} mbar, at 6 → 8 KV and 1.4mA tube current, giving an ion beam (etching current) of 2 μA as measured by an electrometer connected between the target and earth. To maximise the etching current, the target target holder is rotated(mark 1 unit) so that the target appears to be in its characteristic ellipsometric position (see Section 3.3.6).

3.4.2 Etching rate

An estimate of the amount of oxide removed from a target surface using the Argon-ion process can be determined from a knowledge of the etching time and etching current at a given reference argon pressure. If it is assumed that each argon ion is singly charged, the total charge Q bombarding a surface is given by :

$$Q = I.T. \qquad \ldots 3.8$$

where I is the etching current and T the etching time in seconds. From Equation 3.8 it is a straightforward process to determine the number of ions associated with the etching process.

i.e. number of ions (N) = Total Charge (Q)/Electronic charge

... 3.9

Thus if the etching yield (number of molecules/ion) is known, it is possible to determine the number of oxide molecules removed from the bombarded surface, that is :

Etching Yield x no of ions = No. of oxide molecules removed.

Finally from a knowledge of the total area bombarded (etched) and the molecular size of the oxide the total amount of surface etched can be calculated.

3.5 Ellipsometry

The discussion outlined in Chapter 2 has indicated that the presence of an oxide or contaminating layer on the surface of a metal target can play a crucial role in determining the electrical and mechanical processes involved in the microsphere/target impact. Therefore it is important to be able to ascertain the thickness of such oxide or contaminating layers which grow upon the target surface. In this context it is important to appreciate, for example, that even on diamond polished surfaces, an ambient oxide contaminating film rapidly grows the depth of which depends on the type of metal substrate, temperature, time and humidity, but is typically 25—50 Å thick.

Many methods are available for detecting the presence of contaminating layers and include Auger electron spectrometry, ESCA, LEED, FEM, ellipsometry and surface optical spectrometry. However, of these, that chosen for this study was ellipsometry because i) it is a non-destructive method of determining the film growth, ii) the interaction energies are small so that the effect on the contaminating layer is negligible and iii) the technique is sensitive to differences in the oxide layer as small as a monolayer.

The physical principle of this technique involves the measurement of the optical constants (real (n) and imaginary (k) parts of the refractive index) of a surface or layer by determining the ellipticity after reflection from the surface, of incident plane polarised light. In the presence of a contaminating surface layer, there is a modification of the optical constants appropriate to a clean metallic surface, and this enables the optical properties and thickness of the surface layer to be deduced. A detailed description of the theory of this technique can be found in Appendix A.

3.5.1 The ellipsometer facility

This is mounted on two triangular frames attached to the main system, which can be locked in position once the facility has been aligned. Under these conditions, light enters and emerges through two special view ports, which are optically flat kodial glass windows transparent up to 2 μm wavelength. A schematic diagram of a typical ellipsometric arrangement is shown in Figure 3.23. For the present application, where a high spatial resolution is required, it was necessary to modify this basic design to that shown in Figure 3.24. With reference to this figure, light from a He-Neon laser passes through a pin-hole, 0.2 mm in diameter, followed by a collimating lens system to give a target analysing area of $\sim(0.2\text{mm})^2$, i.e. compared to previous ellisometric facilities which had a target analysing area of $\sim(1\text{ cm})^2$. Thus the improved technique developed for the present study satisfies the prerequisite that the impact zone characteristics need to be measured on the micron scale.

Two basic laser ellipsometers have been developed. In the first (Mark 1 system) a Griffin and George meterological laser (wavelength 632.8 nm) is used as the light source with the advantage that no polarizer is required since the emerging light is already polarised.

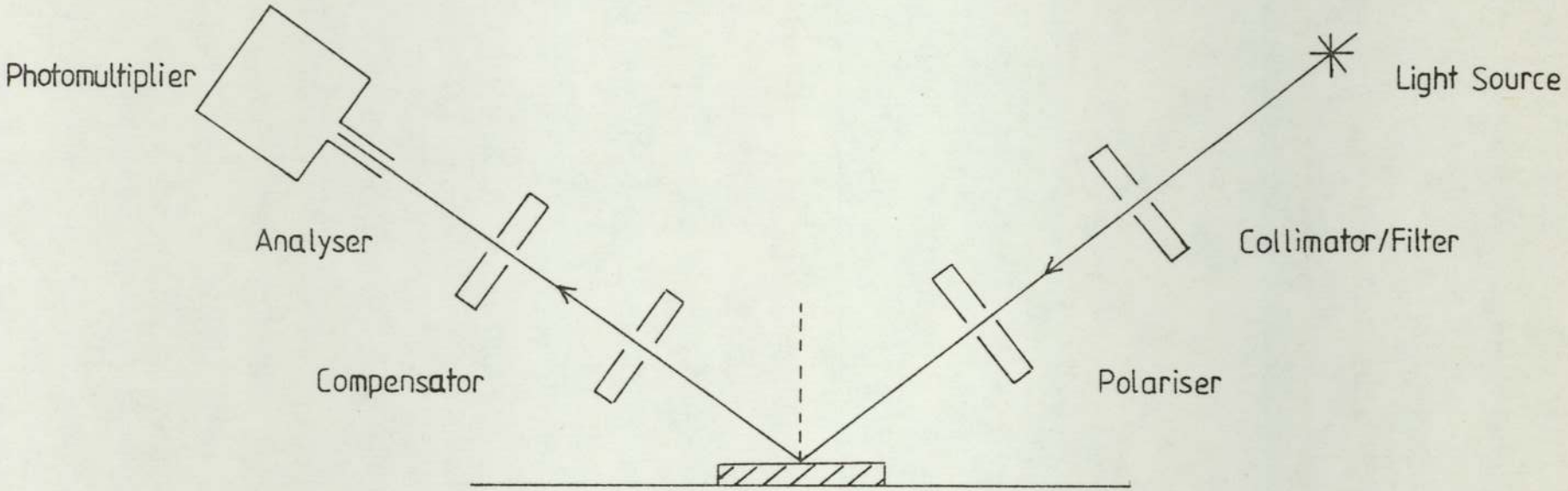

Figure 3.23
Typical ellipsometric arrangement

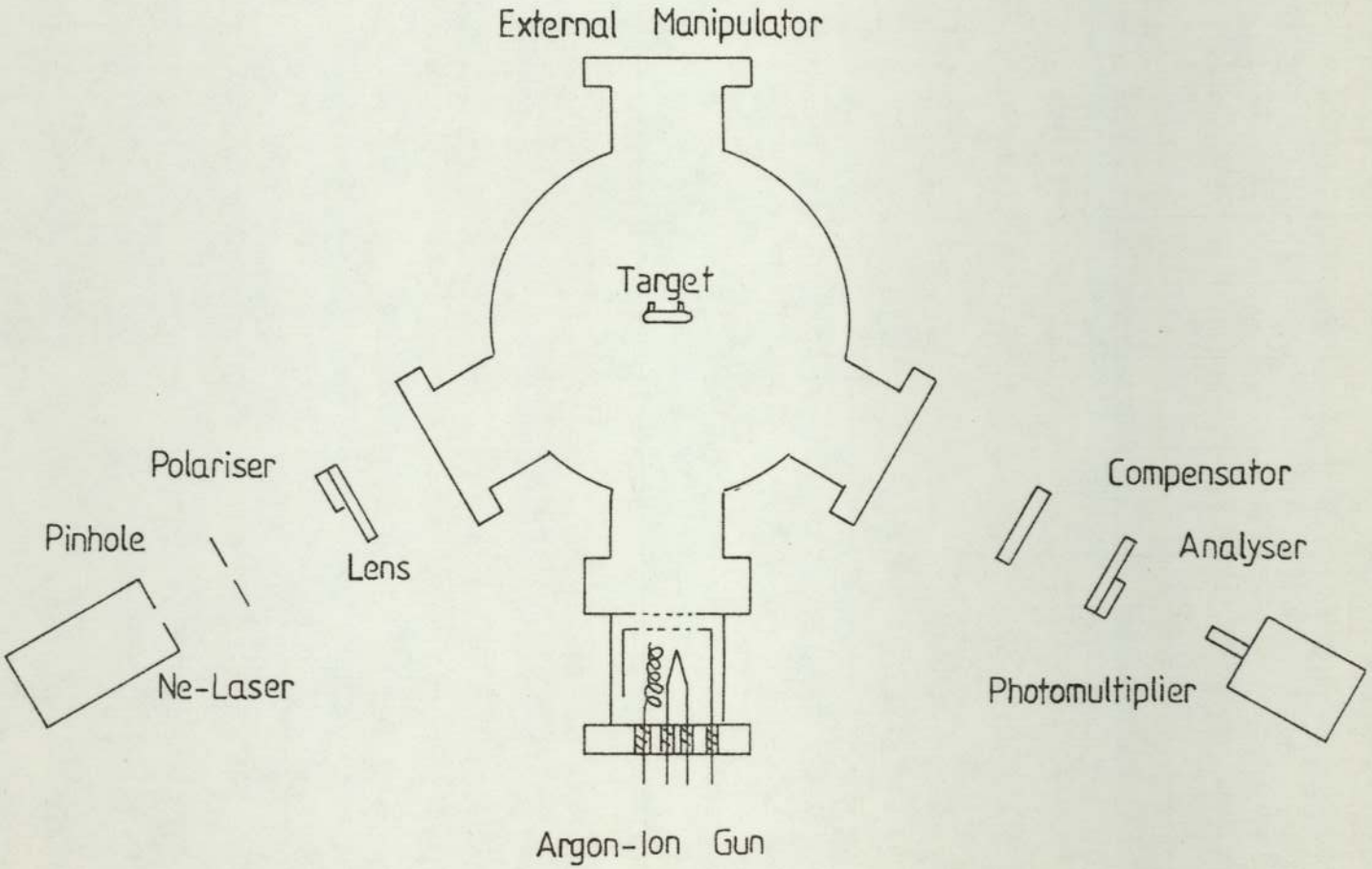

Figure 3.24

Laser ellipsometric facility

On reflection from the target surface light emerges from the chamber and passes through a $\frac{1}{4}$ wave plate and an anlyser (consisting of a H.N.22 polaroid) before being sampled by a photomultiplier (E.M.I. type 6094 B). In the second system (Mark II) a 'Harris' laser is used that produces a strong beam of unpolarised monochromatic light of wavelength 632.8 nm. In this case a polariser is required and the method followed to determine the ellipsometric angles will be described in Section 3.5.2.

3.5.2 Laser Ellipsometric Procedure

As described in Section 3.5.1 two forms of laser ellipsometer have been used. The first (called the Mark I unit) uses a laser which produces polarised light. Essentially the compensator, in this arrangement is used simply as a means of reducing the intensity of the reflected light before it is sampled by the photomultiplier. Rotating the analyser (keeping the compensator fixed) see Figure 3.24, produces a position where the intensity of the transmitted light reaching the photomultiplier, is a minimum. The analyser angle can thus be related to the thickness of the contaminating layer on the target, i.e. a variation in the oxide thickness will produce a change in the analyser value for a constant compensator position. No Δ or Ψ values can be obtained (see appendix A) using this method, since the laser is in a fixed position and thus no variation in the polarizing angle occurs. However, the average variation in the target surface oxide from one impact site to another can be ascertained. Measurements using this facility will be shown in Chapter 4, for a series of impact positions on an aluminium target.

The Mark II laser system allows the Δ and Ψ values to be calculated in a similar manner to that described for a white light source and monochromatic filter outlined in Appendix A. However, the

advantages of the present experimental facility over a typical monochromatic source are that (i) a high intensity beam is available and (ii) a reduced target surface sampling area. Alignment of the laser light in both systems is performed by viewing the laser light via the compensator and analyser, at a position of minimum intensity, using a telescope focussed on the impact position of the target.

3.6.1 Experimental procedure

It is assumed that before any measurements are carried out (i) the microparticle gun has been loaded, (ii) the experimental chamber has been evacuated to $\leq 10^{-7}$ mbar, (iii) the surface of the metal target has been prepared using the technique outlined in Section 3.2, (iv) allignment of the target has taken place and a knowledge of the impact site determined from the external manipulator readings, (v) if semi-conducting and insulating surfaces are being studied that a good electrical contact is made between the rear surface of the material and the target and vi) the microsphere production and detection systems are functioning correctly. The microsphere then appears from the drift tube and impacts on the target surface where its charge is again measured. To enable an accurate characterisation of the impact site at least 50 impact events are recorded for the metal (e.g. copper, stainless steel, titanium, aluminium), semi-conducting (e.g. silicon) and insulating (e.g. p.v.c., glass, tufnal, paxolin, mica, ebonite, cellulose) surfaces. In an event where a particle appears to "stick" to the target, a single trapezoidal drift tube pulse occurs with the corresponding target trace (see Figure 3.11), however in a "bouncing" event, twin pulses are recorded by the drift tube amplifier together with a modified target trace, see Figure 3.25. From the recorded data, the impact velocity (u) return velocity (v)

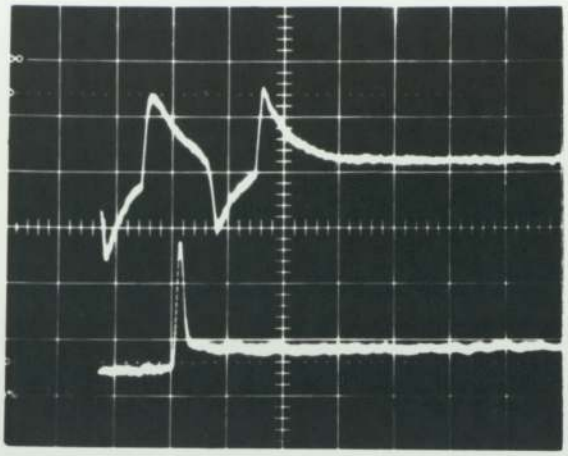

Figure 3.25: Particle bouncing event using a charge sensitive amplifier on the drift tube and a voltage sensitive amplifier on the target

coefficeint of restitution (e) impact charge (q_1), reflected particle charge (q_2) and charge modification ratio (q_2/q_1), if applicable, are determined. However, for the impact studies on highly oxidised metal surfaces the experimental procedure was further modified to include the following technique ;

(i) Bombard the target "test" zone, with microspheres, when the target is in the horizontal mode.

(ii) Rotate the manipulator to bring the target into the position for ellipsometric characterisation of the impact 'test' site (using the mark I target holder).

(iii) Etch the surface for a known time, with the argon-ion facility to remove part of the oxide layer.

(iv) Re-characterise the impact "test" zone using the laser ellipsometer

(v) Rotate the manipulator until the target returns to the horizontal mode for mechanical impact measurements, and the sequence again repeated.

Once the impact data from a number of test sites has been completed the "commercially polished" targets were removed to an S.E.M, where either the impact site was photographed, or microprobe experiments performed (see Section 3.7). In contrast to the metal targets, however, it is important to note that no ellipsometric data was obtained for the insulator and semi-conducting surfaces. The experimental mechanical and electrical data together with the associated ellipsometric readings will be presented in detail in Chapter 4.

3.6.2 Ellipsometric procedure

3.6.2(a) Determination of the reference azimuths

This procedure only applies to the Mark II laser ellipsometer where the angle of polarization can be varied by rotating the polariser (see Figure 3.24). The compensator method used here relies upon the fact that the reference azimuths are the polarizer and analyser readings corresponding to the transmission axis of the polaroids being parallel and perpendicular to the plane of incidence. To obtain quick approximate values each polaroid can be removed and arranged so that light from a lamp reflected off a glass plate, at an angle of approximately 56°, passes through a polaroid. Each polaroid is rotated until minimum intensity occurs in the transmitted light. This method gives the approximate vertical position of the transmission axis. For an aligned ellipsometer the plane of incidence is approximately horizontal therefore returning the polaroids gives the transmission axes perpendicular to the plane of incidence.

Removing the compensator from the ellipsometer, the following process can then be used for the determination of the reference azimuths. With light being reflected from a metal surface (i.e. the

target within the experimental chamber) the polarizer is rotated through 90° so that its transmission axis is parallel to the plane of incidence. The analyser is left with its transmission axis perpendicular to the plane of incidence. A small voltage is applied to the photomultiplier and the output voltage is reduced to a minimum by rotating the polarizer and then the analyser until minimum light is received by the photomultiplier tube. The voltage, to the tube, is then increased and the same procedure repeated for minimum transmitted light until the optimum extinction position is obtained. A more accurate method for determining the extinction position is to use the method of 'bracketing' in which positions of equal intensity either side of the extinction position are determined. These polarizer and analyser azimuth positions are denoted by π_p and α_s respectively (see Appendix A). The polarizer and analyser are then rotated by 90° in the direction of the oncoming light and new extinction positions determined similar to above. The new positions are given by π_s and α_p and for correct allignment should be 90° from the first position. This process is repeated four times in all, to obtain all the reference azimuths.

The polarizer and analyser are set to one of these reference positions and the compensator introduced as in Figure 3.24. The compensator is rotated and the extinction position found by 'bracketing' - this is the compensator reference position and corresponds to the fast or slow axis of the compensator being parallel to the plane of incidence. The alternative compensator reference position can be obtained by rotating the compensator and it should be 90° from the first position.

3.6.2 (b) Determination of Δ and Ψ parameters.

The compensator is first locked at 45° to one of its reference positions, see Section 3.6.2(a). Both the polarizer and analyser are

rotated successively to give minimum light intensity and the extinction positions P_1 and Q_1 found by bracketing. Rotating the polarizer and analyser, not by 180°, enables the new extinction positions P_2 and Q_2 to be determined. This process is repeated until the four extinction positions of the polarizer ($P_1P_2P_3P_4$) and analyzer ($Q_1Q_2Q_3Q_4$) have been obtained for the first reference position of the compensator. It is found that P_1P_3, P_2P_4, Q_1Q_3 and Q_2Q_4 differ by 180°. The process is then repeated with the compensator reference position change by 90°.

To determine the Δ and Ψ values the following is first noted. Both P_1 and P_2 are symetrically placed around π_p thus $(P_1 - \pi_p)$ should equal $(\pi_p - P_2)$. Usually an average is taken, i.e.

$$= \frac{P_1 - \pi_p + \pi_p - P_2}{2} \qquad \ldots 3.9$$

It can also be shown that Q_1 and Q_2 are always seperated by 90°, thus $\alpha_s - Q_1$ should equal $\alpha_p - Q_2$. Again an average is obtained

$$x = \frac{(\alpha_s - Q_1) + (\alpha_p - Q_2)}{2} \qquad \ldots 3.10$$

where the angle $(2x - 90)$ gives the relative phase retardation between the p and s components.

3.6.2. (c) Angle of incidence

The angle of incidence is determined after each alignment process. All the optical equipment, except the laser, is removed from the frames and replaced by 4 sharply pointed spikes mounted in optical sadles. These sadles are positioned so that they are in line with the laser beam, as indicated on Figure 3.26. Applying simple trigonometry allows the angle of incidence ϕ_o to be calculated in terms of the distance between

the spikes. Referring to Figure 3.26, it can be shown that

$$h^2 = f^2 + g^2 - e^2 - 2\,ad \cos 2\emptyset_o \qquad \ldots 3.11$$

Thus determining the angle of incidence $\emptyset_o$, the Δ and Ψ values for the surface and the wavelength (λ) of the light and it is possible to calculate, via a computer program, the n and k values for the substrate and hence the oxide thickness.

3.7 Electron microscope facility and probe

Although viewing the target in an S.E.M. allows the impact site of the "test" microsphere to be found, the actual process which gives rise to the "sticking" phenomena can only be ascertained by viewing the impact contact area. To obtain this information a microprobe technique has been developed which allows experiments to be performed, in an S.E.M., using target materials whose surfaces have been subjected to a few hundred impact events. The basis of this technique is a microprobe manipulator developed by Athwal (110) which uses two electrolytically etched probes $\sim$ 100 nm in diameter mounted radially into an insulated electrical feedthrough, shown in Figure 3.27. Each probe can be located, in turn, precisely on the axis of the S.E.M. by the use of translatory manipulation via the bellows operated pivot adjustable mounting and rotation by a system of gears. The target is mounted into an aluminium stub and an electrical contact formed between the target and stub using conductive silver paint. The target is postioned at 45° to the S.E.M. axis and normally to the probe axis. By arranging for the specimen to be electrically insulated from the earthed mechanical stage, it is possible to measure the emission current drawn from the microparticle. However, one disadvantage of using this form of in-situ experiment is that the working pressure is only $\sim 10^{-3}$ mbar, hence the problem of ignition effects (111),

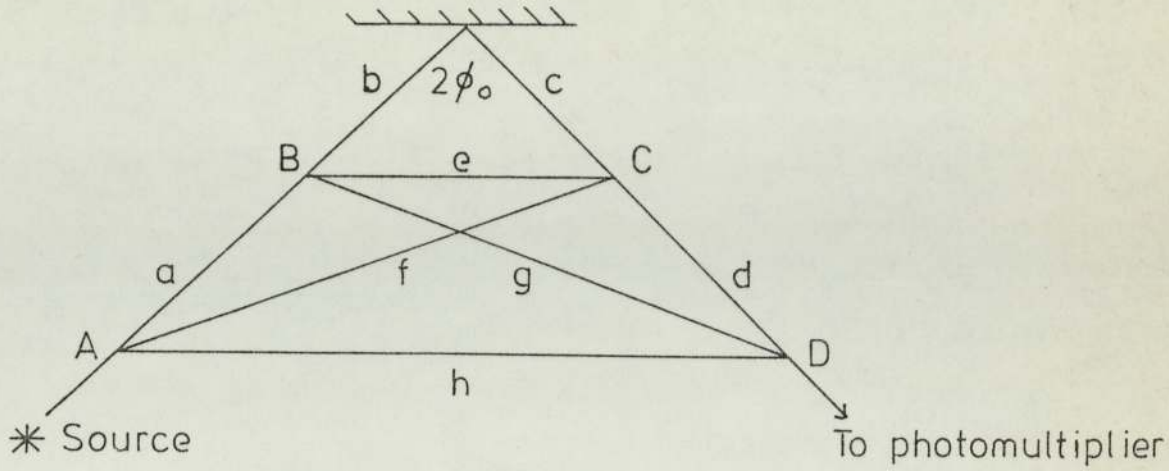

Figure 3.26: Arrangement for measuring the angle of incidence

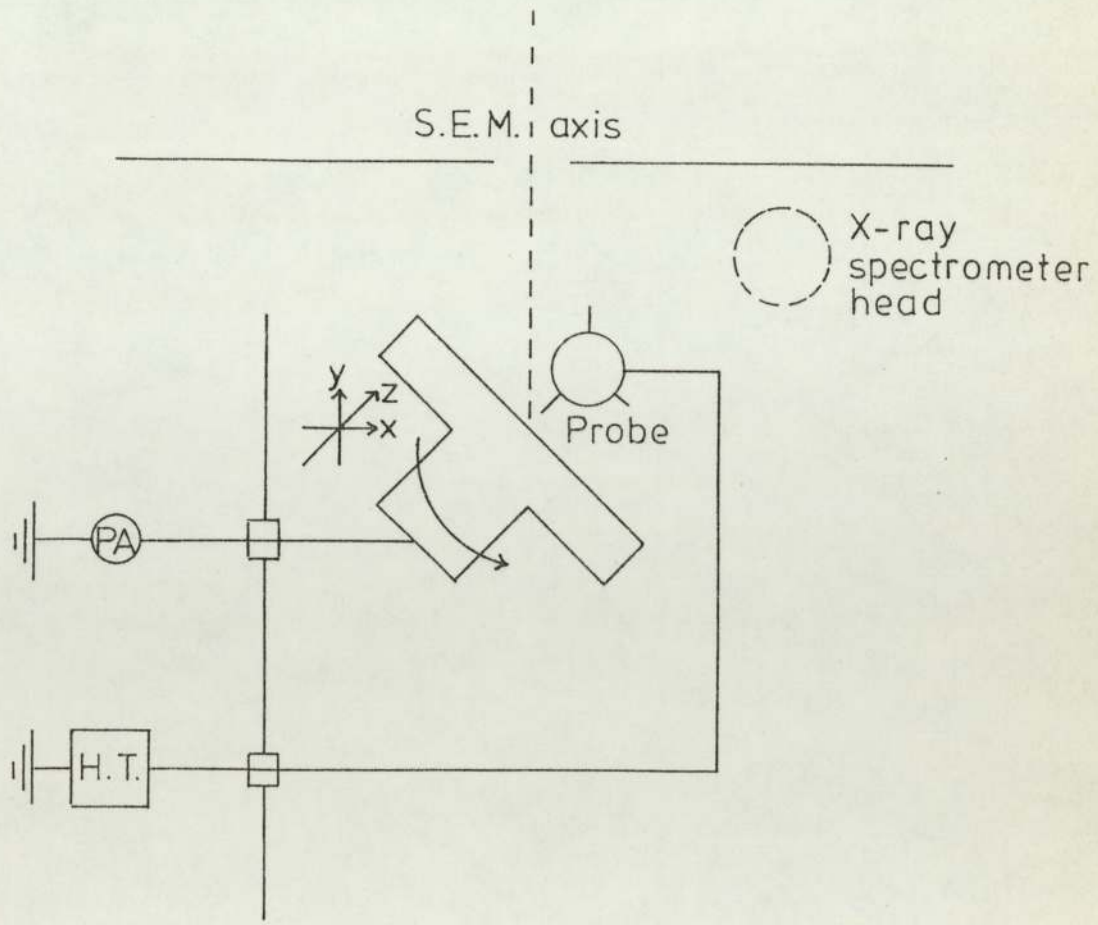

Figure 3.27: Schematic representation of specimen and anode probe assembly as mounted in the scanning electron microscope

inside the experimental chamber, cannot be ignored when applying a high voltage between the tip and the microsphere.

3.7.1 Manipulation Techniques

Once the microprobe and target has been installed in the S.E.M., the following procedure is adopted to enable the micropoint and target to be viewed simultaneously. By adjusting the external bellows assembly, the tungsten tip is located in the middle of the viewing screen making sure it remains visible even at the highest magnification to be used. At this stage the target is not usually in focus being positioned some distance away. The external manipulatory controls of the S.E.M. are now adjusted to locate a microsphere impact site. Once this is achieved the target is brought closer and closer to the tip whilst making sure the microsphere impact position stays in focus. This procedure is repeated until the electron shadow of the tip can be seen on the target surface and the tip and target are both in focus. The final adjustment is to position the tip in the same horizontal plane as the microsphere. This can be determined by measuring the resistance between the tip and the target using an avometer i.e. as the tip touches the target the resistance falls to zero which is taken as zero for the external controls. The tip is then moved a known distance from the target and positioned to the side of the microsphere. Considerable care has to be taken in this procedure so that no, or very little, damage occurs to the tungsten tip. Mechanical and electrical experiments then can be performed as outlined in the following sections.

3.7.2 Mechanical microprobe experiments

To determine whether any inelastic/plastic behaviour occurs in the original impact process, it is necessary to be able to view the

contact area of the microsphere on the target, i.e. requiring that the microsphere be removed from its impact site. As an initial step in this process it is important to have carried out the alignment process (see Section 3.7.1) and to have determined the character of the microparticle using an in-situ KEVEX X-ray analyser. The tungsten tip is then brought close to the microsphere using the external controls, i.e. the target surface is moved under the tip. Eventually contact occurs and the microsphere is removed thereby allowing close inspection of the impact site, which is subsequently recorded on film. Data arising from these experiments can be found in Chapter 4.

3.7.3 Electrical microprobe experiments

After zeroing the external controls (see Section 3.7.1) the tip is positioned at a known height above the microsphere and an external voltage applied to the probe. Two alternative experiments can be performed, the first involves measuring the current-voltage characteristic as the applied voltage between the tip and the microsphere is increased while, the second involves the measurement of the force of adhesion. In this second case, to allow the accurate determination of the applied field, the tip was flattened (by pressing it into the target) so as to give an approximate uniform field between the tip and the target. After each voltage increment (noting the current in each case) the voltage was removed and the target inspected to determine whether the microsphere was still present. Hence, knowing the voltage at which the microsphere leaves the surface under the action of electrostatic repulsive forces, the adhesive force can be calculated via an equation derived by Rhorback (112); viz

$$F_d(\gamma) = \frac{4\pi\varepsilon_o h^2(\gamma-1)E^2}{\gamma^2} \qquad \ldots 3.12$$

In this expression $\gamma = h/R_p$ where h and R_p are the diameter and radius of the microsphere respectively and ε_o the dielectric constant of free space. E the gap field

CHAPTER 4

4.0 RESULTS

4.1 Introduction

The vertical microparticle facility discussed in Chapter 3, has been used to investigate the impact of low velocity, positively charged, microspheres on various target materials under predominantly zero field conditions. Impacting microparticle events are studied in terms of the oscillographic traces recorded by the drift-tube and target amplifiers, where Figures 4.1(a) and 4.1(b) show respectively typical examples of "sticking" and "bouncing" events. The former are characterised by all the particle change being dumped on the target, which decays with a time constant of $\backsim$0.2s, determined by the target capacitance and the input capacitance and resistance of the amplifier. While both the drift-tube and target voltage amplifiers have the same gain (100 for the present voltage amplifiers), their input capacitance are different and this accounts for the unequal heights of the drift-tube and target trace . For the "bouncing" event of Figure 4.1(b) it can be seen that such events are characterized by a small fraction of the incident particle charge being dumped on the target with the reflected particle having a lower velocity (corresponding in this case to a coefficient of restitution $\backsim$0.56). The shape of the target trace can be explained in terms of the total parallel input impedance appearing across the amplifier, where C_1 and R_1 denote, respectively, the effective capacitance and resistance across the amplifier input. Figures 4.2(i) and 4.2(ii) illustrate schematically how the respective "sticking" and "bouncing" event target signals are compiled from the separate particle and target processes.The form of the drift-tube trace has been discussed earlier, (see Section 3.2).

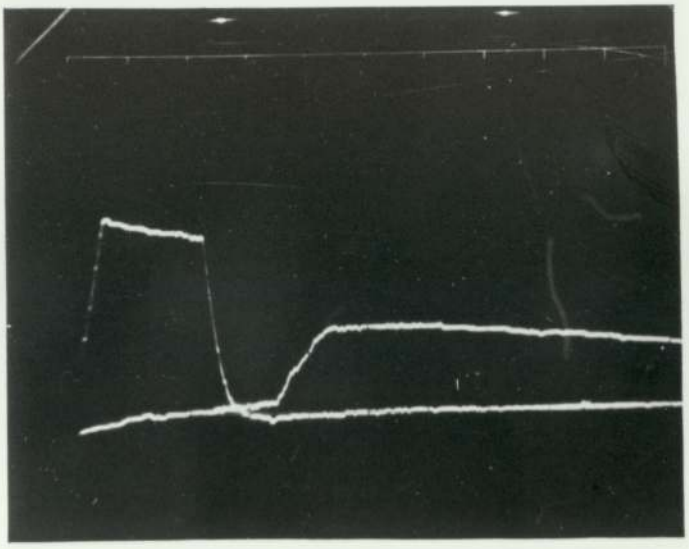

(a)

Target trace
(sen 0·05V/Div)
Drift tube trace
(sen 0·05V/Div)
Time base 1ms/Div

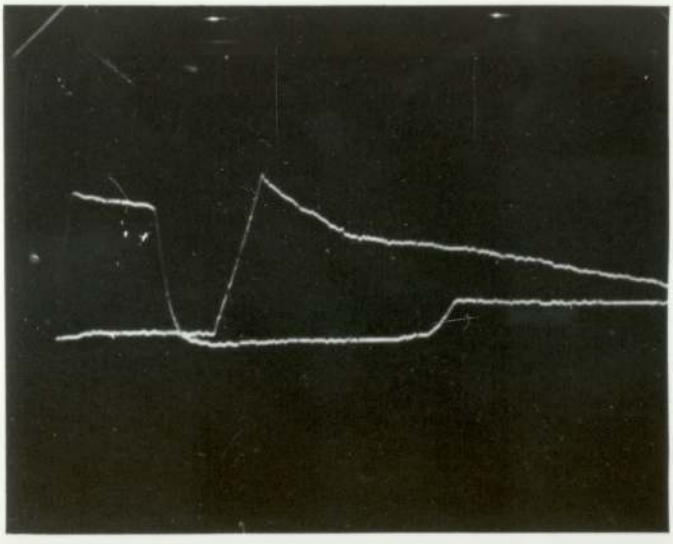

(b)

Target trace
(sen 0·05V/Div)
Drift tube trace
(sen 0·05V/Div)
Time base 1ms/Div

Figure 4.1(a) Particle "sticking" event, (b) Particle "bouncing" event; initial velocity = 7·1 ms^{-1}; reflected velocity = 4 ms^{-1}; 72% charge exchange during impact

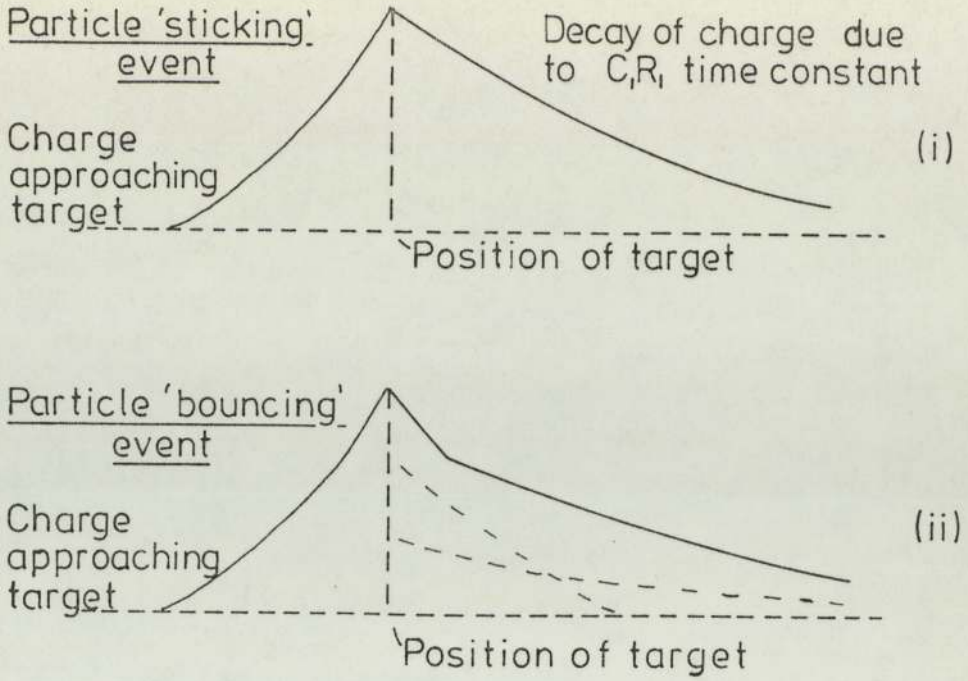

Figure 4.2: Schematic representation of particle 'sticking' and 'bouncing' events. (a) Reflected particle having a reduced positive charge and slower velocity moving away from the target. (b) Decay of small positive charge remaining on the target with C_1R_1 time constant. (c) Resultant waveform, i.e. (a)+(b)

From the theoretical considerations discussed in Chapter 2, it is apparent that the important parameters affecting the impact process are (i) the velocity and charge of the particle, (ii) the microscopic surface conditions of the target, (iii) the relative work functions of the microparticle/target combination and (iv) the target material. Therefore several main lines of investigation have been followed :-

(i) The electrical conductivity of the target oxide has been studied with regard to the impact of carbonyl iron micropheres on metal, semi-conducting and insulating materials.

(ii) Data has been obtained from highly oxidised targets such as aluminium titanium and copper since the type of surface oxide film and its thickness have been found to govern the charge exchange process.

(iii) By selecting different microscopic impact sites, the variation in surface properties have been studied on an ambient oxide aluminium target.

(iv) A microprobe technique has been used to remove the "stuck" microspheres mechanically and/or electrically from their impact sites thus revealing the contact region and providing more detailed information on the impact process.

(v) A range of different microsphere/target combinations have been used to investigate the role played by the work function in the impact event.

(vi) To complement the previous high field data (4,5), the impact of carbonyl iron microspheres on a titanium surface, under high field conditions, has been carried out. However, advantages over previous measurements are (a) the smaller impact zone and (b) the facility for measuring the charge "dumped" during the impact event.

4.2 Mechanical impact data

Unless otherwise stated, all the mechanical data has been obtained using two types of carbonyl iron microspheres, designated types E and H, where Figure 4.3 shows the particle size distribution for the two powders. As mentioned previously, the type E powder is preferred since it is less likely to lead to paralysis of the microparticle gun. The particle impact velocities used for these experiments were in the range $1 \rightarrow 50$ ms^{-1}, corresponding to gun voltages of V_1 = + 2.2 KV and V_2 = - 2.8KV (See Figure 3.6)

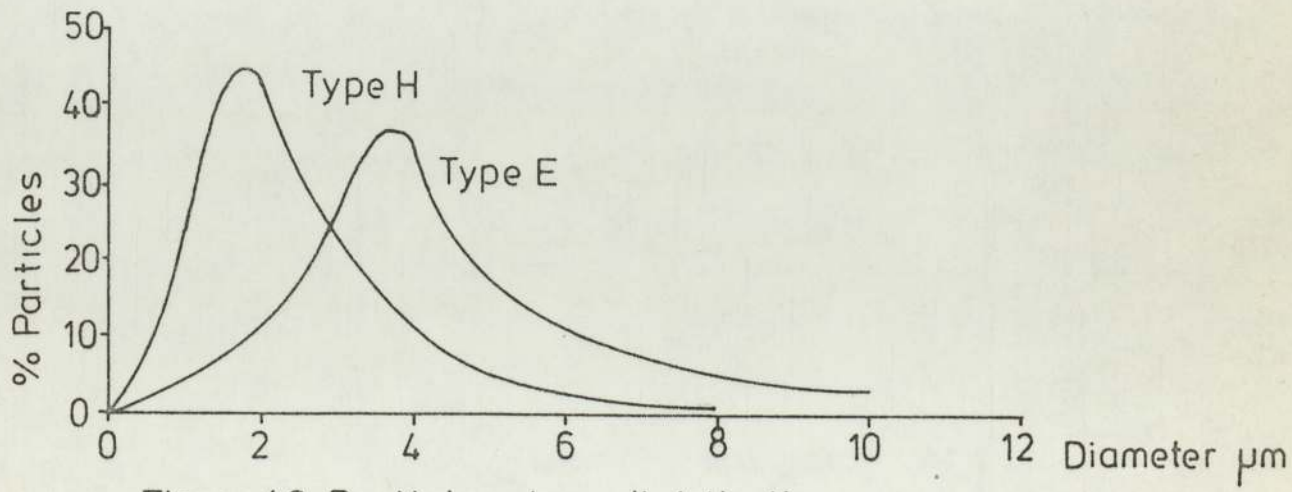

Figure 4.3: Particle size distribution

Impact zone	No of sticking particles	No of bouncing particles	No of bouncing particles with reversed charge	Average coef of restitution	Average reflected/incident charge for positive reflections q_2/q_1	Average ellipsometric readings ϕ (deg.)
1	46	4	1	0·49±0·02	0·04±0·05	127·2
2	45	5	1	0·51±0·09	0·05±0·05	127·3
3	43	7	4	0·52±0·07	0·08±0·09	128·1
4	46	4	2	0·48±0·03	0·05±0·06	128·6
5	41	9	4	0·55±0·07	0·11±0·1	127·0

Table 4.1: Microparticle impact data for five zones on an aluminium target

4.2.1 Metal surfaces

Unless special precautions are taken these surfaces are contaminated by an ambient oxide layer (typically 20→30A° thick) which has grown on the surface, after the polishing process (see Section 3.2), due to exposure to air. For the majority of metal surfaces (e.g. titanium 318, titanium 117, copper and stainless steel) bombarded by microspheres, under zero field conditions, it was typical for over 99% of the low velocity ($< 50\ ms^{-1}$) particles to "stick" to the target surface on impact, i.e. at velocities well below the critical value for elastic impact (11) This type of event is indicated by the oscillograph of Figure 4.1(a). However, with one target material - aluminium - it was found that ~10% of the particles executed "bouncing"behaviour, with the coefficient of restitution typically in the range 0.43 - 0.63. Since this surface was the only one that exhibited a significant 'bouncing' response, it was chosen for a systematic investigation into how the variation of the mean particle impact response varies with surface conditions. Five separate zones distributed at 1.6 cm intervals across the surface of the target were first characterised using the Mark I ellipsometric facility,described in Section 3.5.1,and then bombarded by a sample of 50 microspheres (carbonyl iron Type E). Table 4.1 gives the impact data for the five "test" impact sites, and indicates in each case how many of the incident sample of 50 particles, respectively, "stick" or "bounce", the number of particles that return with a 'reversed' charge, the mean coefficient of restitution of all the bouncing particles and the mean charge modification q_2/q_1 of those particles which return with a reduced positive charge. The complementary ellipsometric readings Ø indicate the variation in the relative oxide thickness from zone to zone. This latter conclusion follows from an optical calibration measurement made in a subsidiary system on an atomically cleaned (argon-ion etched) aluminium surface,where it wasfound that the Ø value was 129.6°, i.e. indicating that

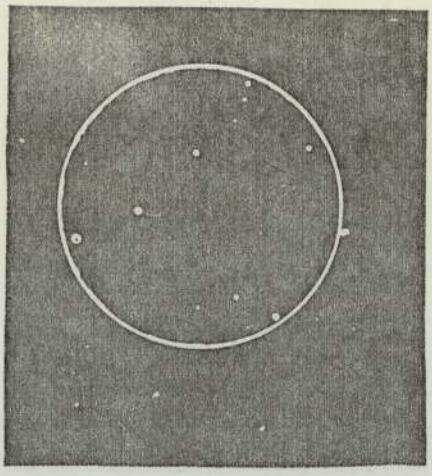

Figure 4.4: Micrograph showing microsphere impact zone; the circled region is the corresponding ellipsometric analysing area

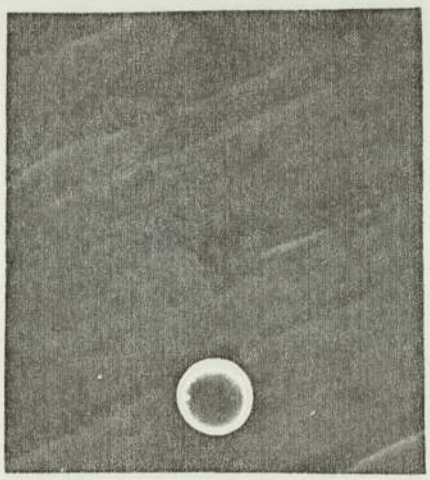

Figure 4.5: Enlarged view of a single microsphere impact site

the larger the measured ellipsometric angle the smaller the oxide layer. With the present regime (Mark I laser system) it was not possible, however, to quantitively measure the absolute thickness of the oxide film; as a guide, though, a change of $\emptyset \sim 1°$ corresponds to a change of ~25 A° in the thickness of the mean oxide coverage.

To give further perspective to the impact regime a target was removed from the experimental chamber for analysis in the S.E.M.. Thus Figure 4.4 is a typical S.E.M. micrograph of the impact zone showing a distribution of $1 \rightarrow 8$ μm diameter particles adhering to the surface,

whilst Figure 4.5 is a magnified view of a single microparticle on the surface.

4.2.2 Highly oxidised metal targets

To increase the thickness of the oxide layer on a metal surface, say aluminium, the commercially polished target was placed in a furnace, under controlled conditions. After oxidising the aluminium target for 14 hours at 450° C, it was placed in the experimental chamber and a known impact position chosen for the investigation. Following the experimental procedure outlined in Section 3.6.1, which involves the cyclic process (i) bombardment of the impact site by 100 test microspheres, (ii) characterisation of the site using the laser (Mark II) ellisometer and (iii) ion-erosion of the surface using the argon-ion facility, the mechanical and electrical behaviour of the "test"surface was analysed. The most significant finding to emerge from the target in this state was that a greater number of "bouncing" events were observed in comparison with a surface which only possessed an ambient oxide coverage.In quantitative terms, Table 4.2 shows the percentage of "bouncing" events as a function of the total etching time,

% of bouncing events	Etching time (hrs)
94	0
82	1/2
93	1
87	2
86	3
85	4
82	5 1/2
71	7
68	8
78	9 1/2
60	11
50	13 1/2
28	15 1/2
10	17 1/2
16	19 1/2

Table 4.2: The percentage of bouncing events as a function of the total etching time for the highly oxidised aluminium surface

where in general the results show that as the oxide is progressively removed the number of "bouncing" events decreases. So far as the "bouncing" events are concerned, Figure 4.6 shows the variation in the coefficient of restitution at a given impact site as a function of oxide thickness (etching time); it shows that there is a slight shift in the distribution towards a lower 'e' value as the oxide thickness is reduced. It should also be noted that it is not possible to obtain a distribution after seven hours of etching since the number of "bouncing" events falls off considerably.

The other most notable result obtained from this highly oxidised surface can be observed with reference to Figure 4.7(a-d). This shows the variation of the impact velocity 'u' with impact charge q_1, and the corresponding surface effects, obtained at the same etching times as the histograms of Figure 4.6. It is possible to divide each graph into three regions which show: (1) particles which undergo a "bouncing" event without charge modification; (2) particles which undergo a "bouncing" process with some form of charge modification, and (3) particles which "stick" to the surface. It is significant that as the oxide is removed by the argon-ion etching process, region (1) gradually vanishes. For an ambient oxide surface, most particles are to be found in region (3) indicating that they "stick" to the surface on impact. A similar process was found to occur for highly oxidised titanium (500°C for 18 hours) and copper (500°C for 4 hours) surfaces. However, whereas the aluminium surface requires etching for $\sim 19\frac{1}{2}$ hours before its ambient state is reached (and the majority of the incident microspheres"stick" to the surface) the titanium and copper surfaces required 1 hour and $1\frac{1}{4}$ hours etching, respectively, before showing conditions representative of their ambient oxide characteristics. This observation points to the fact that either the oxide formed on these targets is very thin or can be removed easily during the etching process. Table 4.3

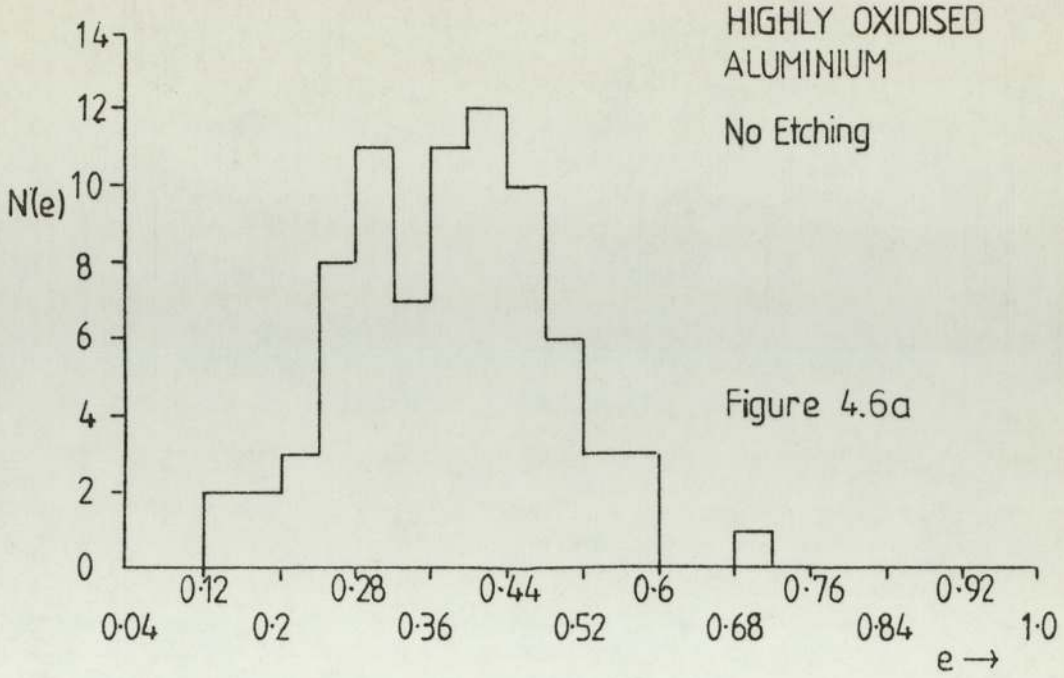

Figure 4.6a

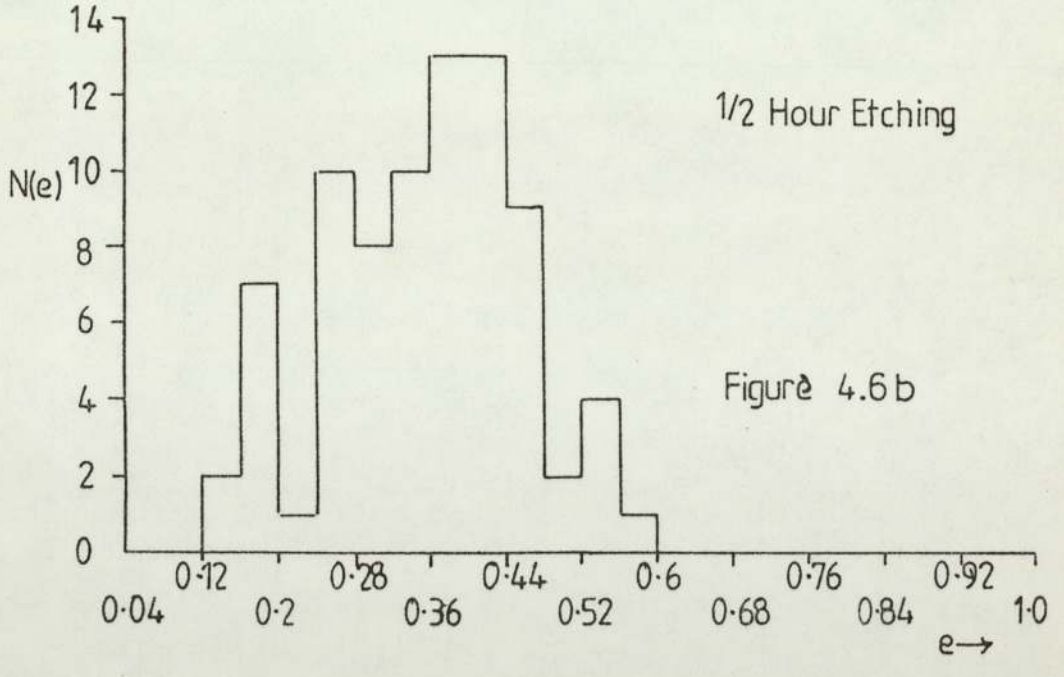

Figure 4.6b

Figure 4.6a-d: e value histograms at different etching times for the highly oxidised aluminium surface

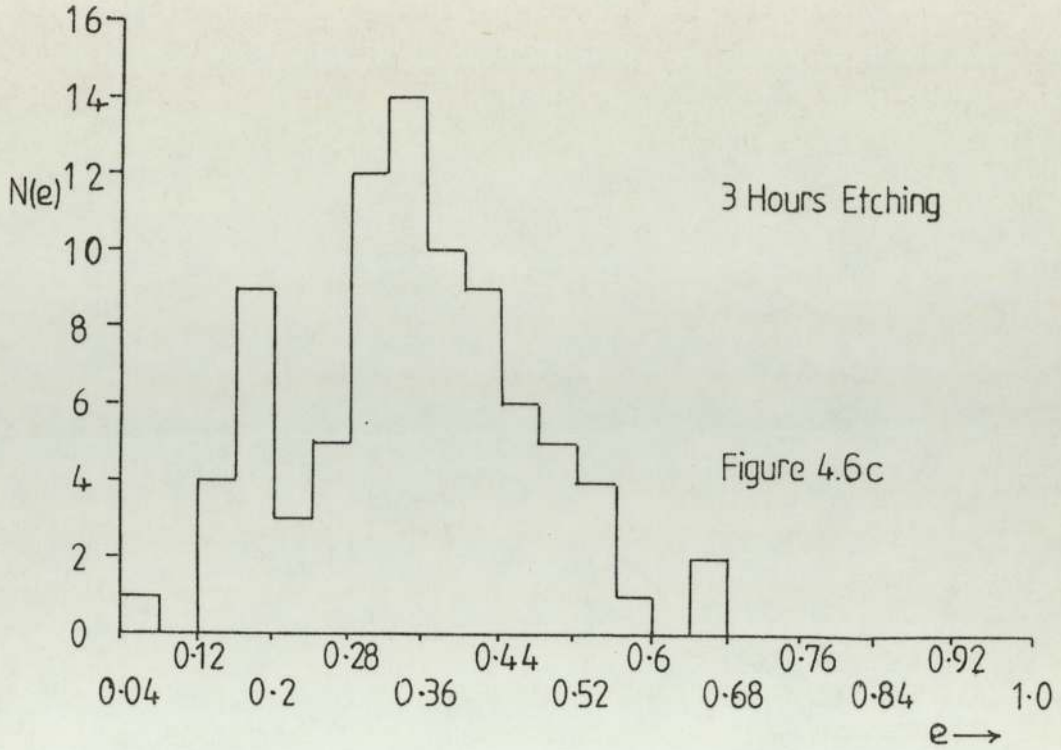

Figure 4.6c

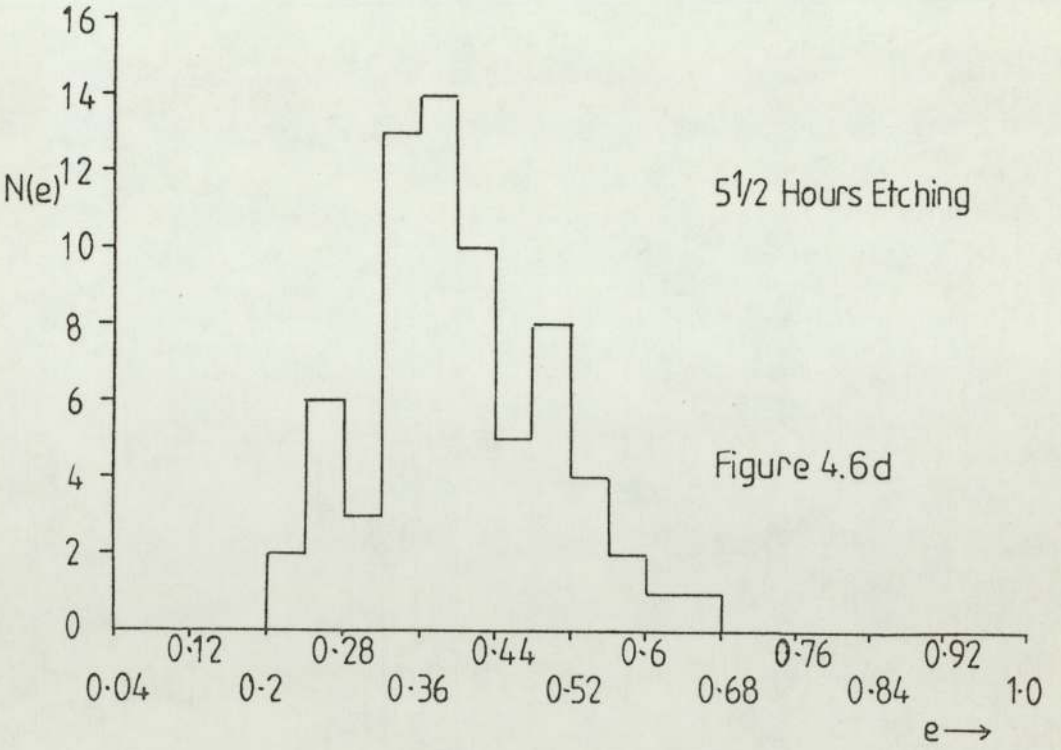

Figure 4.6d

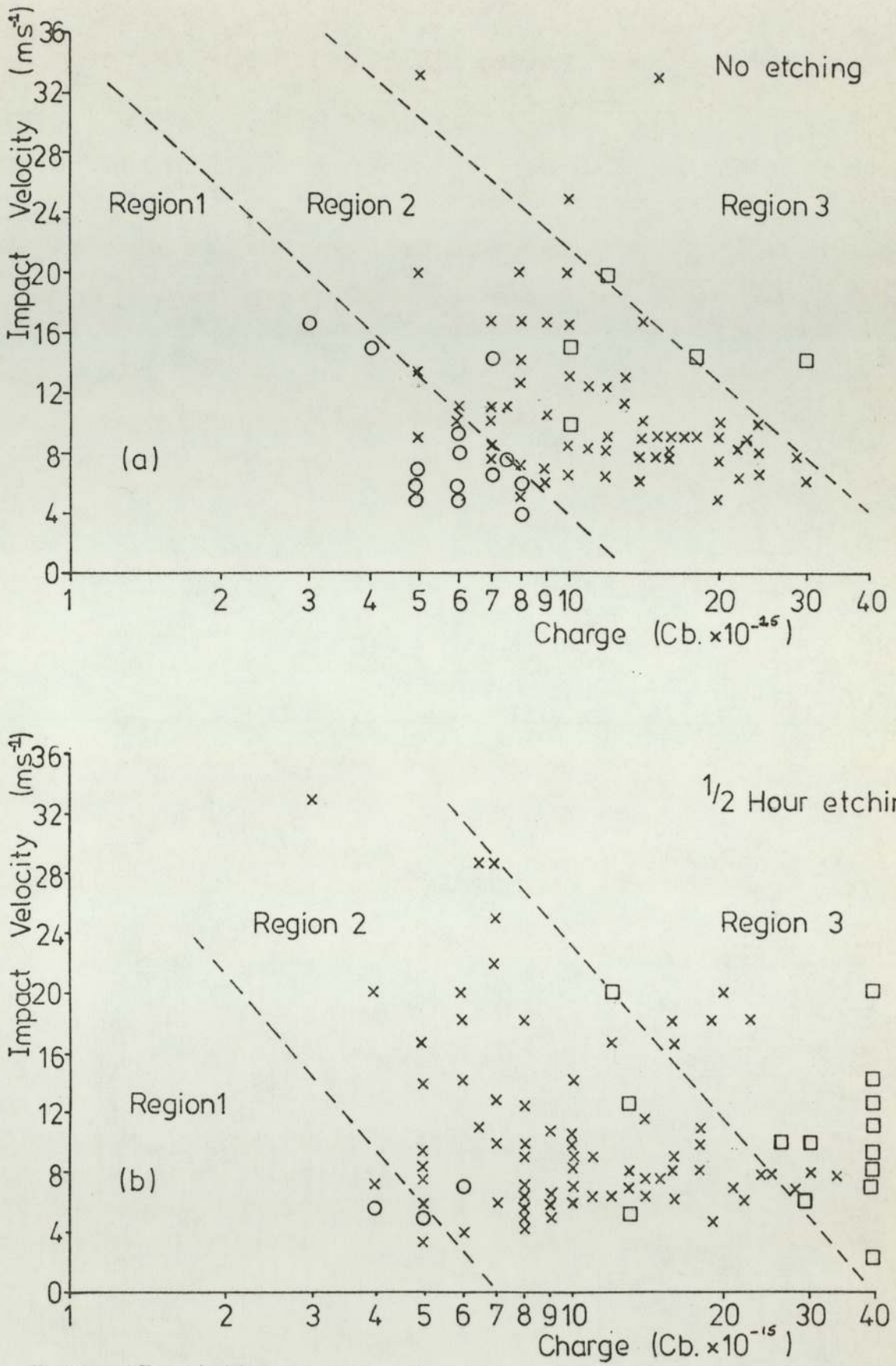

Figure 4.7a-d: The surface impact characteristics of the highly oxidised aluminium surface as a function of the etching time: ○≡'bouncing' particles with no charge modification; ×≡'bouncing' particles with charge modification; □≡'sticking' particles

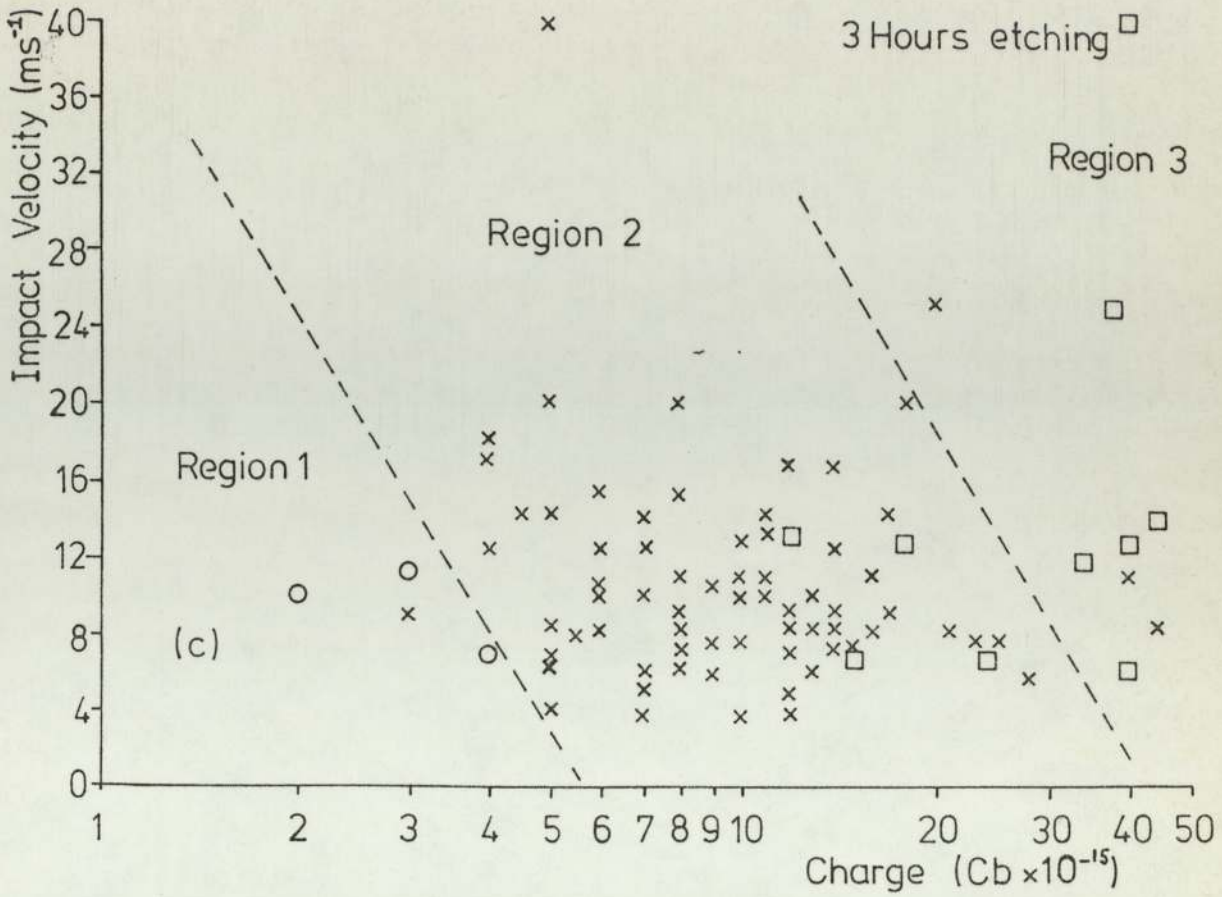
3 Hours etching
Region 3
Region 2
Region 1
(c)
Impact Velocity (ms⁻¹)
Charge (Cb ×10⁻¹⁵)

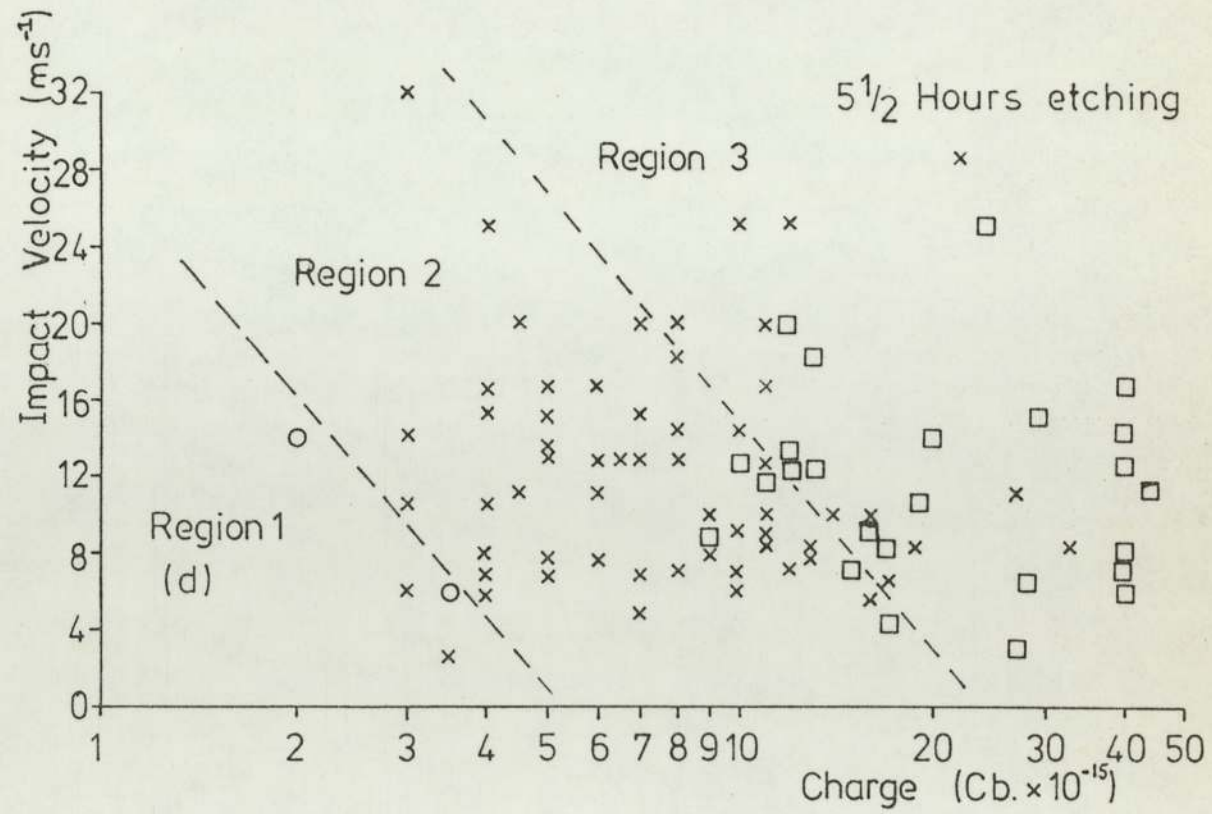
5 1/2 Hours etching
Region 3
Region 2
Region 1
(d)
Impact Velocity (ms⁻¹)
Charge (Cb. ×10⁻¹⁵)

Target specimen	Average coef of restitution
Titanium 318	0·53±0·15
Copper	0·48±0·14

Table 4.3 Average coefficient of restitution for the highly oxidised titanium and copper surfaces

indicates the average coefficient restitution with its standard deviation for the highly oxidised titanium and copper surfaces,

To determine whether the "sticking" process is caused by impact heating arising from the kinetic energy of the particle, experiments were performed on tungsten and molybdenum surfaces (melting points 3387 and 2620°C respectively) in polished and unpolished forms. These surfaces consisted of sheets of material which were cut into 10 mm squares and 'bonded' to a surface in a similar manner to insulator target specimens (see Section 3.3.6). It was observed that both surfaces, after undergoing a commercial polishing process, produced only "sticking" events while unpolished surfaces, after a spirit rinse and ultrasonic cleaning, gave a high percentage of "bouncing" events, (64% for molybdenum and 20% tungsten). Since the impact behaviour observed with the polished Mo andW specimens is in agreement with the other metallic targets, it would appear that impact heating arising from the dissipation of the particles KE does not play a major role in the impact process. Conversely, it does appear that the thickness of the surface oxide contaminating layer is a dominant factor, (see Chapter 5).

4.2.3 Semi-conducting surfaces

It has been shown above that both the thickness and species of the oxide influence the impact behaviour. To determine whether this latter dependance stems from the electrical conductivity of the oxide, impact measurements have been carried out on an ambient oxide semi-conducting material - silicon (n and p type) - in which the resistivity of the slice varied from 1 to 400Ωcm. Each slice was cleaned in a spirit bath and ultrasonically washed before being mounted on a Ni substrate in a similar manner to that of the insulating materials, (see Section 3.3.6). It was observed that no "bouncing" events occurred for any type or resistivity of slice. Also cleaning the slice in HF(to remove the surface oxide) produced no change in the response, i.e., only "sticking" events occurred. However oxidising one of the slices (n-type, resistivity 1.5Ωcm) in a furnace at 1100°C for 6 hours (thus growing a "dry" oxide on the surface) produced a situation where the majority of the incident microspheres "bounced". A similar result was obtained when a "wet" oxide was grown on a slice (produced by placing the slice in a furnace at 1100°C for 6 hours and bubbling nitrogen, through distilled water, in a stream over the slice). As with the highly oxidised metal targets, Figure 4.8 shows the variation of the impact velocity with impact particle charge. Again similar regions arise where (1) no charge modification occurs in a "bouncing" event, (2) "bouncing" occurs with charge modification and (3) a pure "sticking" process occurs. Figures 4.9 (a) and (b) show the e value distribution for the "bouncing" particles, and indicate that the peak in the distribution is shifted further towards 1 in comparison with the results of the highly oxidised aluminium surface, (see Figure 4.6), i.e. less energy is lost in the impact between carbonyl iron microspheres and the highly oxidised silicon surface than in the impact with highly oxidised aluminium.

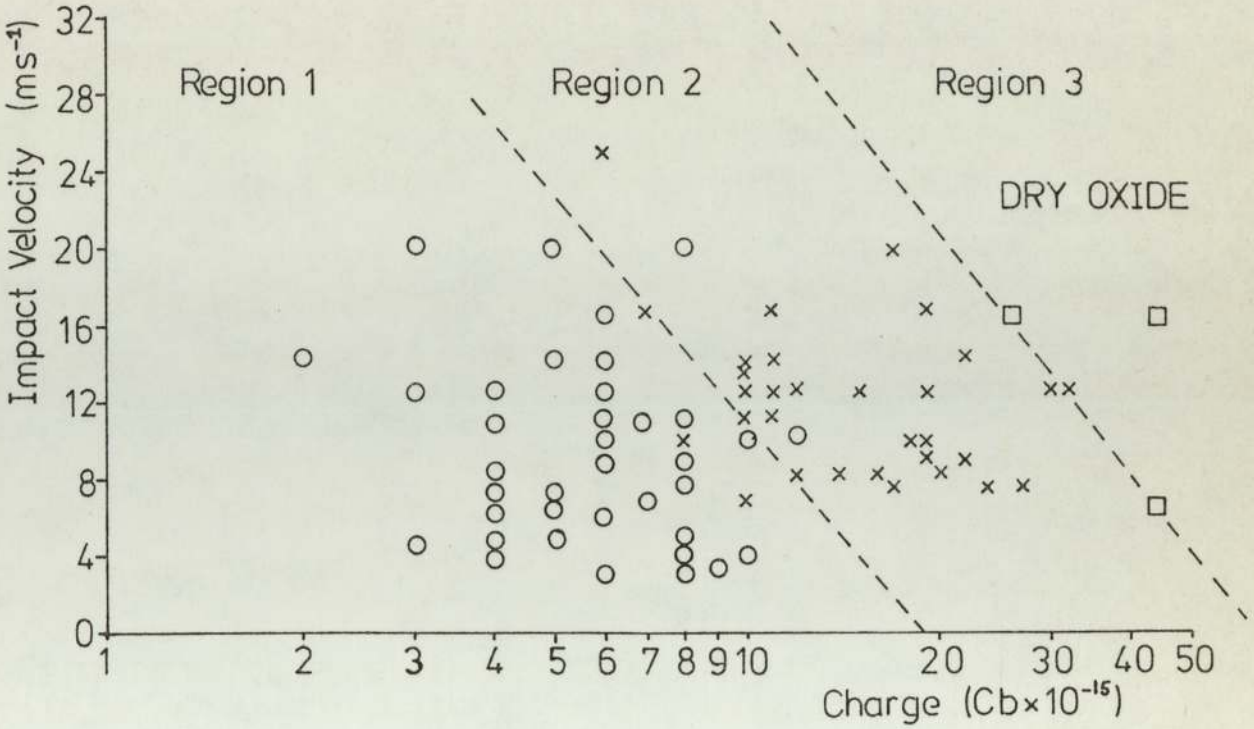

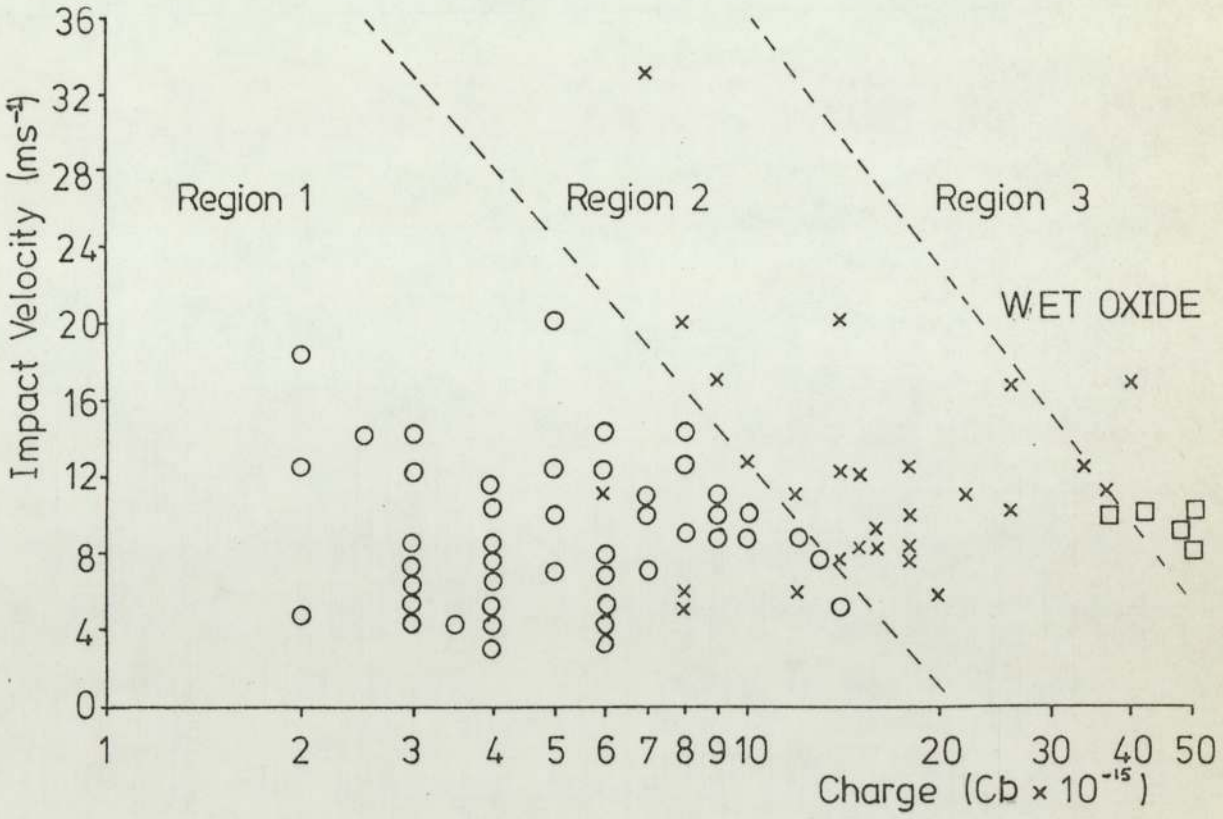

Figure 4.8: The surface impact characteristics of the highly oxidised silicon surfaces; o≡'bouncing' particles with no charge modification; ×≡'bouncing' particles with charge modification; □≡'sticking' particles

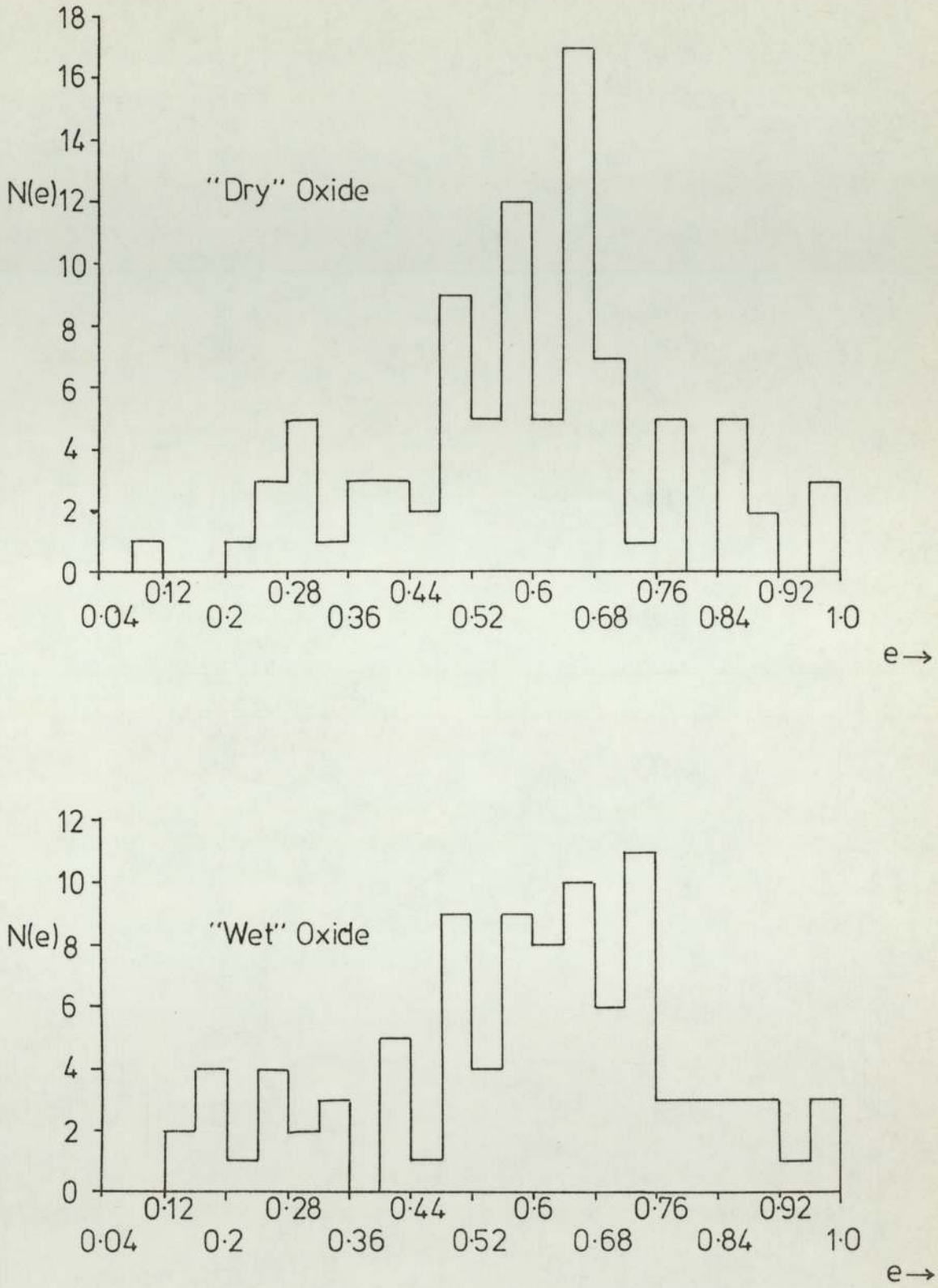

Figure 4.9: e-value histograms for the 'dry' and 'wet' oxide silicon surfaces

4.2.4 Insulating surfaces

Table 3.1 indicates the type and thickness of the various samples used in this study. Each specimen is mounted, using silver conductive paint, on to a Ni substrate before being placed in the experimental chamber. Generally all specimens showed a similar response in which $\sim$99% of the low velocity carbonyl iron microspheres "bounced" on impact, with Figure 4.10(a) - (l) showing typical 'e value' histograms for the various insulating materials. In the case of cellulose, three different impact sites have been used on a single sample, while for mica the variation in target thickness indicates a trend towards a lower 'e' value as the specimen thickness is reduced, i.e., a similar trend to that observed with the ebonite samples. Comparing, for example, the response of glass with p.v.c. highlights the general conclusion that as the hardness of the material increases, the peak in the distribution shifts towards the value of 1. As will be discussed in Chapter 5, the spread in the 'e' values can be associated, at least in part, with the surface roughness of the target sample which is confirmed by the histogram shown in Figure 4.10(k).

An alternative, and more informative method of presenting the results it to plot a graph of e^2v^2 against v, where 'e' is again, the coefficient of restitution and 'v' the reflected particle velocity (14). Thus the data for mica and p.v.c. yields curves shown in Figure 4.11; although there is a large scatter, in the experimental results, the general trend can be easily seen. The form of the curves lend themselves to be characterised in the form of a power law of the form $e^2v^2 = Kv^n$, where K is a constant. Hence a graph of log e^2v^2 versus log v should give a straight line with gradient n and intercept K. The log plots for mica, p.v.c. and ebonite are shown in Figure 4.12, where the straight line has been determined by the method of "least square fit.". From each plot the gradient and

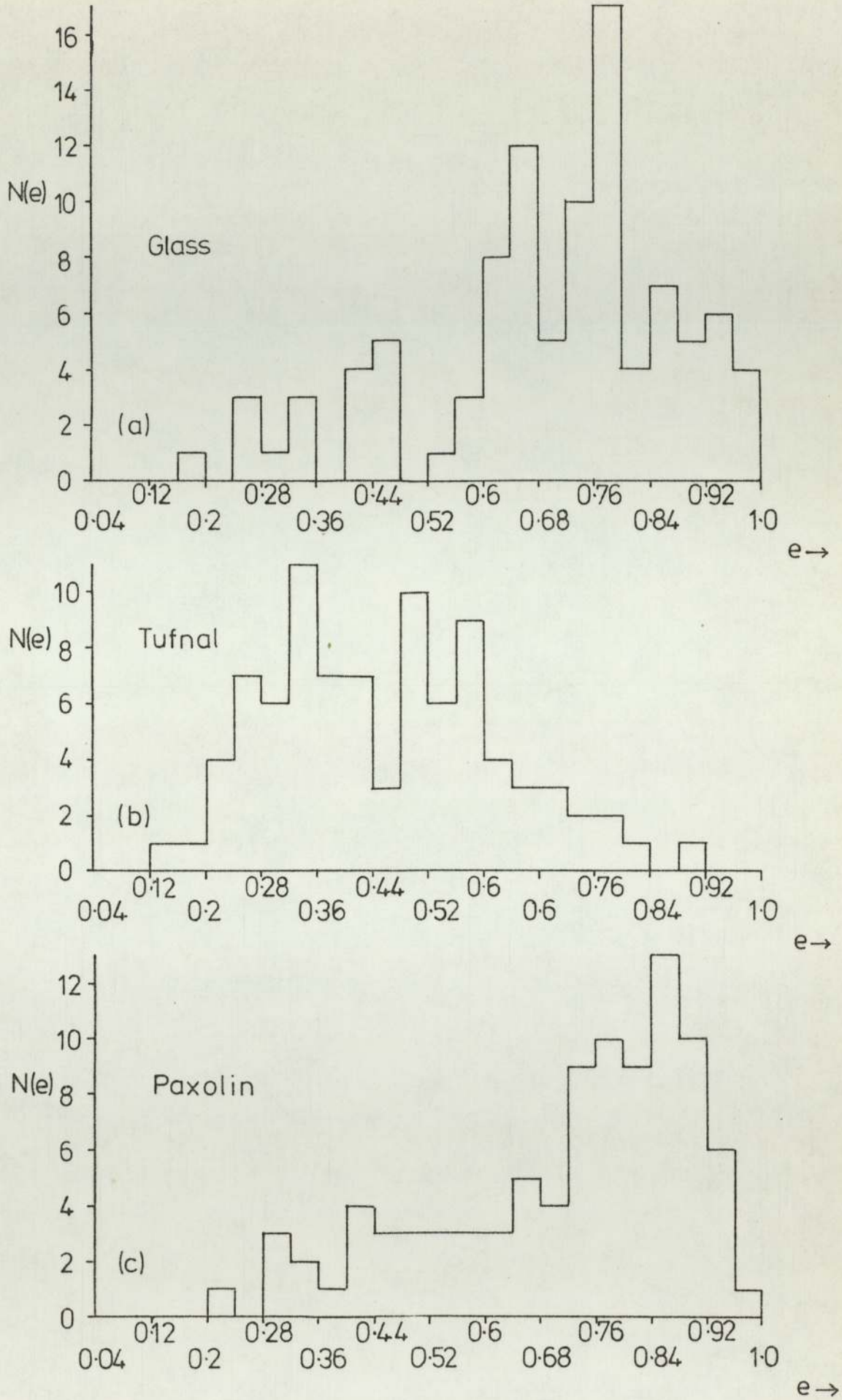

Figure 4.10 a-l: e-value histograms for various insulating materials

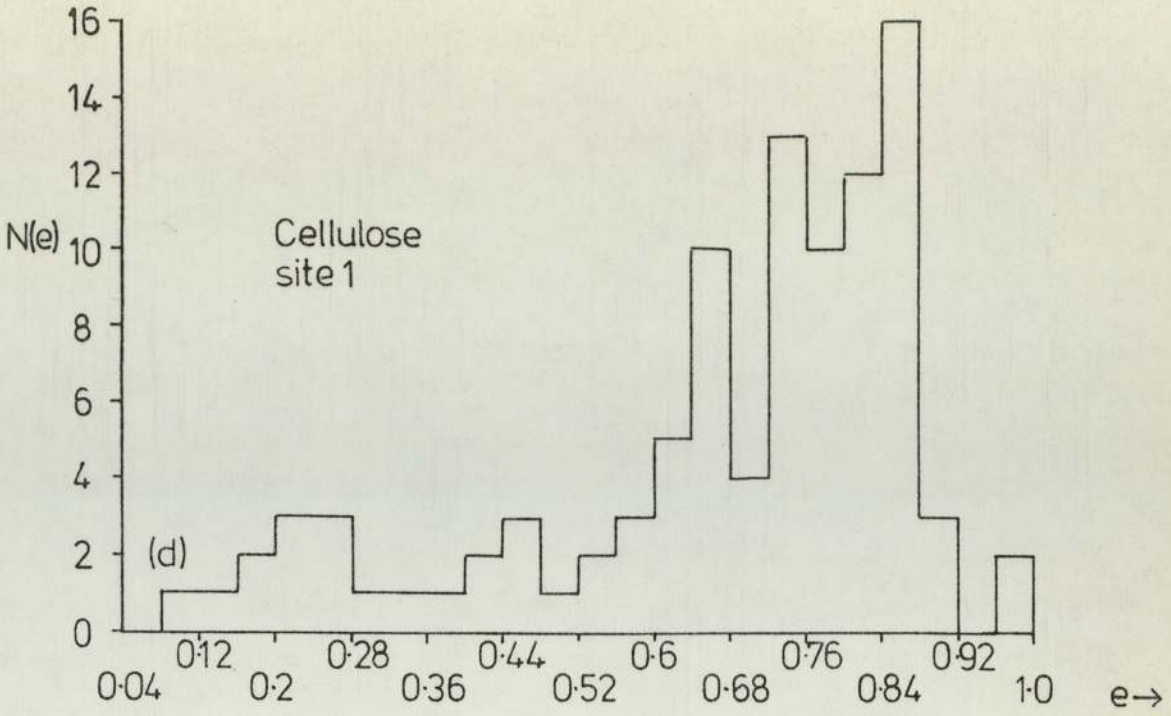
16
14
12
N(e) 10
8
6
4
2
0
Cellulose
site 1
(d)
0·04
0·12
0·2
0·28
0·36
0·44
0·52
0·6
0·68
0·76
0·84
0·92
1·0
e→

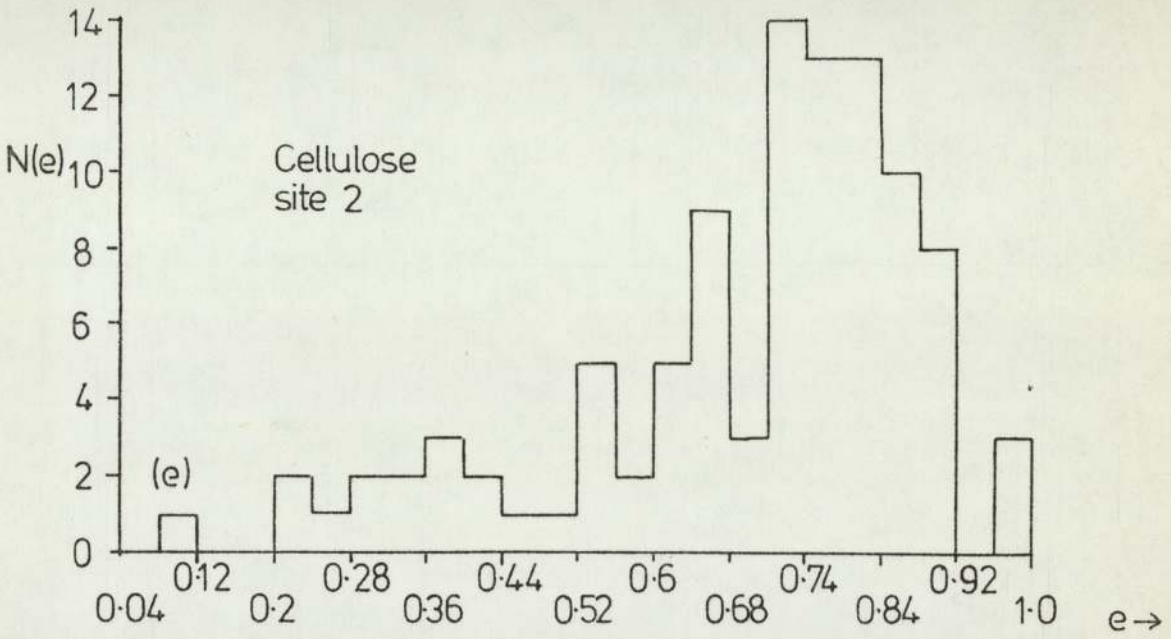
14
12
N(e) 10
8
6
4
2
0
Cellulose
site 2
(e)
0·04
0·12
0·2
0·28
0·36
0·44
0·52
0·6
0·68
0·74
0·84
0·92
1·0
e→

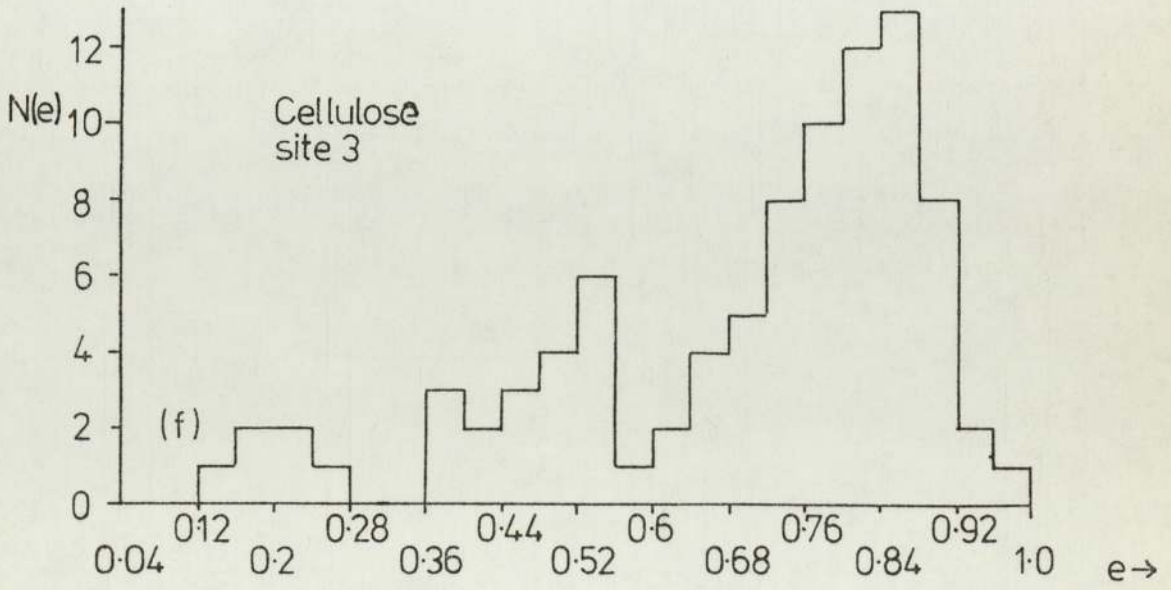
12
N(e) 10
8
6
4
2
0
Cellulose
site 3
(f)
0·04
0·12
0·2
0·28
0·36
0·44
0·52
0·6
0·68
0·76
0·84
0·92
1·0
e→

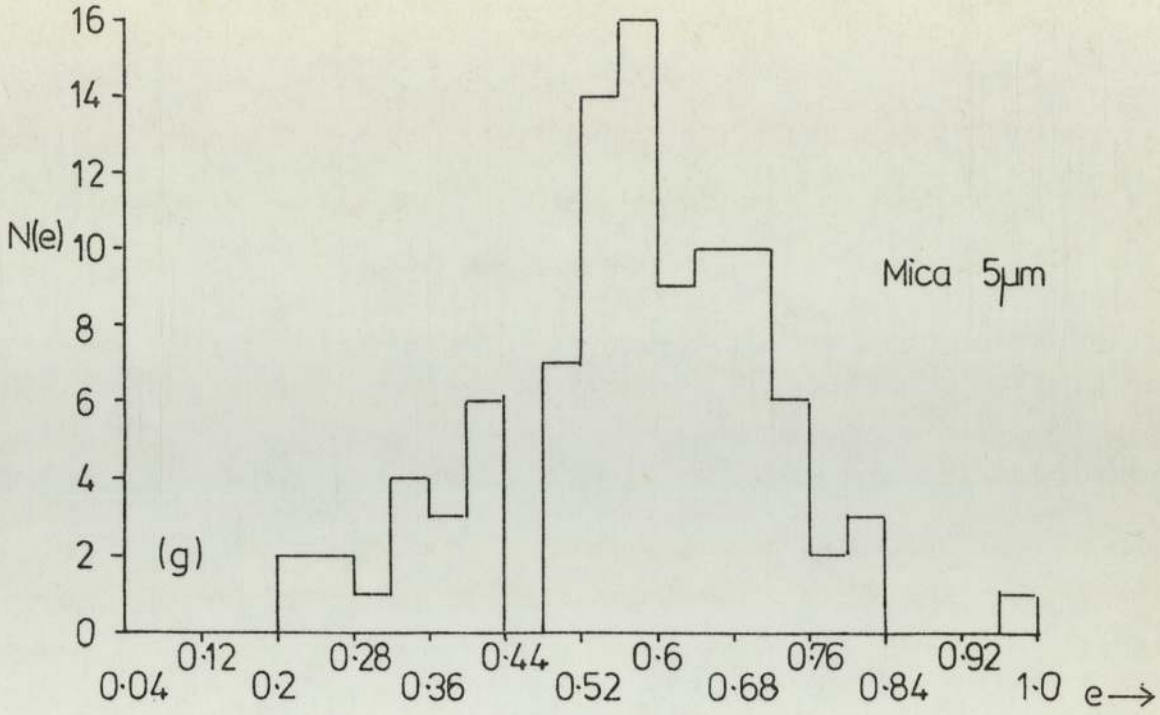
N(e)
16
14
12
10
8
6
4
2
0
(g)
Mica 5μm
0·04
0·12
0·2
0·28
0·36
0·44
0·52
0·6
0·68
0·76
0·84
0·92
1·0
e →

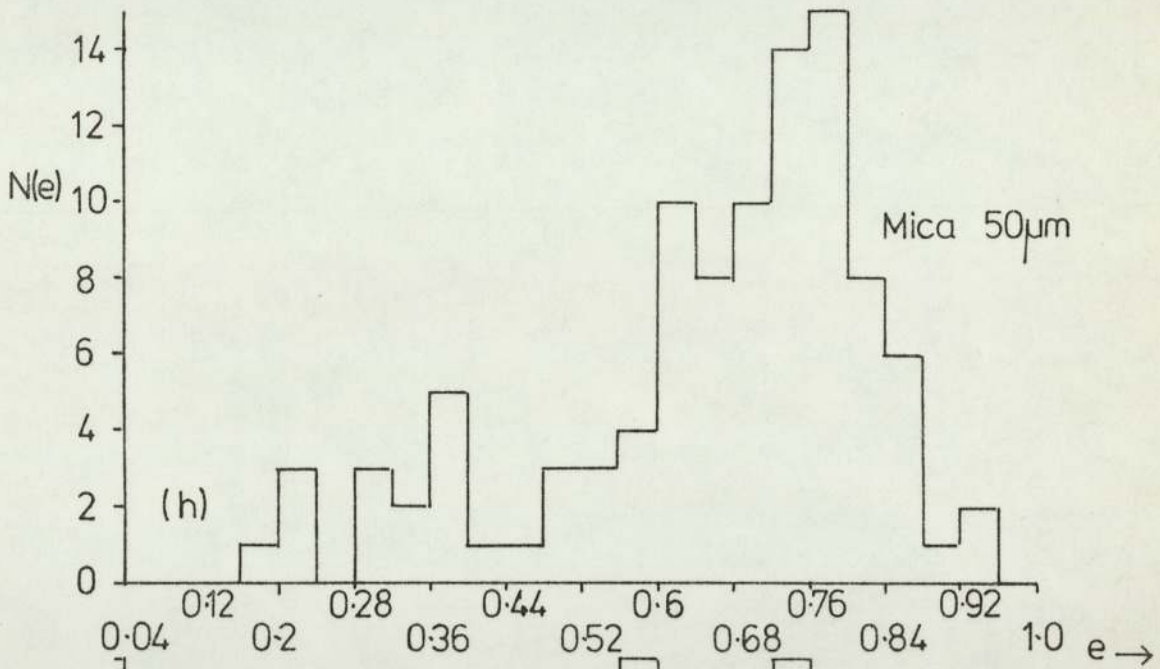
N(e)
14
12
10
8
6
4
2
0
(h)
Mica 50μm
0·04
0·12
0·2
0·28
0·36
0·44
0·52
0·6
0·68
0·76
0·84
0·92
1·0
e →

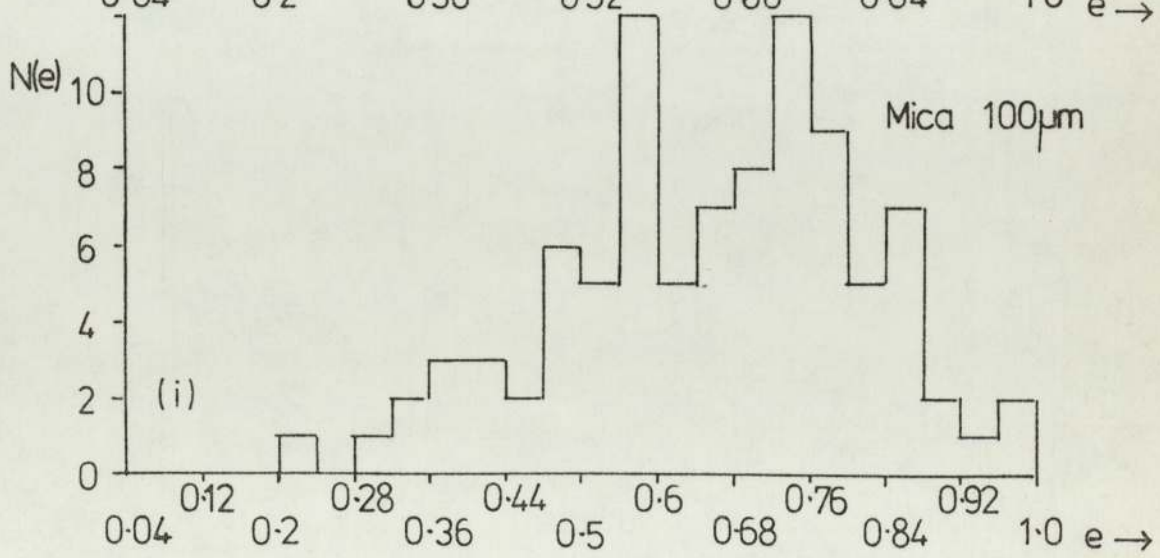
N(e)
10
8
6
4
2
0
(i)
Mica 100μm
0·04
0·12
0·2
0·28
0·36
0·44
0·5
0·6
0·68
0·76
0·84
0·92
1·0
e →

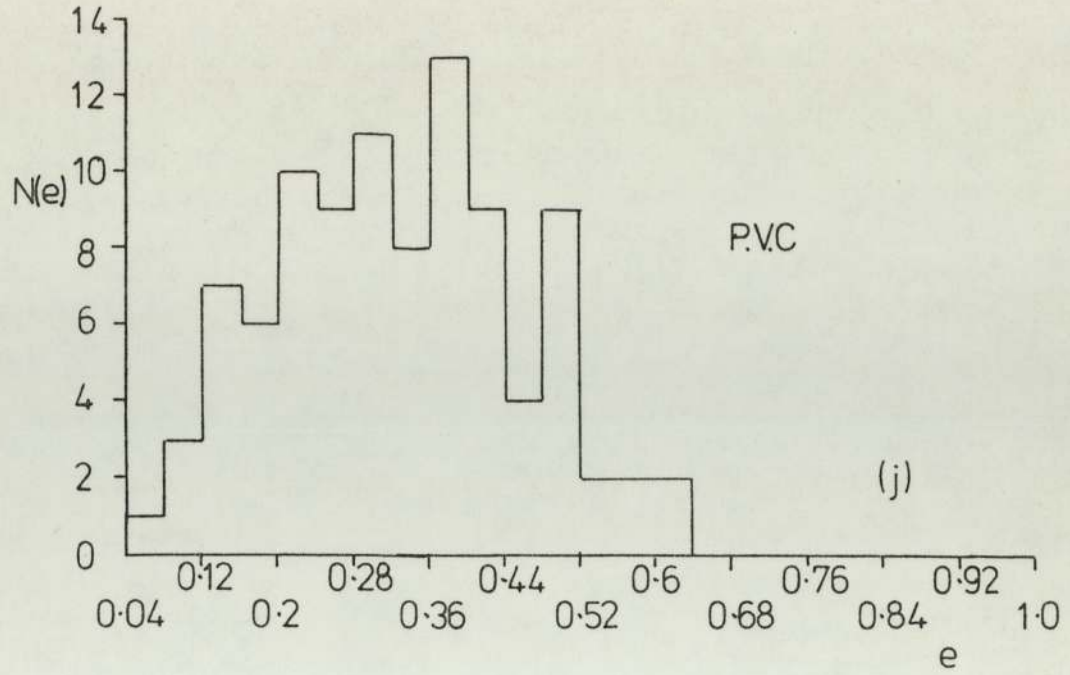
N(e)
14
12
10
8
6
4
2
0
P.V.C
(j)
0·04
0·12
0·2
0·28
0·36
0·44
0·52
0·6
0·68
0·76
0·84
0·92
1·0
e

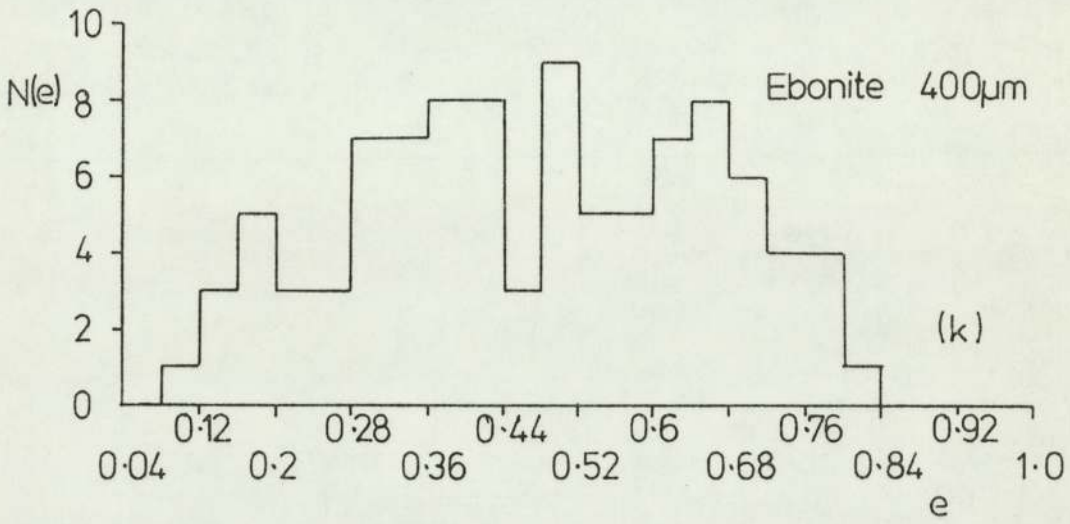
N(e)
10
8
6
4
2
0
Ebonite 400μm
(k)
0·04
0·12
0·2
0·28
0·36
0·44
0·52
0·6
0·68
0·76
0·84
0·92
1·0
e

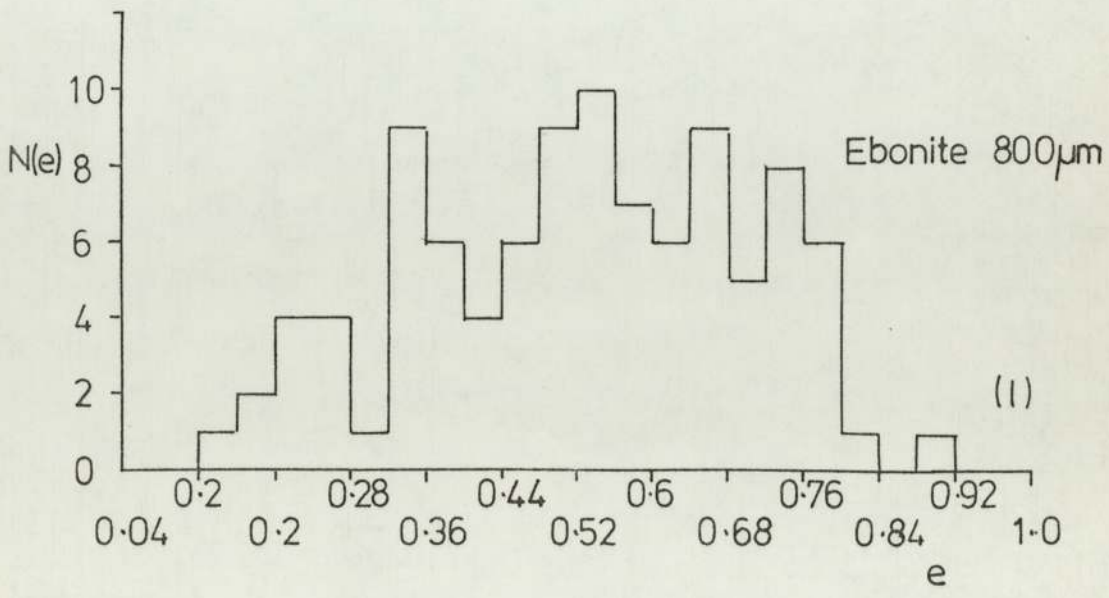
N(e)
10
8
6
4
2
0
Ebonite 800μm
(l)
0·04
0·2
0·28
0·36
0·44
0·52
0·6
0·68
0·76
0·84
0·92
1·0
e

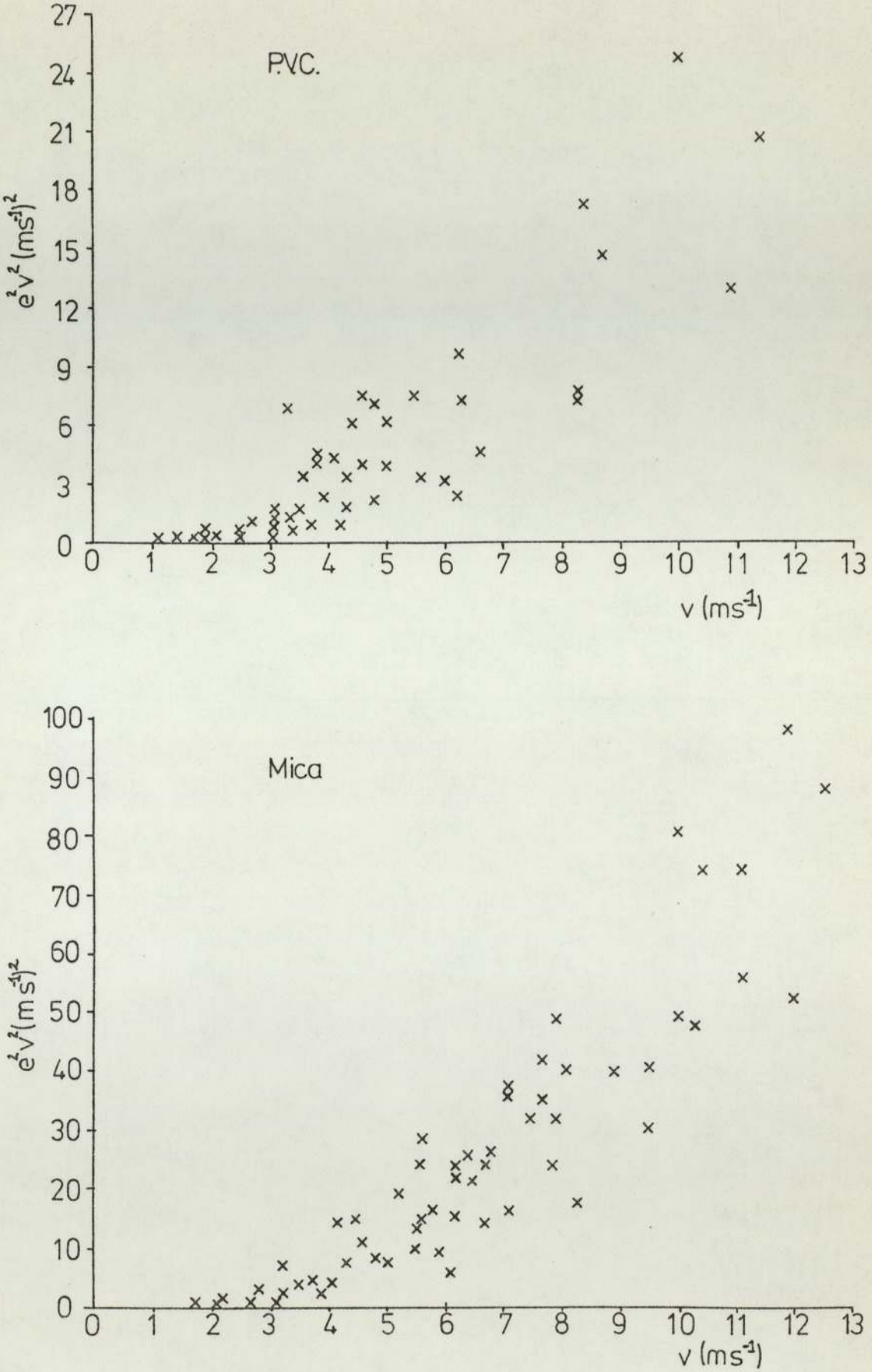

Figure 4.11: Graphical plots of e^2v^2 as a function of v for P.V.C. and Mica

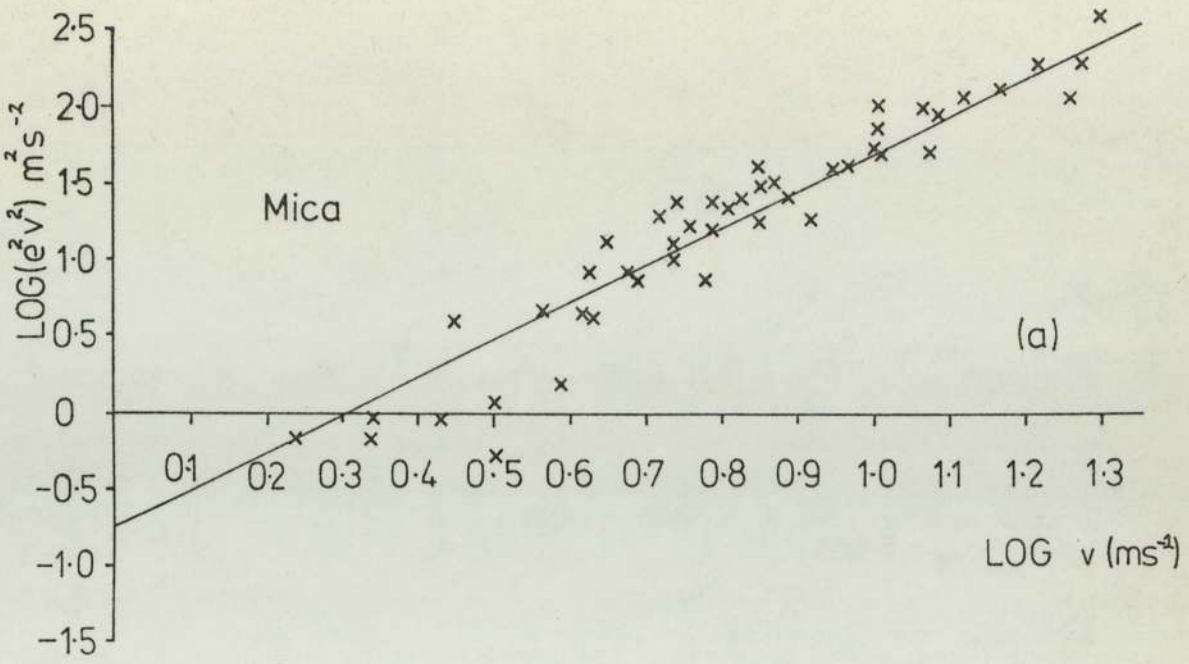

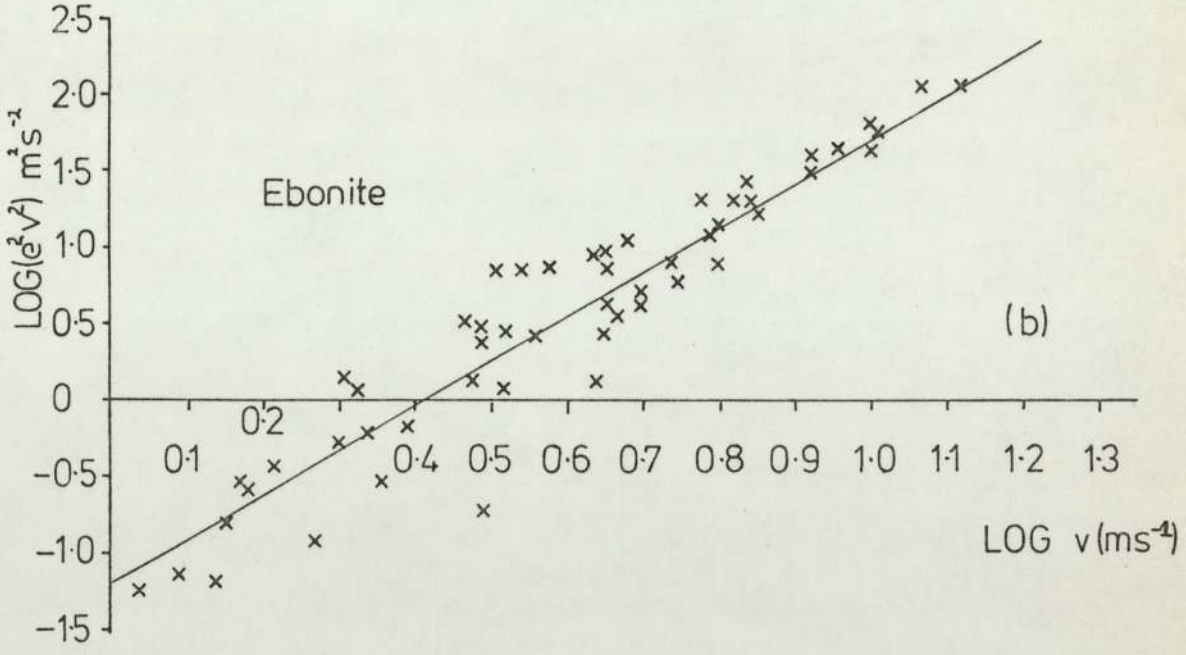

Figure 412a-c: Graphical plots of $\log e^2v^2$ against $\log v$ for Mica, Ebonite and P.V.C.

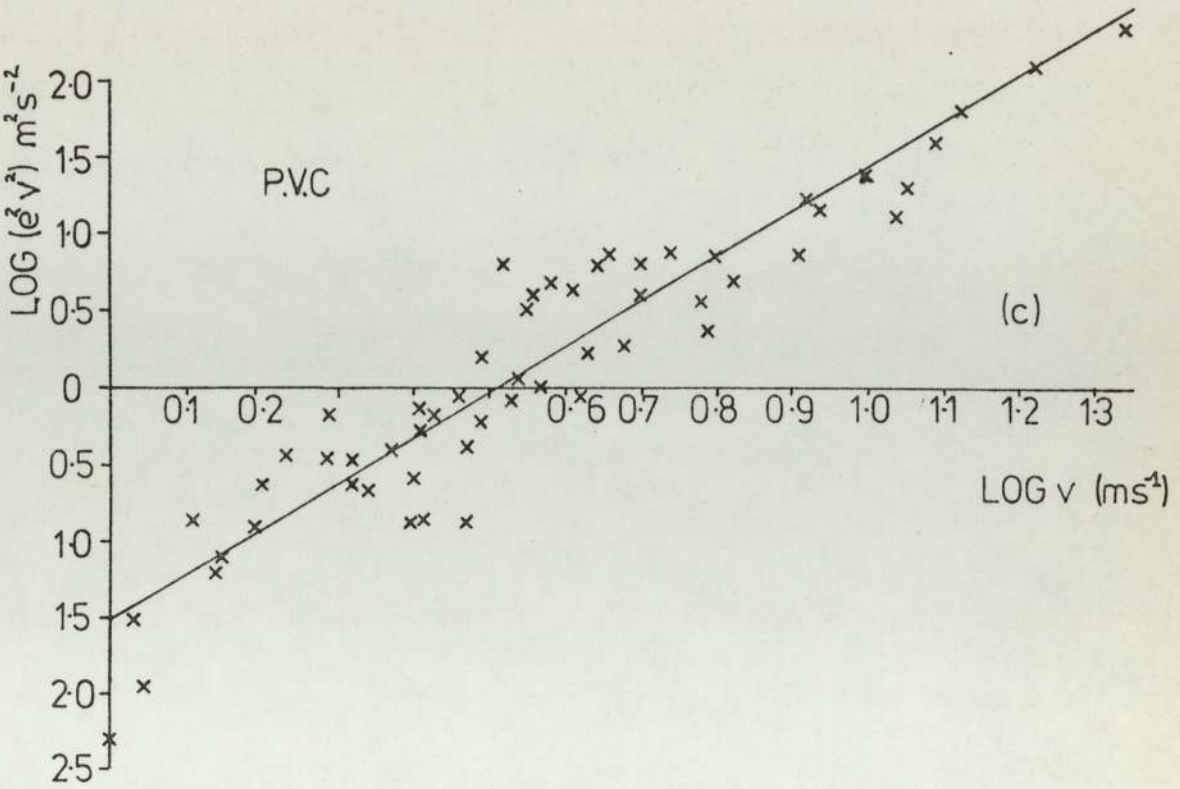

intercept values are n = 2.446, K = 0.175 for mica, n = 2.853, K = 0.0652 for ebonite and n = 2.887, K = 0.0322 for p.v.c. The significance of this data will be discussed in Chapter 5, however, briefly, as $n \rightarrow 2$ and $K \rightarrow 1$ the impact process becomes more elastic.

4.3 Electrical Impact Data

In contrast to the previous section, which was concerned with the mechanical aspects of the particle impact events, this section concentrates on highlighting the features of the drift-tube and target signals (oscillograph traces) that provide information about the charge exchange process occurring during the same sample of particle events. An account will now be given, in these terms, of the response from a variety of target surfaces.

4.3.1 Ambient oxide surfaces

4.3.1(a) Titanium/Stainless steel/Copper

It has already been mentioned that it is very rare for a particle to execute a "bouncing" impact process with any of the above surfaces, hence only "sticking" occurs on impact. Thus Figure 4.13 shows a typical "sticking" event, for stainless steel, in which a charge sensitive amplifier has been used to record the drift-tube trace and a voltage sensitive amplifier, the target trace. However, the contact potential, arising from the work function difference of the particle/target combination (see Chapter 5) plays a significant role in the impact between carbonyl iron microspheres and titanium (318 or 117), where charge reversal behaviour is observed, see Figure 4.14.

4.3.1(b) Aluminium

As stated previously in Section 4.2.1, aluminium is the only metal surface studied, to date, that shows a significant amount of "bouncing". Typically 10% of the incident particles bounce, and in these cases, it is usual for the reflected particle to possess a reduced charge, such as shown in Figure 4.15. Table 4.1, which is based on a detailed study of this surface, shows the average charge modification ratio $q_m (\equiv q_2/q_1)$ and the standard deviation, for the incident positively charged particles, which return with a reduced positive charge. From this it can be seen that even for a $(200\ \mu m)^2$ "test" impact zone the variations in the electrical properties of the surface are very large. It should also be noted that there were a consistent number of events ($\sim$4%) where the reflected particle possessed a negative change, which is in agreement with the results of Texier (101,102). This effect is thought to arise, in a similar manner to that mentioned above for titanium, from the work function differences of the microparticle/target combination.

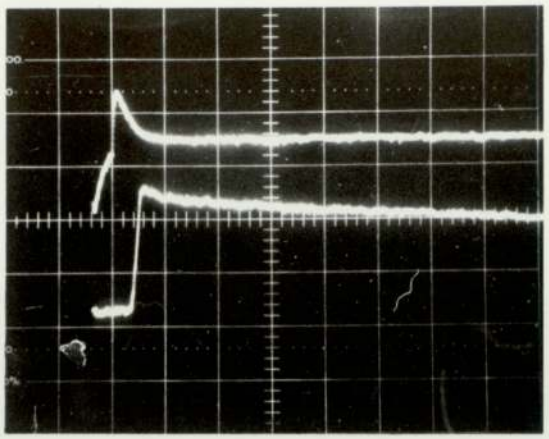

Drift tube trace
sen(0·005V/Div)

Target trace
sen (0·02V/Div)

Time base 1ms/Div

Figure 4.13: 'Sticking' event observed in the impact of carbonyl iron microspheres on a stainless steel target

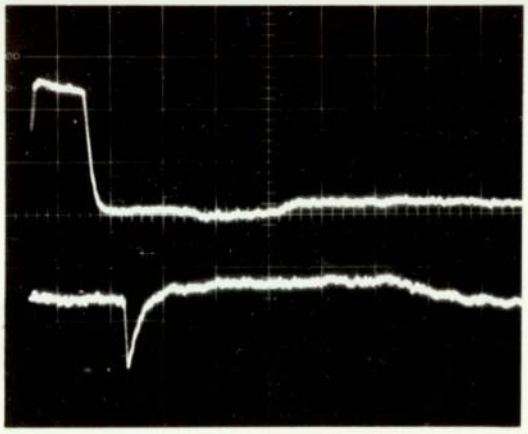

Drift tube trace
sen(0·02V/Div)

Target trace
sen (0·005V/Div)

Time base 1ms/Div

Figure 4.14: Zero field charge reversal behaviour observed in the impact between carbonyl iron microspheres and a titanium target

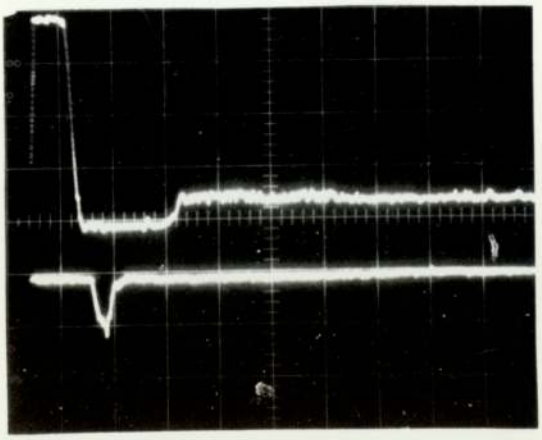

Drift tube trace
sen(0·02V/Div)

Target trace
sen (0·005V/Div)

Time base 1ms/Div

Figure 4.15: "Bouncing" event in which the reflected particle possesses a reduced positive charge and a slower velocity (incident velocity=14·3ms^{-1}; reflected velocity=6·9ms^{-1}; 85% charge exchange during impact)

4.3.2 Highly oxidised metal surfaces

From the results outlined in section 4.2.2 it has been shown that when a carbonyl iron microsphere impacts onto a highly oxidised metal surface that the probability of a "bouncing" event occurring increases as the surface oxide thickness increases. On this basis the returning particle will travel back through the drift-tube, after the impact event, leading to, usually, a twin trapezoidal drift-tube trace. Typical oscillographic data obtained from the impact of carbonyl iron microspheres on a highly oxidised aluminium target, having varying thicknesses of surface oxidation, i.e., at different etching times, are shown in Figure 4.16 (i), (ii), and (iii). From these it is evident that, (a) charge has been lost during the impact event, and (b) that the reflected particle has a slower velocity. As a further comment on these oscillographs it is clear that Figure 4.16(ii) indicates that the particle has not returned through the drift-tube, since the second drift tube pulse is absent; in cases like this it has probably been in collision with either the earthed grid (see Figure 3.6), or its stainless steel surround, before returning to the target, as indicated by the second target trace. From the twin trapezoidal drift-tube traces (of which typical examples are shown in Figure 4.16 (i) and (iii)) it is possible to estimate the amount of charge lost during the impact event. Thus, using a procedure outlined in Section 3.6.1 where the surface of the aluminium target is progressively bombarded and argon-ion etched to remove the surface oxide, Table 4.4 shows the average charge modification value q_m as a function of the etching time for a single impact site. Each charge modification value is the average of the data determined from the particles which appear in Region 2 of Figure 4.7. It can be seen that the q_m values show only a slight variation throughout the etching process. Similar oscillographic data can be obtained for the highly oxidised titanium and copper surfaces (showing 88% and 78% of the incident particles bounce

(i)

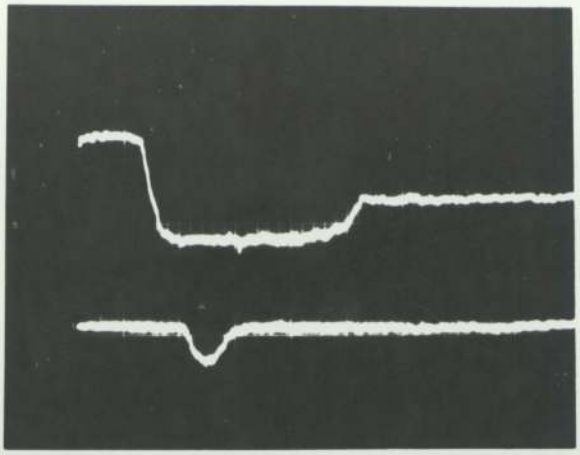

No etching

Drift tube trace
sen(0·02V/Div)

Target trace
sen(0·005V/Div)

Time base 1ms/Div

Initial velocity=9·1 ms^{-1}; reflected velocity=4 ms^{-1}

(ii)

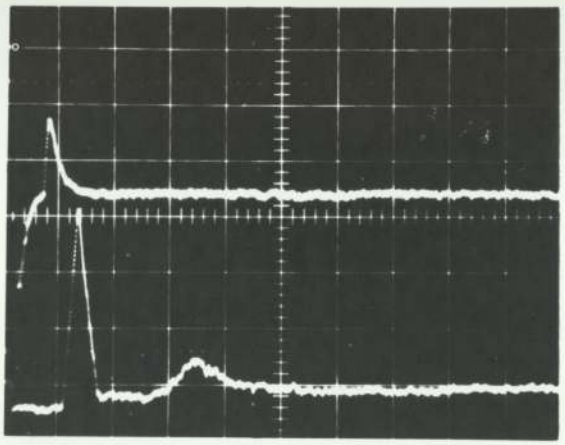

1 Hour etching

Drift tube trace
sen(0·005V/Div)

Target trace
sen(0·02V/Div

Time base 2ms/Div

Initial velocity=10 ms^{-1}; reflected velocity=5·6 ms^{-1}

(iii)

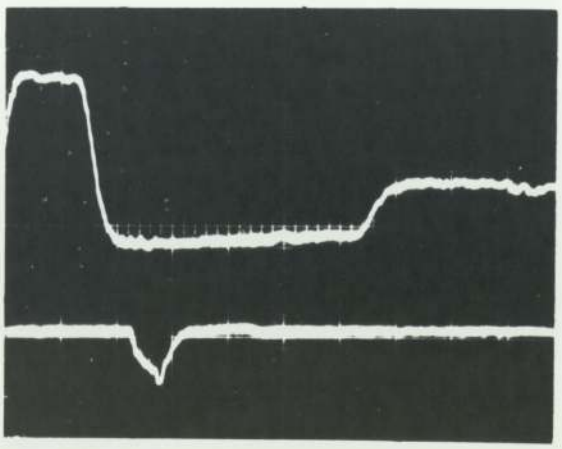

8 Hours etching

Drift tube trace
sen(0·02V/Div)

Target trace
sen(0·005V/Div)

Time base 1ms/Div

Initial velocity=9·1 ms^{-1}; reflected velocity=3·2 ms^{-1}

Figure 4.16: Oscilloscope traces for the highly oxidised aluminium surface

Average reflected/incident charge for positive reflections q_2/q_1	Etching time (hrs)
0·77±0·15	0
0·75±0·12	1/2
0·78±0·08	1
0·73±0·12	2
0·68±0·14	3
0·71±0·12	4
0·69±0·12	5 1/2
0·69±0·13	7
0·66±0·12	8
0·69±0·13	9 1/2
0·7 ±0·12	11 1/2
0·74±0·09	13 1/2
0·74±0·13	15 1/2
0·77±0·17	17 1/2
0·73±0·15	19 1/2

Table 4.4: The variation of the charge modification ratio with etching time

respectively). However, the average charge modification values determined for the unetched titanium and copper surfaces are 0.37 and 0.44 respectively, indicating that more charge is lost in the impact process between carbonyl iron microspheres and these latter two surfaces, than in the corresponding impact event with aluminium.

It has already been pointed out in Section 4.2.2 that three distinct particle behaviour patterns can be highlighted if the incident particle velocity is plotted against the incident particle charge: i.e. corresponding to regions of "sticking", "bouncing" with charge modification and "bouncing" with no charge modification. The initial particle charge is thus seen to play a crucial role in determining whether the particle "sticks" to the surface; in particular, particles which possess

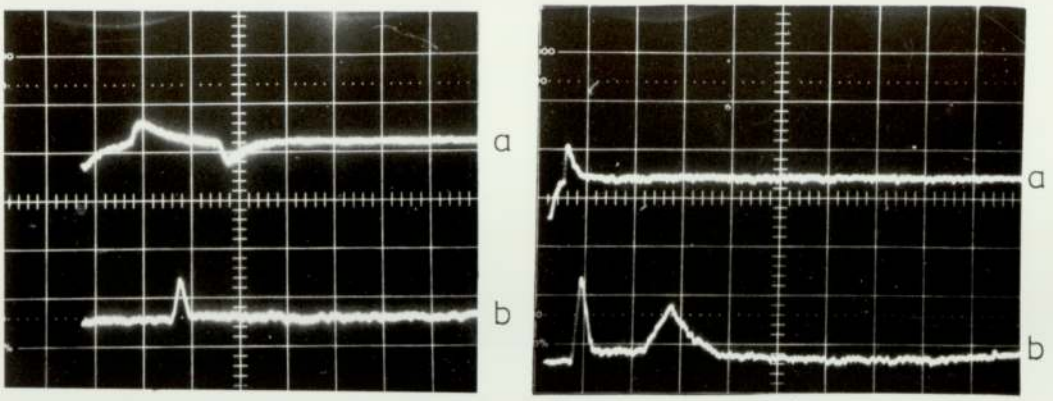

(i) DRY OXIDE (ii)

Time base 0·5ms/Div Time base 2ms/Div

a = drift tube trace; sen(0·005V/Div)
b = target trace; sen(0·02V/Div)

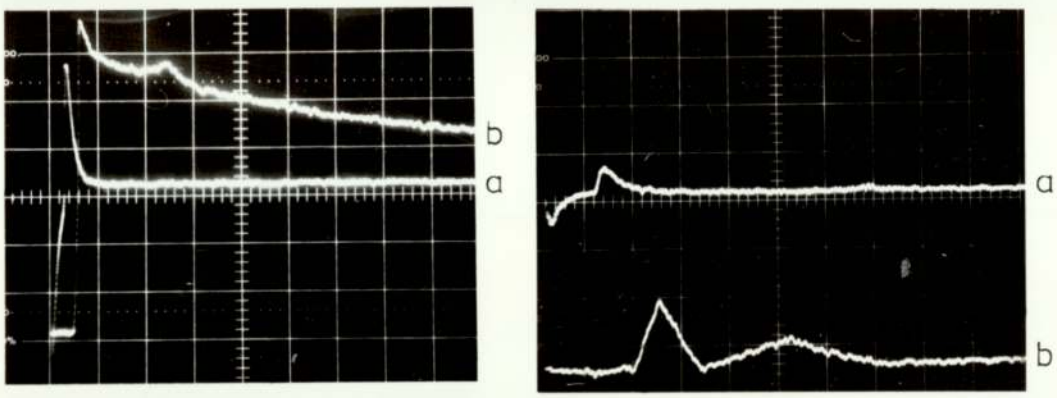

(iii) WET OXIDE (iv)

Time base 2ms/Div Time base 1ms/Div

a = drift tube trace; sen(0·005V/Div)
b = target trace; sen(0·02V/Div)

Figure 4.17: Oscilloscope traces for the highly oxidised silicon surfaces

a large charge (due to their large mass) invariably "stick" to the surface on impact, whilst small, low charge, particles tend to "bounce". As a general comment on this behaviour it may well be that since the particle charge is related to the particle potential, which determines the amount of tunnelling and electron-phonon scattering (see Section 2.3.2) in the oxide junction, a sufficient temperature rise may occur leading to welding and hence "sticking" on impact. However, this idea will be discussed more fully in Chapter 5.

4.3.3 Semi-conducting materials

Figure 4.17 shows the variation in the charge modification for microspheres incident on silicon targets having "wet" or "dry" oxides. From a comparison of this set of traces it can firstly be concluded that the nature of the oxide does not appear to significantly influence the particle interaction. Rather, the percentage of charge 'dumped' on the target depends on the incident charge of the particle as indicated by Figure 4.17(iii) where 90% of the charge is lost on impact, i.e., the larger the incident charge the greater the possibility of a "sticking" event. It is also typical for a high proportion of the events to show multiple bouncing on the target surface illustrated by (i) the absence of a return particle drift-tube trace and (ii) a second, reduced amplitude, target trace. The value of using an incident velocity/incident charge plot for characterising the particle response is once more illustrated in Figure 4.8, where, again, the three zones of interest arise, of which comment has already been made in Section 4.3.2. As a final point, it is of interest to note that the average value of the charge modification ratio (q_m) for the region where particles "bounce" with some loss of charge on impact (see Figure 4.8), is given as 0.86 ± 0.09 for the "dry" oxide and 0.792 ± 0.24 for the "wet" oxide.

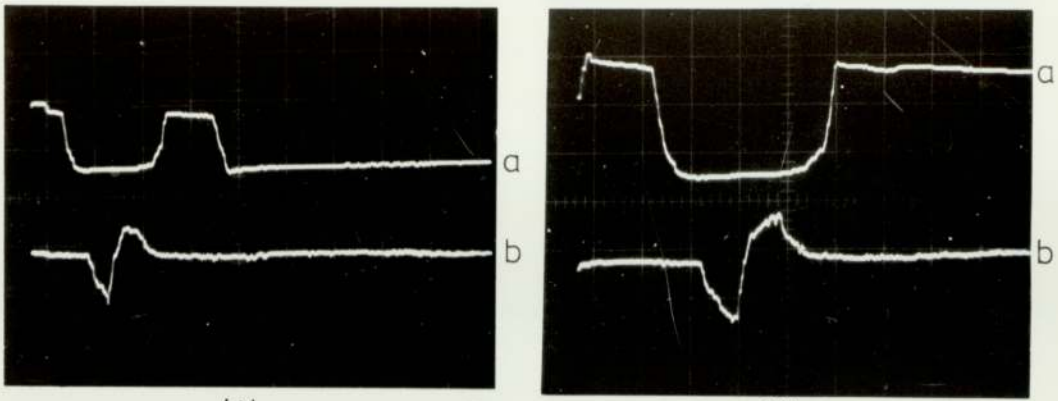

(i) GLASS (ii)

Time base 1ms/Div Time base 1ms/Div

a = drift tube trace; sen (0·02V/Div)
b = target trace; sen (0·005V/Div)

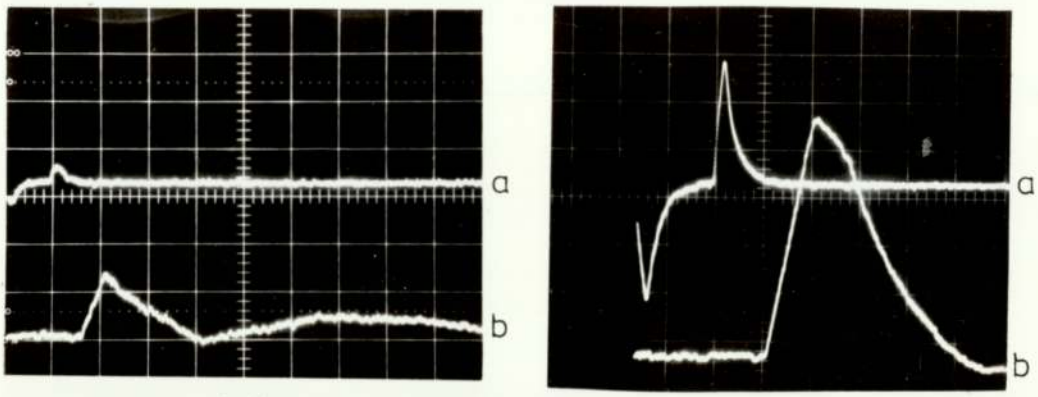

(iii) EBONITE (iv)

Time base 2ms/Div Time base 1ms/Div

a = drift tube trace; sen (0·005V/Div)
b = target trace; sen (0·02V/Div)

Figure 4.18: Typical insulator surface oscilloscope traces

4.3.4 Insulating materials

Figure 4.18 shows a sample of charge modification oscillographs obtained from glass and ebonite which are typical of all the insulating materials used in this study. In addition, multiple "bouncing" occurs in many cases as indicated by the target trace of Figure 4.18(iii). The average charge modification values for each insulating surface used in this investigation can be found in Table 4.5, where it can be seen that the

Specimen material	Average reflected/incident charge for positive reflections q_2/q_1
Glass	0·91±0·04
Mica(5um)	0·9 ±0·07
Mica(50um)	0·9 ±0·05
Mica(100um)	0·9 ±0·02
Paxolin	0·91±0·04
Tufnal	0·88±0·06
Red-fibre	0·84±0·11
Cellulose(1)	0·94±0·07
Cellulose(2)	1·0 ±0
Cellulose(3)	0·91± 0
Ebonite(400um)	0·73± 0·16
Ebonite(800um)	0·78±0·21
P.V.C.	0·66±0·6

Table 4.5: Insulator charge modification ratios

softer materials, such as P,V.C. give rise to more charge being 'dumped' during the impact process. On occasions it is evident that the decay of the induced charge on the target, as the reflected particle leaves the surface, is exponential in form (see Figure 4.18(iv)). This is thought to arise where the particle leaves the target at an oblique angle and thus has a low "normal" velocity to the target surface. Under this condition the returning particle does not pass through the drift tube (since no return pulse is seen) but escapes into the vacuum system. This phenomenon

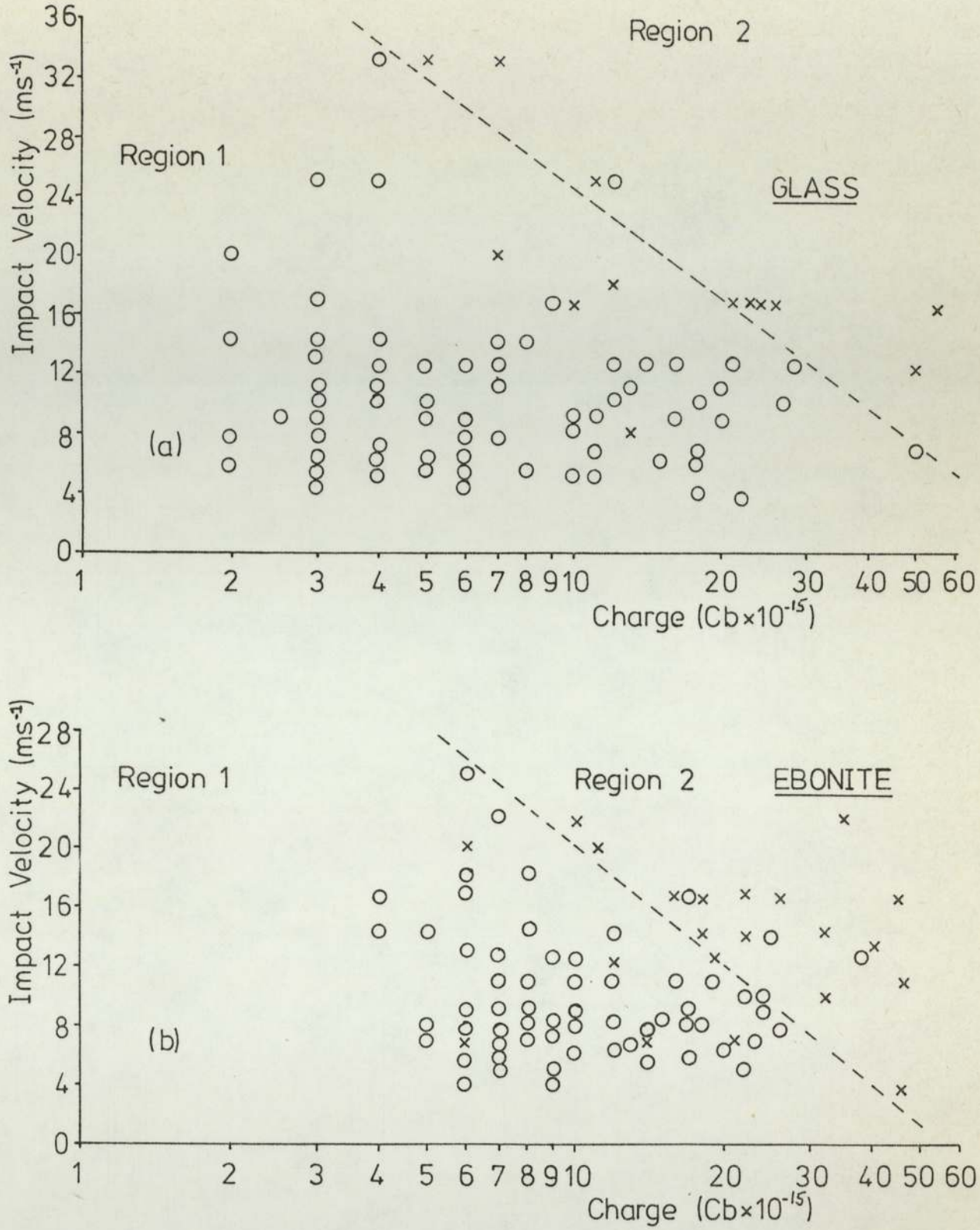

Figure 4.19 a-b: The surface impact characteristics of the glass and ebonite surfaces; o≡'bouncing' particles with no charge modification; ×≡'bouncing' particles with charge modification

is more noticeable with an insulating surface which is (i) mechanically soft and (ii) has large variations in surface topography.

As with the highly oxidised metal and semi-conducting surfaces the impact behaviour of each particle can be characterised by using a plot of the incident particle velocity against the incident particle charge. Typical plots for glass and ebonite (0.4 mm) are shown in Figure 4.19 from which regions of (1) "sticking" and (2) "bouncing" with charge modification can be highlighted. However, it is apparent that there is a large overlap in the two regions. It should also be pointed out that, whereas in the highly oxidised metal case, the regions would appear to be determined by the particle charge and the electrical characteristics of the microsphere/target combination, the size of the impact area and the amount of charge "rubbed off" during impact are thought to be the important parameters in the impact between a microsphere and an insulating surface.

4.4 Interpretation of the ellipsometric data

The complementary laser ellipsometer facility has been used to monitor the surface conditions of the oxidised aluminium target after each etching process, see Section 3.6.1. Using the Δ and Ψ values measured after 19½ hours of etching, which correspond to a thickness equivalent to an ambient oxide surface, and the optical constants of aluminium, which are available in the literature(113) it is possible to compute the thickness of the oxide present on the aluminium target at the other etching times, and these, together with the film thickness are given in Table 4.6. However, for etching times from $0 \rightarrow 5\frac{1}{2}$ hours, the ellipsometric values for Δ and Ψ become invalid due to the oxide being slightly absorbing at these oxide thicknesses. Therefore, the corresponding oxide film thickness has been estimated using the procedure outlined in Section 3.4.2, in which an etching yield of 0.1 atoms /ion has been used throughout the calculation . It should

Etching time (hrs)	Δ degs	Ψ degs	Film thickness Å
$19\frac{1}{2}$	39·62	146·09	25
$17\frac{1}{2}$	39·12	146·03	29
$15\frac{1}{2}$	38·41	145·86	34
$13\frac{1}{2}$	37·28	143·09	55
$11\frac{1}{2}$	35·82	138·84	91
$9\frac{1}{2}$	33·58	132·59	144
8	31·5	125·59	206
7	30·4	116·88	294
$5\frac{1}{2}$	-	-	400
4	-	-	506
3	-	-	577
2	-	-	648
1	-	-	719
$\frac{1}{2}$	-	-	754
0	-	-	790

Table 4.6: Ellipsometric data

also be pointed out that the ellipsometric data can only be thought of as giving an average value, since the film thickness and optical constants are highly dependent on the crystallographic orientation. In addition, the measured changes in Δ and Ψ can be interpreted as the variation of oxide thickness and changes in the chemical composition respectively. More detailed information on the composition and structure of the relevant oxide layer will be discussed in Chapter 5.

Although highly oxidised copper and titanium targets have also been used, time did not allow a comprehensive ellipsometric study to be performed on these surfaces.

4.5 Micropoint probe measurements

As described in Chapter 3, two experiments have been performed with the mobile microprobe. The first involves mechanically moving the microsphere from its impact site using an electrolytically etched tip, while the second involves the application of a high field between the tip and microsphere to determine if (a) electron emission occurs from the microsphere or (b) the microsphere can be moved by the electrostatic force generated by the electric field.

4.5.1 Mechanical data

The procedure adopted in the mechanical microprobe experiments is as described in Section 3.7.2, in which all the target surfaces possess an ambient oxide layer. Table 4.7 shows the microsphere/target combinations

Microsphere / Target combination	Impact damage
1 Carbonyl iron(typeH)/ Titanium 318	No
2 Carbonyl iron(typeE)/ Titanium 318	Yes
3 Carbonyl iron(typeE)/ Aluminium	Yes
4 Carbonyl iron(typeE)/ Stainless steel	Yes
5 Carbonyl iron(typeH)/ Stainless steel	No
6 Carbonyl iron(typeH)/ Copper	No

Table 4.7: Mechanical microprobe data

used throughout this study together with a comment on whether any impact "damage" is evident after the microsphere has been moved from its impact site. Microsphere impact "damage" is visible on particle/target combinations 2, 3, 4 (see Table 4.7), although it is not seen for every impact site. All other microsphere/target combinations showed no visible target damage.

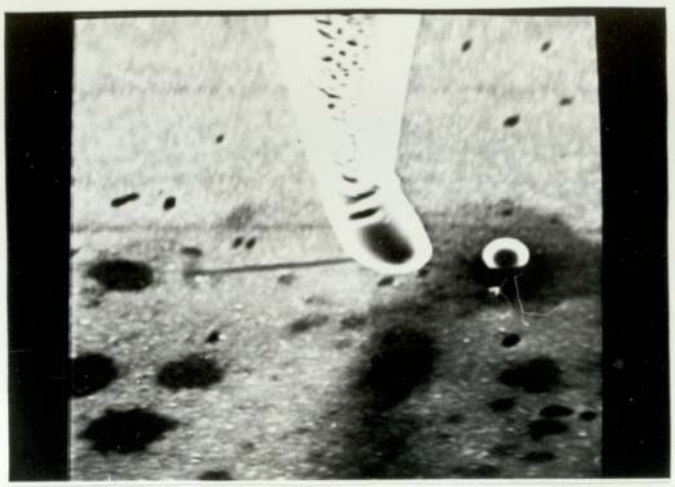

(a)

(b)

Figure 4.20: Mechanical microprobe data; (a) before movement of the microsphere, (b) impact site

Figure 4.20 shows the tungsten tip and the particle before and after mechanical movement of the microsphere in a case where impact damage is visible. The most noticeable effect is seen on the aluminium surface, where the size of the impact site is of the order of the contact area. Damage may, however, be occuring in the other particle/target combinations but the actual indentation arising from the impact event may be too small to resolve in the S.E.M.

As further evidence of the affect the microsphere charge has on the impact process, it has been observed that impact damage on a titanium 318 target is observed when type E carbonyl iron powder is used, while no damage occurs for the type H powder. Since the particle size distribution is larger for the E type powder, than for the H type, it can be expected that in the former case, significantly larger charged particles are involved in the impact process. It should also be mentioned that once the microprobe and particle came into contact, adhesion processes dominate and the particle "sticks" to the tungsten tip; when this occurs the only way of removing the particle is to apply a field between the tip and target.

4.5.2 Electrical data

As in the mechanical data section, the same microsphere/target combinations are used. The microprobe tip is positioned a known distance (usually 20 μm) above the adhering microsphere, using the technique described in Section 3.7.1, and the current/voltage characteristics recorded as the high voltage is increased. Typically, as the voltage was raised the current would increase slowly until suddenly a large "current jump" would occur and thereafter, it would rise more slowly to an ultimate level of $\sim 10^{-7}$A (determined by the external safety resistor). A slow reduction in voltage caused the current to remain at a high value until it would suddenly

"switch" off, i.e., giving a hysterisis effect. On subsequently viewing the target/microprobe system, it was invariably found that (i) the microsphere was missing, (ii) crater formation was visible on the target surface and (iii) the microprobe tip was damaged. The most probable cause of these effects is either sharp lipped craters, resulting from the microsphere leaving the target surface and giving rise to field electron emission sites which cause a "breakdown" of the microprobe/target gap, or more probably, an "ignition"process associated with the poor vacuum pressure of the S.E.M. which again causes a similar breakdown of the microprobe/target gap. Typical microprobe/microsphere/target photographs, before and after the application of the high field, are shown in Figures 4.21(a) and (b) for the particle/target combination of carbonyl iron/stainless steel. In Figure 4.21(b) the surface damage is clearly evident. However, not all the microspheres leave the surface under the application of the high field and in these cases Fowler-Nordheim (36) plots can be obtained. Figures 4.22(a) and (b) show typical plots which yield field enhancement (β) factors of $\sim$5 and $\sim$19 respectively, i.e., typical of a hemispherical body on a planar surface. Thus, it is of significance to note that the impact of a microsphere onto a high voltage electrode would be the unlikely cause of electrical breakdown, due to field enhancement, since β factors $\sim$ 200 are usually required.(114,115)

To calculate the force required to remove a microsphere from the target surface, using the equations due to Rhorbach (see Section 3.7.3) requires the microsphere to be in a uniform field. However, it is possible to circumvent this problem by using the "flattening" technique described in Section 3.7.3. Hence it can be assumed that an approximate uniform field exists between the microprobe tip and target. The procedure adopted to find the voltage at which a microsphere is repelled from the target surface at a given microprobe/target gap, involves progressively raising the voltage in 100 V increments while at the same time monitoring the

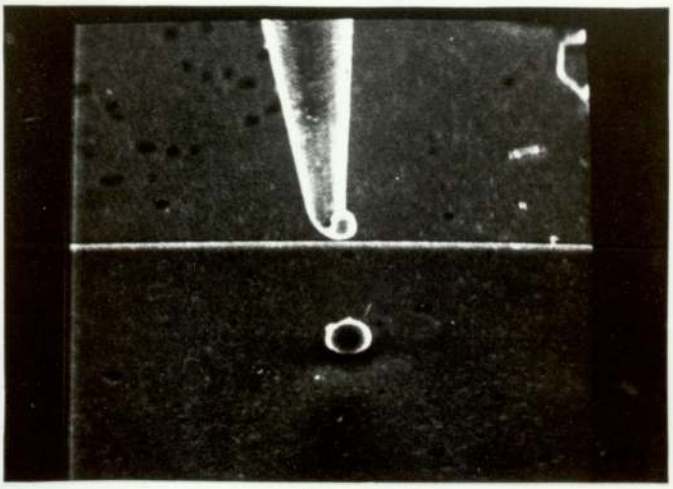

10μm

(a)

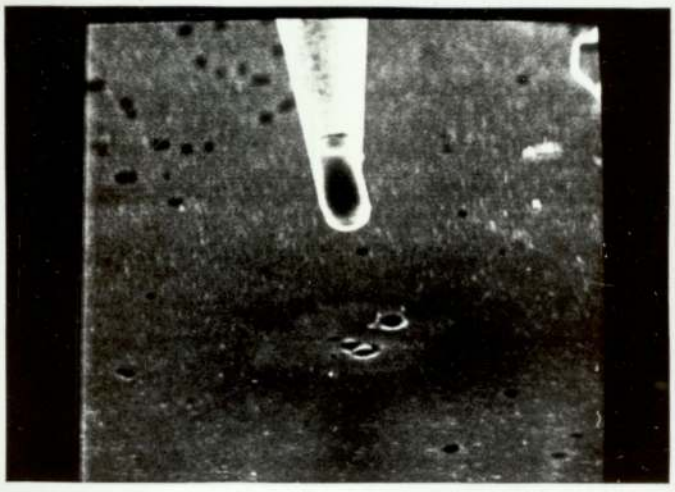

10μm

(b)

Figure 4.21 : Electrical microprobe data;
(a) microprobe and particle before the application of the electric field,
(b) after applying the field

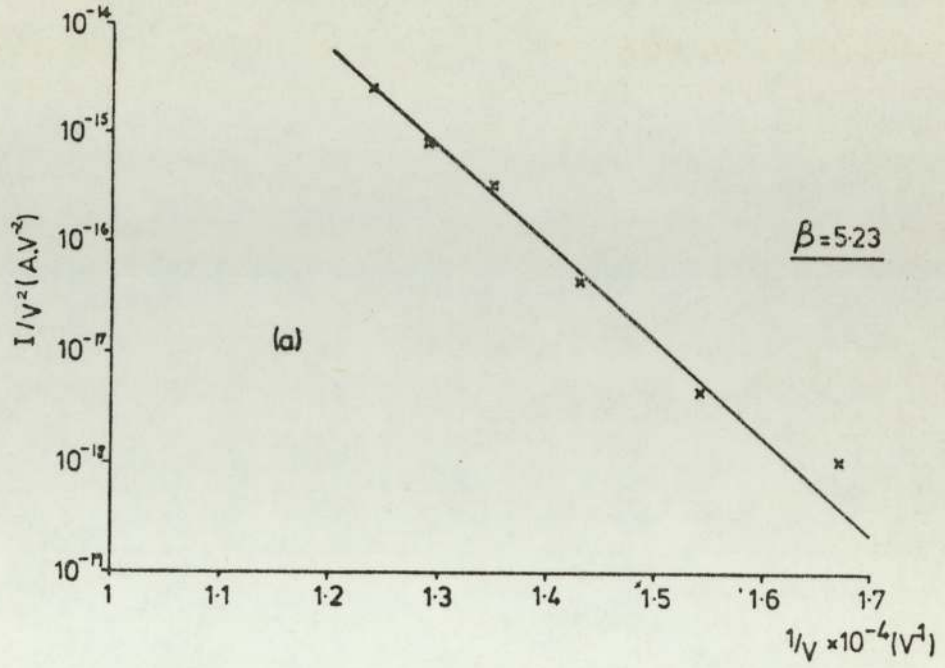

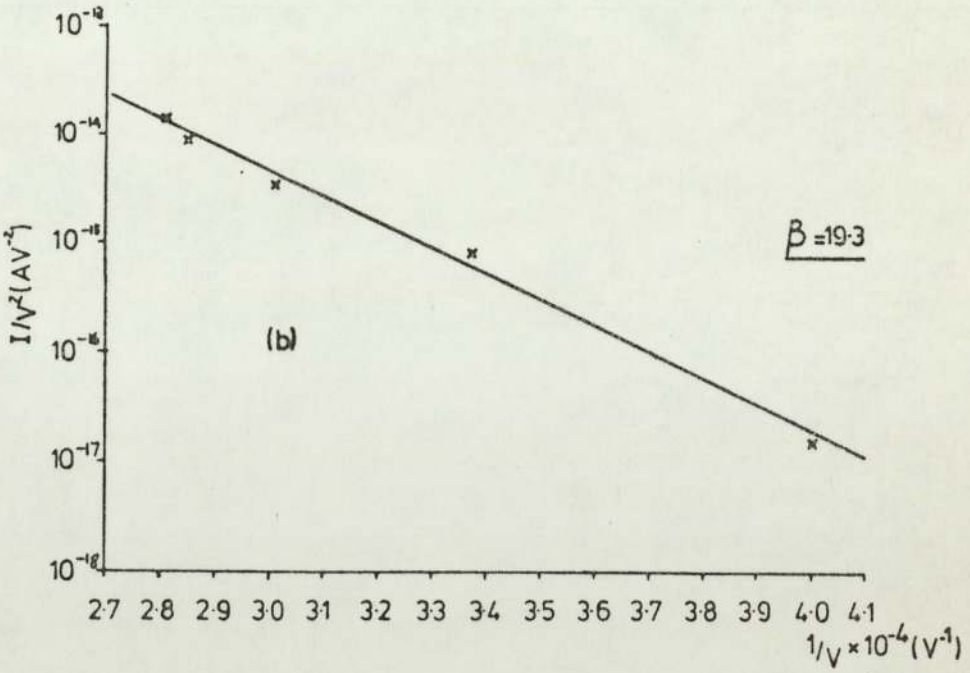

Figure 4.22a-b: Fowler-Nordheim plots for a microsphere on a titanium target surface

emission current. When a current is recorded, the voltage is reduced to zero and the target examined to check if the microsphere is still present. In fact it is usually found that as soon as an emission current arises the microsphere will have left the surface. Knowing the applied voltage and the microprobe/target gap, the force required to remove a microsphere from the target surface can be calculated. For microspheres which do not leave the target surface, the microprobe/target gap is reduced and the same process repeated. Table 4.8 shows the calculated repulsive

Impact experiment	Electrostatic repulsive force $N \times 10^{-6}$
1	6·95
2	6·95
3	33·6
4	6·95
Control experiment	
1	10
2	17·9
3	17·9
4	17·9
5	28·1

Table 4.8: Microprobe repulsive force data

force for the carbonyl iron microsphere (type E)/titanium (318) combination. As a check on the calculated values, a control experiment was performed using carbonyl iron microspheres (Type E) "sprinkled" onto a titanium 318 surface, since this allows the adhesive force for a particle resting on the target to be calculated, see Table 4.8. It can be seen that all the values are of the same order of magnitude indicating that the force holding the microsphere on the target surface after an impact event is mainly due to adhesion.

There are, however, a finite number of events where the microsphere remains on the surface after reducing the gap and re-applying the voltage. In these cases the microsphere was removed mechanically and it was usually found that an impact site existed below the microsphere where for the same microsphere/target combination no visible impact site occured when the microsphere was removed by the mechanical process outlined in Section 3.7.2. This points to the fact that the impact indentation may be caused by some form of electrical/charge exchange process.

4.6 Contact time measurements

It is an obvious prerequisite for measuring the contact time, that a microsphere must undergo a "bouncing" event on impact. Accordingly, the data already presented in section 4.2 indicates that only insulating or highly oxidised metal surfaces can be used. Data has thus been restricted to measuring the contact time of carbonyl iron (Type E) microspheres with a glass surface. As a preliminary exercise to get some idea of the time involved, we can substitute the physical parameters of this system into equation 2.8 which subsequently gives a theoretical value for the contact time of 9×10^{-9} s. However, an important point to remember is that this calculation is based on an asumption that the impact takes place on a flat surface whereas experimentally this is not always the case. The anticipated ideal schematic pulse shapes for the output waveforms, when a voltage sensitive amplifier or a charge sensitive amplifier are used to measure the contact time, are shown in Figure 4.23. The voltage amplifier ultimately used was based around a high slew rate/large bandwith F.E.T integrated circuit, the LH 0032CG , which is used in the non-inverting configuration ,shown in Figure 4.24, while the charge sensitive amplifier is that supplied by Daresbury Laboratories, of which details have already been given. Since high speed storage is required, data cannot be

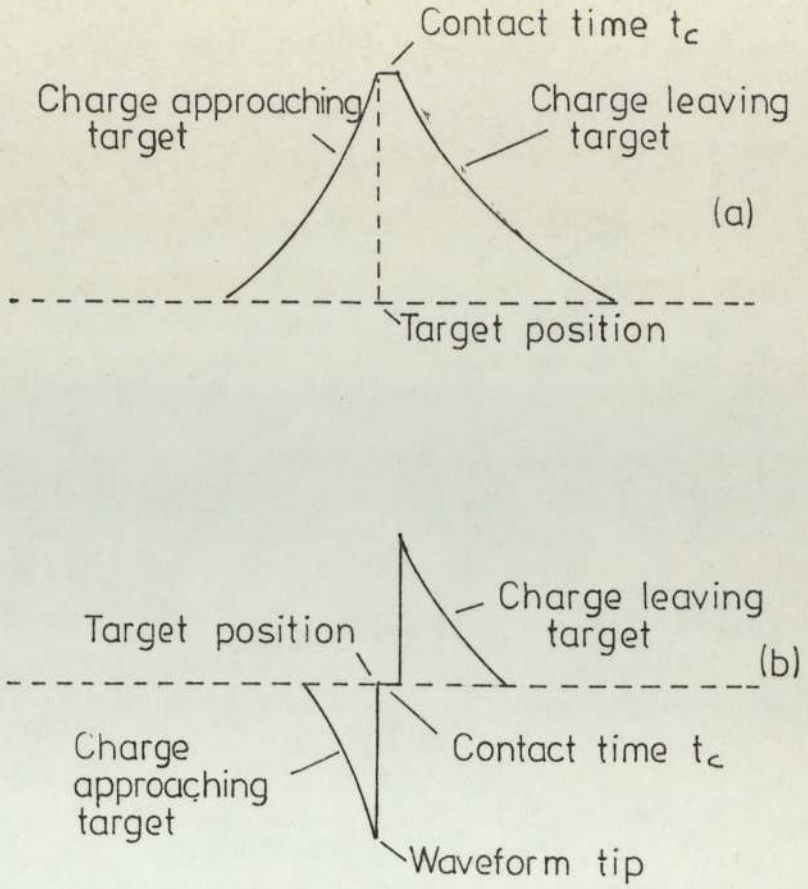

Figure 4.23: Schematic contact time waveforms;
(a) voltage sensitive amplifier;
(b) charge sensitive amplifier.

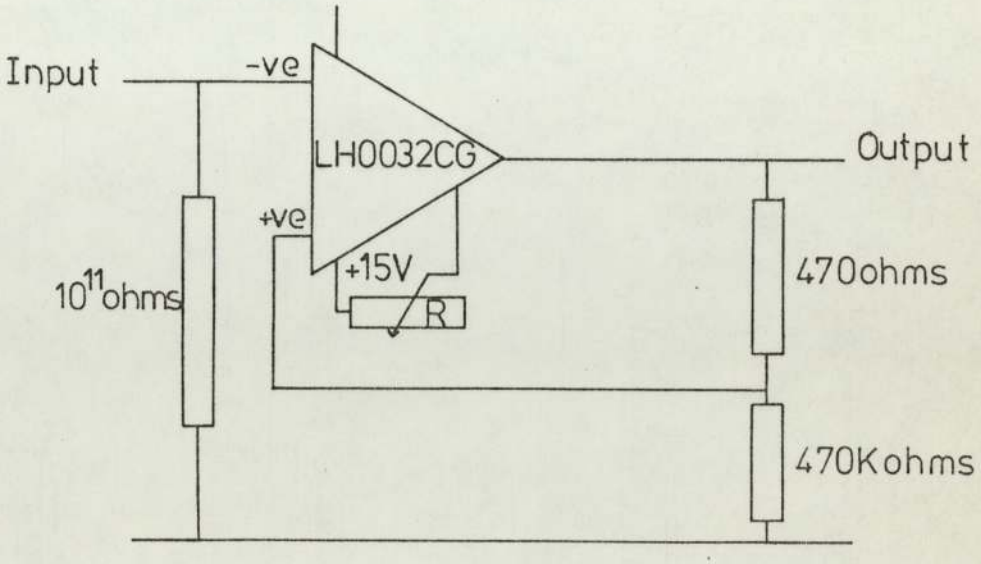

Figure 4.24: Voltage sensitive target amplifier

recorded on the digital storage oscilloscope because its sampling rate for digitisation is too low. Therefore data is recorded on the Hewlett-Packard storage oscilloscope (10 nsec/cm time base speed).

In the event it was observed, for particle impact velocities in the range $1 \rightarrow 10\ ms^{-1}$, that neither type of amplifier produced a flat portion indicative of the contact time (see Figure 4.23). Also at the speeds required to detect the contact time, the charge sensitive amplifier only inverts the signal, giving no differentiation of the pulse. Therefore, in this case, the flat region indicating the contact time, would be situated at the tip of the waveform as shown in Figure 4.23 (b). Figure 4.25(a) and (b) are the observed traces for the voltage sensitive amplifier and charge sensitive amplifier respectively. Although no contact time region is evident, it is possible to conclude that the contact time must be less than 5×10^{-7} s, which is in agreement with the theory.

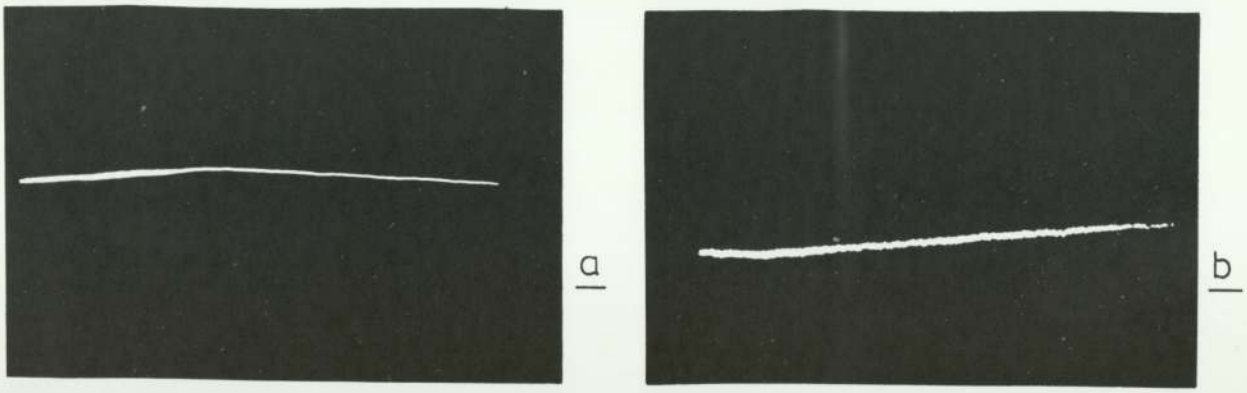

Figure 4.25: Contact time oscillographs; a=voltage sensitive amplifier; b=charge sensitive amplifier

One approach to improve the resolution of this technique would be to increase the contact time. Since equation 2.8 indicates that the

contact time is proportional to the radius of the microsphere, 50 μm diameter carbonyl iron microspheres have been used in the dust source gun. However, little success has been obtained due to their poor charging efficiency.

4.7 Alternative microparticle sources

Extending experiments to the use of alternative microparticle materials has many attractions: for example, the "sticking" or "bouncing" phenomena which are associated with the impact behaviour on many target materials may depend on the type of impacting microparticle. However, attempts at using an insulating dust source, such as alumina (particle radius $\sim$ 1μm) produced only a situation where, although particles emerged from the reservoir (see Section 3.3.2), their charging efficiency was so low that they collected in the high field charging region and did not pass into the experimental chamber. In the case of a semi-conducting powder - such as, silicon, the charging efficiency is far greater than for the insulating powder and the observed particle impact behaviour shows that these particles "stick", on impact, with an ambient oxidised metal target surface, i.e. a similar process to carbonyl iron powder.

It has already been mentioned that the "sticking" process may result from the kinetic energy of the incident particle being converted into heat on impact. The role played by the target in such a process has been investigated using tungsten (see Section 4.2.2). However, the carbonyl iron microsphere may undergo softening (116) and melting in the impact event. To determine this effect chromium powder has been used in the microparticle gun. Since the oxide on chromium has a far higher melting point than the oxide on carbonyl iron (i.e. Cr_2O_3 2538K and Fe_2O_3 1730 K) the impacting particle may not melt and thus "bouncing" will be more likely. However, tests showed that "bouncing" events using these particles were still absent on ambient oxide metal surfaces.

4.8 High field measurements

By using the charge sensitive amplifier, which allows the impact particle charge to be measured in the presence of a high field, measurements were performed on a commercially polished titanium target under high field conditions. The high voltage isolation of this amplifier is ± 2KV (see Figure 3.12) therefore data, at higher voltages can only be obtained by removing the amplifier and recording the incident and reflected particle charges using the drift-tube detector. However, to allow the high voltage range of the amplifier to be used fully, the gun voltages were set at V_1 =+1.3 KV and V_2 = -1.9 KV.

4.8.1 High field charge reversal behaviour

Referring to Figure 3.6, for $V_T \leqslant 0$ microspheres will be attracted towards the target and impact will occur following acceleration across the gap. On impact there is a possibility of charge reversal and consequently the microsphere will be re-accelerated across the gap. The bouncing behaviour depends on the microscopic conditions at the point of impact and this has been shown to give rise to a large spread in the charge reversal measurements. To overcome this, it was found necessary to use some form of averaging, whereby each point plotted is the average of 10 events under constant field conditions. Figure 4.26 shows the charge reversal results obtained, for the titanium 318 surface. From this it is observed that the (q_2/q_1) ratio increases as the macroscopic field increases, i.e., the charge reversal efficiency increases as the applied voltage increases. However, it has also been shown previously, that titanium exhibits charge reversal behaviour even under zero field conditions, suggesting that the efficiency of the process might not just depend on the response to the applied field E, but also on some intrinsic contribution arising from the work function differences between the interacting surfaces. Oscillographs indicating the charge reversal behaviour for a

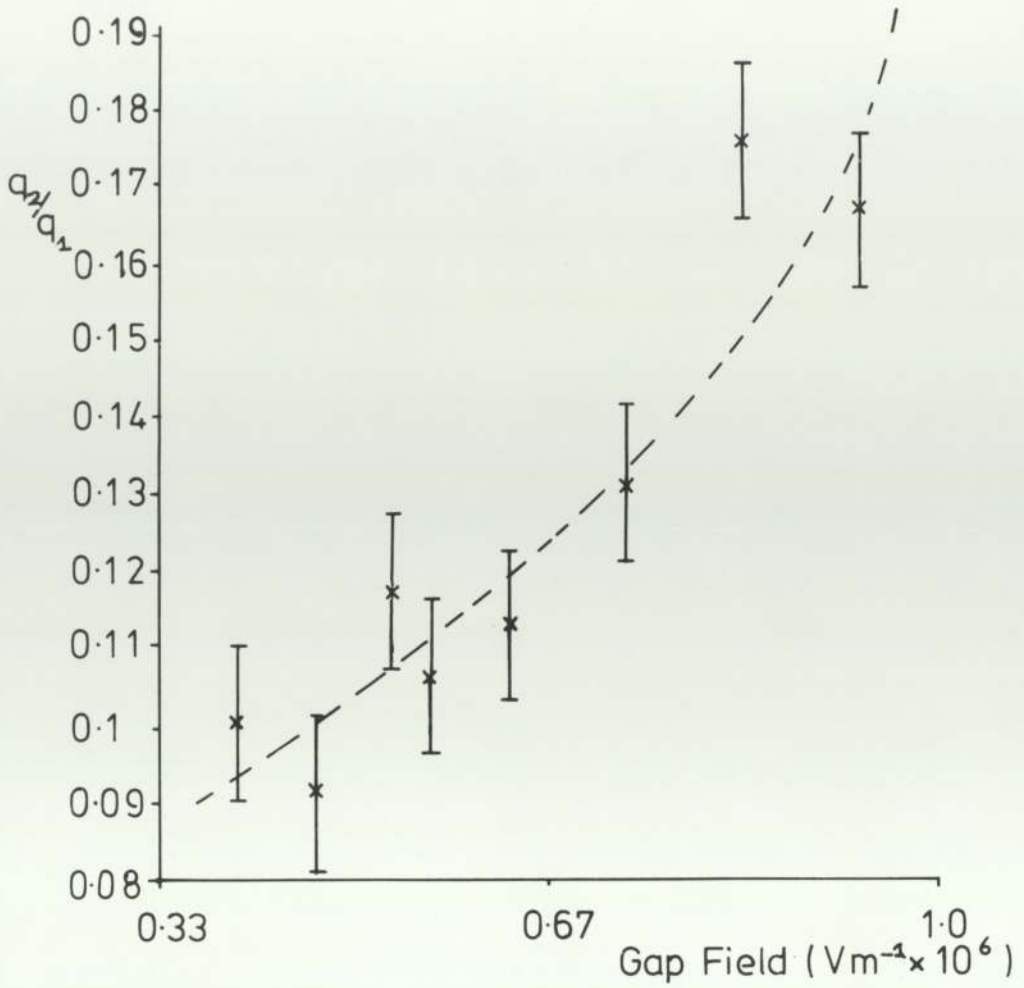

Figure 4.26: Charge modification ratio (q_2/q_1) versus the gap field

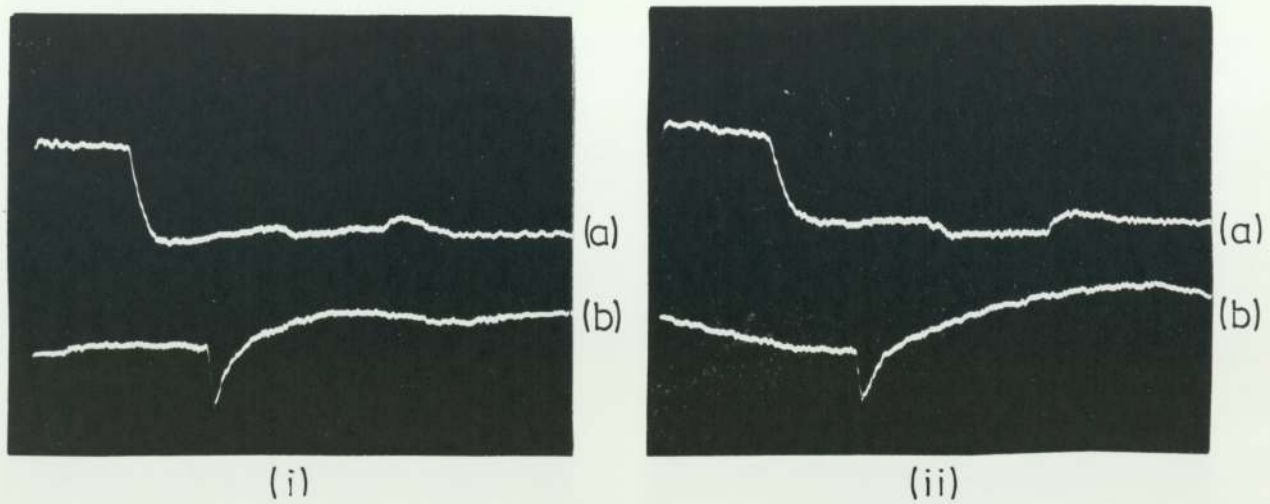

Figure 4.27: Charge reversal oscillographs; (a)=drift tube trace (sen 0·02V/Div); (b)= target trace (sen 0·005V/Div); time base 1ms/Div; (i)=gap field $4{\cdot}7 \times 10^5 Vm^{-1}$; (ii)=gap field $5{\cdot}7 \times 10^5 Vm^{-1}$

test gap of 3 mm can be seen in Figure 4.27 which shows that the charge reversal efficiency increases with the applied field. Using this same charge amplifier the charge 'dumped' on the target in presence of the electric field can be determined. Results on titanium indicate that the conservation of charge is obeyed, i.e. the charge on the microsphere before impact is equal to the charge 'dumped' on the target minus the charge carried by the reflected microsphere.

4.8.2 High field charge repulsion behaviour

For target voltages in the range $0 < V_T \ll V_1$, the positively charged microsphere experiences a repulsive force as it enters the 3 mm gap. However, at low fields ($3 \times 10^{+4} \rightarrow 6 \times 10^{+4}$ Vm^{-1}) contact will still occur and possibly involve charge reversal due to the contact potential difference arising from the differing work function of the colliding materials. For $V_T > V_1$ a microsphere will be repelled by the target and brought to rest before impact, and in consequence there will be complete in-flight momentum reversal. Conversation of energy considerations would indicate that when the gap voltage reaches the 1.3 KV gun voltage, repulsion of all the microspheres should occur. In practice, however, repulsion is apparently found to start for some microspheres at a gap voltage of + 1.2 KV, whilst complete repulsion of all the incident microspheres does not occur even at voltages of + 1.8 KV across the test gap. The percentage of positive charge reversals as a function of the test gap voltage is shown in Table 4.9. It should be noted that gap voltages greater than + 1.8 KV could not be used due to amplifier noise. This arises from random charge generation caused by mechanical vibration of the "test" gap. Figure 4.28 shows the variation of the impact microsphere velocity with the impact microsphere charge as the gap voltage is increased. Each plot shows that low velocity and small charged microspheres appear to "stick" to the target

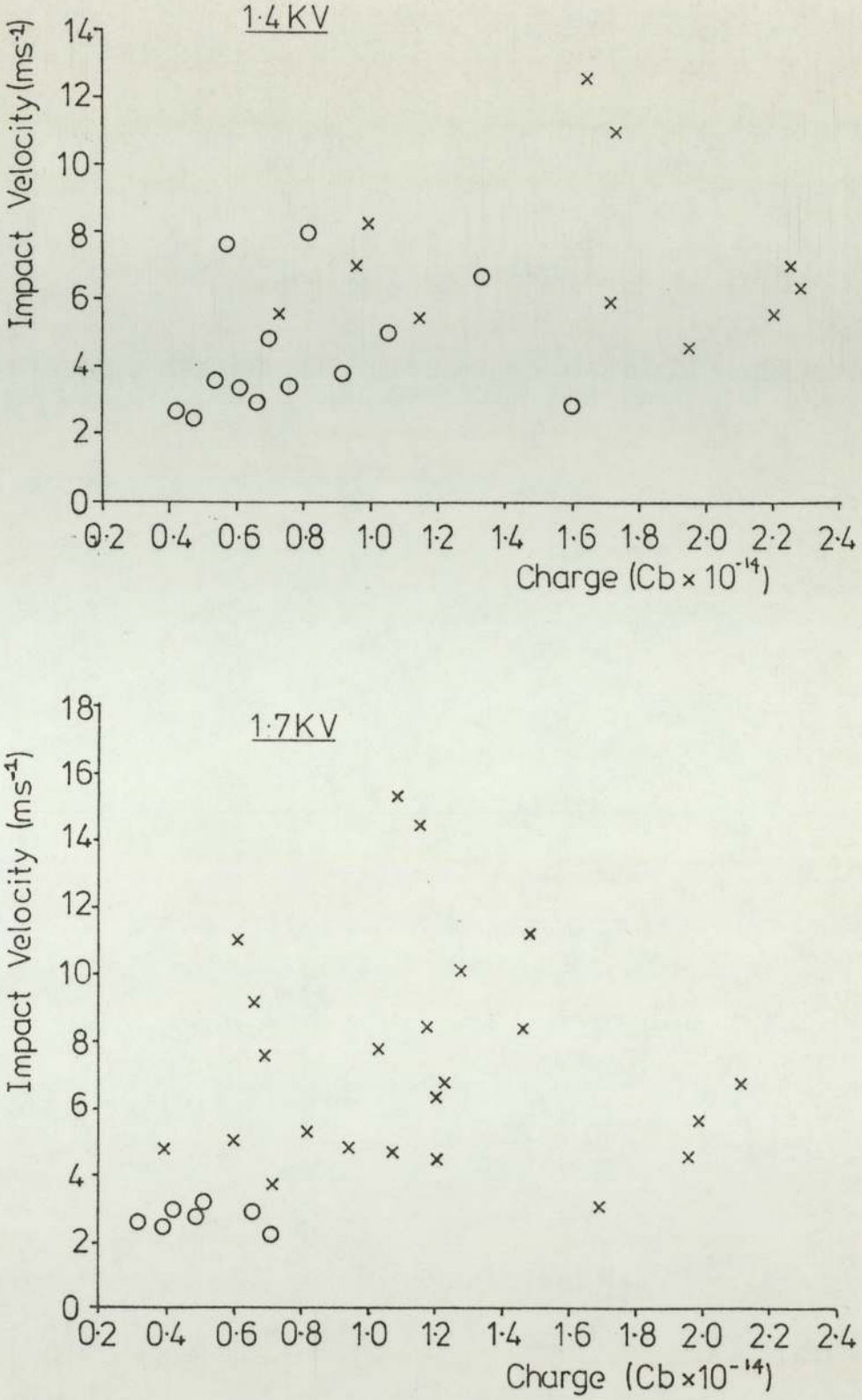

Figure 4.28 : Impact characteristics of the titanium 318 surface at different gap voltages; o="sticking" particles; × = "bouncing" particles

% of positive charge reversals	Gap voltage KV
8	1·2
14	1·3
46	1·4
62	1·5
96	1·6
77	1·7
88	1·8

Table 4.9: Percentage of positive charge reversals as a function of the test gap voltage

surface even when $V_T > V_1$. An explanation can be offered to account for the above phenomena: As the positively charged microsphere passes into the high field zone, conditions are favourable for field electron emission to occur from the earthed grid (see Figure 3.6) to the microsphere, a process that has been originally considered by Hurley et al (117). This would subsequently lead to a reduced microsphere charge and hence the repulsive force generated by the high field would be insufficient to stop the microsphere impacting on the target surface. It is important to note that this type of process only occurs in a high field gap situation.

CHAPTER 5

5.0 DISCUSSION OF EXPERIMENTAL FINDINGS

5.1 Introduction

The theories outlined in Chapter 2 will be called upon extensively in this section to account for the mechanical and electrical behaviour observed throughout the simulated impact studies and the microprobe manipulation experiments. However, it is of interest, initially, to comment on the improved spatial resolution of the new vertical microparticle facility with reference to the impact measurements obtained from the 5 test impact sites on an ambient oxide aluminium surface, described in Section 4.2.1. This new and more refined technique indicates that the scatter in the 'e' values, as shown by the standard deviations in Table 4.1, associated with the individual bouncing events within a given $(200\ \mu m)^2$ impact zone is much smaller than has been previously obtained when results were averaged over $\sim 1\,cm^2$. This observation suggests that the mechanical properties of a surface do not change appreciably within a 200 μm range. In contrast, however, the electrical response, as measured by the q_2/q_1 values, still show a large scatter - thus indicating that the microscopic electrical properties of the surface that determine the change exchange process, (e.g. substrate work function, oxide thickness and species), have to be defined on the micron scale. Therefore it is of interest to discuss the microscopic mechanical and electrical phenomena that can give rise to the scatter in the data. Finally, the importance of both the electrical and mechanical conditions will be considered in a high voltage gap situation. As with previous chapters the mechanical and electrical aspects of the particle impact will be considered separately.

5.2 Interpretation of the mechanical results

From the experimental results outlined in Chpater 4, it is apparent that two different types of impact process have been encountered, i.e., "sticking" and "bouncing". For all the ambient oxide metal surfaces, except aluminium, microspheres appear to "stick" to the target surface on impact while for highly oxidised metal surfaces and insulators the "bouncing" process is clearly evident. Whilst the mechanical data obtained from these bouncing impacts is generally in agreement with the macroscopic experiments performed by many authors, there are, however, two important differences between the micro and macro systems, viz., (i) that in this study the critical velocity for a microsphere impact is $\sim 250\ ms^{-1}$, while in a macroscopic system, it is only $0.1\ ms^{-1}$, and (ii) the large amount of scatter in the recorded data, can in some cases be as much as 50%, while in a typical macroscopic experiment the scatter is < 10% (29). These observations point to the importance of defining the differences between the micro and macro systems, and in particular isolating those microscopic properties of the electrode surface which, not only give rise to the scatter in the 'e' values, but are also responsible for the "sticking" process observed in the impact between many microsphere/target combinations.

5.2.1 Surface topography

It is apparent that not even the finest polished surface is completely flat, thus in a microsphere/target contact process, the size of the target features are important in determining the 'real area' of contact. A target polished to a $\frac{1}{4}$ um diamond finish typically possesses many irregular features of which polishing grooves,

of the order of 0.1 μm, together with contaminant material from the polishing medium are probably the most dominant. The polishing process may also give rise to a Bielby layer (118) which possesses a different structure to that of the underlying solid material. Bowden and Tabor (119) have noted that these changes in surface structure are detectable to a depth of many particle radii. In practice it is found, for example, that there are regions where 'work hardening' (see Section 5.2.4) has occurred while other regions possess an overlayed structure.

The presence of surface roughness can also determine the type of contact by refining the size of the adhesive forces. Thus it has been recognised by Whitehouse et al (120) and Greenwood et al (121), for example, that asperity deformation in surface contacts can be elastic but more usually plastic in nature, while Pollock (122) has produced calculations which show that the attractive force between a small asperity and a flat surface can be large enough to produce plastic deformation. Therefore it is reasonable to assume that the surface microtopography may well play a major role in the "sticking" behaviour observed between a microsphere and an ambient oxide surface. Equally an impact onto a sharp edge, asperity or polishing groove may well raise the contact pressure at the point of impact that plastic deformation may develop and hence lead to increased adhesive forces so giving rise to a "sticking" process. In a "bouncing" event, such as that which occurs between a carbonyl iron microsphere and an ambient oxide aluminium or highly oxidised metal surface, a reduction in the e-value of $\sim 60\%$ can occur in a multipoint impact, shown in Figure 5.1. On the other hand for the impact in a valley or groove, in which equipartition of energy occurs, a change in the value

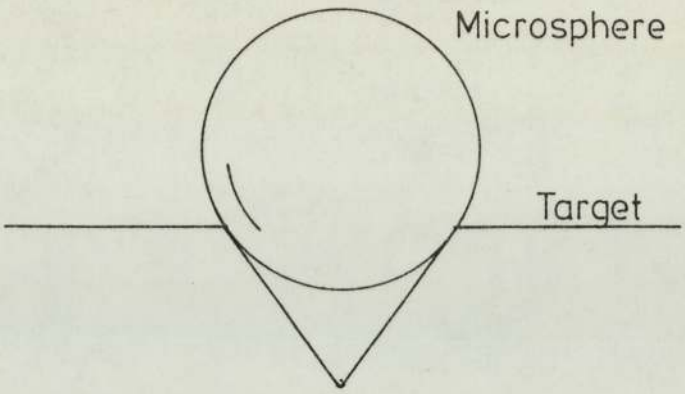

Figure 5.1: Microsphere impact regime

of the coefficient of restitution from e to e/ $\sqrt{2}$ can arise (123) In this context, it has been observed by Latham et al that, in many cases of microsphere impact, "stuck" microspheres are found to be concentrated along surface features such as scratch grooves (26). Since, in many cases, no bouncing occurs in an impact event between a microsphere and an ambient oxided metal target surface, it is not possible to determine, in detail, the effect played by the surface topography since no e-value can be determined. However, the surface topography is found to be crucial in the microsphere/insulator impact behaviour where all of the insulating materials investigated promote bouncing. In particular for the harder materials such as glass, the distribution of 'e' values is far sharper than for softer materials, such as P.V.C., as indicated in Figure 4.10. In this latter case many of the reflected particles were observed to leave the surface at non-normal angles and this was thought to be due mainly to the surface roughness. On impact, it is possible for multi-impact events to occur, (shown schematically in Figure 5.2), in a similar manner as that occurring in the impact on a metal surface. Thus many particles leaving the surface do not pass through the drift tube but escape

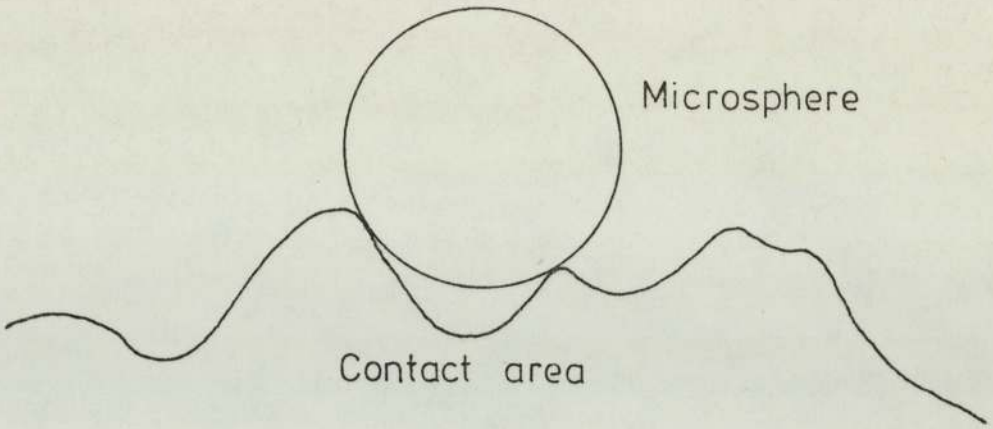

Figure 5.2: Microsphere impact onto an insulator surface

into the vacuum system - this type of event is indicated by the exponential decay of charge shown in Figure 4.18 (iv).

To investigate the effect of the surface topography, each insulator target specimen had it surface roughness measured using a "Talysurf" profilometer where Figures 5.3 (i),(ii) and (iii) show the profiles obtained for glass, p.v.c. and red-fibre. Both the p.v.c. and red-fibre profiles indicate a general trend for the thickness of the sample to vary across the surface, however, for the red-fibre, within a $(200\mu m)^2$ analysing area (the accuracy of the present vertical microparticle facility) the variation in thickness is $\sim 10\mu m$. In the case of the glass, the surface is remarkably flat. It should also be mentioned that the surface profile is taken across only one region of the specimen containing the contact area. To analyse a profilometer trace a procedure is followed that involves dividing each 0.1 μm zone, see Figure 5.3, into 10 parts to give a 10μm resolution across the surface. Then recalling that the vertical sensitivity is 2 μm per division (for the red-fibre sample), it is possible to compute the surface angle with reference to the planar surface conditions. For

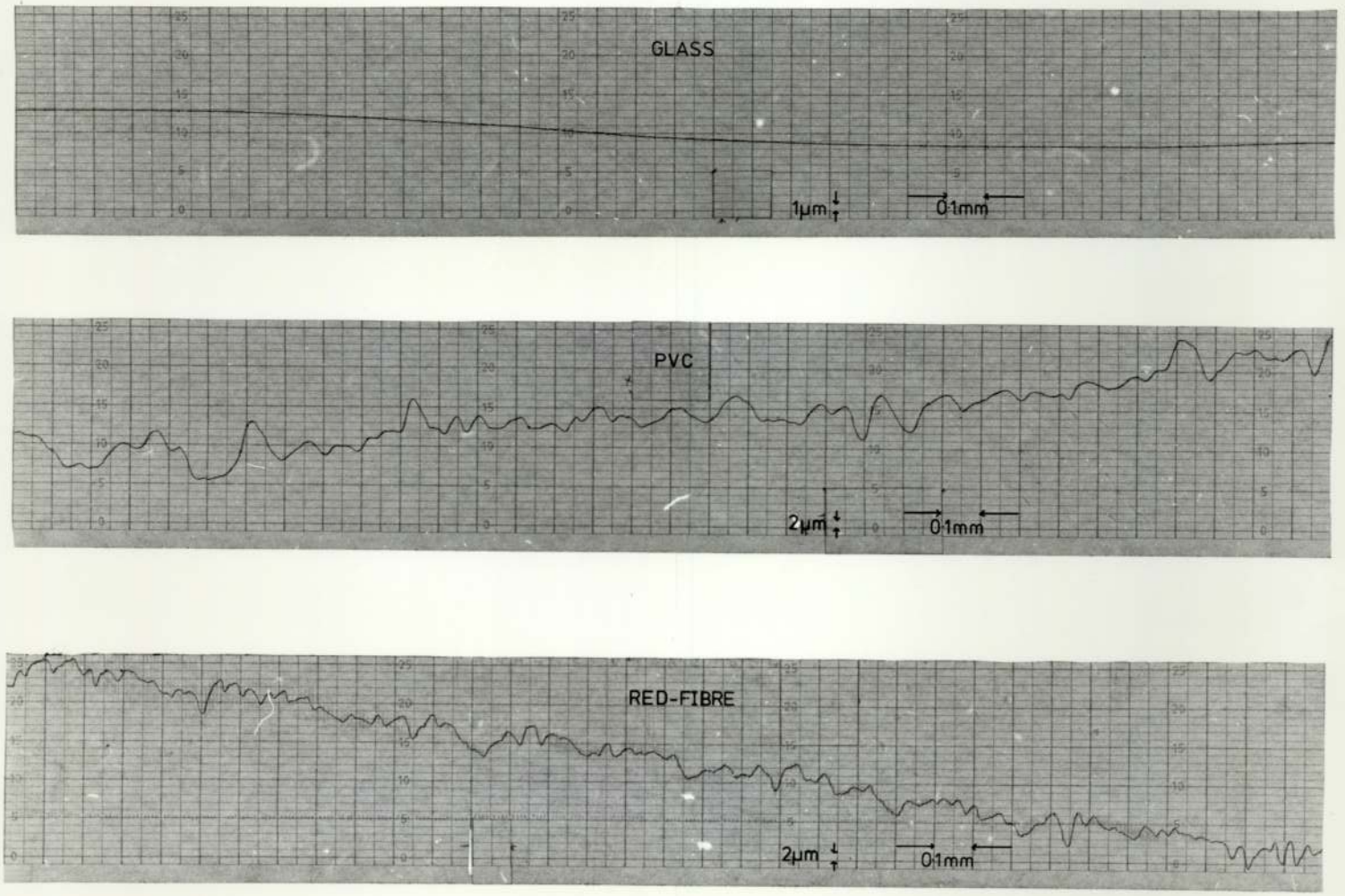

Figure 5.3: Surface roughness profiles for (i) Glass, (ii) PVC, (iii) Red-fibre

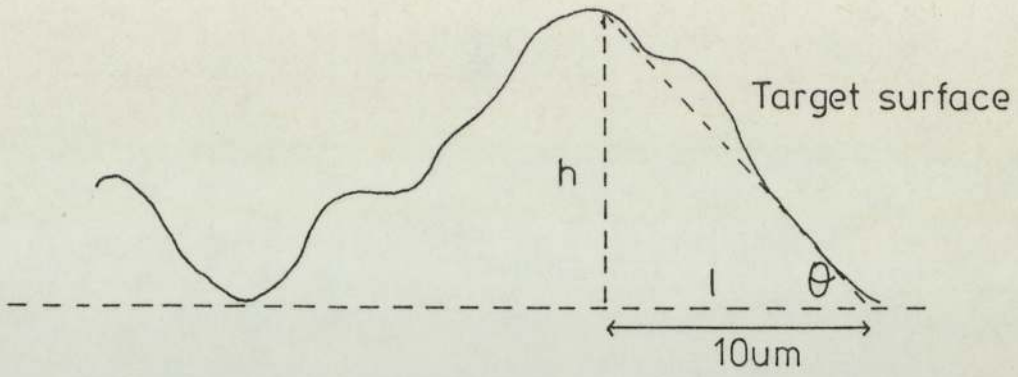

Figure 5.4: Surface angle measurement

example, with reference to Figure 5.4, if h is the height of the surface feature and l the length (10 μm), then tan θ = $\frac{h}{l}$ where θ is the surface angle measured from the planar surface. This process has been performed for ~300 samples on the red-fibre surface, and from the θ values obtained a histrogram has been plotted as shown in Figure 5.5. Although the distribution is not smooth, due to an averaging process for h and l, the general shape is significant. It is seen that the peaks in the distribution occur between 4 and 6 degrees and the maximum surface angle lies at ~30°; there is also a significant distribution of angles in the 0° → 2° range indicating a relatively flat surface. Assuming, therefore, that this distribution is typical of the impact zone the anticipated variation in the 'e' value for this surface is thus calculated to be from the true value e to 0.50e as θ varies from 0° to 30°. Thus the red-fibre histogram would tend to be shifted to a higher value, with the lower e-values being shifted by a larger amount since these correspond to large oblique angle reflections. Mathematically the envelope of the surface angle distribution can be described by the function

$$A \cdot \frac{1 + x^2}{e^{x/2}}$$ where A is a constant,

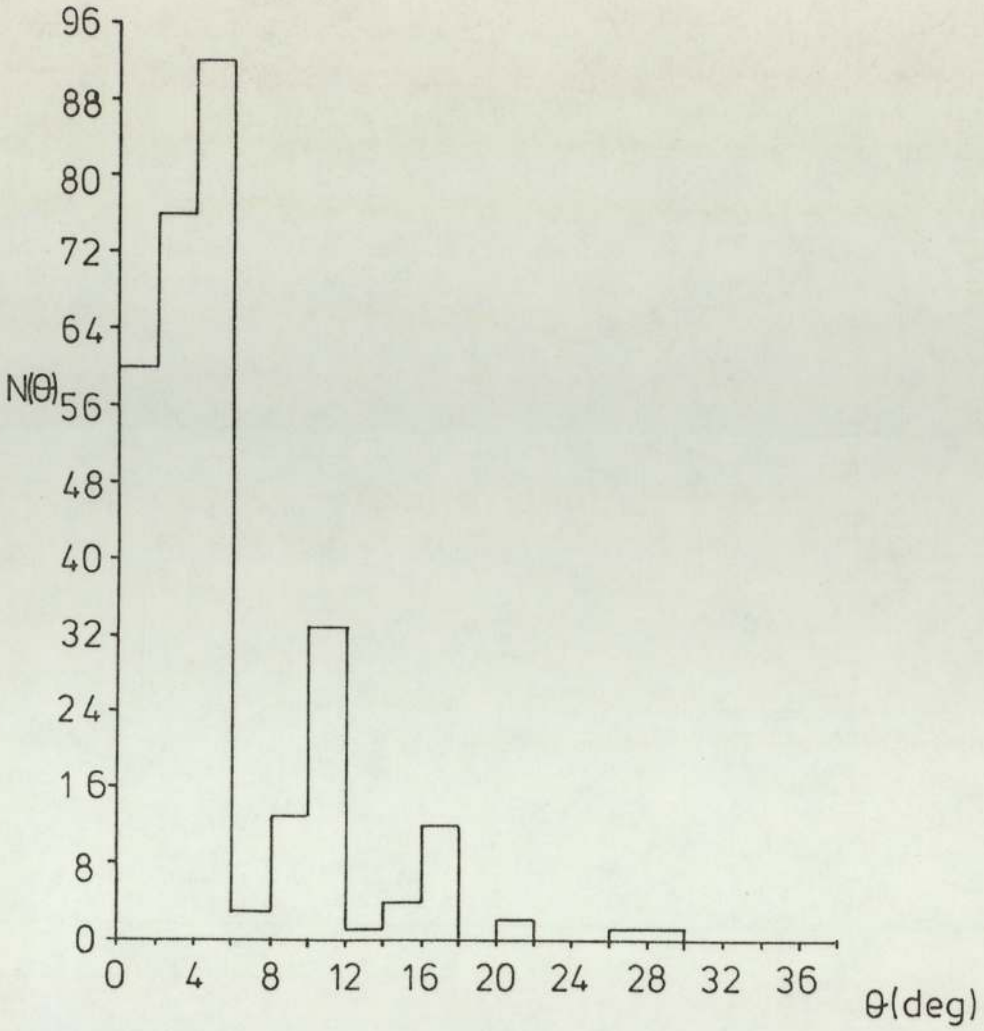

Figure 5.5: Surface angle distribution (θ) for red-fibre

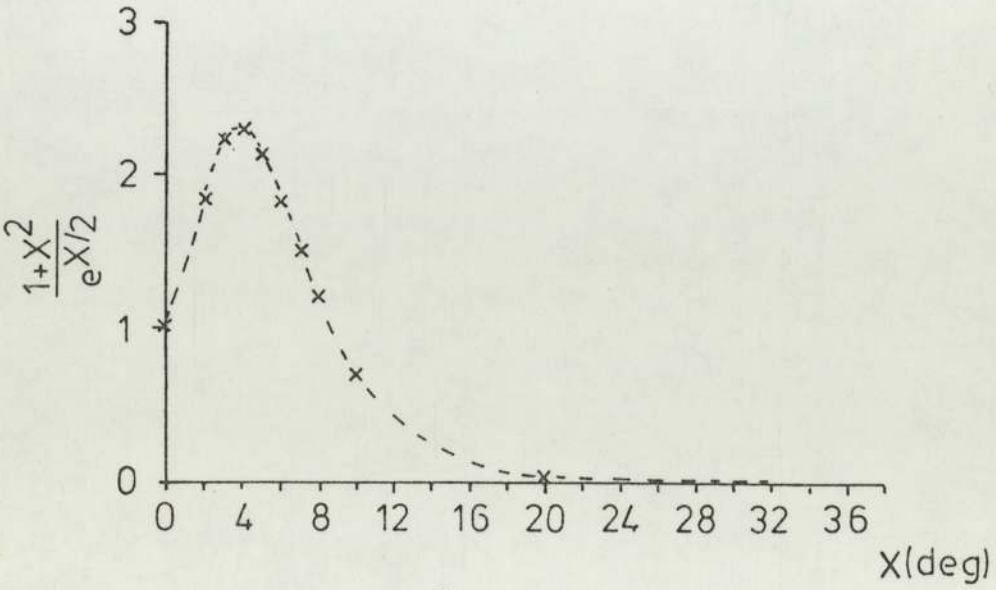

Figure 5.6: $\frac{1+X^2}{e^{X/2}}$ as a function of X

Figure 5.6 shows this function with A normalised to 1. Although the other surfaces could have been similarly analysed, time did not allow such a process to be carried out.

5.2.2 Strain rate effects and hardness

It is known that full plasticity occurs in conventional hardness testing measurements and arises when the mean contact pressure is $\sim 3Y$, where Y is the macroscopic yield stress (19). For comparison Hutchings(13) has derived an expression for the mean contact pressure developed during a microscopic elastic impact (see Section 2.1.1) which for the case of a 2μm radius carbonyl iron microsphere impacting on a stainless steel target, at an impact velocity of 10 ms^{-1}, gives the mean elastic contact pressure P_e as $5.875 \times 10^{9} Nm^{-2}$. Although this value is less than the critical pressure (P_c) required for plastic impact, viz, $2.13 \times 10^{10} Nm^{-2}$, corresponding to an impact velocity of 250 ms^{-1}, it is nevertheless greater than the mean contact pressure for plastic flow obtained from conventional macroscopic hardness testing measurements. Therefore it is important to discuss the various reasons for this discrepancy in values and to ascertain what role hardness and strain rate play in the impact process.

In a normal static hardness test, an indentor is pressed into the material under investigation until an indentation forms. The hardness of the surface is then calculated by dividing the load on the indentor by the indentation area (so obtaining the Meyer hardness value). If H is the hardness and Y the uniaxial flow stress then :

$$H = KY \qquad \ldots 5.1$$

where K is a constant related to the indentor geometry. For an elastic process, which allows the material under test to return to its original shape once the load is removed, K$\ll$ 3. This type of test has been used more recently by Johnson et al (83), Pollock et al (88), and Pollock (123) in relation to the adhesion effects between a micro indentor and a surface. However, in a dynamic macroscopic situation the Shore solerscope is normally used. This involves dropping a standard sphere from a known height onto an anvil of the material and by measuring the rebound height, the coefficient of restitution can be calculated for the surfaces. It is known that hard materials suffer less deformation and hence promote a high recovery of energy from the elastic stresses. This behaviour is clearly seen from the histograms of Figure 4.10, for the microscopic impact of carbonyl iron microspheres with insulating surfaces. In contrast to the static hardness testing measurements where the time to form the indentation can vary from several seconds to several hours, the opposite situation occurs in the dynamic test where materials are subjected to high loads for a very short period of time - hence high strain rates. Both Tabor (19) and Davies (17), using 5 - 10 mm radius hardened steel spheres, and Davis and Hunter (124) with conical indentors, have studied the effect of dynamic hardness at strain rates of $\sim 10^2$ s^{-1} on metals and alloys. Tabor (15) has found that the dynamic hardness (H) is a function of the incident and reflected particle velocity such that

$$H^{*} = \frac{\frac{1}{2}m\,(u^2 - \frac{3}{8}\,v^2)}{V_a} \qquad \ldots 5.2$$

where m is the mass of the indentor, u and v are the impact and reflected particle velocities respectively and V_a is the volume of the indentation, which is given by :

* This is also the definition of the mean inelastic pressure, P ie P=H

$$V_a = \pi D^2 . (R_p - D/3) \quad \ldots 5.3$$

Here $D = R_p - (R_p^2 - a^2)^{\frac{1}{2}}$ where R_p is the radius of the sphere and 'a' the contact radius. Although equation 5.2 has been derived for a macroscopic system it can equally be applied to the "bouncing" events of this study, observed with many of the microsphere/target combinations*. Thus comparing, again, the glass and the p.v.c. surfaces; in the latter case the indentation produced on impact is likely to be far larger than in the former case hence the p.v.c.surface would possess a lower dynamic hardness value than the glass surface. Dynamic hardnesss effects have been studied by Chaudhri and Brophy (125) on fused silica and by Chaudhri et al (29) at strain rates of $\sim 5 \times 10^5 s^{-1}$, on NaCl, LiF and MgO crystals. These latter authors found that the dynamic hardness increased with strain rate with the most marked effect being observed with MgO. Moreover, plastic identation, and even cleavage cracking, occurred with the impact of WC and glass spheres (0.27 — 1 mm in diameter) on targets of the above materials at impact velocities of 75 — 250 ms^{-1}. In all of the experiments a large percentage of the particles were observed to bounce, which is in contrast to the behaviour observed with many ambient oxided metal surfaces used in this study; however such events displayed a large loss of energy, up to 95%, in the impact process. This effect has been reported by other investigators and is demonstrated by the histograms in Chapter 4. The strain rate effects associated with the dynamic impact process were found to be much greater than those expected from quasi-static strain hardening measurements. Notably, most of the observations in crack growth could be explained by Chaudhri et al in terms of dislocation densities and the imposed stresses, while it was observed that the stress effects were evident both during loading and unloading, such that crack formation

* Dynamic hardness > Static hardness, since the pressure resisting indentation is greater than that occuring in a similar indentation under static conditions (19)

continued as the particle was in the process of leaving the surface.

In the case of a carbonyl iron microsphere impacting onto a stainless steel target, the contact time calculated from equation 2.8, is found to be $\sim 9 \times 10^{-9}$s and the corresponding strain rate $\sim 2 \times 10^{6} s^{-1}$, (see Section 2.1.1.) which is larger than that considered by Chaudhri et al (29). Therefore the "sticking" phenomena may be due to the high strain rates causing changes in the surface structure and severe compression of the oxide interface (between the particle and target). For microsphere/insulator impact events, a high percentage of the incident particles exhibit bouncing, with the result that 'harder' materials give a higher the 'e' value: however the spread associated with the 'e' values may well be due to different impact sites behaving mechanically different from others at high rates of strain.

Thus although other techniques exist for measuring the mechanical properties of a material under conditions of high rates of strain, the measurement of the dynamic hardness, by particle impacts, provides another useful tool.

5.2.3 Surface films and mechanical strength

In many practical situations, a particle impacts onto a surface possessing a contaminating layer, usually in the form of an oxide, and this may undergo severe deformation leading to plastic flow. Therefore it is important to discuss the role played by such layers and in particular the mechanical strength of the surface oxide film. Pollock et al (88) have observed plastic flow arising from the static micro-indentation study of a platinum- tungsten contact and found rupturing of the contact junction at the weaker of the two metals. Also in a major study, performed by Gane (126), on the

direct measurements of the strength of metals on a sub-micrometric scale, using tungsten and tungsten carbide tips on aluminium and gold surfaces, it was found that when the stress was applied to an external surface, the condition of the surface played a major role in determining the mechanical strength. For the case of a single crystal in contact with a hard metallic surface, the strength that could be sustained was about five times less than the theoretical strength - probably due to the high local stresses in the interfacial region. However, introducing a surface film increased the mechanical strength of the material to its theoretical single crystal value which Gane assumed was due to the surface layer removing most of the stress concentrations. Therefore, for surfaces which do not support a surface oxide it is not surprising that the 'e' values determined by many authors (4,5) are significantly lowered. This surface oxide behaviour is thus more likely to affect micro impacts than macro events*, which is indicated by the dynamic yield pressure (P_y) being larger in a microsphere/planar target impact event than in a corresponding macroscopic event; a fact borne out by the critical impact velocity (v_c)** for macrospheres being $0.1 ms^{-1}$ compared with an equivalent value of $\geq 250\ ms^{-1}$ for microspheres. Latham et al (26) have pointed out that the difference between micro and macro systems might well be caused by the differences in the localised mechanical behaviour of single crystal and polycrystalline targets to impact events. Verification of this assumption for the case of the static indentation measurements over a small contact region ($\sim 1\mu m^2$) by Gane and Cox (127) has shown that the hardness may be 2 to 3 times higher than the macroscopic value.

Shewman (128) has also shown that ductile films deform elastically under the impact of microspheres, whereas brittle films

* In macro impacts plastic deformation may still occur even in the presence of the surface oxide

** see page 189, and refs19, 26

tend to crack, in a similar manner to the LiF MgO and NaCl materials used in the macro experiments of Chaudhri et al (29), equally the metal substrate will tend to flow through the cracks. In addition the type of oxide can influence the adhesive forces (88) arising from the impact. Thus for mechanically hard films, it would be expected that the 'e' values obtained from the bouncing experiments would be higher than for soft materials. For the oxidised surfaces used in this study, i.e., copper, titanium, silicon, molybdenum and tungsten, the corresponding 'e' values are 0.48, 0.53, 0.55, 0.48 and 0.43 respectively, which is in agreement with their surface oxide microhardness values (129); for the oxidised aluminium surface the average 'e' values varied from 0.44 to 0.34 as the oxide was removed, which indicates that a high percentage of the energy is lost on impact. For aluminium, where its surface oxide is Al_2O_3, it should be expected that the 'e' value should be much higher since its oxide has a greater hardness value compared with the other oxides. However mechanically, the formation of the hydroxide on the aluminium surface, due to the presence of water vapour, has been found (130) to cause a reduction in the Youngs modulus for the surface by up to 50%.

5.2.4 Work Hardening

This may be explained by considering a static indentation test involving a sphere being pressed into a planar surface. Initially, the surface deforms elastically, however as the stress increases the elastic limit of the surface may be exceeded and plastic deformation occur. The process continues until the stresses are spread over an area such that the stresses are within the elastic limit of the deformed material. Thus at the end of this process plastic flow has stopped and the elastic properties of the material are again able to support the load; if the load is then removed the surface deforms

elastically . On applying a new load of a value which is equivalent to that removed, the surface deforms again elastically until the load fits the original deformation. If the load is now increased, plastic deformation again occurs, i.e., the elastic limit is exceeded, and there is a further increase in work hardening. It has been pointed out in Section 5.1 that the vertical microparticle facility developed in this study allows the impact area to be reduced to $\sim(200\mu m)^2$; therefore in the "bouncing" events which occur for certain surfaces there is a possibility that several impact events occur at previous impact sites, thus if work-hardening takes place different surface mechanical responses can be envisaged which will give rise to a change in the 'e' value.

5.2.5 Contact area and contact time

An estimation of the contact time and contact area is extremely important in understanding the physical processes operating during an impact event between a microsphere and a target electrode. In fact, once the microsphere is in contact with the plane, the size of the contact area governs the magnitude of the adhesive forces, see Section 5.2.1; equally the contact time determines the charge transfer (9) (to be discussed in a later section). Mcfarlane and Tabor (131) have found that for two solid surfaces to adhere to each other they must be brought together over a large area of real contact without the application of large stress forces, otherwise the elastic properties of the surfaces will tend to reduce the adhesive force when the stress is removed. For softer metals, such as indium, the contact junction is far more ductile, and so is more easily deformed which would thus increase the contact area. For the case of a carbonyl iron microsphere (2μm radius) impacting

on a stainless steel electrode at a velocity of 10 ms^{-1}, the contact time has been calculated to be 9×10^{-9}s, and using the same mechanical parameters, the contact radius 'a' from equation 2.2, is given as 1.54×10^{-7}m. (hence the contact area=7.45×10^{-14} m^2)

Although it has not been possible to make a conclusive experimental measurement of the contact time, it is possible to say that the contact time for a 2 μm radius carbonyl iron microsphere impacting on a glass surface is less than 5×10^{-7}s. Evidence for short contact times is also available from other sources (29,125), but in particular Chaudhri et al (29) have found that in the impact between a glass sphere (270 μm diameter) and a LiF target at an impact velocity of 150 ms^{-1}, the contact time is $\sim 1.2 \times 10^{-6}$, while in another experiment Chaudhri and Walley (132) have obtained values of 1.9×10^{-6}s for 1 mm diameter steel spheres impacting on Borosilicate.

5.2.6 Shock and collision parameters

The hypervelocity study of Smith and Adams (32) indicates that in cases where plasma is produced the ions generally arise from the prcjectile material only. To explain this, Smith et al suggested that two shock waves are produced at the impact contact points, with one wave travelling in the projectile while the other travels in the target. The velocity of the shock waves depend on the mechanical properties of the materials and their angle of contact θ.

When θ is small, the shock waves are attached to the contact points and no shocked material is exposed to the surface, so no plasma is produced. Penetration of the target leads to an increased θ so that a stage can be reached where θ becomes critical, such that the velocity of one of the shock waves becomes greater than that of the contact points. Under these conditions the shock wave detaches itself

from the contact points giving rise to highly shocked material plasma formation. The theory shows that for the particle/target combinations Fe/W or Mo detachment first occurs for the Fe projectile, while for the Fe/Cu or Al combination the target shock wave is the first to become detached.

A somewhat different approach has been adopted by Dietzel et al (39) which involves considering hydrodynamic flow in the hypervelocity regime. Hence a partition of the initial K.E. of the particle occurs on impact giving internal energy (reversible elastic strain energy) and internal heating, and both surfaces become 'shocked'. In the case of Fe/W and Fe/Au, up to 40% of the incident energy is trapped as internal energy and 10% as kinetic energy. However, in a metal-insulator contact only a small amount of internal energy is trapped by the particle. Generally, with increasing impact velocity, an increasing fraction of the internal energy is converted into heat. Dietzel et al, on this basis, have defined shock parameters for the projectile and highlighted the particular importance of the product B/ρ, where B is the shock parameter and ρ the density of the target material. For high B/ρ values, a large amount of energy is lost as heat on impact, thus reducing the amount of energy available for the rebound , and hence the coefficient of restitution. However, in the case of low velocity impact ($\sim 10\ ms^{-1}$) by the microspheres of the present study, where the impact velocity is much less than the critical velocity for an inelastic process ($> 250\ ms^{-1}$), no such behaviour is expected to occur.

In a low velocity collision between a microsphere and a planar target electrode, where the impact velocity is below the

the critical value for inelastic deformation (11), it is to be expected that most of the initial kinetic energy is stored by elastic forces in the target which is subsequently given up to kinetic energy in the rebounding particle. Experiments, however, indicate that this type of situation only arises in microsphere/insulator contacts: in microsphere/metal contacts, it has correspondingly been shown that the majority of the particles stick to the surface. However in both cases energy will be dissipated during the collision as elastic waves within the target material. Expressions relating the percentage of energy lost during collision by elastic waves have been developed by Hunter (23) for a purely elastic collision, and by Hutchins (27) for a plastic impact process - such as would arise in the impact between carbonyl iron microspheres and the insulating materials. Using the expressions outlined in Section 2.1.4 yields a value of< 3% for the impact of a carbonyl iron microsphere onto a stainless steel target, and a value of < 0.5% in the case of a carbonyl iron microsphere impacting onto a p.v.c. surface. Both values agree favourably with those obtained by Chaudhri et al (29) in the impact between W.C. and glass spheres with MgO, NaCl and LiF crystals where <10% of the initial energy was lost as elastic waves and by Hutchings(27), using the 'e' values obtained by Uetz and Gommel (20), for the impact of hard steel spheres on mild steel at $\sim$70 ms^{-1}, where < 3% of the energy was lost as elastic waves. In conclusion therefore, it appears that the change in the coefficient of restitution is likely to be small for any type of impact and to have little effect in the sphere/target impact events.

5.2.7 Angle of erosion

If a microsphere impacts onto a target surface at a non-normal angle, which may arise either from poor target allignment

(see Section 3.3.7) or more probably from the surface topography of the target, surface erosion may occur causing a corresponding reduction in the reflected microsphere velocity. Hence it is important to consider such effects and the conditions which promote such behaviour. In a microscopic study, De Haller (133) has observed two types of erosion occurring at different impact angles: The first showed a flattened and highly deformed surface when the impact angle was large and the second a scratched (less deformed) surface at low impact angles. In a further epxeriment performed by Wellinger the erosion observed was found to depend not only on the impact angle but on the type of target material. Bitter (28) has determined the deformation wear when a microparticle impacts upon a target as

$$W_D = {}^1/_2 \; m \; \frac{(u \sin\alpha - K)^2}{L} \qquad \ldots 5.4$$

where W_D is the deformation wear per unit volume of material lost, m and u are the mass and impact velocity of the impinging particle respectively, α is the impact angle, K is a constant determined from the mechanical constants of the material and L the energy required to remove unit volume of material. The above expression has been tested for cast iron pellets (0.3 mm diameter) impacting onto a glass target where it has been found that erosion only occurs beyond a 20° impingement angle. Similar data has been obtained by Finnie (134) for annealed and unannealed glass, however, here erosion was found to start when $\alpha \sim 20°$. Goodwin et al (135) have found an almost linear decrease in erosion as the particle size was reduced from 100 μm to 5 μm. Below 300 ms^{-1} quartz particles, 5μm diameter, were found to cause no detectable erosion. Thus in the present low veloctity microsphere study very little erosion will arise.

5.2.8 Impact heating

If it is assumed that during an impact that the available kinetic energy is dissipated locally in the contact zone, it is reasonable to expect the impact velocity of the surfaces to play a major role in determining the time of contact and hence the total amount of heat energy produced. Using a mass spectrometer, Smith and Adams (32) have estimated the temperature rise in the hypervelocity impact between a charged iron microsphere and a slatted molybdenum electrode and have found temperature rises of between 2,000 and 4,000 K for particles possessing velocities of 2 — 4 km s^{-1} respectively. This is in general agreement with Hansen (34) who obtained temperature rises of 3000 — 20,000 K for particle velocities in the range 10 km s^{-1} — 40 mk s^{-1}. Ruddolph (31) also discovered an impact heating effect associated with his microparticle studies. Here plasma was found to form in the impact event at velocities $\geq$ 0.8 km s^{-1} with the total volume vaporised proportional to the incident kinetic energy. For the case of very high velocities, $\geq$ 20 km s^{-1}, when all the internal energy was used for heating and most of the vaporised material ionised, the plasma yield was proprtional to the square of the impact velocity.

However for low velocity impacts, Tabor (136) has found that temperature rises of 5 — 10°c were observed in the normal impact of macrospheres onto a sharp spike. Using a different treatment, Chakrabarti et al (49) in their field calculations, carried out for an impacting charged microsphere against a cathode protrusion, found that for particles of 100 μm in radius and with velocities up to 100 ms^{-1}, the maximum temperature rise did not exceed 400 K.* Furthermore, Chakrabarti (137) has calculated the frictional heating produced by

* The temperature rise in a microsphere/highly oxidised target contact junction would be expected to be higher than in a microsphere/clean metal target contact junction due to the lower thermal conductivity of the oxide. This should lead to a 'sticking' event if thermo-mechanical welding is operative. In practice a 'bouncing' event arises

the impact of 4 — 10 μm iron microspheres on a tungsten surface at an incident velocity up to 100 ms^{-1} and found that the temperature rise is only $\sim$ 100°C. In another study Chaudhri et al (29) have estimated the frictional heating produced in the impact of 0.4 mm diameter W.C. spheres with velocities $\sim$ 100 ms^{-1}, on an MgO target and found that the temperature rise was 1,5 K. Thus, it is to be expected that the impact events observed in this study are associated with very little friction/kinetic energy heating. In further evidence of this conclusion the results obtained using molybdenum and tungsten surfaces, see Section 4.2.2, would seem to indicate that any heating process produced by the mechanical impact is not responsible for the "sticking" process since these surfaces, which possess an oxide whose melting point is lower than the base material, produce a significant amount of "bouncing".

As a final point it is important to remember that during any heating process, heat is dissipated rapidly into the bulk material. Smith and Adams (32) have estimated, from a method developed by Carslaw and Jaegar, (138), for refractory metals that $\sim$ 50% of the energy released by the impact, of a projectile with a target, would be conducted away in $\sim 10^{-8}$ S, which is of the order of the contact time used in this study.

5.2.9 Insulator surface phenomena

Figure 4.10 shows the distribution of 'e' values for the insulating surfaces used in this study. These indicate that there is a tremendous amount of scatter associated with the data, arising it is thought, mainly from the hardness of material and the surface topography, see Section 5.2.1. A similarly large scatter in the 'e' values has also been reported by Latham et al (26) in the microsphere/metal target impact in a high field test gap. On the other hand

in a microscopic study of millimetre sized steel spheres in contact with a steel target, Hutchings (13) has observed (i) very little scatter in the 'e' values and (ii) a gradual decrease in the 'e' value as the impact velocity was raised from 50 — 90 ms^{-1}. In an attempt to explain this discrepancy, it is necessary to analyse the insulator data more fully. Figure 4.11 shows the variation of $\log e^2v^2$ against $\log v$ (where v is the reflected particle velocity) from which it is possible to construct a linear function between the two variables such that (14)

$$\log e^2v^2 = n \log v + K \qquad \ldots 5.5$$

where n is the gradient of the graph and K is a constant given by the intercept value. Alternatively the above equation may be written in the form

$$e^2v^2 = Kv^n \qquad \ldots 5.6$$

which indicates that the coefficient of restitution is not a constant but is dependant on the reflected particle velocity. The implication of this result will now be discussed more fully with regard to the work of Tabor (118), who has derived a function associated with the impact of a steel sphere, dropped from a height h_1 onto a steel anvil to the reflected particle height, h_2. Assuming that the dynamic yield pressure P, during contact, remains constant and is independent of (i) the impact velocity and (ii) the deformation produced, the rebound velocity v is given by :

$$v = K (u^2 - 3/8\ v^2)^{3/8} \qquad \ldots 5.7$$

where u is the impact velocity and K is a material constant. It is clearly seen that v is not proportional to u which implies that e is not a constant. Tabor has verified this expression experimentally,

along with many others, and noticed a gradual decrease in the e-value as the impact velocity was increased. At sufficiently low impact velocities, the collisions will be elastic and so the coefficieint of restitution will be unity. Tabor's corresponding expression for the mean pressure during an inelastic process, assuming a value of 0.3 for Poissons ratio is :

$$P^5 = \frac{h_2^4}{(h_1 - 3/8\ h_2)^3} \quad \frac{mg}{109\ Rp^3} \quad \frac{1}{(1/E_1 + 1/E_2)^4} \qquad \ldots 5.8$$

where m and Rp are respectively the mass and radius of the impacting sphere, g the acceleration due to gravity and E_1 and E_2 Youngs Modulii for the sphere and target respectively. In the case of the impact between a carbonyl iron microsphere and an insulating surface such as glass, a constant value would have to be introduced into the above expression, to account for the change in Poisson's ratio. However, since the numerical values of Poissons ratio are highly insensitive, the above relationship for P will be retained Replacing h_1 and h_2 by $u^2/2g$ and $v^2/2g$ respectively leads to the following expression for the mean inelastic pressure

$$P^5 = \frac{v^8/(2g)^4}{(u^2/2g - 3/8\ v^2/2g)} \quad \frac{mg}{109\ Rp^3} \left(\frac{1}{1/E_1 - 1/E_2}\right)^4 \qquad \ldots 5.9$$

which reduces to

$$P^5 = \frac{v^8}{(u^2 - 3/8\ v^2)^3} \quad \frac{m}{218\ Rp^3} \quad \left(\frac{1}{1/E_1 + 1/E_2}\right)^4 \qquad \ldots 5.10$$

Substituting for the density ρ of the sphere ($\equiv$ particle mass/ particle volume) leads to

$$P^5 = \frac{v^8}{(u^2 - 3/8.v^2)^3} \quad : \quad A \qquad \ldots 5.11$$

where A is a constant given by $\frac{4}{3 \times 218} \pi \rho \left(\frac{1}{1/E_1 + 1/E_2}\right)^4$

To obtain a relationship which contains the function e^2v^2, the impact velocity u can be replaced by v/e to give

$$e^2v^2 = \frac{v^2}{\left(\frac{A^{1/3}\, v^{2/3}}{P^{5/3}} + \frac{3}{8}\right)} \qquad \ldots 5.12$$

This expression is similar to that plotted in Figure 4.11, i.e. $e^2v^2 = Kv^n$, that is

$$K.v^n = \frac{v^2}{\left(\frac{A^{1/3}\, v^{2/3}}{P^{5/3}} + \frac{3}{8}\right)} \qquad \ldots 5.13$$

which may also be rearranged for the inelastic pressure P, viz

$$P^5 = \frac{A\, v^2}{-(v^2/Kv^n - \frac{3}{8})^3} \qquad \ldots 5.14$$

For a purely elastic process $n \rightarrow 2$ and $K \rightarrow 1$ giving from equation 5.6 that

$$e^2v^2 = v^2 \qquad \ldots 5.15$$

or $e^2 = 1$

Using a similar substitution the expression for the mean elastic pressure P_m is given by

$$P_m{}^5 = \frac{Av^2}{\left(\frac{5}{8}\right)^3} \qquad \ldots 5.16$$

$$\text{that is } P_m{}^5 = B.v^2 \qquad \ldots 5.17$$

where $B = A / (\frac{5}{8})^3$ This expression is similar to that obtained by Hutchings (13) for a purely elastic process, see Section 2.1.1 and by Tabor when $h_1 = h_2$ in equation 5.8 If the values obtained from the graphs of log e^2v^2 versus log v are reviewed for Ebonite, Mica and

P.V.C. it is seen that the n and K values are 2.853, 0.0652 (for Ebonite), 2.446, 0.175 (for Mica) and 2.887,0.0322 (for P.V.C.) Since it has already been pointed out that as $n \rightarrow 2$ and $K \rightarrow 1$ the impact process becomes more elastic, the e value should thus approach 1. This is evident from Figures 4.12 (a) and 4.12(c) which for the case of Mica produces n and K values closest to the elastic process, and an 'e' value distribution nearer to 1. Softer materials such as P.V.C. have low n and K values indicating more kinetic energy is lost in the impact event. Hence by using a log-log plot, as in Figure 4.12, it is possible to obtain values which can be related to the elasticity of the material under test. However, experimentally, this can be seen to involve the recording of a large amount of impact data pointing to conclusion that some form of data acquisition process should be used in which data and results can be determined automatically - such a system will be described in Chapter 6 as the basis of a microprobe dynamic hardness testing device.

5.3 Interpretation of the electrical results

Although the particle "sticking" phenomena and its dependance on the electrical properties of the target surface is probably the most significant finding to emerge from this study, it will be helpful to the subsequent discussion to briefly review the electrical data arising from the impact of carbonyl iron microspheres on various types of target surface :

(i) With the exception of aluminium $\sim 99\%$ of the incident particles stick to the surface of ambient oxided metal targets.

(ii) Aluminium targets yield $\sim 10\%$ "bouncing" events with the reflected particle possessing a reduced charge and velocity.

(iii) For certain particle/target combinations, e,g. Fe/Al and Fe/Ti there are a finite number of events where the reflected particle returns with a negative charge,

(iv) Deliberately oxidising semiconducting and metallic surfaces tends to increase the number of bouncing events.

(v) Insulating surfaces yield ~ 99% bouncing events.

and (vi) The magnitude of the particle charge appears to play a significant role in the impact process.

The principle aim of the remainder of this chapter will be, firstly, to discuss the differing charge exchange behaviour outlined above and, more particularly, to suggest a mechanism which can give the required conditions to account for the "sticking" phenomenon.

5.3.1 Affect on differing particle/target work functions

It is apparent from section 4.3.1 that for certain particle/target combinations, e.g. for carbonyl iron/aluminium and carbonyl iron /titanium 318 charge reversal behaviour has been observed. It should be added that no special target surface preparation is required to produce the charge reversal process and the effect is readily observed with ambient oxide surfaces. From the theoretical considerations of chapter 2 it is clear that the intrinsic field, arising from the differing microsphere/target work functions will either augment or reduce the tunnelling gap field arising from the potential on the charged microsphere. It should further be noted that the effect will be more noticeable under low bias conditions. To demonstrate this work function influence, it is necessary to compare the average values of the work function as given in the literature

for the target and microsphere materials used throughout this investigation, viz :

$\emptyset Fe \sim 4.38$ $\emptyset Al \sim 4.19$, $\emptyset Mo \sim 4.32$,

$\emptyset W \sim 4.56$ $\emptyset Si \sim 4.79$ $\emptyset Cu \sim 4.46$

$\emptyset Ti \sim 3.84$

From these values it is evident that the impact regimes of carbonyl iron/titanium, carbonyl iron/aluminium and carbonyl iron/molybdenum correspond to the type of reversed biased tunnelling junctions ($\emptyset p > \emptyset_T$), outlined in Section 2.2.2. Conversely, the combinations of carbonyl iron/copper and carbonyl iron/tungsten correspond to a tunnelling juction which is forward biased since $\emptyset p < \emptyset_T$. Therefore, in the carbonyl iron/Ti and Al combinations, the impact data should exhibit a percentage of negatively charged particles returning through the drift tube, since the intrinsic field is in opposition to the gap field arising from microsphere/target potential across the target oxide. In the case of a Mo target, where $\emptyset p \sim \emptyset_T$, the intrinsic field is small so that the charge exchange process will be dominated by the gap field.

Since the intrinsic field has been shown to play an influential role in the electrical process occuring during an impact event, it should also be noted that the formation of an oxide on a target surface can cause changes in the work function (see later). As an illustration,in the specific case of the argon-ion etching of a titanium surface an increase in the work function has been observed (139). Thus a situation may arise where etching causes a complete reversal of the tunnelling regime, i.e. a change from a "reversed" to a "forward" biased situation, which then inhibits any charge reversal. Finally, Texier (140) has assumed that the charge

exchange mechanism is due to the contact potential difference arising from the differing work function materials.

5.3.2 Surface oxide film growth

From Chapter 2 it is apparent that the thickness of the contaminating oxide film on the target electrode controls (i) the tunnelling process and (ii) the incidence of electron-phonon scattering interactions during the impact event. In addition the field emission of electrons from a Beukema type trigger discharge process, see Section 2.3, are also governed by the type of contaminating film. Therefore, a detailed consideration must be given to how the growth and type of such contaminating films could account for the widely different electrical responses which occur in the impact of a carbonyl iron microsphere on the various target surfaces. In particular the ambient oxide surface film thickness will be reviewed for each target surface used in this investigation.

Firstly it should be appreciated that surface analytical techniques have revealed that inhomogeneities in composition through the surface films is a common feature of their structure. For example, in the case of a metal exposed to the atmosphere, the film region near the substrate is likely to be rich in ions of the base material, whilst the exposed layer will be richer in oxygen. When for example a clean metal copper target is exposed to air it obtains an equilibrium layer of $\sim 25\text{Å}$ (9, 141, 142). Thus Cathcart et al (143) who studied the effects of a Cu_2O film on a single crystal copper face have detected strains in the film which they concluded were due to anistropy in the oxide film, while the X-ray crystallographic studies of Boris amd Sparks (144) showed that the film thickness varies with crystallographic orientation of the substrate. This latter point could

have a profound effect on the charge exchange mechanism. in this study, which is highly dependent on the target surface oxide thickness. From S.E.M. studies on the oxide growth on a copper target at $\sim 500^{o}c$, it has been reported (9) that the oxide surface is characterised by hemispherical oxide nodules of $\lesssim 0.05\mu m$ which is a markedly different topography compared to the ambient oxide form. Thus it may be that this change of topography may play a significant role in the impact mechanisms exhibted in microsphere/target collisions and in particular give rise to a spread in the e-values exhibited by the "bouncing" particles due to multi-impact events (see Section 5.2.1). It is also reasonable to suggest that the oxide may consist of two species namely Cu_2O and CuO - in fact on the oxidised surfaces produced on copper in this study, a black oxide was found to form rapidly (CuO), which after cooling and ultrasonically cleaning the target, was progressively removed leaving only a Cu_2O red oxide.

In considering the films formed on aluminium in air at room temperature, Hass (145) has reported that the oxide grows quickly to about 20Å after which it grows at a reduced rate over a period of a month to reach a thickness of ~50Å. These experiments were carried out in ordinary air , which no doubt contained some water vapour and hence an hydroxide film could have formed. On the other hand, the experiments of Carbrera et al (146) were carried out both in dry air and humid air. In dry air, a film thickness of 15Å was rapidly reached increasing thereafter to about 20Å after 35 days. Carbrera also found that the oxidation rate was a function of the water vapour pressure. While on aluminium surfaces deposited in a vacuum, Fane et al (147) found that on exposing these surface films to air, the final oxide thickness, measured ellipsometrically, was observed to be between 40Å and 55Å depending on the initial

state of oxidation, time of exposure and humidity. All these investigations agree with the value ~25Å obtained for the thickness of the surface oxide film on an ambient oxide film used in this study (see Section 4.4). The other case of interest is the nature of the oxide formed at elevated temperatures. Farrell et al (148) have studied the oxidation of aluminium in the temperature range 25°–610°C using ESCA techniques and observed that the outermost 30Å – 50Å consists of a layer structure mainly made up of hydrocarbons and of adsorbed gases which probably consist of O_2, CO_2 and H_2O; the pure oxide layer, therefore, is located between the metal substrate and the "contaminant" layer. Measurements made at high temperatures revealed that the outer contaminating film was significantly reduced to that present on ambient oxide surfaces. It has also been found (149) that following the interaction of oxygen with a polycrystalline aluminium surface there is a reduction in the work function of the oxygen/metal system. This may seriously effect the charge exchange mechanism since the intrinsic field (see Section 5.3.1) is likely to change.

Turning now to the other target materials studied it has been observed that the surface oxide on stainless steel targets contain a high percentage of chrome oxide provided no heat treatment of the target has taken place (150,151). Latham et al (9) have observed, ellipsometrically, that the equilibrium oxide is 38Å ± 5Å which is in good agreement with the results of Fane et al (147). It should also be noted that whereas the oxide on copper is semiconducting, that on stainless steel is a non-absorbing dielectric. Adreeva and Kazaren (152) have investigated the oxide film growth on freshly evaporated titanium films when exposed to air and found that a film

of 12Å to 25Å formed rapidly and increased to 55Å after an exposure of 74 days. Also the oxide film grown on titanium at temperatures below 800° C in either pure oxygen or air has the composition TiO_2 and shows a rutile structure, although Tamashov et al (153) have reported that at the metal interface the oxide is mostly TiO while at the surface it is TiO_2. Finally Andreeva et al (154) have studied the oxide film growth on molybdenum up to 300° C and have found it possesses the composition of MoO_3.

5.3.3 Conductivity of surface films

It is reasonable to assume that the conductivity of a surface film on a metal target electrode plays an important role in the charge exchange and tunnelling behaviour which follows the impact between a microsphere and a target surface, see Chapter 2. However, many of the theoretical models discussed in Chapter 2 are derived for ideal surfaces and do not take into account the presence of such surface films; it should be recognized that the practical polycrystalline surfaces used throughout this investigation show wide variations in the oxide film properties over their surface, such as local variations in the band gap and interband states. Another important parameter of the contaminating layer is the dielectric constant, since, as shown in Chapter 2, this determines to some extent, the temperature rise in the tunnelling junction. Now in many earlier investigations the value used for the dielectric constant of the medium was the low frequency value, however under the present circumstances of very short contact times ($\sim 10^{-8}$ s) the high frequency values are more appropriate. It can be shown that the refractive index (n), from the definition of Maxwells field theory leads to the relation

$$n = \sqrt{\mu \varepsilon_r} \qquad \ldots 5.18$$

where μ and ε_r are the relative permeability and dielectric constant of the medium respectively.

For wavelengths greater than 1 cm, the above expression is approximately true. Thus for the case of the impact between a microsphere and a target where the contact time is $\sim 10^{-8}$ s, the above equation is also valid. For simplification we may write $\mu \sim 1$ for many non-ferromagnetic materials, thus $n = \sqrt{\varepsilon_r}$ can be used for determining the dielectric constant in the equations derived by Klein (see Section 2.3.2).

Finally, it has been pointed out by Simmons (38) that the tunnel characteristics are dependant upon the dielectric constant of the insulating film; i.e., the smaller the value of ε_r the lower the tunnel resistivity, especially for low bias conditions. Since the dielectric constant of most materials is a function of temperature (155), it follows that the tunnel characteristics are an intrinsic function of the thermal properties of the insulating oxide layer, as well as of the electrodes. These concepts will now be developed in the following discussion of the particle impact process.

5.4 Particle "sticking" phenomena

As already stated in the case of an ambient oxided metal surface, it is observed that over 99% of the incident microspheres "stick" to the surface on impact, the exception being aluminium where ~10% 'bouncing' occurs. It is therefore important to discuss the reasons for the "sticking" phenomena in terms of the solid-solid interaction and charge exchange processes occurring before and during

impact. It follows from the previous sections that only a small fraction of the mechanical energy lost during a collision is dissipated as elastic waves ($\sim$ 3%); the remainder is presumed lost through K.E. heating processes and elastic/plastic effects. However it is unlikely that kinetic energy heating produces a thermo-mechanical weld since the temperature rises during the impact of the low velocity microspheres in this study are extremely small, see Section 5.2.8. This conclusion was confirmed experimentally by the investigation of the impact of carbonyl iron microspheres on molybdenum and tungsten targets, possessing commercially polished and oxidised surfaces, which showed that the temperature developed during the impact event is not the dominant factor, (see Section 4.2.2). Therefore, the "sticking" phenomena would not appear to be associated with a purely mechanical impact. In further support of this contention, the present experimental regime, where the impact velocity range is 1 - 20 ms^{-1}, is well below the 200 — 500 ms^{-1} quoted by other investigators for the critical microparticle velocity for inelastic impact, (26, 30, 31, 32). In addition it should be remembered that nearly all particles"bounce" from an insulating glass surface where the predicted critical velocity differs very little from that of, say aluminium. Therefore some other process/processes must be giving rise to the "sticking" phenomena.

5.4.1 The effect of the attractive forces between a sphere and a plane

It is evident from Chapter 2, that as a charged microsphere approaches the target electrode, it experiences several attractive forces on approach, these include the image force (arising from the induced charge on the target) and Van der Waal forces while once impact occurs adhesive forces,due to molecular attractions, dominate.

Thus, in a typical "bouncing" event, shown in Figure 4.18, the microsphere will have to overcome the total effect of these forces if it is to escape from the target surface. Therefore, it is of interest to determine the magnitude of these forces, and hence the total work that the microsphere must perform in order to leave the target surface . Consider, therefore, the typical case of a carbonyl iron microsphere, of radius 2 μm, mass $\sim 2.6 \times 10^{-13}$kg, moving with an impact velocity 'u' of 10 ms^{-1}, the total K.E. of the particle before impact is $\sim 1.3 \times 10^{-11}$J. If, for simplicity, it is assumed that the 'e' value for the interacting surfaces is 0.5, which is typical of the values obtained in the bouncing impact studies of highly oxidised metal surfaces, it follows that the reflected particle will have a K.E. of $\sim 3.3 \times 10^{-12}$J. Hence, for the "sticking" events observed with many ambient oxide metal surfaces, the work done by the attractive forces mentioned above must be $> 3.3 \times 10^{-12}$J if the particle is to remain on the target surface.

To determine the work done by the image force, it is necessary to consider two extreme cases: (i) for sphere/plane separations $> 20{,}000$Å the image force is small and thus can be neglected and (ii) at sphere/plane separations ≤ 25Å the sphere is assumed to be in contact with the surface oxide. Therefore, over the range 20,000 − 25Å the work done by the image force is calculated to be 8.62×10^{-14} J which is much smaller than the energy required to stop the particle leaving the surface. More importantly, the values determined from the image force calculations, are for clean metal surfaces only whereas in practice the presence of the surface oxide contaminating layer would cause a significant reduction in the image force. Also, during the impact event, charge exchange is taking place, so that the reflected particle would possess, not only a smaller velocity, but also

a reduced charge which would again significantly reduce the image force. A similar evaluation can be carried out for the long and short range Van der Waal forces, which yields a value of 6.3×10^{-18}J for the work done on the microsphere, i.e., again insignificant compared to the energy of the microsphere. As a final comment on these two attractive force mechanisms, it should be mentioned that before the impact event, the effect of both the image force and Van der Waals force on the microsphere is to cause its velocity to increase, whereas after impact only the Van der Waal's force is unchanged hence a "bouncing" event should arise. Although no equivalent energy calculation can be performed for the contact adhesion effects, it has been shown in Chapter 2 that the adhesive force is $\sim 1.85 \times 10^{-7}$N. However, in the impact event the elastic forces of the surfaces dominate which should again promote a "bouncing" process (see Section 2.4.3). Since the total work done against all of these attractive forces is much lower than that required to stop the particle escaping from the target surface, it would appear that all the particles should execute "bouncing" events: the fact that in practice over 99% of the incident particles "stick" to the target surface can only mean that the attractive forces arising from the image charge, Van der Waal effects and adhesion do not govern the "sticking" process.

To further emphasise this conclusion it is of interest to determine the adhesive force holding the microsphere on the target surface, that had to be overcome, in the basic microprobe technique outlined in Section 3.7. The calculation, explained earlier, yields adhesive force values in the range 6.95×10^{-6} — 3.36×10^{-5}N for the case of carbonyl iron (type E) microspheres impacting on an ambient oxide titanium 318 target, which is similar

to the values determined from the control experiment, (1×10^{-5} — 1.78×10^{-5}N) where microspheres are "sprinkled" onto a titanium target surface. Although these values differ slightly from the adhesive force value calculated theoretically using equation 2.94, it should be pointed out that in this equation that the Hamaker constant has been only approximated, which could lead to an increase in the adhesive force.

This paradox may be overcome if it is assumed that before or during the impact event that the microsphere is heated either by a Beukema type field emission process (45) or by electron-phonon scattering associated with electron tunnelling within the oxide junction (see Chapter 2), then significantly larger adhesive forces may arise during the impact as a result of the increase in ductility and reduction in hardness of the impacting materials (84, 156) or in extreme cases the microsphere may microweld to the surface. On cooling, the adhesive force will generally reduce due to contraction and fracture of the weld yielding values similar to a microsphere "placed" on the target surface and observed in the control experiment mentioned above. The following section will therefore, determine the temperature rise involved in both heating processes.

5.4.2 Thermo-electric Welding I

Such a model has been described by Beukema (45) in his modified trigger discharge mechanism, where it was assumed that in-flight field emission raised the temperature of the particle surface sufficiently to cause local melting and hence welding on impact. From his analysis the temperature rise ΔT to be anticipated with the present zero field regime (shown in Section 2.3) would be :

$$\Delta T = 2.I.Vt^{\frac{1}{2}} / \pi R_a^2 \ (\pi K \rho c)^{\frac{1}{2}}$$

where V is the potential of the charged sphere with respect to the target, I is an approximately constant emission current that flows for an "approach" time t, R_a is the radius of the electron impact region whilst K, ρ and c are the thermal conductivity, density and specific heat of the particle respectively. Substituting values for these parameters which are relevant to this study yields a value of $\triangle T = 90$ K. Since this is considerably smaller than the rise required to melt the iron microsphere (melting point 1800 K), it would appear that this mechanism is also unlikely to be responsible for the "sticking" phenomena. It should also be appreciated that the electron emitting surface of this model, namely the target, is covered with an oxide layer which will inhibit electron emission and therefore further minimise the heating effect.

5.4.3 Thermo-electric Welding II

This second mechanism could result from the energy dissipation associated with the electron-phonon scattering processes in the interfacing oxide region between the particle and target, where the electron tunnelling process described in the model of Latham and Brah (9) is taking place. It is assumed that the electron-phonon scattering process (61) produces a temperature rise given by equation 2.71:

$$\text{i.e.} \quad T = \frac{\sigma \varepsilon_0 \varepsilon_r E^2}{c}$$

where E is the applied field across the target oxide, c the specific heat capacity per unit volume, σ is a constant whose value lies between 0.7 and 0.9, ε_0 and ε_r are the dielectric constants of free space and the oxide respectively. To evaluate the above expression, it is necessary to determine the potential of the charged microsphere when

it comes into contact with the target oxide surface. For the conditions which are appropriate to this study, i.e., a 2 μm radius microsphere possessing a charge of 10^{-14}C impacting on a 25Å thick target oxide film, the potential of the sphere with respect to the target, calculated from equation 2.74 as explained in Chapter 2, is ~11V Table 5.1 indicates how the temperature rise in the tunnelling oxide junction depends on the type of contaminating oxide film, its physical parameters and its thickness. The high frequency dielectric constant has again been used throughout (see Section 5.3.3) while the value of σ was chosen to be 0.85 (see Section 2.3.2). The results indicate that for a 25Å oxide film temperature rises in the range $\sim$ 148 — 460K could occur, while a significant decline occurs at 100Å, i.e., ~9 — 31 K. Although these temperatures are very much higher than predicted by the previous thermo-electric welding mechanism, they do not appear to be large enough to cause melting of the oxide surface in the sub-micron junction. It is however important to note that the above values have been determined for microparticles which possess a relatively small charge. Thus, if the radius of a microsphere is doubled, there will be a corresponding increase in the charge acquired during the contact charging process in the micro-particle gun, (see Section 3.3.2). This in turn will lead to an increase in the sphere/target potential. Therefore since the temperature rise in the tunnelling junction is proportional to the square of the sphere/target potential, much larger temperature rises can be envisaged. Corroboration of this "size effect" has been observed with the microprobe experiment for different particle size distributions (see Section 4.5), where the H type carbonyl iron powder/stainless steel target combination (whose oxide posesses a high percentage of Cr_2O_3) indicates no visible impact site markings while for the corresponding case of E type carbonyl iron microspheres

Target Oxide	Dielectric constant	Specific heat capacity(J kg K)	Density $kg.m^{-3}$	Temp. rise in tunnelling junction at 25 Å	at 100 Å	Melting point K
Al_2O_3	3·83	774·98	3965	148·34	9·27	2290
TiO_2	6·59	705·6	4170	326·18	20·39	2098
Cu_2O	8·12	429·15	6000	459·26	28·7	1503
CuO	8·06	531·7	6400	344·95	21·56	1599
WO_3	5·88	336	7160	355·95	22·25	1746
MoO_3	~5*	562·8	4692	275·75	17·23	1068
Fe_2O_3	9·25	525·44	5240	489·28	30·58	1838
SiO_2	2·38	741·06	2650	176·5	11·03	1880
Cr_2O_3	6·25	794·65	5210	219·85	13·74	2573

* = approx. value

Table 5.1: Temperature rise in the tunnelling junction as a function of the target surface oxide parameters

visible evidence of the impact can be seen in several cases . It should also be pointed out that the target surface oxide can be assumed to be non-uniform giving regions that are less than 25Å thick (9), (see Section 5.3.2); since T is inversely proportional to s^2 (where s is the thickness of the target oxide) larger temperature rises could occur locally where $s < 25Å$. A similar effect could result from the high strain rates involved during the impact process (see Section 5.2.2) since these may cause a compression of the target oxide and hence a reduced value for s.

The decrease in the calculated temperature rise occurring in the sub-micron tunnelling junction, as the target oxide thickness is increased, leads to a reduced probability of a microweld occurring on impact. This is therefore put forward as a reason for the advent of the "bouncing" events observed with highly oxidised metal surfaces. Further support for this contention comes from the experimental results on a highly oxidised aluminium surface which indicates that the number of bouncing events gradually increases as the oxide thickness increases. Referring to Table 5.1, which illustrates the material dependance of the mechanism, the "bouncing" behaviour should occur first with aluminium, since its tunnelling junction temperature is the smallest, followed by silicon and stainless steel. Evidence for this latter point can be found in the results on highly oxidised silicon and copper targets where a thinner oxide is required on silicon to promote "bouncing" than that needed for copper. A particularly surprising experimental result was that the titanium surface needed to support only a thin oxide before "bouncing" behaviour occurs, i.e., in contradiction to the predicted tunnelling oxide temperature rise shown in Table 5.1. However, if the work functions of the microsphere/target combination

is considered, see Section 5.3.1, it is observed that the intrinsic field, of the present impact regime, leads to a reversed biased junction which opposes the field across the sub-micron junction and in consequence a smaller temperature rise could be anticipated. This work function difference between the microsphere.target combination also accounts for the charge reversal behaviour observed with the titanium surface (see Section 4.3.1).

Another apparently anomalous target response occurs in the impact event between carbonyl iron microspheres and an ambient oxide aluminium target. Referring to the "bouncing" events observed with this surface they are seen to include two different forms; (i) reflected particles which possess a negative charge arising from work function differences similar to that explained above for titanium and (ii) a "bouncing" behaviour in which the reflected particle possesses a reduced positive charge. This second type of response is significantly different from other target materials. One possible explanation of this latter phenomena involves the hardness of the surface oxide (Al_2O_3) where it may be suggested that little or no compression of this oxide occurs during impact. Hence, taking into account the relative work functions of the microsphere/target combination, the resulting field across the oxide may only give rise to a reduced tunnelling effect leading to incomplete charge transfer between the microsphere and target during the contact time. Thus the temperature rise in the sub-micron junction will be too small to cause a microweld to occur, hence the particle will "bounce" with a reduced positive charge.

Finally the microprobe data indicates in many cases, that there is no obvious impact site, at least not discernible in the S.E.M., for many of the impact events where particles "stick" to the

target surface. Therefore for a "sticking" process to occur the temperature rise in the sub-micron junction does not have to be sufficient to cause melting, since a modest increase in temperature can give rise to "softening" and plastic impact which leads to larger adhesive forces as reported by Gane et al (84) on the adhesion of germanium at high temperatures. In addition, the microprobe data indicates that, where impact sites are observable, the temperature rise is occurring in the target oxide and is not due to the modified trigger discharge process of Beukema (45).

5.5 The effect of the microsphere velocity and charge on the impact process

The variations shown by the impact velocity/impact charge data for the highly oxidised aluminium, silicon, molybdenum, copper and tungsten targets, of which Figures 4.7 and 4.8 are representative of the data, indicates that for particles which possess high velocities and/or large charges, some form of charge modification, and in extreme cases "sticking", occurs on impact. Since we are concerned with particles which have impact velocities in the range 1 - 50 ms^{-1} the variation in the strain rate will be relatively small, although compression of the target oxide may still be taking place, therefore it is to be expected that the particle charge will be the dominant factor. On this basis we now can use an argument similar to that discussed in the previous section to explain the surface impact characteristics of a highly oxidised target surface. In the region where all particles appear to "stick" to the target surface, the microsphere/target potential arising from the particle charge is relatively high, giving rise to tunnelling and hence a large temperature

rise in the sub-micron contact junction leading to (i) larger contact adhesive forces arising from plastic deformation or (ii) a microweld, both of which could precipitate a "sticking" event. In the intermediate region, where particles "bounce" but undergo some form of charge modification, the sphere/plane potential during an impact event gives rise to a reduced tunnelling effect and incomplete charge transfer during the contact time. The temperature rise in the tunnelling junction is subsequently small, hence no plastic surface effects arise and the adhesive forces are insufficient to cause "sticking". For the final zone, where particles "bounce" with no charge modification, the sphere/plane potential is too small to allow any tunnelling to take place and hence no charge transfer occurs. In consequence the temperature rise in the sub-micron junction is minimal and hence promotes the type of "bouncing" behaviour which is observed with insulating materials. Similar zones can also be identified on the impact velocity versus impact charge data of Figure 4.19 obtained from the insulating target materials. However, since the insulating targets are too thick to allow any form of tunnelling, the evidence of charge modification in these experiments must be attributed to the mechanical processes that occur during the impact event. Thus, the main loss of charge is thought to arise from charge being "rubbed" off the microsphere during impact. Such a process will depend on the surface microtopography and surface deformation of the target. The former case leads to multiple impacts while the latter gives rise to a surface contact area which may be far larger than that calculated for a purely metal/metal contact, see Section 5.2.5. Both charge removal processes would be more likely for large diameter particles (hence large charges) a conclusion which is supported by the experimental evidence shown in

Figure 4.19. Although these ideas have been put forward to explain the charge behaviour occurring at insulating surfaces, it must also be pointed out that similar processes could arise in microsphere/highly oxidised metal contacts.

5.6 High field effects

In the present zero field study,the impact behaviour of a microsphere on a metal target electrode is found to depend upon (i) the target material, (ii) the work functions of the microsphere and target, (iii) the surface contaminating oxide layer, (iv) the charge on the microsphere and (v) the strain rate effects involved during the impact. To determine how these processes might effect the behaviour of microparticles in a high voltage gap, and in particular initiate its breakdown, it is first necessary to briefly review the mechanism of microparticle initiated breakdown. In this a clump of material is torn from one of the electrodes under the action of the electrostatic forces associated with the applied gap field and then accelerated across the gap to impact on the opposite electrode. Depending on the impact conditions two types of event may occur that can give rise to breakdown; firstly, if the impact velocity is high enough, a microplasma can be produced on impact which can in turn trigger the breakdown of the gap, while secondly a momentum and charge reversal process may occur, leading to K.E. enhancement (see Chapter 1), which, after a multi-transit impact, may eventually lead to a sufficiently energetic impact for the formation of a microplasma.

In many high voltage systems, naturally occuring microparticles (radii 0.1 — 5 μm) have been observed to cross the gap on the initial

application of the high voltage (157). Since these are generally thought to consist of both parent electrode materials and contaminants resulting from the polishing process,it is important to consider which types of material should ideally be used for the electrodes if the energy-enhancing "bouncing" behaviour described above is to be suppressed. However, as insulating particles are unlikely to undergo charge exchange, the discussion can be simplified to consider the contrasting situations of a positively charged, metallic microparticle impacting on (i) an ambient oxided cathode electrode and (ii) a highly oxidised cathode electrode. In the first case, the influence of the particle/target work functions will be almost negligible since a high percentage of the microparticles can be assumed to be of the same material as their parent electrodes. Under these circumstances the charge reversal mechanism is therefore controlled by the electrical and mechanical properties of the surface oxide film. In a real gap situation, where fields exceed $\sim 6 \times 10^6$ Vm^{-1}, all the surfaces approach a common charge reversal response (5), and hence only the mechanical properties, i.e., e-values, of the oxide surface will control the velocity enhancement process. Therefore, to suppress the "bouncing" process, it is ncessary to choose a surface whose e-value is relatively small, i.e., such as aluminium. To inhibit the field-controlled charge reversal process, a thick oxide could be artificially grown on the target surface, since under these conditions particles will "bounce" with the reflected particle possessing a virtually unmodified positive charge and hence will not be re-accelerated across the gap. However, the possibility must not be discounted that as the particle moves away from the cathode electrode, the field in the microparticle/cathode region could be great enough for a trigger discharge (see Section 2.3) to occur which may lead to breakdown of the total gap. This type of event is more likely to occur

for the larger charged particles and for cathode surfaces which possess many irregularities; from this point of view the electrode surface should be initially polished and cleaned to remove large contaminants. This type of breakdown could occur for all types of highly oxidised metal surface used in this study since "bouncing" behaviour is promoted when an oxide is artificially grown on a target electrode.

Finally, the effect of a "sticking" event should also be considered, since a protruding particle resting on the cathode surface could give rise to field enhancement and consequently field electron emission. The Fowler-Nordheim plots of Figure 4.22 indicate that the β factor associated with such a microgeometry lies in the range 5 –19 which is in agreement with the enhancement calculated theoretically for the case of a sphere resting on a cathode. In practice, however, one requires enhancement factors > 200 to produce the correct conditions for breakdown of the high voltage gap, hence the effect of a "sticking" microparticle is thought to effect the breakdown process very little under these circumstances.

CHAPTER 6

6.0 A dynamic hardness measuring device incorporating automatic data acquisition

6.1 Introduction

The fundamental studies reported in Chapter 4 of the impact behaviour of the low velocity, positively charged, metallic microspheres on planar targets under zero field conditions have shown that there are generally two types of interaction, termed "bouncing" and "sticking" events. Insulating targets give rise, almost exclusively, to the former type of event, whilst metal targets promote both types of events, where the relative numbers of each, within a given sample, generally depends on the thickness and electrical properties of the surface oxide. The distinction between their alternative patterns of behaviour lies in the fact that electrical charge is exchanged during an impact with a metal target and can give rise to local welding processes, whereas in the case of insulating targets the interaction is electrically "passive" and results in a "bouncing" event that is solely characteristic of the mechanical interaction between the surfaces. This latter observation therefore points to the possibility of applying the experimental techniques used in these microsphere impact studies as the basis of a dynamic probe for measuring non-destructively the variations in microhardness across extended-area specimens. Such a facility could be used immediately for the study of electrically insulating surfaces with every prospect of its application being extended tometal specimens when the more complex interactions associated with these surfaces is more fully understood. It should also be noted that the proposed

technique represents the microscopic analogy of the traditional macroscopic Shore solerscope system which measures the dynamic hardness of a surface in terms of the coefficient of restitution, or e-value, between a reference sphere bouncing from a planar "test" anvil.

In considering the practical requirements of such a micro testing facility, account must be taken of another important characteristic of the impact data detailed in Chapter 4, viz. the significant scatter that is observed among the e-values associated with individual bouncing events at a given microscopic "test" zone. This therefore points, in the first place, to the physical need of recording a relatively large number of events in order to make an accurate measurement of the mean e-value of a given site, and in the second place, to the practical need of automating the data acquisition and recording systems, using microprocessor techniques, in order to provide an "immediate" display/read-out of the required information. This chapter is devoted to describing just such a prototype system.

6.2 System Logic

6.2.1 General concept

Referring to Figure 6.1, a "test" microsphere is produced by an auto-trigger controlled pulse unit whose function is to fire the microparticle gun. The microsphere, having an initial velocity u and charge q_1, first passes through a drift tube charge detector and then either bounces off the specimen target to return through the drift tube with both a reduced final velocity v and charge q_2, or sticks to the specimen target. The output of the F.E.T. op.amp passes into an interface unit and finally into the computer/display,

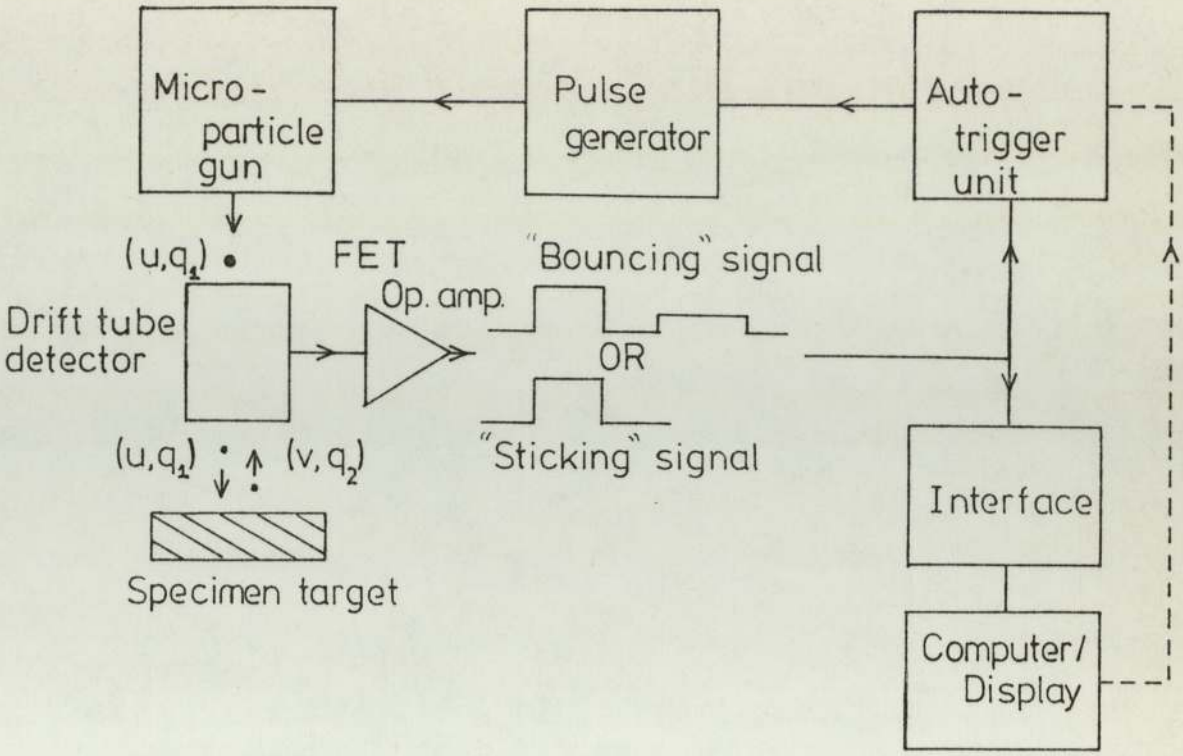

Figure 6.1: Block diagram of the data acquisition system

where the "software" is used to discriminate between a "bouncing" and "sticking" event, and rejects the latter. The display then presents the digital voltage of the analogue signal and the time period of both trapezoidal pulses. Coincident with the operation of the interface, the trapezoidal pulse is fed into the auto-trigger unit which controls the supply of microspheres in such a way that it is impossible for a second "test" microsphere to enter the system whilst the previous event is being processed. Details will now be given of the design and function of the various components of this system.

6.3 System Hardware

In this section details are given of the design and operational mode of the constituent elements of the overall data recording system outlined above.

6.3.1 Auto-trigger unit

The basic function of this module is to control the "firing" of the microparticle gun. It is based on a free-running oscillator of frequency ~ 1 H_z that provides a regular train of pulses for triggering the high voltage pulse generator that "fires" the microparticle gun. However, as already outlined in Section 6.2.1, the unit also has a built-in facility for "latching" the oscillator when a particle is detected by the drift tube; a manual re-set facility is then available for re-starting the oscillator. The complete circuit of the module is shown in Figure 6.2 which for ease of understanding, can conveniently be broken down into the following sequence of sub-elements : input pre-amplifier, comparator, pre-amplifier, C.M.O.S. latch, relay/driver and a free-running oscillator.

6.3.1(a) Input pre-amplifier

The smallest trapezoidal signal, appearing at the output of the drift tube amplifier, which can be discriminated from the background noise is ~ 20 mV. Hence this voltage has been adopted as the minimum threshold value for "latching" the auto-trigger unit. Since this value is too low to use directly, for causing the following comparator to switch "state", it is necessary to introduce some amplification. Referring to Figure 6.2, this is achieved by using a 741 S operational amplifier in a non-inverting configuration to produce a voltage gain of ~ 200. Before use, the input is shorted allowing the off-set null to be adjusted to give zero output.

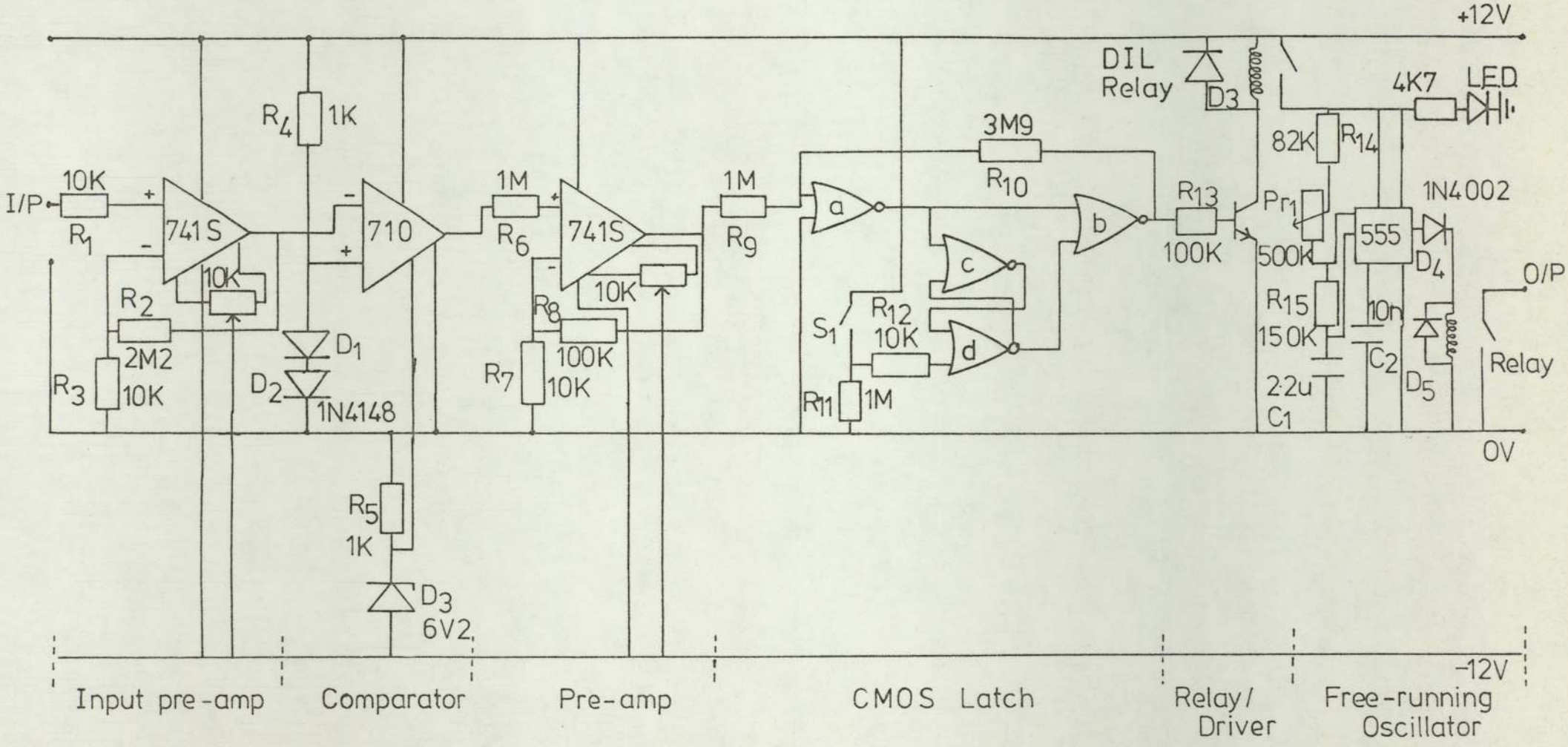

Figure 6.2: Circuit diagram of the auto-trigger unit

6.3.1(b) Comparator

The output from the pre-amplifier described above is fed directly into the inverting input of a high speed comparator, (R.S. Type 710). A reference voltage, which can be conveniently derived from the series chain of R_4, D_1 and D_2 connected between the +12 V and OV rails, is connected to the non-inverting terminal. In this arrangement, the value of R_4 is determined by the maximum current which can pass through D_1 and D_2. To obtain the correct output voltage 'swing', the comparator requires a + 12 V rail and - 6 V rail, where the - 6 V rail is derived from a zener diode (6.2V) and its associated current limiting resistor.

When the magnitude of the variable input voltage exceeds the reference voltage at the non-inverting terminal, the output of the comparator changes state; i.e. provided both voltages have the same polarity with respect to earth. Thus when both inputs are positive the output switches from + 3.2 V to approximately - 0.5 V (a T.T.L. compatible signal) . With no variable input voltage, the output of the comparator remains at $\sim$ 3.2 V. In practice, a 20 mV signal at the input to the pre-amplifier will, after amplification, cause the comparator to change from a "high" to a "low" state. However for maximum stability, it is important to keep the supply leads as short as possible and to use stabilised supply voltages.

6.3.1(c) Pre-amplifier

Although the output of the comparator can drive a T.T.L. gate directly C.M.O.S. (operating voltage + 3 V to + 18 V) is the logical choice for the reset latch since relays and large voltage "swings" are to be used in the latter part of the auto-trigger network.

However, the "latch" requires a "high" logic level of 0.7 V_{DD} to V_{DD} (where V_{DD} is the supply voltage) and a "low" logic level of V_{SS} to 0.3 V_{DD} (where V_{SS} is the ground level, OV) thus the output of the comparator requires amplification. A non-inverting amplifier based around the 741 operational amplifier is used, with a voltage gain of 10, such that its output "swings" between the positive rail voltage (V_{DD}) and ground (V_{SS}) as the output of the comparator changes stated from 'high' to 'low'. As with the input pre-amplifier a similar "setting-up" procedure is adopted when adjusting the off-set null.

6.3.1(d) C.M.O.S. latch

A C.M.O.S. 4001B gate provides a latch that will turn off but not turn on again until manually reset. If the output of the pre-amplifier is "high" (positive supply rail) the output of the C.M.O.S. latch will be "high". To prevent triggering on noise signals gates "a" and "b", together with the two resistors R_9 and R_{10} form a Schmitt trigger which provides noise immunity. A "low" at the input to R_9 causes the output of gate "a" to go "high", together with the output of gate "d" which then inhibits the output of gate "b" after it has gone "low". Reset is achieved, manually, using a push-to-make switch.

6.3.1(e) Relay and driver circuit

In many cases it is possible to drive a D.I.L. (Dual in line) relay directly from the output of the C.M.O.S. latch, however, for protection it is far better to use a driver transistor (B.C.109) with the relay energising coil connected into the collector circuit.

The back e.m.f. produced as the relay operates does not reach the C.M.O.S. integrated circuit since the driver transistor provides some immunity. The base resistor R_{13} is chosen such that the current drawn from the latch is small but still large enough to turn the transistor "hard on" when the output of the latch is "high".

6.3.1(f) Free-running oscillator

This device is constructed around a bipolar 555 timer unit used in the astable mode. The schematic output waveform produced by this device is shown in Figure 6.3 where the times T_1 and T_2 are given by $T_1 \sim 0.7\ (R_{14} + R_{15})\ C_1$ and $T_2 \sim 0.7\ R_{15}\ C_1$ while the frequency of the oscillation (f) is :

$$f = \frac{1}{T_1 + T_2}$$

The variable preset Pr_1 allows R_{14} to be adjusted giving a range of values for T_1. An important point to note with this type of

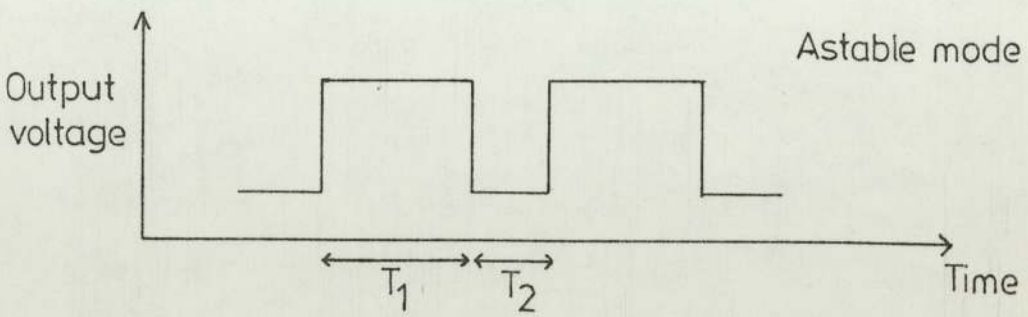

Figure 6.3: Schematic timer waveform

timer is that for satisfactory operation the timing capacitor C_1 should be of the low leakage current variety, i.e. silvered mica, polycarbonate, polystyrene or polypropylene. The power supply to the 555 timer is controlled by the D.I.L. relay driven via the C.M.O.S. latch while the output of the 555 is connected to a miniature relay with special precautions taken by using D_4 and D_5, to prevent the back e.m.f. destroying the output stage. In this case no driver transistor is necessary since the 555 I.C. can "source" or "sink" $\sim$ 200 mA of current which is sufficient to energise the relay. Double pole output relay contacts are used to control the pulse generator, while also providing isolation to the sophisticated driving circuitry.

6.3.1(g) Operating Principles

It is possible to consider two alternative practical situations in the first no signal is present at the input pre-amplifier while in the second, a trapezoidal pulse, arising from the passage of a microsphere through the drift tube, gives rise to a signal appearing at the input pre-amplifier. In the first case, the output of the high speed comparator remains 'high' (+ 3.2 V), therefore the C.M.O.S. latch input is 'high' leading to the condition that the output of the latch is 'high'. As a result, sufficient current is now available for the driver transistor to switch "hard-on" and operate the D.I.L. relay. The power supply is thus connected to the free-running oscillator which then drives the pulse generator at its operating frequency.

In the second case, the positive trapezoidal pulse causes the comparator to switch state from "high" to "low". The C.M.O.S. latch then turns off the D.I.L. relay, thus isolating the free

running oscillator . Further triggering of the pulse generator stops and can only be restarted using the manual reset facility. An L.E.D. is used to monitor the power supply to the oscillator, being on when the pulse generator is running and switched off when the unit is latched. Figure 6.4 shows the output waveform of the free-running oscillator, while Figure 6.5 is the internal view of the auto-trigger unit.

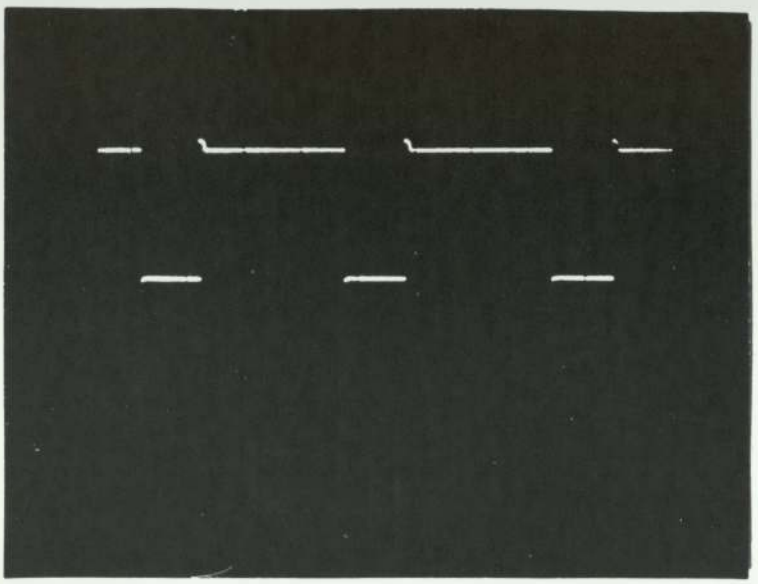

Figure 6.4: Output waveform of the free-running oscillator

6.3.1 (h) Buffer amplifier

As a final practical consideration, a non-inverting unity gain buffer, shown in Figure 6.6 needs to be placed between the

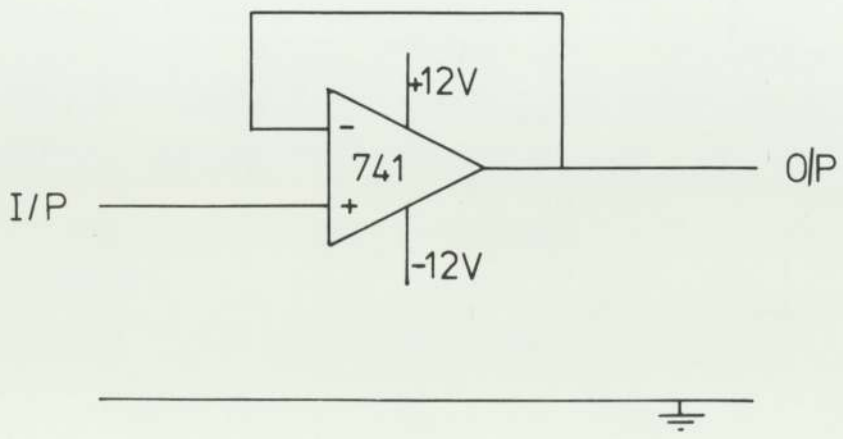

Figure 6.6: Unity gain buffer amplifier

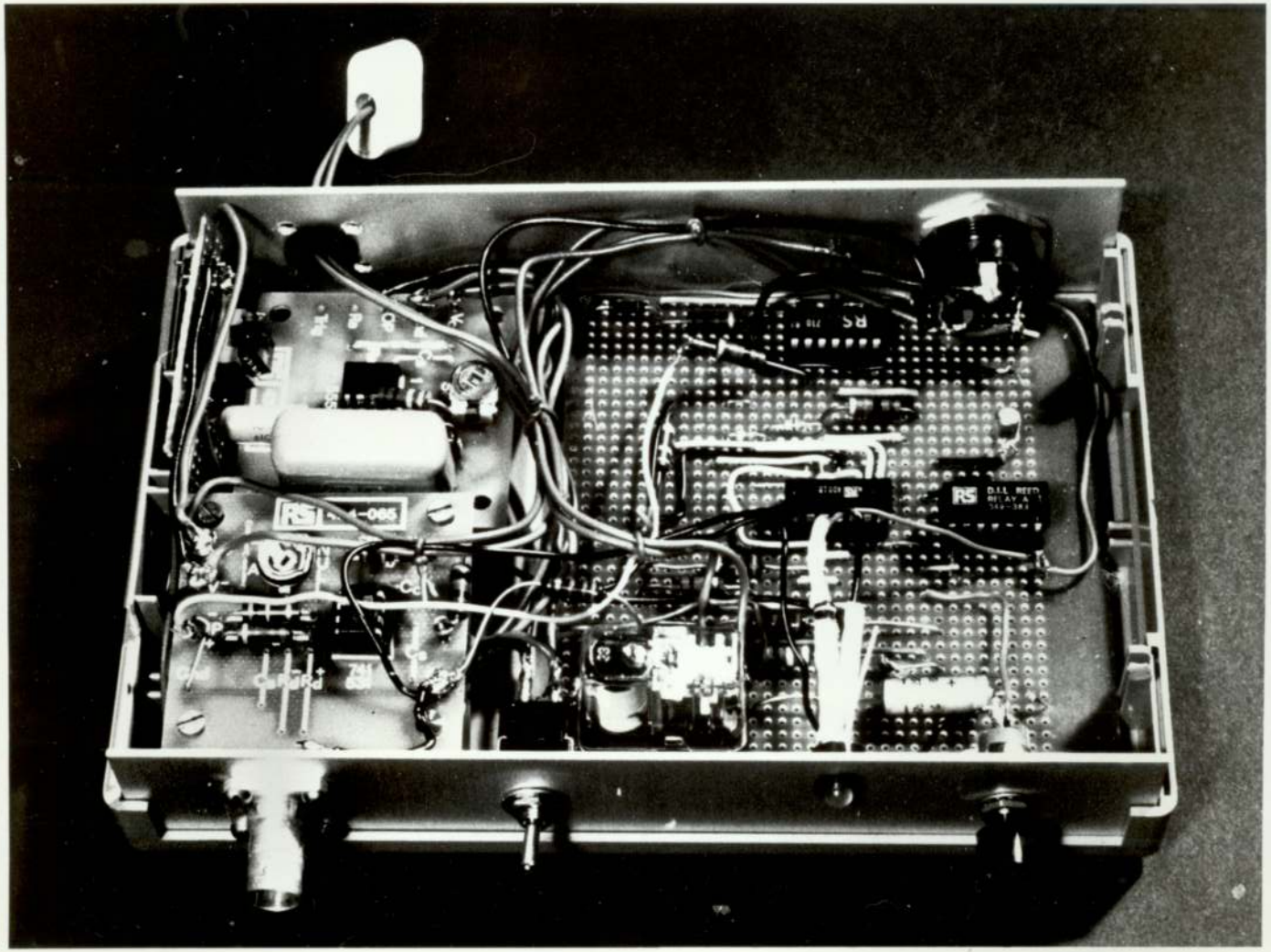

Figure 6.5: Internal view of the auto-trigger unit

output of the drift tube detector and the input pre-amplifier of the auto-trigger unit. This prevents undue "loading" and drift in the d.c. level of the drift tube amplifier. It is important to maintain the d.c. level at 0.V. otherwise the triggering level of the auto-trigger unit will be affected, i.e., if the d.c. output is below zero, the unit may continue to operate the pulse generator even when a charged particle passes through the drift tube.

6.3.2 The interface unit

The function of the interface unit is to convert the analogue input voltage to its characteristic 8-bit data word. This is performed by an analogue-to-digital converter (A.D.C.), type R.S. 427E (conversion time 15 μs), and the peripheral timing devices. The complete interface circuit is shown in Figure 6.7 and for ease of explanation can be broken down into the following units: input pre-amplifier, clock generator/timing pulses and the A.D.C.

6.3.2(a) Input amplifier

The A.D.C. allows analogue voltages in the range 0 to 2.55 V (the reference input voltage) to be converted into their digital equivalent. However, the voltage of the output of the drift tube amplifier usually lies in the range 20 mV (minimum value) to 120 mV (maximum value). Therefore to allow the maximum range of the A.D.C. to be used, amplification is necessary. Figure 6.7 shows the non-inverting, a.c.coupled, amplifier, built around the 741S, which is used to provide a voltage gain of 20. Thus, for a 120 mV input signal an output voltage of 2.4 V can be realised. In this particular case, it is important to use the 741 S since

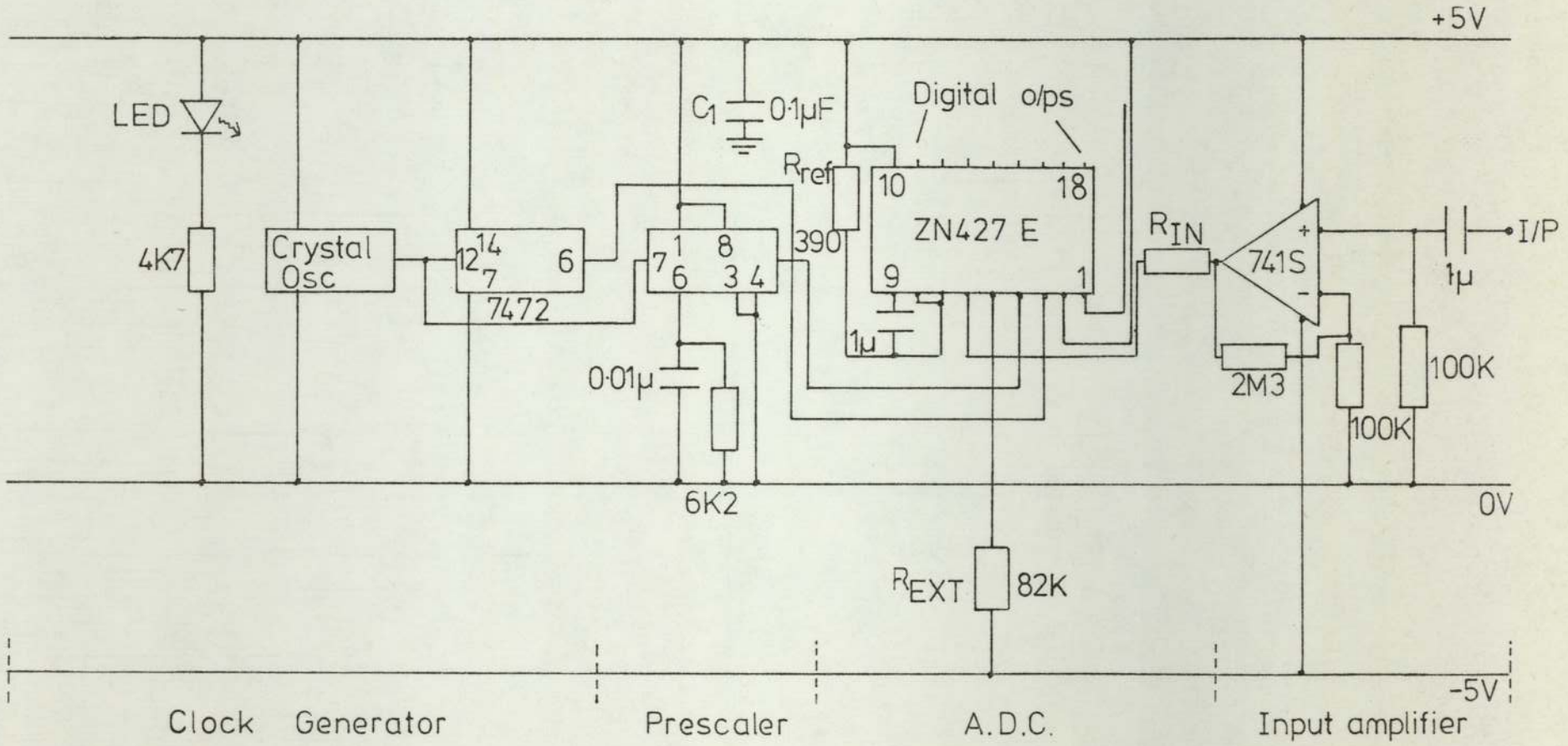

Figure 6.7: Circuit diagram of the interface unit

it has the same response as the operational amplifier in the drift tube detector, (see Section 3.3.5); thus no distortion of the waveform should arise. As with the previous amplifiers, a similar procedure is used in the off-set null adjustment.

6.3.2(b) Clock generation and timing pulses

Clock pulses are derived from a 1 MH_z crystal oscillator module, shown in Figure 6.7, whose output feeds a T.T.L. master-slave J-K flip-flop (7472) in a "divide by two" mode. The pulses are fed into the clock input of the A.D.C., whose maximum clock period is 1.66 μs. "Start conversion" (S.C.) pulses, (see Section 6.3.2(c) are generated using a divide by 100 pre-scalar I.C. fed directly from the crystal oscillator module, where capacitors C_1 and C_2 provide the necessary power supply decoupling and high frequency bypass to ground respectively.

6.3.2(c) Analogue-to-digital conversion

The ZN427E is an 18 pin device which incorporates tri-state output buffers, a voltage switching D to A convertor, a 2.55V precision reference, a fast comparator and approximation logic. The circuit values of figure 6.7 are used for ± 5 V supply rails, with R_{REF} being chosen to give a value of 6.4 mA and C_{REF} ($\sim$1μF) to provide stabilisation and decoupling. Since the A.D.C. is designed to be fairly insensitive to changes in I_{EXT}, from 25 μA to 150 μA, the value of R_{EXT} , for a-5V rail, is determined to be 82 KΩ (giving I_{EXT} of 65 μA). The output enable pin is connected to the +5 V rail so that when an end of conversion (E.O.C.) pulse occurs the outputs are "enabled" and can be "read". Figure 6.8 shows the internal view of the interface unit.

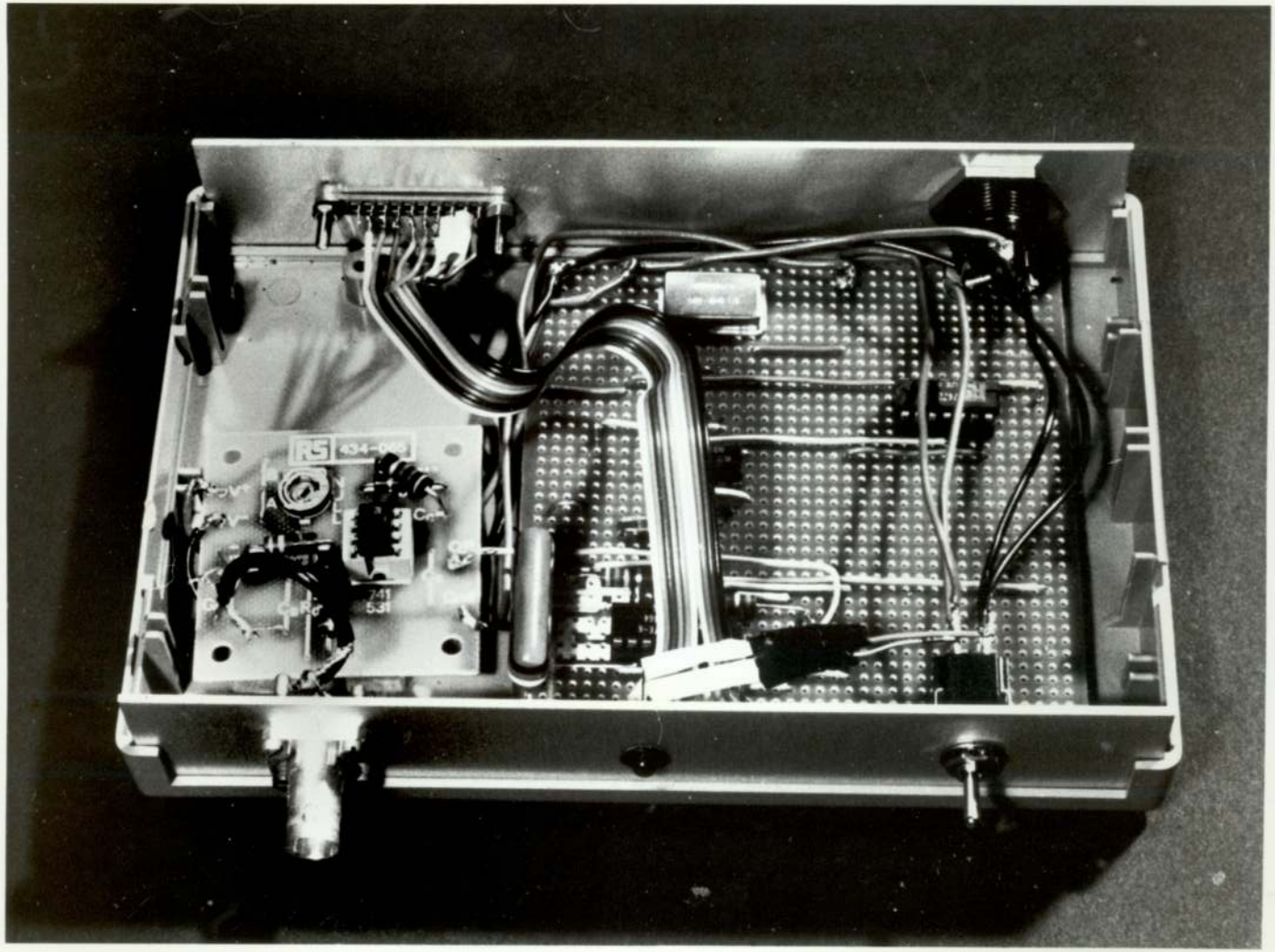

Figure 6.8: Internal view of the interface unit

The conversion sequence is initiated by a "start conversion" pulse (in this case every 100 μs) which sets the most-significant-bit (M.S.B.), pin 11 to 1 and all other bits to 0. A short time is required for the M.S.B. to settle, thus the negative edge of the clock pulse should not occur until 1.5 μs after the negative edge of the S.C pulse. At this stage, with reference to Figure 6.9, a voltage of $\frac{1}{2}$ $v_{ref\ in}$ is produced at the output of the D.to A. convertor

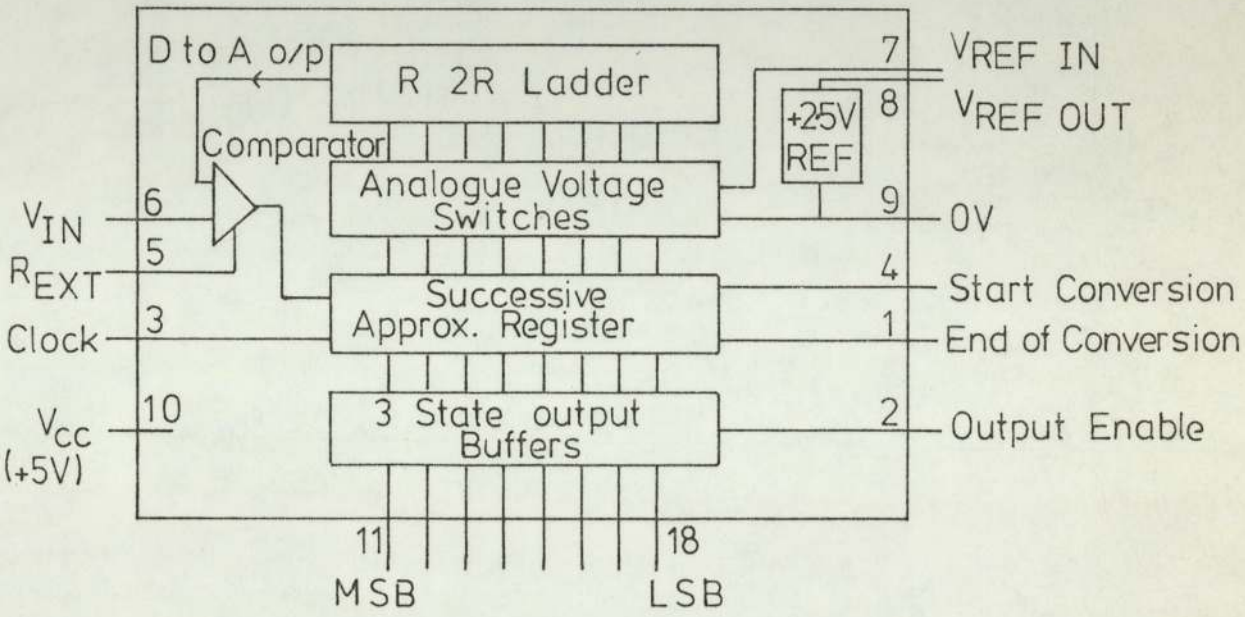

Figure 6.9: Internal structure of the A/D converter

and compared with the input voltage V_{IN}. If $V_{ref\ in} > V_{IN}$, the M.S.B. is set to 0 at the first negative going clock pulse, otherwise a 1 is retained. At the same time bit 2 is switched and again the D to A output is compared with V_{IN} and a 1 or 0 allocated to it. The process is repeated for all 8 bits so that when the E.O.C. pulse goes "high", the 8 bit word is a true representation of the analogue input voltage; this remains valid until the arrival of the next start conversion pulse. Since the output of the A.D.C. is T.T.L. compatible, it can be connected directly to the 8 bit parallel J2 user port on the C.B.M. Commodore P.E.T.

6.3.2(d) Interface connection and choice of software

Figure 6.10 shows the contact identification of the rear edge-on view of the J2 user port connector. The upper contacts are used for diagnostics, while the lower pins are used in connection with the interface. Table 6.1 indicates the pin-identification character and the signal description for the lower pins. The lower contacts A, M and N which refer to digital ground, input/output to the versatile interface adapter (V.I.A.) and digital ground, are not used in the present interface connection. The E.O.C. output from the A.D.C. is connected to C.A.1, which is the edge sensitive input of the 6522 V.I.A. chip, while the digital outputs are connected to the PAØ to PA7 pins (PAØ being the M.S.B. and PA7 the L.S.B.).

Since data has to be recorded and transferred to memory within the PET computer at 100 μs intervals, a BASIC program cannot be used. This is because the time interval to increment the BASIC statements is too long compared to the time between S.C. pulses (100 μs), which would lead to loss of information. Thus, the reading and storing of the digital data has to be performed using a machine code subroutine. As a comparison, the minimum time interval for sampling a large amount of data from an external device when using BASIC is 1/30th sec., while in machine code it is 1/25,000th sec. The outline of the program to accomplish the reading, storing and manipulation of the data will be discussed in the following section.

6.4. System Software

The computer program which is used to obtain the data from the A.D.C. via the parallel user port J2, is shown in Appendix B. The

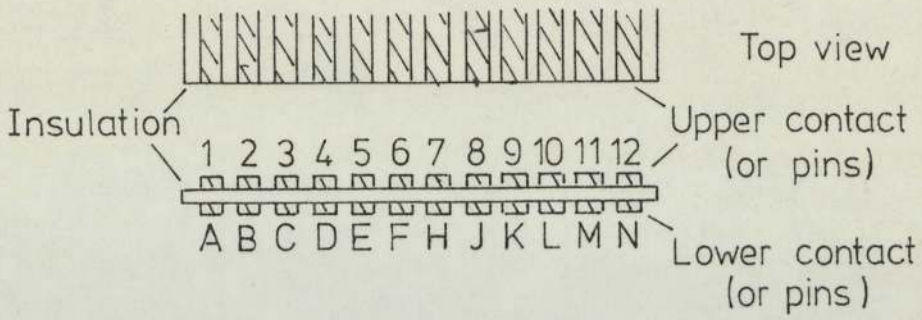

Figure 6.10: Contact identification of the J2 user port

Pin identification character	Signal label	Signal description
A	GND	Digital ground
B	CA1	Standard edge sen. i/p of 6522 VIA
C	PA0	I/O lines to peripherals, which can be programmed idependently of each for input or output
D	PA1	
E	PA2	
F	PA3	
H	PA4	
J	PA5	
K	PA6	
L	PA7	
M	CB2	Special I/O pin of VIA
N	GND	Digital ground

Table 6.1: Pin identification character for the lower pins on the J2 user port

program is written in BASIC and is essentially a closed loop. The machine code subroutine, appearing in the DATA statements, sets the pins PAØ to PA7 as inputs and pin CA1 ready for a positive transition (i.e. E.O.C. pulse) so that information on PAØ to PA7 can be "latched" into the input register of the V.I.A. chip. To enable the machine code program to "run", the first instruction of the subroutine sets the "INTERUPT" (of the V.I.A. chip) thus disabbling the keyboard scanning routine, which operates 60 times a second in the normal BASIC program. Two buffers are used to store the hexadecimal data; in the first, the number of counts (i.e. the number of 100 μs events) in a pulse are recorded (see later), while in the second is located the hexadecimal voltage of each count. Within the subroutine are instructions to prevent the program starting on a "low part" (i.e. positive to negative transition) of the trapezoidal drift tube waveform, shown in Figure 6.11, and also

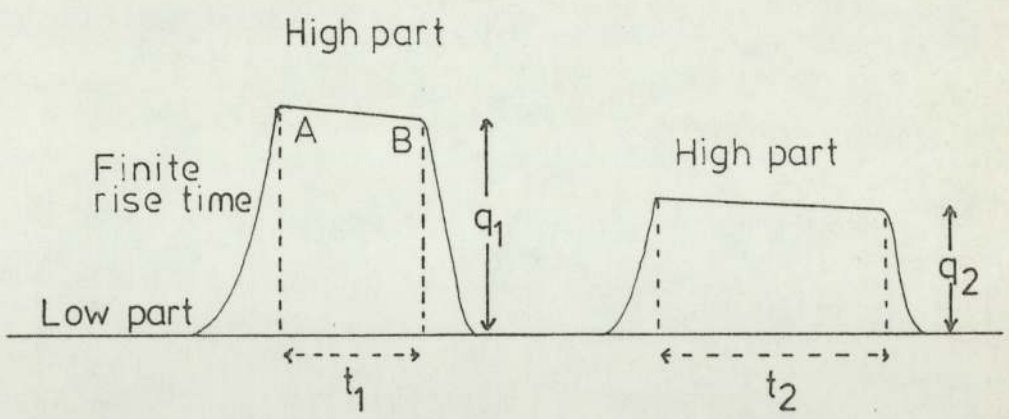

Figure 6.11: Trapezoidal drift tube pulses for a "bouncing" event

to set the threshold level above which readings are stored. At the end of the subroutine is an "END" instruction which returns the PET back to BASIC. The BASIC program then extracts the information from the buffers, converts it from hexadecimal to decimal and displays on

V.D.U. (Visual Display Unit), the number of samples in the first and second trapezoidal pulses, together with the digital voltages of each sample. Once two pulses have been displayed, the program returns to the machine code subroutine to await the next block of data from the A.D.C.

6.5 Data acquisition procedure

The computer program is loaded from tape and can be initiated using the "RUN" command provided the following conditions have been satisfied, (i) the microparticle gun is loaded, (ii) the interface is active and (iii)the d.c. output level of the drift tube amplifier is at zero. At this stage the computer "sits" in the machine code subroutine. The auto-trigger unit is then set to operate the pulse generator (see Section 6.3.1) and to start the production of microparticles. If it is assumed that a pulse of the form shown in Figure 6.11 is produced, which is representative of a "bouncing" event, the trigger unit will latch as soon as the transient input voltage rises above its threshold. At the same time, the interface will have been continually sampling the analogue input voltage from the drift tube amplifier; however,digital information will not have been stored in the buffer locations in the PET unless the signal is above the threshold level designated in the machine code subroutine. Assuming this is the case, the machine code subroutine is "run" and the V.D.U. prints out the number of pulses within each waveform and the corresponding digital voltage of each pulse, see Figure 6.12. For example, if the first pulse contains 10 counts, the time for the whole pulse would be 1 ms, since S.C. pulses occur every 100 μs. It follows that since the length of the drift tube is 1 cm, this is equivalent to a particle having a velocity of 10 ms^{-1}. A corresponding

argument applies to the second pulse. The maximum digital output from the A.D.C. is 1, 1, 1, 1, 1, 1, 1, 1, (decimal equivalent 255), which corresponds to a 2.55V analogue input signal. Thus it is a straightforward process to determine the analogue input voltage from the digital output shown on the V.D.U.

6.5.1 Data capture errors

These can arise from a variety of unwanted signals detected by the drift tube amplifier :-

(i) The returning particle might occasionally "stick" to the drift tube giving rise to a signal which will decay over to a time period > 20 millisecs, (see Section 4.1). If this signal is above the threshold limit, for data storage, digital data will continually be recorded leading to a false pulse length. Since the number of locations available in each buffer is only 256, which is equivalent to a pulse length of 25.6 millisecs, it follows that all the buffer locations can be filled leading to a false pulse length. To reduce this effect it is, therefore, important to ensure that the target surface is aligned accurately at 90° to the incoming particle.

(ii) In the present facility microspheres emerge from the drift tube and pass through an earthed grid before impacting on the target surface, see Figure 3.6. Since this grid has only a 90% particle transparency there is finite number of events where a microsphere passes through the drift tube but does not arrive at the target. In this case a single pulse is recorded and in any subsequent event, only the first trapezoidal pulse will

be measured, since to return from the machine code subroutine requires that two pulses have been detected by the drift tube.

(iii) A further spurious effect arises from a switching transient (from the pulse unit) sometimes being present, which is counted as the first pulse, thus producing a similar effect to that above.

To accommodate all of the above problems the BASIC program, shown in Appendix B, has been modified to store and display three separate pulses (see Appendix C). Thus if triggering occurs via a single switching transient two buffer locations are still available to store a complete microparticle event.

Finally it is important to discuss the reasons for choosing a 100 μs start conversion pulse and this can be considered with regard to the data presented on the V.D.U. from the capture of a single or double trapezoidal event, shown in Figure 6.12. Firstly, the 100 μs interval is easy to generate from a 1MHz crystal oscillator via a prescaler I.C. While secondly the trapezoidal pulse, by nature, has a finite rise time, see Figure 6.11, hence data is stored before the pulse reaches its maximum height, with the same process occurring on the fall of the pulse. Since the length of the pulse is determined from A to B, see Figure 6.11, counting errors arise. Thus if the S.C. pulses occur every 50 μs these errors would increase and if a larger conversion time is used, percentage errors would be large, especially for the high speed particles, (i.e. short times within the drift tube). Therefore 100 μs appears to be the best compromise to reduce the errors. Since erroneous counts arise from the measurement of a trapezoidal pulse, data is not automatically analysed, at present, but is transferred, manually, into a BASIC program shown in Appendix D, which calculates

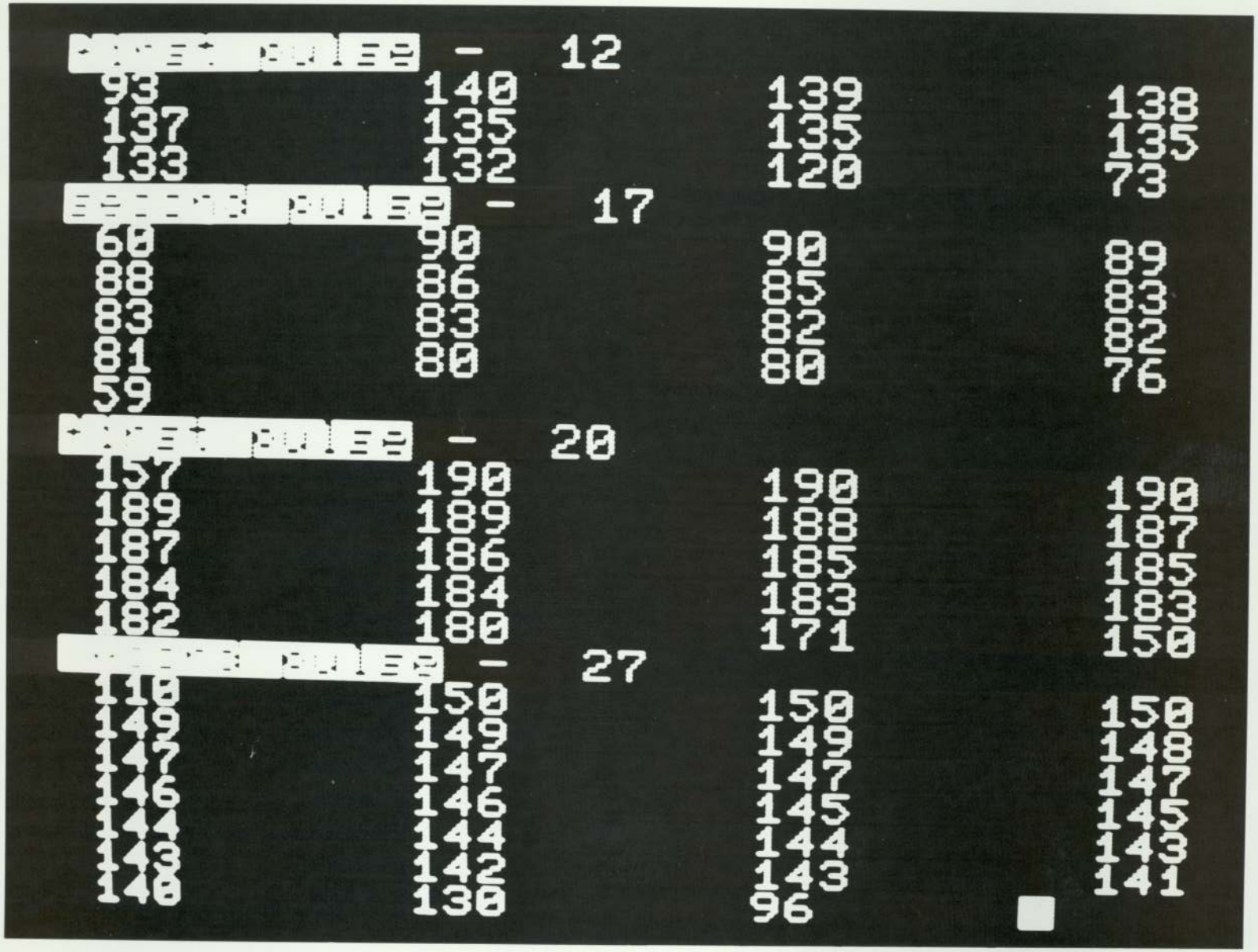

Figure 6.12: Typical V.D.U. display

the INCIDENT VELOCITY (U), the RETURN VELOCITY (V), the COEFFICIENT OF RESTITUTION (e), the INCIDENT PARTICLE CHARGE (q_1), the REFLECTED PARTICLE CHARGE (q_2) and the CHARGE MODIFICATION (q_2/q_1). No mathematics are required before entering the data into this program, only the number of counts and the maximum digital voltage is needed.

6.6 Future improvements

Whilst the system described in this chapter goes a long way towards the development of a fully automated data acquisition process, there are, however, several limitations which require some future modification,

(i) At present, the auto-trigger unit is manually re-set after a pulse has been recorded, whereas, ideally, contact M on the J.2. user port (see Section 6.3.2(d) could be used as a control, such that when two/three trapezoidal pulses have been stored, a positive transition from the C.B.2 pin (contact M) resets the auto-trigger unit.

(ii) A new "solid state" pulse unit should be substituted for the older valve unit currently being used, since the latter represents a source of electronic noise, which while not important in the pulse generation of the microparticle, can represent an intolerable level of interference with the signals associated with the interface.

(iii) To reduce the counting errors, it has been pointed out, in Section 6.5.1, that a particle should remain in the drift tube for a maximum period of time so that, in the timing sequence, a large number of counts can be taken.

This can be realised either by (a) slowing down the microparticles by using lower microparticle gun voltages, see Section 3.3.2, or (b) increasing the length of the drift tube. Of these options (b) is the more ideal, since (a) could lead to an unacceptable reduction in the probability of a particle being generated by each triggering pulse.

By incorporating all of the above refinements, it is possible to visualise a complete automatic system in which data is extracted, processed and presented as the parameters outlined in the dynamic hardness section. As a final comment, it should be pointed out that even though the present system has a spatial resolution of 200 μm^2, modifications to the microparticle collimating system could produce an impact microzone of < 50 μm^2.

6.7 Dynamic hardness measuring procedure

When using the complete data acquisition system as the basis of a microscopic dynamic hardness testing device, it is necessary, as explained in Section 6.1, to record at least 100 consecutive events of the type shown in Figure 6.11, for each microzone. However, before considering in detail how the recorded information is processed, it is important to note three important advantages that this technique has over conventional hardness testing tools. Firstly, the present system has the facility for a rapid 'turn-over' of data, in that once the information from a given "test" impact site has been obtained, a second site can be selected on the 'test' sample. In this way, the variation in hardness across the 'test' surface can be rapidly measured. Secondly, the data is obtained from a 200 μm^2

test impact area which is sufficiently localised to reveal variations in the microscopic hardness across the test surface. This in marked contrast to the extended area measurements of conventional macroscopic hardness testing systems. Finally, the process described in this paper is non-destructive in nature, which implies that the surface returns to the same mechanical state that it had before being "tested". It should be pointed out that in conventional static hardness testing systems, the test surface would undergo structural changes during the loading period.

The recorded data, from the computer program shown in Appendix D, has been used to provide four types of information relating to the parameters defined at the end of the last section,

(i) A graph of the impact velocity 'u' versus the coefficient of restitution 'e', showing how the surface under test behaves as the impact velocity increases. A typical plot obtained for mica is shown in Figure 6.13, where the

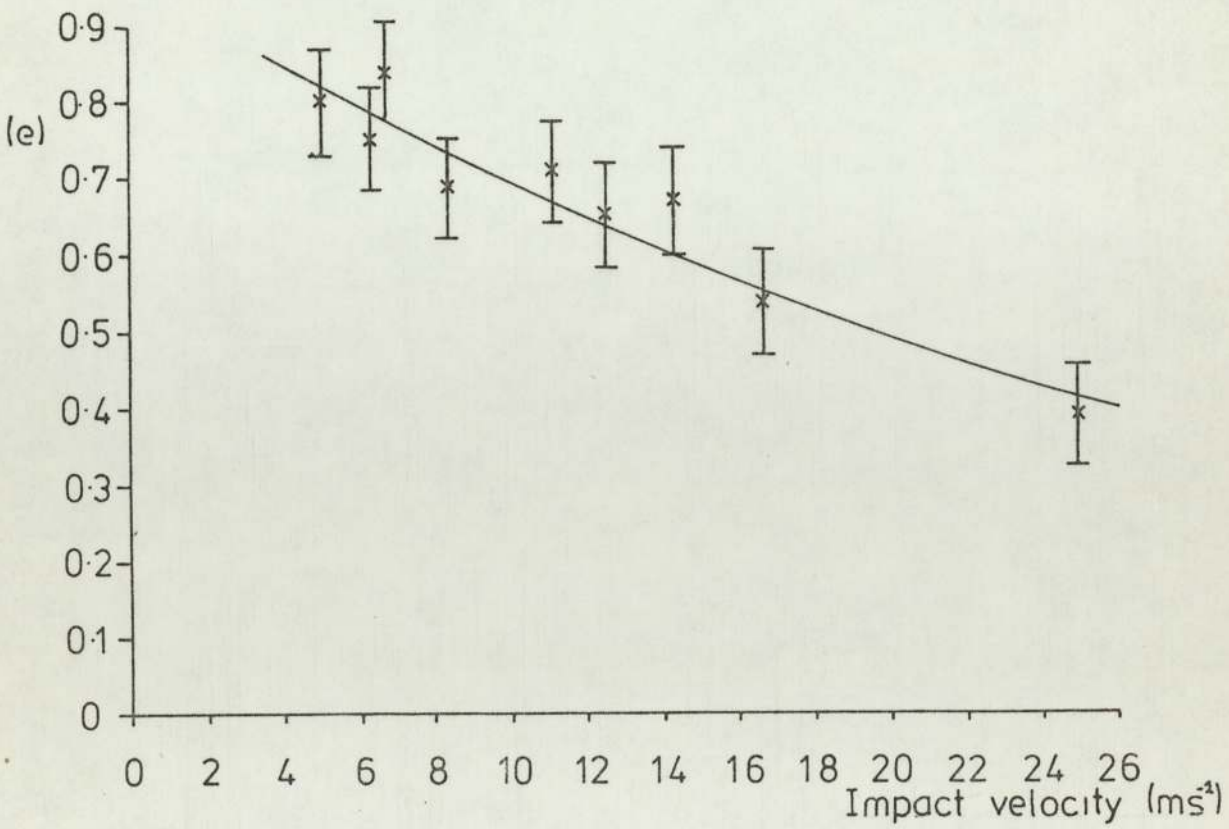

Figure 6.13: The variation of the coefficient of restitution with impact velocity for the mica surface

error bars indicate the "spread" about the average 'e' value. Generally a high 'e' value corresponds to a high dynamic hardness and indicates that a small amount of energy has been lost in the collision.

(ii) The variation in the hardness between neighbouring 200 μm^2 zones on a cellulose target is indicated by the histograms shown in Figure 4.10. It is readily observed that the peak in the distribution is not constant which is further evidence that the hardness of a surface needs to be measured on the micron scale.

(iii) A plot of log $e^2 v^2$ against log v from which the gradient (n) and intercept (K) can be related to the hardness and material constants of the specimen. Typical plots are shown in Figure 4.12 for P.V.C. and mica which yield gradient and intercept values of n = 2.44, K = 0.175 (for mica) and n = 2.89, K = 0.0322 (for P.V.C.). Generally as $n \rightarrow 2$ and $K \rightarrow 1$, the impact becomes more elastic resulting in a higher dynamic hardness value, see Section 5.2.9.

(iv) The charge modification ratios (q_2/q_1) can be related to the size of the contact area, and the type of contact. For a highly deformable solid, the contact area is larger resulting in more charge being "rubbed off" in the contact process, while for surfaces possessing many microinhomogeneties, multiple contacts can arise resulting in a similar charge reduction process.

CHAPTER 7

7.0 Conclusion

It has been established that the impact process between a positively charged microsphere and a planar target electrode surface is highly complex involving a wide range of physical processes. Although the mechanical and electrical effects of any impact event are inter-related, they have, for convenience, been dealt with separately. On this basis, the theoretical analysis of the fundamental mechanical and electrical processes which occur in the impact event, has involved respectively the mechanisms by which energy may be lost during an impact (i.e. elastic waves) and all the charge interaction and exchange theories suitably modified for the zero field conditions of this study. Included in these categories are the calculations of the attractive forces occurring before and during the impact, i.e. Van der Waal and image force, and the contact adhesive force arising from molecular attractions.

In order to investigate the relative influence of these processes, a simulation technique has been used in which low velocity, positively charged, carbonyl iron microspheres, produced from a dust-source gun, are fired vertically downwards onto a range of target surfaces where the impact "test" zone is $\sim(200\mu m)^2$. The particles are characterised in terms of their charge and velocity using a drift tube detector placed before the target so that the data obtained from the incident and reflected particles can be used to calculate the coefficient of restitution and charge modification ratio which are respectively assumed to be indicative of the mechanical and electrical impact processes. The target surface oxide condition has been found to play a particularly important role in the impact

interactions, and for studying this a laser-based ellipsometer has been used for characterising the target surfaces. Measurements have been made on ambient oxided metal, semi-conducting, highly oxidised metal and insulating surfaces. In addition, a detailed survey has been made on how the variation of the thickness of the oxide on an aluminium surface influenced the resulting impact process. A particularly useful technique involving a microprobe has also been developed which allows a microsphere to be removed from its impact site, either by mechanical movement or under the action of an applied electric field, and thereby gives a clearer indication of the impact phenomena that have occurred at the contact junction.

The most notable finding to emerge from these measurements was that certain combinations of impacting surfaces promote "bouncing" events while others show only "sticking" events. The former events are characterised by some of the initial particle charge being "dumped" on the target surface so that the reflected particle has both a lower charge and velocity; in the latter case, all the charge is "dumped" on the target and no "return" particle is observed. It was found that, with the exception of aluminium, for all the ambient oxide metal surfaces studied, $\sim$99% of the incident carbonyl iron microspheres"stick" to the surface on impact; for the aluminium target $\sim$10% of the incident particles "bounce" with a reduced positive charge. In the case of highly oxidised (metal and semi-conducting) surfaces, it is observed that the incidence of particle "bouncing" increases as the surface oxide thickness increases. In contrast to the above behaviour, insulating target surfaces give rise to $\sim$ 99% "bounding" events. Accordingly, it was possible to apply the technique to measure the microscopic mechanical properties of this type of

target in terms of the e-values.

Although such measurements exhibit trends which are similar to those observed in macro systems, they also highlighted two important differences between the micro and macro systems: namely that (i) in the micro system the critical velocity for an inelastic process has a much higher value compared with macro systems, and (ii) micro systems exhibit a larger scatter in their impact data.

In considering the electrical phenomena associated with the impact of charged microspheres on highly oxidised and insulating targets, it has been observed that there is generally a loss in charge during the impact process, whose magnitude depends on the size of the charge on the impacting microsphere: i.e., particles possessing a high charge invariably "stick" to the target surface while small charged particles "bounce" with some form of charge modification. This dependance of the nature of the impact event on the microsphere charge is also borne out by the microprobe data referred to above where impact surface "damage" was found to be related to both the size of the microsphere and the type of target material.

The experimental data has been discussed in terms of the theoretical concepts reviewed in Chapter 2, to provide a physical explanation for the "sticking" and "bouncing" phenomena. In the case of a microsphere/insulator target contact, the loss of K.E. during a "bouncing" impact can be attributed mainly to the softness of the target material, and the surface microtopography of the target. The associated loss of electrical charge is not, however, related to any form of charge exchange, but instead arises from charge being "rubbed" off the particle during the contact process as a result of the

surface deformation, contact area and surface topography of the target. For an impact event occurring between a microsphere and an ambient oxided metal, semi-conducting or highly oxidised metal surface the attractive forces arising from Van der Waal and image charge interactions, together with the adhesive force, play only a minor role in the impact behaviour. Hence a model based on a thermal heating process arising from the electron-phonon scattering in the contact oxide junction, where charge exchange is taking place, is favoured to explain the "sticking" and "bouncing" phenomena. According to this interpretation the temperature rise is thought to cause either a microweld or increased adhesive forces during the contact time which is sufficient to cause a particle to "stick" to the surface. This model also takes into account the dielectric constant of the oxide film, together with the relative work functions of the microsphere/target combination, and suggests that there will be a reduced temperature rise in the tunnelling junction as the surface oxide thickness increases which is the reason for the advent of "bouncing" events. Finally, the anomalous behaviour of the ambient oxided titanium and aluminium surfaces (where charge reversal is observed) can be explained in terms of the difference in the relative work functions of the interacting materials.

The most important technological implication arising from this study is the use of the technique to study, non-destructively, the mechanical properties of extended surfaces. To demonstrate this, a computer controlled data handling system was developed which enables on-line acquisition of the velocity and charge of a "bouncing" particle. Using this system it is possible to determine (i) the variation of the coefficient of restitution with the impact velocity, which can lead to information on the hardness of the "test" surface.

and (ii) the variation of log e^2v^2 as a function of log v (where v is the reflected particle velocity), which if plotted gives a straight line where the gradient (n) and intercept (K) values can be related to the elasticity of the surface, such that as $n \rightarrow 2$ and $K \rightarrow 1$ the impact process becomes more elastic. Thus, these microsphere impact studies can be used as the basis of a microprobe dynamic hardness technique which possesses many advantages over conventional hardness testing devices: Thus (i) it allows a rapid "turnover" of data in that once a "test" impact zone has been examined a second test site on the same sample can be selected in-situ, (ii) the process is non-destructive and leaves the surface with the same mechanical properties before and after the test and (iii) the test zone is $\sim (200\ \mu m)^2$ where in conventional devices measurements are determined over an extended area.

Finally, it can be said that the theoretical analyses and experimental developments of this study have gone a long way to clarifying the physical nature of the particle impact response. However, there remain several areas where future investigations may lead to a better understanding of the impact phenomena. Firstly, a "mono-sized" particle should be used since the variations of the particle charge arising from the typical spread of microsphere sizes influences the impact phenomena. Secondly, the role played by the non-uniform surface oxidation of a polycrystalline target still needs further clafication. Thirdly, the impact behaviour of particles on atomically clean metallic electrodes should be studied under zero field conditions, since the "sticking" phenomena is closely related to the contaminating surface oxide thickness. It should also be mentioned that the extension of the dynamic hardness microprobe system to clean metal surfaces would also be highly advantageous since at

present only data from the "bouncing" impact of charged microspheres on highly oxidised metal and insulating surfaces has been processed. In this context the microparticle gun should be modified to allow insulating microspheres to be "fired" at metallic surfaces. Also the automatic data acquisition process needs further improvement so as to produce a viable commercial unit. This would entail modification of the computer software and complete control of the microparticle pulse generator unit, (see Section 6.6).

APPENDIX A

A.1 Ellipsometry - Basic Principles

The underlying principles involved in ellipsometry lie in the theory relating to the reflection of electromagnetic radiation from a surface as outlined by Drude,(158,159,160,161). However, the optical technique was not developed until sometime later when Tronstad (162) and Winterbottom (163) used it to study surface contamination and corrosion effects.

In the consideration of light reflected from a surface there are two principal directions to which reference is normally made; these are parallel and perpendicular to the plane of incidence and are often denoted as azimuth directions. Referring to Figure A1, consider light in medium (O) being reflected in the interface of medium (1), where n_0 and n_1 are the refractive indices of the two mediums respectively, ϕ_0 the angle of incidence and ϕ_1 the angle of refraction. For such a regime the Fresnel reflection coefficients for light reflected at the interface between media 0 and 1 are given by $r_{01}(p,s)$, where r is the amplitude of the reflected light vector divided by the amplitude of the incident light vector. i.e.,

$$r_{01}(p) = \frac{(n_0 \cos\phi_1 - n_1 \cos\phi_0)}{(n_0 \cos\phi_1 + n_1 \cos\phi_0)} \quad \ldots\ldots \text{A.1}$$

and

$$r_{01}(s) = \frac{(n_0 \cos\phi_0 - n_1 \cos\phi_1)}{(n_0 \cos\phi_0 + n_1 \cos\phi_1)} \quad \ldots\ldots \text{A.2}$$

In these equations p and s refer, respectively to vectors parallel and perpendicular to the plane of incidence. Similar expressions are obtained for the transmission coefficients. The relationship of these reflection

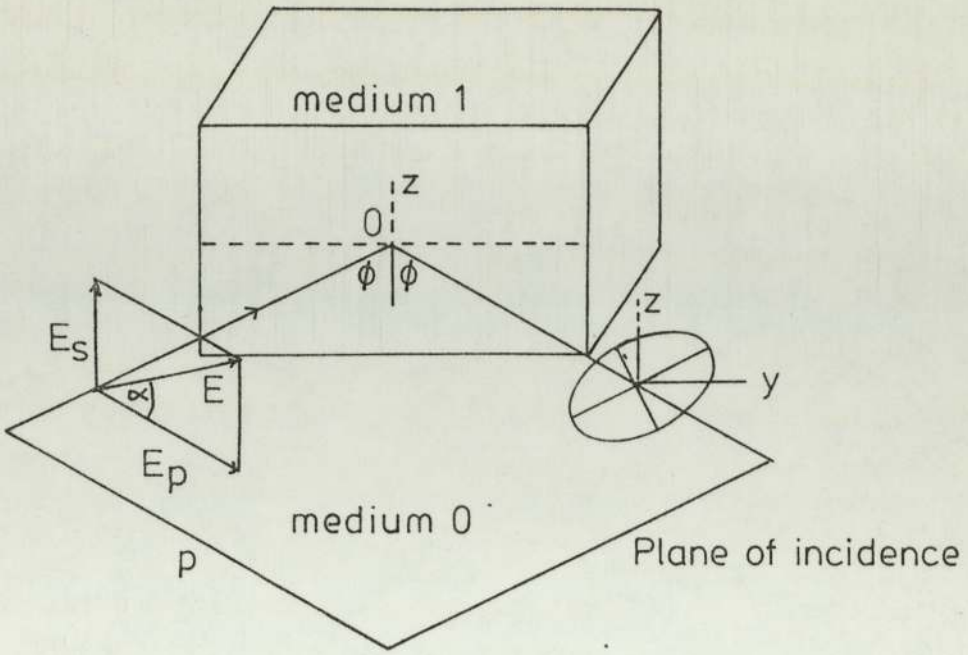

Figure A.1: Reflection of plane polarised light at the interface between medium 0 and 1

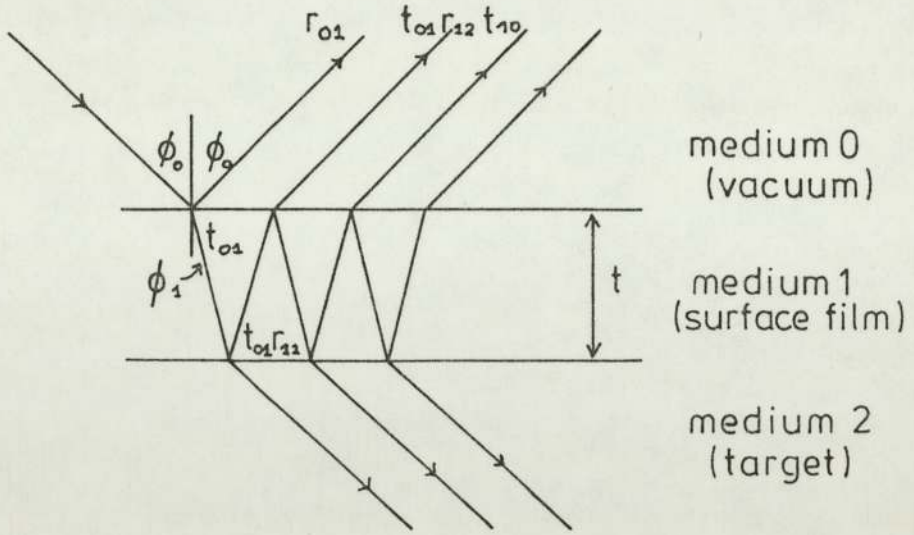

Figure A.2: Reflections in a surface film

coefficients to the instrument readings Δ and Ψ (see Section 3.6.2) is given by

$$\frac{r_p}{r_s} = \tan\Psi e^{i\Delta} \qquad \ldots A.3$$

The polariser and analyser values determine the angles Δ and Ψ respectively which represent the amplitude and phase retardation of the reflected light.

A.1.1 Non-absorbing materials

Figure A.2 shows that the incidence of light on an oxide covered surface can give rise to multiple reflections and transmissions. If the incident ray has unit amplitude, then r_{01} represents the amplitude of the transmitted ray at the (0,1) interface. A similar argument can be put forward for r_{12} and t_{12} at the (1,2) interface. The phase difference between successive reflected and transmitted rays depends on the film thickness (d), the angle ϕ_1 the radiation wavelength (λ) and the refractive index of the film or layer. The Fresnel reflection coefficients for such a surface are given by :

$$r_p = \frac{r_{01}(p) + r_{12}(p)\exp D}{1 + r_{01}(p)r_{12}(p)\exp D} \qquad \ldots A.4$$

with a similar expression for r_s, where

$$D = \frac{4\cos\phi_1 n_1 d}{\lambda} \qquad \ldots A.5$$

A.1.2 Absorbing materials

The property that characterises an absorbing media is that if possesses a complex refractive index such that $N_1 = n_1 - ik_1$, i.e. it absorbs power. Thus the Fresnel coefficients become complex, together with D which is given by :

$$D' = \frac{4\pi i \cos\phi_1 N_1 d}{\lambda} \qquad \ldots A.6$$

Ditchburn (164) has shown that for a film free surface, the values of n and k are related to the parameters Δ and Ψ, obtained from the instrument reading. Thus it follows that

$$n^2-k^2 = \sin^2\phi_o[1 + \tan^2\phi_o(\cos^2 2\Psi - \sin^2 2\Psi \sin^2\Delta)(1 + \sin 2\Psi \cos\Delta)^{-2}] \qquad \ldots A.7$$

and $$2nk = (\sin^2\phi_o \tan^2\phi_o \sin 4\Psi \sin\Delta)(1 + \sin 2\Psi \cos\Delta)^{-2} \qquad \ldots A.$$

which are equations giving n and k independent of ϕ_1 Hence by measuring Δ and Ψ, together with the angle of incidence, the optical constants n and k can be evaluated for the film free surface. As the surface film grows Δ and Ψ will change, yielding the pseudoconstants n′ and k′ which are evaluated, ignoring the preserve of the surface film from the instrument angles Δ' and Ψ'.

A.1.3 The compensator method of ellipsometry

The method described here is applicable to both the arrangement shown in Figure 3.23 and the Mark II laser system outlined in Section 3.6.2. After passing through the polariser, light becomes plane polarised and is incident upon the specimen at an angle Ψ defined as the angle between the plane of polarisation and the plane of incidence, i.e., as shown in Figure A.3. On reflection, from the specimen, the light becomes elliptically polarised with (i) a reduction in amplitude of thebeam and (ii) the parallel (p) and perpendicular (s) components suffering a phase change with respect to each other. Ellipticity arises because the tip of the electric vector rotates in an ellipse with an ellipticity χ (i.e., the ratio of the minor to the major axis and azimuth X of the major axis).

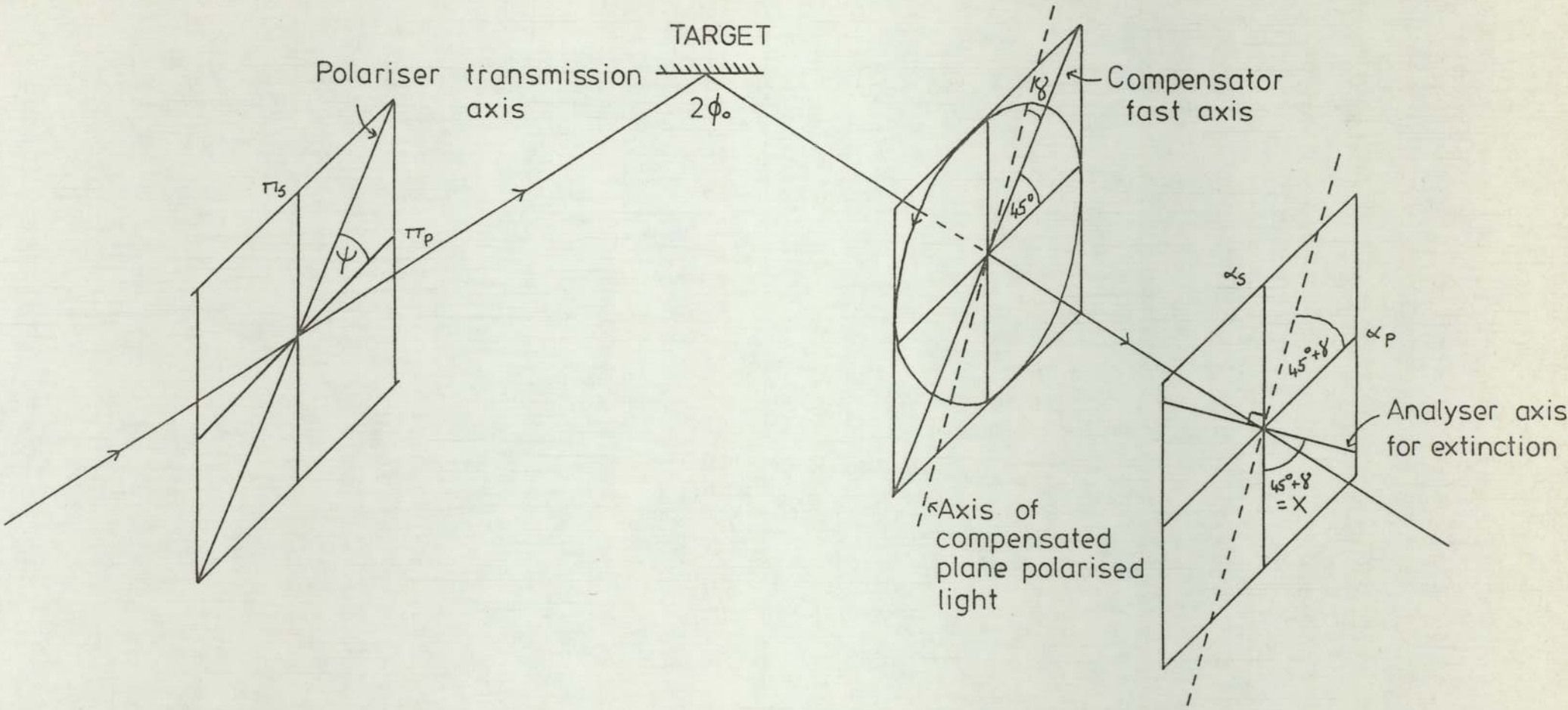

Figure A.3: Transmission axes for an alligned ellipsometer

The elliptically polarised light passes through a compensator consisting of a thin slice of birefringent substance (such as mica), orientated so that its optic axis is parallel to the surface of the slice, and emerges as plane polarised light. Finally light passes through an analyser and determination of its azimuth γ is found by rotating the analyser polaroid until zero or a minimum intensity occurs at the photomultiplier. This condition only arises when the analyser transmission axis is set at 90° to the direction of light emerging from the compensator (see Figure A.3). To simplify the procedure the compensator is set so that its fast axis is at 45° to the plane of incidence resulting in the amplitude of the reflected (p) and (s) components, (i.e. Ep and Es) being equal. The ellipticity γ is related to the phase difference occurring betweenthe (p) and (s) components by

$$\tan \Delta : \quad \frac{\tan 2\gamma}{\sin 2X} \qquad \ldots \text{A.9}$$

but since X = 45° it follows that sin 2.x = 1,

$$\text{i.e.} \quad \tan \Delta = \tan 2\gamma$$
$$\text{or} \quad \Delta = 2\gamma \qquad \ldots \text{A.10}$$

It can be readily observed from Figure A.3, that the azimuth of the compensator and analyser are both at 45° + γ, which is the extinction position for the analyser. This azimuth is 45° + γ with respect to $\propto$p which is parallel to the plane of incidence. Experimentally, it is the total angle (45° + γ) that is measured

$$\text{thus} \quad X = 45° + \gamma = 45 + \Delta/2$$

$$\text{giving} \quad \Delta = 2X - 90° \qquad \ldots \text{A.11}$$

There are four possible settings for extinction when the compensator is used, with four polariser and analyser values for each. The parameters

Δ and Ψ are usually determined from an average of 32 possible readings in a manner described by McCracken et al(165) and Archer.(166). However, in practice, it is usual to obtain four pairs of polarizer and analyser readings for two positions of the compensator.

APPENDIX B.1

Computer program for storing two trapezoidal waveforms

```
REM=== DATA CAPTURE
REM===
REM=== RESET SIZE OF MACHINE
PRINT"3" : POKE53,47 : CLR
REM=== DECLARATIONS
DC=826 : N$="" : LD = 3*4096 : LC = 3*4096+5*256
REM=== MACHINE CODE LOADER
FORI=DC TO  1000
READN$ : IF N$<>"END" THEN GOSUB1900:POKEI,N:PRINT"I,N:NEXTI
REM=== MAIN DATA CAPTURE PROGRAM
PRINT"3"
SYS DC
X = PEEK(LC) : Y = PEEK(LC+1)
PRINT"FIRST PULSE2 - "X" READINGS"
FORI=0TOX-1 : PRINT PEEK(I+LD) , : NEXT I : PRINT
PRINT"SECOND PULSE2 - "Y" READINGS"
FORI=XTOY-1 : PRINT PEEK(I+LD) , : NEXT I : PRINT
GO TO 1200
REM
N = 0 : FOR Z = 1 TO LEN(N$)
L$=MID$(N$,Z,1)
IF L$=>"0" AND L$<="9" THEN N = N * 16  + VAL(L$)
IF L$=>"A" AND L$<="F" THEN N = N * 16  + ASC(L$) - 55
NEXT Z
RETURN
REM=== DATA
DATA 78
DATA A0,00
DATA A2,00
DATA 20,64,03
DATA AD,4D,E8
DATA 29,02
DATA F0,F9
DATA F0,F9
DATA AD,41,E8
DATA C9,30
DATA 90,07
DATA 9D,00,30
DATA E8
DATA 4C,3F,03
DATA 8A
DATA F0,E3
DATA 99,00,35
DATA C8
DATA C0,02
DATA D0,DB
DATA 58
DATA 60
DATA AD,4B,E8
DATA 09,01
DATA 8D,4B,E8
DATA AD,4C,E8
DATA 09,01
DATA 8D,4C,E8
DATA A9,00
DATA 8D,43,E8
DATA 60
DATA "END"
```

APPENDIX C.1

Computer program for storing three trapezoidal waveforms

```
REM=== DATA CAPTURE
REM===
REM=== RESET SIZE OF MACHINE
PRINT"3" : POKE53,47 : CLR
REM=== DECLARATIONS
DC=826 : N$="" : LD = 3*4096 : LC = 3*4096+5*256
REM=== MACHINE CODE LOADER
FORI=DC TO 1000
READN$ : IF N$<>"END" THEN GOSUB1900:POKEI,N:PRINT"";I,N:NEXTI
REM=== MAIN DATA CAPTURE PROGRAM
PRINT"3"
SYS DC
X = PEEK(LC) : Y = PEEK(LC+1) : Z=PEEK(LC+2)
PRINT"FIRST PULSE2 - "X" READINGS"
FORI=0TOX-1 : PRINT PEEK(I+LD) , : NEXT I : PRINT
PRINT"SECOND PULSE2 - "Y" READINGS"
FORI=0TOY-1 : PRINT PEEK(I+LD+256 ) , : NEXT I : PRINT
PRINT"THIRD PULSE2 - "Z" READINGS"
FORI=0TOZ-1 : PRINT PEEK(I+LD+512 ) , : NEXT I : PRINT
GO TO 1200
REM
N = 0 : FOR Z = 1 TO LEN(N$)
L$=MID$(N$,Z,1)
IF L$=>"0" AND L$<="9" THEN N = N * 16  + VAL(L$)
IF L$=>"A" AND L$<="F" THEN N = N * 16  + ASC(L$) - 55
NEXT Z
RETURN
REM=== DATA
DATA 78
DATA A0,00
DATA A2,00
DATA 20,64,03
DATA AD,4D,E8
DATA 29,02
DATA F0,F9
DATA F0,F9
DATA AD,41,E8
DATA C9,30
DATA 90,07
DATA 9D,00,30
DATA E8
DATA 4C,3F,03
DATA 8A
DATA F0,E3
DATA 99,00,35
DATA C8
DATA C0,02
DATA D0,DD
DATA 58
DATA 60
DATA AD,4B,E8
DATA 09,01
DATA 8D,4B,E8
DATA AD,4C,E8
DATA 09,01
DATA 8D,4C,E8
DATA A9,00
DATA 8D,43,E8
DATA 60
DATA "END"
```

APPENDIX D.1

Computer program for handling the trapezoidal data

```
FOR I=1TO3
READ A(I)
DATA 10,20,50
FOR J=1TO3
READ B(J)
NEXT
DATA 2,4,5
FOR K=1TO3
READ C(K)
NEXT
DATA 10,20,50
FOR M=1TO3
READ D(M)
NEXT
DATA 20,20,20
FOR P=1TO3
T=C(P)/D(P)
Q=B(P)/A(P)
U=10/C(P)
V=10/D(P)
K=(1E-16)*A(P)
L=(1E-16)*B(P)
PRINT"U="U;"V="V;"E="T;"Q1="K;"Q2="L;"Q="Q;
NEXT
```

LIST OF REFERENCES

1. Brah, A.S., and Latham, R.V., J. Phys. E.: Sci.Instrum. 9, 119 - 23, (1976)

2. Shelton, H., Hendricks, C.D., and Wuerker, R.J., J. Appl. Phys. 31, 1243-50, (1960)

3. Friichtenicht, J.F., Rev. Sci. Instrum. 33, 209-14, (1965)

4. Brah, A. S., Ph.D. thesis, University of Aston, (1977)

5. Mohindra, S., Ph.D. thesis, University of Aston, (1981)

6. Latham, R.V., J. Phys.D.: Appl. Phys. 5, 2044-54, (1972)

7. Cranberg, L., J. Appl. Phys. 23, 518-22, (1952)

8. Slivkov, I. N., Sov. Phys. Tech. Phys. 2, 1928-34, (1957)

9. Latham, R.V., and Brah, A.S., J. Phys. D.: Appl. Phys. 10, 151-167, (1977)

10. Bjork, R.L., Proc. VIth Sym. on Hypervelocity Impact (U.S. Dept. of Commerce, Washington, D.C.), 2, 1, (1963)

11. Cook, M.A., The Science of High Explosives, (New York: Reinhold), (1958)

12. Hertz, H., J. Reine, Agnew. Math., 92, 156-165, (1889)

13. Hutchings, I.M., J. Phys. D.: Appl.Phys. 10, L179-83, (1977)

14. Andrew, J.P., Phil. Mag. 9, 593-610, (1930)

15. Tabor, D., The Hardness of Metals (Oxford: Clarendon Press), (1951)

16. Timoshenko, S., Theory of Elasticity (New York: McGraw-Hill), (1934)

17. Davies, R.M., Proc. Roy.Soc. London. A197, 416-432, (1949)

18. Ishlinsky, A.J., J. Appl. Math. Mech. (U.S.S.R.). 8, 233-258, (1 44)

19. Tabor, D., Proc. Roy. Soc. Am. A192, 247-74, (1948)

20. Uetz, H., and Gommel, G., Wear. 9, 282-296, (1966)

21. Lamb, H., Phil. Trans. Roy. Soc. A203, 1-42, (1904)

22. Raman, C.V., Phys. Rev. 15, 277-284, (1920)

23. Hunter, S.C., J. Mech. Phys. Solid. 5, 162-171, (1952)

24. Miller, G.F., and Pursey, H., Proc. Roy. Soc. A223, 521-541, (1954)

25. Miller, G.F., and Pursey, H., Proc. Roy. Soc. A233, 55-69,(1955)

26. Lathan, R.V., Brah, A.S., Fok, K., Woods, M.D., J. Phys. D.: Appl Phys. 10, 139-151, (1977)

27. Hutchings, I.M., J. Phys. D.: Appl. Phys. 12, 1819-1824, (1979)

28. Bitter, J.G.A., Wear. 6, 5-21, (1963)

29. Chaudhri, M., Wells, J.K., and Stephens, A., Phil. Mag. A. 43, 643 - 664, (1981)

30. Dietzel, H., Neukum, G., and Rauser, P., J. Geophys. Res. 77, 1375-95, (1972)

31. Rudolph, V., Z. Naturforsch. 24a, 326-331, (1969)

32. Smith, D., and Adams, N.G., J. Phys. D.: Appl. Phys. 6, 700-719, (1973)

33. Auer, S., and Sitte, K., Earth Planet Sci. Letters. 4, 178-183, (1968)

34. Hansen, D.D., Appl. Phys. Letters, 13, 89-91, (1968)

35. Schottkey, W., Z. Physik, 14, 63-106, (1923)

36. Fowler, R.H., and Nordheim, L., Proc. Roy. Soc. A119, 173-81, (1928)

37. Young, R., Ward, J., and Scire, F., Phys. Rev. lett. 27, 922-4, (1971)

38. Simmons, J.G., J. Appl. Phys. 34, 1793-1803, (1963)

39. Simmons, J.G., J. Appl. Phys. 34, 2581-2596, (1963)

40. Sommerfeld, A., and Bethe, H., Handbuck der Physik von Geiger und Sched, (Julius Springer-Verlog, Berlin), 24/2, p. 450, (1933)

41. Holm, R., J. Appl. Phys. 22, 569-74, (1951)

42. Miles, J.L., and Smith, P.H., Sol. State.Elect. Dev. Conf. (Univ. of Michigan), (1 63)

43. Simmons, J.G., J. Appl. Phys. 35, 2472-81, (1964)

44. Menon, M.M., and Srivastava, K.D., J. Appl. Phys. 45, 3832-35, (1974)

45. Beukema, G.P., J. Phys. D.: Appl. Phys. 7, 1740-55, (1974)

46. Olendzkaya, N.S., Rad. Eng. and Elec. Phys. 8, 423-9, (1963)

47. Martynov, E.P., and Ivanov, V.A., Rad. Eng. and Elec. Phys. 14, 1732-35, (1969)

48. Udris, Y., Rad. Eng. and Elec. Phys. 5, 226-37, (1960)

49. Chakrabarti, A.K., and Chatterton, P.A., Proc. VIth Int. Cont. on Disch. and Elec. Ins. in Vac. Swansea, 16-21, (1974)

50. Martynov, E.P., Soc. Phys. Tech. 16, 1364-8, (1972)

51. Chatterton, P.A., Menon, M.M., and Srivastava, K.D., J. Appl. Phys. 43, 4536-42, (1972)

52. Lorraine, P. and Corson, D.R., Electromagnetic Field Waves, (San Francisco: W.F. Freeman & Co.), (1970)

53. Miller, H.C., J. Appl. Phys. 38, 4501-4, (1967)

54. Morse, P.M., and Feshbach, H., Methods of Theoretical Physics, II, (New York, McGraw-Hill), (1953)

55. Charbonnier, F.M., Bennette, C.J., and Swanson, L.W., J. Appl. Phys. 38, 627-33, (1967)

56. Kawamura, H., Ohkura, M., and Kikuchi, T., J. Phys. Soc. Jap. 9, 541-45, (1954)

57. Hamano, K., Jap. Jour. Appl. Phys. 13, 1085-1092, (1974)

58. Morgan, D.V., Howe, M.J., Pollard, R.D., and Waters, G.P., Thin Sol. Films, 15, 123-131, (1973)

59. Morgan, D.V., Guile, A.E., and Bektore, Y., Thin Sol. Films, 66, 435-438, (1980)

60. Klein, N., and Burstein, E., J. Appl. Phys. 40, 2728-2740, (1969)

61. Klein, N., Advances in Phys. 21, 605-45, (1972)

62. Frohlich, H., Report in the British Electrical and Allied Ind. Res. Assoc. L/T, 113, (1940)

63. Seitz, E.F., Phys. Rev., 76, 1376-1393, (1949)

64. O'Dwyer, J.J., J. Phys. Chem. Solids, 28, 1137-1144, (1967)

65. O'Dwyer, J.J., J. Appl. Phys. 40, 3887-90, (1969)

66. Shockley, W., Solid St. Electron. 2, 35-67, (1961)

67. Plessner, K.W., Proc. Phys. Soc. London. 60, 243-56, (1948)

68. Budenstein, P.O., Hayes, P.J., Smith, J.L., and Smith, W.B., J. Vac. Sci. Tech. 6, 289-303, (1969)

69. Smith, J.L., and Budenstein, P.O., J. Appl. Phys. 40, 3491-98, (1969)

70. Smythe, W.R., Static and Dynamic Electricity (McGraw-Hill), (1968)

71. Davis, M.H., Q. Journal. Mech. and Appl. Math., 27, 499-511, (1964)

72. London, F., Trans. Far. Soc., 33, 8 - 26, (1937)

73. Lifshitz, E.M., Dzyaloshinski, E.M., and Pitaevskii, L.P., Adv. Phys. 10, 165-209, (1961)

74. Hamaker, H.C., Physica, 4, 1058-72, (1937)

75. Dahneke, B., J. Coll. and Int. Sci. 40, 1 - 13, (1971)

76. Cassmir, H.B.G., Proc. Kon. Med. Akad. Wetenschap. Ser B. 51, 793 - 815, (1948)

77. Lifshitz, E.M., Soviet, Phys. JETP. 2, 73 - 83, (1956)

78. Hargreaves, C.M., Proc. Kon. Med. Akad. Wetenschap. Ser. B. 68, 231-256, (1965)

79. Van Blokland, P.H.G.M., and Overbeek, J.T.G., Chem. Soc. Faraday Trans. I. 2367-2651, (1978)

80. Derjaguin, B.V., Kolloid, Z., 69, 155-164, (1934)

81. Young, T., Misc. Works. Vol. I, (Murray), p.418, (1805)

82. Dupré, Theorie Mechanique de la Chaleur (1869), (See Davis, J.T., and Rideal, E.R.,: Ind. Phen. (London:Academic Press)), (1963)

83. Johnson, K.L., Kendall, K., and Roberts, A.D., Proc. Roy. Socl. Ser A. 324, 301-13, (1971)

84. Gane, N., Pfaelzer, P.F., and Tabor, D., Proc. Roy. Soc. Land. A. 340, 495-517, (1974)

85. Bradley, R.S., Phil. Mag. 13, 853-862, (1932)

86. Derjaguin, B.V., Muller, V.M., and Toporov, Yu.P., J. Coll. Int. Sci. 53, 314-326, (1975)

87. Muller, V.M., Yushchenko, V.S., and Derjaguin, B.V., J. Coll. Int. Sci 77, 91-101, (1980)

88. Pollock, H.M., Shufflebottom, P., and Skinner, J. J. Phys. D.: Appl. Phys. 10, 127-138, (1977)

89. Krupp, A., and Sperlung, G., J. Appl. Phys. 37, 4176-80, (1966)

90. Van der Temple, M., Adv. Colloid Int. Sci. 3, 137-159, (1972)

91. Hays, D.A., Photo Sci. Eng. 22, 232-235, (1978)

92 Watson, P.K., Electrostatics, 1979, 1 - 8, (Conference on Electrostatic Phenomena) (1979)

93. Higginbotham, I.G., Williams, R.H., and McEvoy, A.J., J. Phys. D.: Appl. Phys. 8, 1033-43, (1975)

94. Berry, J.S., and Higginbotham, I.G., J. Phys. A. Math. Geo. 8, 1842-51, (1975)

95. Berry, J.S., J. Phys. A. Math. Gen. 9, 1939-45, (1976)

96. Friichtenicht, J.F., Nuc. Inst. Methods. 28, 70-78, (1964)

97. Brah, A.S., and Latham, R.V., Prov. VI - DEIV. 11-15, (1974)

98. Brah, A.S., and Latham, R.V., J. Phys. D.: Appl. Phys, 8, L109-111, (1975)

99. Brah, A.S., and Latham, R.B., Proc. VII-DEIV, 97-100, (1976)

100. Brah, A.S., Mohindra, S., and Latham, R.V., Proc. VIII DEIV. C6, 1 - 9, (1978)

101. Texier, C., Rev. Phys. Appl. (France), 13, 13-22, (1978)

102. Texier, C., Rev. Phys. Appl. (France), 13, 165-70, (1978)

103. Laurenson, L., Vacuum, 30, 275-81, (1980)

104. Harper, W.R., Contact and Frictional Electrification (London: Oxon. U.P.)

105. Vibrans. G., J. Appl. Phys. 35, 2855-2857, (1964)

106. Read, F.H., Adams, A., and Solo-Monteil, J.R., J. Phys. E.: Sci. Inst. 4, 625-32, (1971)

107. Wehner, G.K., Advance. Electron. Electron. Phys. 7, 289-298, (1955)

108. Farnsworth, H.E., and Taul, J., J. Phys. Chem. Solids, 9, 48-56, (1958)

109. Fitch, R.K., Khorassany, M., and Mawlood, T.N., Proc. 7th Int. Vac. Congr. and 3rd Int. Conf. on Sol. Surf. Vienna, 285-288, (1977)

110. Athwal, C.S., Ph.D. thesis, University of Aston, (1981)

111. Latham, R.V., High Voltage Vacuum Insulation; The Physical Basis Academic Press), (1981)

112. Rhorbach, F., Rpt. CERN, 71-38, (NTIS), (1971)

113. Halford, J.H., Chin, F.K., and Norman, J.E., J. Opt., Soc., Am., 63, 786-792, (1973)

114. Alpert, D., Lee, D.A., Lyman, E.M., and Tomanschke, H.E., J. Vac. Sco. Technol. 1, 35-50, (1964)

115. Little, R.P., and Whitney, W.T., J. Appl. Phys, 34, 2430-32, (1963)

116. Tsuchiya, K., and Tannai, T., Elec. Eng. in Hap. 89, 8-17, (1969)

117. Hurley, R.E., and Parnell, T.M., Brit. J. Appl. Phys, (J. Phys.D.) 2, 881-888, (1969)

118. Bowden, F.P., and Tabor, D., Friction and Lubrication of Solids, II, (Oxford Univ. Press), (1950)

119. Bowden, F.P., and Tabor, D., Friction and Lubrication of Solids, (London - Oxford Univ. Press), (1964)

120. Whitehouse, D.J., and Archard, J.F., Proc. Roy. Soc. Lond. A316, 97-121, (1970)

121. Greenwood, J.A., and Williamson, J.B., Proc. Roy. Soc. London A295, 300-19, (1966)

122. Pollock, H.M., J. Phys. D.: Appl. Phys. 11, 39-54, (1978)

123. Taylor, G.I., J. Inst. Civil. Engrs. 26, 496-519, (1946)

124. Davis, C.D., and Hunter, S.C., J. Mech, Phys, Solids, 8, 235-254, (1960)

125. Chaudhri, M.M., and Brophy, P.A., J. Mater. Sci. 15, 345-352, (1980)

126. Gane, N., Proc. Roy. Soc. Lond. A317, 367-91, (1970)

127. Gane, N., and Cox, J.M., Phil. Mag. 22, 881-891, (1970)

128. Shewman, P.G., Transformations in Metals, (McGraw-Hill, New York), (1969)

129. Samsanov, G.V., The Oxide Handbook, (Plenum - New York), (1973)

130. Grosskreuty, J.C., Surface Sci. 8, 173-90, (1967)

131. McFarlane, J.S., and Tabor, D., Proc. Roy.Soc. Lond. A202, 224-253, (1950)

132. Chaudhri, M.M., and Walley, S., Phil. Mag. A37, 153-165, (1978)

133. De Haller, P., Erosion und Kavitations-erosion. Handbuch der Werkstoffprufung, Vol. 2, (Springer-Verlag), 471-488, (1939)

134. Finnie, I., Wear, 3, 87-103, (1960)

135. Goodwin, J.E., Sage, W., and Tilley, G.P., Proc. Inst. Mech. Engrs. 184, 279-91, (1969)

136. Tabor, D., Surface Colloid. Sci. 5, 245-312, (1972)

137. Chakrabarti, A.K., Ph.D. thesis, University of Liverpool, (1975)

138. Carslaw, H.S., and Jaeger, J.C., Conduction of Heat in Solids. 2nd Ed. (London - Oxford University Press), 256-8, (1959)

139. McCracken, G.M., Rep. Prog. Phys. 38, 241-327, (1975)

140. Texier, C., Phys. Abstracts, No. 6700, 1-11, (1979)

141. Roberts, S., Phys. Rev. 118, 1509-18, (1960)

142. Butcher, E.C., Dyer, A.J., and Gilbert, W.E., J. Phys. D.: Appl. Phys. 1, 673-87, (1968)

143. Cathcart, J.V., Epperson, J.B., and Peterson, C.F., Acta. Metallurgy, 10, 699-708, (1962)

144. Boris, B.S., and Sparks, C.J., Acta, Crystallogr. 14, 569-78, (1961)

145. Hass, G. J. Opt. Soc. Amer. 39, 532-540, (1949)

146. Carbrera, N., and Mott, N.F., Rep.Progr.Phys. 12, 163-184, (1949)

147. Fane, R.W., and Neal, W.E.J., J. Opt. Soc. Amer. 60, 790-793, (1970)

148. Farrell, T., and Naybour, R.D., Natur Phys. Sci. 244, 14-15 (1973)

149. Agarwala, V.K., and Fort, T., Surf. Sci. 48, 527-536, (1975)

150. Hill, R.M., and Weaver, C., Trans. Faraday Soc. 54, 1140-52, (1958)

151. Park, R.L., Houston, J.F., and Schreiber, D.G., J. Vac.Sci. Tech. 9, 1023-31, (1972)

152. Andreeva, V.V., and Kazaren, V.I., Dolk. (Proc) Acad. Sci. USSR, Phys. Chem Sect. 123-148, (1958)

153. Tomashov, N.D., Alkovskii, R.M., and Tabushnerev, M., Dolk. Akad. Naukm (U.S.S.R.) Tom. 141, 2, (1961)

154. Andreeva, V.V., and Alekseeva, E.A., Dohl. Akad. Nauk, (U.S.S.R.) 134, 106-109, (1960)

155. Von Hippel, A.R., Dielectric Materials and Applications, (Wiley - New York) Pt.V, (1961)

156. Brenner, S.S., Wriedt, H.A., and Oriani, R.A., Wear. 68, 169-190, (1981)

157. Jenkins, J.E., and Chatterton, P.A., J. Phys. D.: Appl. Phys. 10, L17 - 23, (1977)

158. Drude, P., Ann. Phys. (Leipzig), 32, 584-591, (1887)

159. Drude, P., Ann. Phus. (Leipzig), 34, 489-510, (1888)

160. Drude, P., Ann. Phys. (Leipzig=, 36, 532-552, (1889)

161. Drude, P., Ann. Phys. (Leipzig), 39, 481-514, (1890)

162. Tronstad, L., Trans. Faraday Soc. 29, 502-514, (1933)

163. Winterbottom, A.B., Opt. Studies of Metal Surfaces (Bruns Bukhandel, Trondheim, 1955)

164. Ditchburn, R.W., J. Opt. Soc. Am. 45, 734-8, (1955)

165. McCracken, F.L., Passaglia, E., Stromberg, R.R., and Steinberg, H.L., J. Res. Nat. Bur. Std. 67A, 363-377, (1963)

166. Archer, R.J., Phys. Rev. 110, 354-358, (1958)

Physica 104C (1981) 17–24

MICROSCOPIC SURFACE PROCESSES ASSOCIATED WITH THE BOUNCING IMPACT OF CHARGED MICROPARTICLES ON HIGH VOLTAGE ELECTRODES

S. COOK and R.V. LATHAM

Department of Physics, University of Aston in Birmingham, Birmingham B4 7ET, U.K.

A vertically mounted dust-source microparticle facility has been used to study the semi-elastic impact behaviour of 0.1–10 μm diameter, positively charged, carbonyl iron microspheres with velocities in the range 1–50 ms^{-1} on a variety of target materials under zero field conditions and at a pressure of $\leq 10^{-7}$ mbar. The most significant finding has been that for non-metallic surfaces, such as glass, 99% of the incident particles undergo bouncing events with negligible charge exchange, whereas the incidence of bouncing events with metal targets is $\leq$1%. Aluminium, however, is an exception, and detailed measurements are reported on how the impact behaviour at localised sites depends on the surface conditions as monitored by a laser-based ellipsometer facility having a spatial resolution of $\approx$200 μm. A discussion is also included of the physical mechanisms that could account for the widely differing impact responses of the target materials studied.

1. Introduction

There have already been extensive reports, both from the author's laboratory [1–7] and elsewhere [8, 9] on simulation studies of the bouncing impact behaviour of charged microparticles in a high voltage vacuum gap. Our UHV experimental system is based on a microparticle gun which accelerates positively charged microspheres of diameter 0.1–10 μm to velocities of $\approx$1–50 ms^{-1} for undergoing controlled semi-elastic bouncing impact events on "commercially" polished target electrodes. "Test" surfaces may be further cleaned in situ by either Ar-ion etching or electron bombardment treatments, whilst their *mean* atomic state can be monitored by an ellipsometer facility prior to them being subjected to particle impact experiments. Results to date have shown that both the elastic character of an impact event and the efficiency of the associated charge exchange mechanism are strongly dependent on (i) the combination of target and particle materials, (ii) the target surface conditions (e.g. oxide coverage) and (iii) the magnitude of the gap field. Although a theoretical model has been proposed to explain these findings [6], it is difficult to evaluate since the recorded data exhibits a very large scatter due, it is thought, to the large variation in the microscopic properties across the target surface.

To confirm this assumption, and to obtain more detailed information on the impact process, the technique requires an improved spatial resolution, ideally in the micron range. This involves reducing both the impact zone for the test micro-particles and the spot size of the analytical ellipsometric facility making it possible to more accurately correlate the local properties of the surface with the observed particle impact behaviour. For this initial series of experiments the impact regime is further simplifed by making measurements under zero-field conditions.

A survey is also presented of the physical mechanisms that can operate during the impact process and hence influence the bouncing behaviour of particles. In this, particular attention will be given to the thermal effects associated with the charge transfer processes of in-flight field emission from the target to the particles and the electron tunnelling through the oxide junction contact, since these are thought to account for the widely differing particle bouncing behaviour between the various metal target materials studied.

2. Experimental procedure

Earlier results were obtained using the microparticle gun firing in the horizontal direction, with the result that microparticles emerging from the collimating apertures were deflected by gravity, thus making for a large degree of scatter on the target surface. To overcome this limitation the system has been modified to that shown in fig. 1, where the gun is now mounted vertically. With this new arrangement, microparticles emerge from the gun and its associated electrostatic focusing/decelerating lens to pass through a series of four collimating apertures before impacting on the target surface. The impact zone is now governed principally by the size of the final collimating aperture which for the present measurement was chosen to have a diameter of 1 mm. Full details of the operational principles and performance of the basic microparticle facility, including the drift tube detecting system can be found in refs. 3 and 5.

In order to use the complementary horizontal-plane ellipsometry facility (shown in fig. 2) for characterising the mean condition of the impact zone for the vertical firing regime, it has been necessary to develop the new target manipulator shown in fig. 1. With this, the target can be bombarded by microparticles when in the horizontal plane and on rotation through 180°,

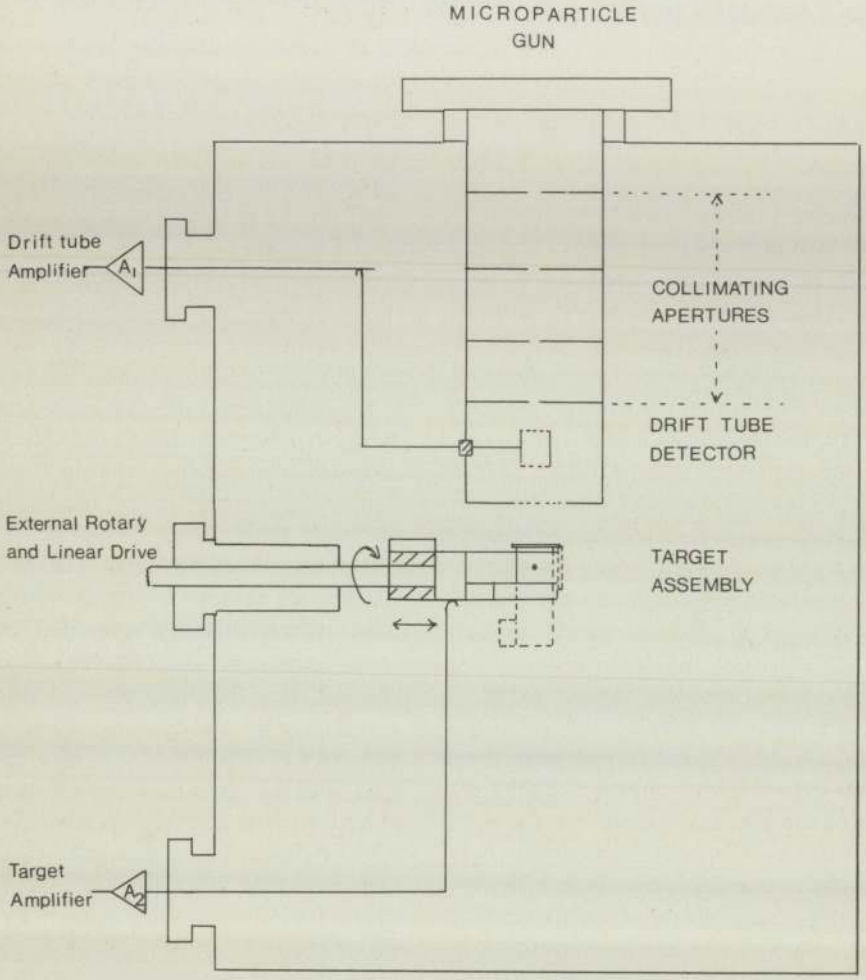

Fig. 1. Experimental regime of the vertical impact microparticle facility.

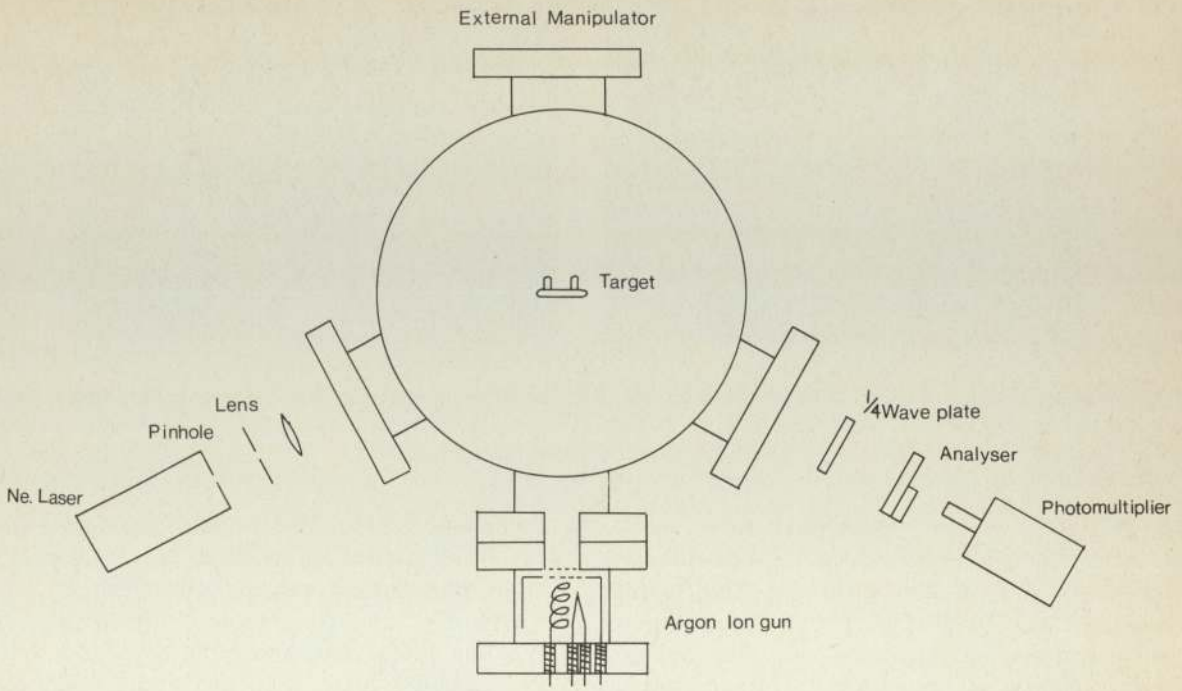

Fig. 2. Laser ellipsometric facility.

the cradle supporting the target pivots under the action of gravity thus bringing the target into a vertical position as shown by the dotted position in fig. 1. This now allows the ellipsometric facility to be used. A final rotation of 180° causes the cradle to return under gravity to its original position bringing the target back into its horizontal plane.

The series of experiments used "commercially" polished target surfaces (i.e. using a preparation sequence of 1/4 micron diamond polish, a spirit rinse and a final ultrasonic cleaning treatment), and were conducted at a pressure of $\approx 10^{-7}$ mbar which corresponds to the conditions used in earlier studies [1–10]. To investigate the variation of the mean particle impact response with surface conditions, five separate zones distributed at 1.6 mm intervals across the surface of the target are bombarded by a sample of 50 microspheres (0.2–5 μm diameter and having velocities in the range 1–50 ms^{-1}). Each zone then has its local surface conditions monitored with the ellipsometer facility shown in fig. 2, in which a Ne-laser is used for the light source. A target analysing area of approximately 0.2 mm can be realised with a 0.17 mm pin hole and lens system. Viewing through the quarter wave plate and analyser with a telescope, the laser beam is sighted onto the microparticle impact zones. With the photomultiplier in position the analyser is rotated until minimum intensity occurs, thus allowing the relative surface state of the impact zones to be determined.

3. Results

Impacting microparticle events are studied in terms of the oscillographic traces recorded by the drift-tube and target amplifiers where figs. 3(i) and (ii) shown, respectively, typical examples of "sticking" and "bouncing" events. The former are characterised by all the particle charge being dumped on the target, which decays with a time constant of ≈ 0.2 s determined by the target capacitance and the input capacitance and resistance of the amplifier. While both the drift-tube and target voltage amplifiers have the same gain

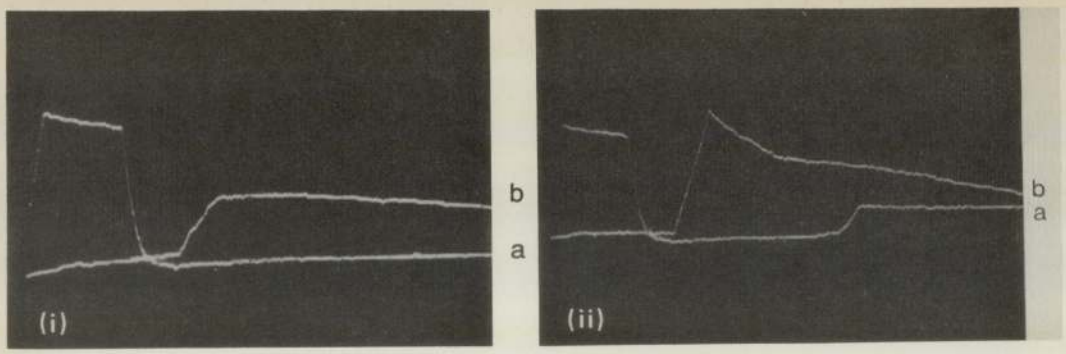

Fig. 3. (i) "Particle sticking" event. a = drift tube trace (sen. 0.05 V/div); b = target trace (sen. 0.05 V/div). Time base, 1 ms/div. (ii) "Particle bouncing" event. a = drift tube trace (sen. 0.05 V/div); b = target trace (sen. 0.05 V/div). Time base, 1 ms/div; initial velocity = 7.1 ms^{-1}; reflected velocity = 4.0 ms^{-1}; 72% charge exchange during impact.

(100 for the present amplifiers) their input capacitance are different, which accounts for the unequal heights of the drift-tube and target traces. For the "bouncing" event of fig. 3(ii) it will be seen that such events are characterised by a small fraction of the incident particle charge being dumped on the target with the reflected particle having a lower velocity (restitution coefficient ≈0.86). The shape of the target trace can be explained in terms of the total parallel input impedance appearing across the amplifier, where C_1 and R_1 denote, respectively, the effective capacitance and input resistance across the amplifier input. Fig. 4(i) and (ii) illustrate schematically how the respective "sticking" and "bouncing" event target signals are compiled

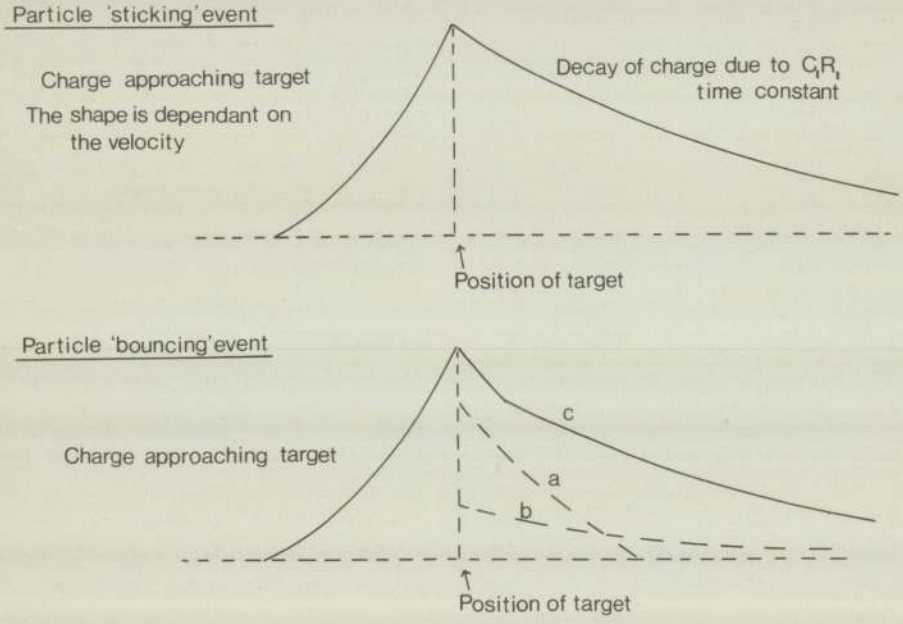

Fig. 4 Schematic representation of particle "sticking" and "bouncing" event. (a) Reflected particle having a reduced positive charge and slower velocity moving away from the target. (b) Decay of small positive charge remaining on the target with the C_1R_1 time constant. (c) Resultant waveform, i.e. (a) + (b).

from the separate particle and target processes. The form of the drift-tube traces will be assumed to be self-evident; but, in any case this point has been discussed in detail elsewhere [5, 10].

The most significant findings to emerge from comparative measurements made on conducting and insulating surfaces under zero field conditions is that the particle bouncing is very much more common with insulating surfaces. With metal surfaces such as titanium, copper and stainless steel, it is typical for over 99% of the low velocity ($\lesssim 5\,\mathrm{ms}^{-1}$) particles to stick to the surface, i.e. at volocities that are apparently below the critical value for inelastic impact [11]. On the other hand for insulating surfaces, such as glass, over 99% of the particles bounce with negligible charge modification and with rebound velocities that gives coefficients of restitution typically in the range 0.44–0.8.

However, with one metallic target material – aluminium – it was found that ≈10% of the particles executed bouncing behaviour, with the coefficient of restitution typically in the range 0.43–0.63. Although the reflected particle generally possessed a reduced positive charge, which was in agreement with the bouncing behaviour observed with other metal targets, there were consistently a finite number of events where the charge on the reflected particle had been partially reversed so that it returned through the drift tube as a negatively charged particle. This general pattern of behaviour is in good agreement to that reported by Texier [8, 9].

Since this material was the only one that exhibited a significant "bouncing" response it was chosen for the systematic investigation described in the previous section. Thus, table 1 gives the impact data for the five "test" impact sites, and indicates how many of the incident sample of 50 particles, respectively, "stick" and "bounce", the number of particles that return with a "reversed" charge, the mean coefficient of restitution of all the bouncing particles, and the mean charge modification ratio Q_2/Q_1 of those particles that return with a reduced positive charge. The complementary ellipsometric readings ϕ indicate the variation in the relative oxide thickness from zone to zone.

From an optical calibration measurement made in a subsidiary system on an atomically clean (argon-ion etched) aluminium surface, it was found that the ϕ-value was 129.6°, thus indicating that the larger the measured ellipsometric angle the smaller the oxide layer. With the present regime it was not however possible to quantitatively measure the absolute thickness of the oxide film; as a guide though, a change of $\Delta\phi \sim 1°$ corresponds to a change of ≈25 Å in the thickness of the mean oxide coverage.

To give further perspective to the impact regime, a target was removed from the specimen chamber for analysis in the S.E.M. Thus, fig. 5(i) is a typical S.E.M. micrograph of the impact zone showing a distribution of 1–8 μm diameter particles adhering to the surface, whilst fig. 5(ii) is a magnified view of a single microparticle on the surface.

Table 1
Microparticle input data for five zones on aluminium target

Impact zone	No. of sticking particles	No. of bouncing particles	No of bouncing particles with reversed charge	Average coef. of restitution	Average reflected/Incident charge for positive reflections Q_2/Q_1	Average ellipsometric readings ϕ (deg.)
1	46	4	1	0.49 ± 0.02	0.04 ± 0.05	127.2
2	45	5	1	0.51 ± 0.09	0.05 ± 0.05	127.3
3	43	7	4	0.52 ± 0.07	0.08 ± 0.09	128.1
4	46	4	2	0.48 ± 0.03	0.05 ± 0.06	128.6
5	41	9	4	0.55 ± 0.07	0.11 ± 0.1	127.0

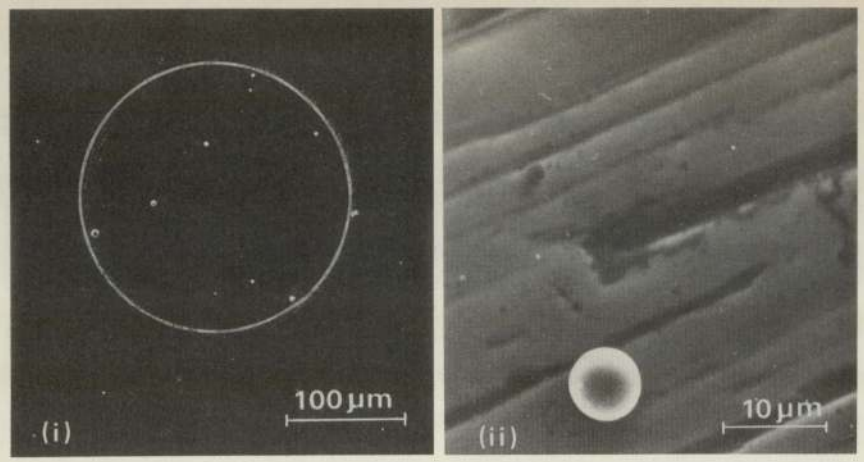

Fig. 5. (i) Micrograph showing microparticle impact zone: the circled region is the corresponding ellipsometric analysing area. (ii) Enlarged view of a single microparticle impact site.

4. Discussion

Although the particle "sticking" phenomenon, and its dependence on the electrical properties of the target surfaces, is the most significant finding to emerge from the investigation, we shall comment first on the physical implications of the systematic studies of the local particle impact behaviour over the surface of an aluminum target using the new vertically orientated microparticle facility and its associated ellipsometer probe. Referring to table 1, it will be seen first that there is no apparent correlation between the variation in both coefficient of restitution e and the charge modification ratio Q_2/Q_1 with the corresponding ellipsometric angle ϕ that can be taken as a measure of the mean state of surface oxidation at each zone. This therefore implies that maximum variation in oxide thickness of $\approx$40 Å between zones 4 and 5, i.e. corresponding to $\Delta\phi \sim 1.6°$, is too small to have any significant influence on either the mechanical or electrical interactions of the particles. There is, however, one important respect in which the data from this new and more refined technique differs markedly from early investigations [5] where results were averaged over an impact area of $\approx$2 cm^2; namely that there is a very much smaller scatter among the e-values associated with the individual bouncing events within a given (200 μm)^2 impact zone (see standard deviations given in table 1). This observation therefore suggests that the mechanical properties of surfaces do not vary greatly within a 200 μm range. In contrast, however, the electrical response, as measured by the Q_2/Q_1 ratio, still shows a large scatter (particularly if the small percentage of charge reversal events are taken into account), thus indicating that those microscopic electrical properties of surfaces that determine charge exchange process [6] (e.g. substrate work functions, oxide thickness and species) have to be defined on a micron scale.

We turn now to the physical origin of the zero-field particle "sticking" phenomenon that commonly occurs on target surfaces which closely resemble those found on the "commercially" polished electrodes conventionally used in high voltage devices. Three mechanisms must be considered.

(i) *Thermo-mechanical* welding, such as might be associated with a high velocity impact event where there is considerable plastic deformation and possibly melting of the impacting materials [11, 12]. This possibility is however discounted in the present experimental regime where the impact velocity range of 1–20 ms^{-1} is well below the 200–500 ms^{-1} quoted by other investigators for the critical microparticle velocity for inelastic impact [5, 11–13]. In further support of this

contention it should be remembered that nearly all particles bounce from an insulating surface where the predicted critical velocity [14] differs very little from that of, say aluminium.

(ii) *Thermo-electric welding I*, such as described by Beukema [15] in his modified trigger discharge model, where it was assumed that in-flight field electron emission raised the temperature of the particle surface sufficiently to cause local melting and hence welding on impact. From his analysis, the temperature rise ΔT to be anticipated with the present zero-field regime would be

$$\Delta T = 2iVt^{1/2}/\pi R_a^2 (\pi K \rho C)^{1/2},$$

where V is the potential of the charged sphere with respect to the target, i is an approximately constant emission current that flows for an "approach" time t, R_a is the radius of the electron impact region, whilst K, ρ and C are the thermal conductivity, density and specific heat of the particle, respectively. Substituting values for these parameters, as defined by Beaukema [15], for the case of a 3 μm radius ion microsphere having a charge of $\approx 10^{-15}$ C and a velocity of $\sim 7\,ms^{-1}$, which is typical of the present regime, we find $\Delta T \approx 80$ K. Since this is considerably smaller than the rise required to melt the iron sphere (melting point 1800 K), it would appear that this mechanism is also unlikely to be responsible for the "sticking" phenomenon. It should also be appreciated that the electron emitting surface of this model, namely the target, is covered with an oxide layer which will inhibit electron emission and further minimise the heating effect.

(iii) *Thermo-electric welding II*, such as could result from the energy dissipation associated with electron–phonon scattering processes in the interfacing oxide region between the particle and target where the electron tunnelling process described in the model of Latham and Brah [6] is taking place. It is proposed that this mechanism could dissipate sufficient energy to raise the temperature of the sub-micron junction region to a value at which melting, and hence welding, could occur. Although we have no direct evidence of this process, it is possible to cite the well-known thermally-based breakdown processes that occur with M.I.M. thin film dielectric devices as indirect evidence in support of this model [16]. It is also perhaps significant that the "sticking" phenomenon is more prevalent with metals such as titanium that have an insulating oxide film, and hence a higher tunnelling resistivity, than with aluminium ambient oxide which is very much more "lossy" due to the presence of hydroxyl ions [17, 18].

5. Conclusion

From studies based on a new low-velocity microsphere probe that is capable of investigating the impact response of $(200\,\mu m)^2$ isolated zones of a target surface, it has been established that the "scatter" observed among the individual impact events arises principally from variations in the microscopic electrical properties of the target surface: in particular, it is thought that these same properties determine whether a particle undergoes a "sticking" or "bouncing" event. The precise physical mechanism responsible for particle "sticking" remains uncertain, although one based on thermal heating through electron–phonon scattering processes in the oxide contact junction is currently favoured. To gain further insight into this phenomenon, it is intended to exploit the versatility of this new microparticle facility by extending these studies first to atomically clean target surfaces, and ultimately to high field impact regimes similar to those existing with operational high voltage electrode assemblies.

Acknowledgement

The authors wish to thank the Science Research Council for its support of this work.

References

[1] A.S. Brah and R.V. Latham, Proc. VI-DEIV (1974), 11.
[2] A.S. Brah and R.V. Latham, J. Phys. D: Appl. Phys. 8 (1975) L109.
[3] A.S. Brah and R.V. Latham, J. Phys. E: Sci. Instrum. 9 (1976) 119.
[4] A.S. Brah and R.V. Latham, Proc. VII-DEIV (1976) 97.
[5] R.V. Latham, A.S. Brah, K. Fok and M.O. Woods, J. Phys. D: Appl. Phys. 10 (1977) 139.

[6] R.V. Latham and A.S. Brah, J. Phys. D: Appl. Phys. 10 (1977) 151.
[7] A.S. Brah, S. Mohindra and R.V. Latham, Proc. VIII-DEIV. C6 (1978) 1.
[8] C. Texier, Rev. Phys. Appl. (France) 13, 1 (1978) 13.
[9] C. Texier, Rev. Phys. Appl. (France) 13, 4 (1978) 165.
[10] A.S. Brah, Ph.D. Thesis, University of Aston in Birmingham.
[11] H. Dietzel, G. Neuburn and P. Ranser, J. Geophys. Res. 77 (1972) 1375.
[12] V. Rudolph, Z. Naturf. 24a (1969) 326–331.
[13] D. Smith and N.G. Adams, J. Phys. D: Appl. Phys. 6 (1973) 700.
[14] M.A. Cook, The Science of High Explosives, (Reinhold, New York, 1958) 263.
[15] G.P. Beukema, J. Phys. D: Appl. Phys. 7 (1974) 1740.
[16] R.V. Latham, J. Phys. D: Appl. Phys. 5 (1972) 2044.
[17] J.G. Simmons, J. Appl. Phys. 34 (1963) 2581.
[18] D. Meyerhofer and S.A. Och, J. Appl. Phys. 34 (1963) 2535.